

UNCLASSIFIED

AD NUMBER

AD132167

LIMITATION CHANGES

TO:

Approved for public release; distribution is unlimited.

FROM:

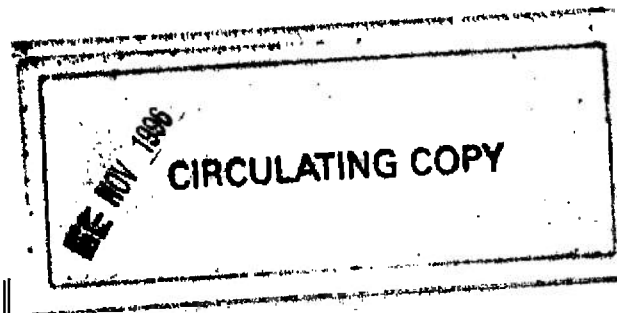
Distribution authorized to U.S. Gov't. agencies and their contractors;
Administrative/Operational Use; MAR 1957. Other requests shall be referred to Ballistic Research Lab., Aberdeen Proving Ground, MD.

AUTHORITY

BRL ltr 22 Apr 1981

THIS PAGE IS UNCLASSIFIED

132167



REPORT NO. 1005 PART I
MARCH 1957

PROCEEDINGS
OF THE
AERODYNAMICS RANGE SYMPOSIUM
JANUARY 1957

UNCLASSIFIED PAPERS

PROPERTY OF U.S. ARMY
STINTO BRANCH
BEL. APO, MD. 21005

Department of the Army Project No. 5B03-03-001
Ordnance Research and Development Project No. TB3-0108

BALLISTIC RESEARCH LABORATORIES



ABERDEEN PROVING GROUND, MARYLAND

Destroy when no longer
needed. DO NOT RETURN

BALLISTIC RESEARCH LABORATORIES

REPORT NO. 1005 PART I

March 1957

PROCEEDINGS
OF THE
AERODYNAMICS RANGE SYMPOSIUM
JANUARY 1957

UNCLASSIFIED PAPERS

PROPERTY OF U.S. ARMY
ORDNANCE BRANCH
TAG. REG. NO. 21003

Department of the Army Project No. 5B03-03-001
Ordnance Research and Development Project No. TB3-0108

ABERDEEN PROVING GROUND, MARYLAND

INTENTIONALLY LEFT BLANK.

TABLE OF CONTENTS

PART I

	Page
INTRODUCTION	5
LIST OF CONFEREES.	7
AGENDA	13
UNCLASSIFIED ABSTRACTS	17
UNCLASSIFIED TECHNICAL PAPERS	
A Correlation of Free-Flight Transition Measurements on Various Blunt Nose Shapes by Use of the Momentum-Thickness Reynolds Number W. R. Witt, Jr. and J. Persh	23
Advances in the Dynamic Analysis of Range Data C. H. Murphy.	45
Survey, Calibration and Reduction Techniques Used at the Thompson Aeroballistics Laboratory W. H. Allan and E. L. Dunn	85
Wake Visualization Studies in the Aeroballistics Range G. V. Bull and C. B. Jeffery.	127
The Controlled-Temperature-Pressure Range: Specification, Problems of Measurement, and Recent Programs F. D. Bennett.	149
Two Aeroballistic Range Topics: (1) Mass Asymmetry*; (2) Dynamic Stability J. D. Nicolaides.	183
An Application of Aeroballistics Range Techniques to Models with Digonal Rotational Symmetry G. H. Tidy and M. E. Thomas.	219

* With J. E. Long and G. Parrish

TABLE OF CONTENTS

	Page
Sabots Used at the Thompson Aeroballistics Laboratory	
W. H. Allan	241
Model Launching Techniques and Other Items Related to	
Range Firings J. E. Long.	273
APPENDIX: List of Published Descriptions of Ranges.	297
DISTRIBUTION LIST.	A1

INTRODUCTION

These volumes contain the papers presented at the Aerodynamics Range Symposium, sponsored by the Ballistic Research Laboratories. The meeting was held at Aberdeen Proving Ground on 24 and 25 January 1957.

The purposes of the symposium were to introduce the free flight range technique to a wider audience and to discuss applications of the technique to problems beyond the shell flight mechanics area.

Until recently, it has been generally felt that free flight ballistic ranges are limited principally to measurement of the small amplitude motion of shell. The papers show much broader applications of ranges. These include investigations of : nonlinear dynamics of shell, motion of aircraft models and of burning rockets, basic problems in fluid mechanics, and the design of hypersonic re-entry vehicles.

It now appears that the applicability of free flight spark photography ranges and of the older yaw card technique is limited only by the imagination of the user. Among the still incompletely explored possibilities are the application of telemetry to heat transfer measurements and to measurement of fluid properties at very high Mach Numbers.

The success of the meeting suggests that a similar meeting should be held within the next two years to help exploit the rapid expansion in free flight range technology.



C. L. POOR
General Chairman

INTENTIONALLY LEFT BLANK.

LIST OF CONFEREES

In addition to representatives of the Ballistic Research Laboratories, the following attended the Aerodynamics Range Symposium.

ADALIA LIMITED
Montreal, P. Q.
Reid, J. B.

AEROPHYSICS DEVELOPMENT CORP.
Pacific Palisades, California
Bitondo, D.

AIRCRAFT ARMAMENT, INC.
Cockeysville, Maryland
La Costa, N. S.

AIR FORCE ARMAMENT CENTER
Eglin Air Force Base, Florida
Haltom, C. M.
Jacobs, R.
Stevens, J. E.

AIR FORCE MISSILE TEST CENTER
Patrick Air Force Base, Florida
Burgess, J. A.
Mason, H. P.

APPLIED PHYSICS LABORATORY
Silver Spring, Maryland
Cramer, R. H.
Cronvich, L. L.
Wallskog, H. A.

ARMY BALLISTIC MISSILE AGENCY
Huntsville, Alabama
Reed, T. G.

ARO, INC.
Tullahoma, Tennessee
Kingery, M. K.
Zazzi, A. J.

AVCO MANUFACTURING COMPANY
Lawrence, Massachusetts
Munson, T. R.
Stephenson, W. B.

BELL AIRCRAFT CORPORATION
Buffalo, New York
Meullen, N. F.
Pearce, K.
Whalen, R. J.

BOEING AIRPLANE COMPANY
Seattle, Washington
Bateman, R. E.
Martin, D.
Wichita, Kansas
Wallace, R. E.

BRITISH JOINT SERVICES MISSION
Washington, D. C.
Clarke, A. E.
Walker, N. K.

BUDD COMPANY
Philadelphia, Pennsylvania
Bomberger, E. E.
Kessler, E. L.
Simpson, E. L.
Zettlemoyer, E. A.

BUREAU OF ORDNANCE, NAVY DEPARTMENT
Washington, D. C.
Baker, W. K.
Donoghue, F. D.
Griffin, T. F.
Nicolaidis, J. D.

CANADAIR
Montreal, P. Q.
Jackman, D. A.
Luckert, H. J.

CANADIAN WESTINGHOUSE COMPANY
Hamilton, Ontario
Leavitt, J. N.

CANADIAN ARMAMENT RESEARCH AND
DEVELOPMENT ESTABLISHMENT

Quebec, P. Q.
Bull, G. V.
Greenwood, E. W.
Tidy, G. H.
Waldock, D. A. G.

CHAMBERLAIN CORPORATION

Waterloo, Iowa
Caponi, E. R.

CHICAGO MIDWAY LABORATORIES

Chicago, Illinois
Malis, M. F.

COMPUTING DEVICES OF CANADA LTD.

Ottawa, Ontario
Howland, J. L.
Jeffery, C. B.
Smith, J. E.

CONVAIR

Dangerfield, Texas
Goin, K. L.
San Diego, California
Frick, C. W.
Katz, E.
Romig, M. F.
Starr, S. V.

CORNELL AERONAUTICAL LABORATORY, INC.

Buffalo, New York
Russo, A. L.
Whiting, A. A.

DEFENCE RESEARCH BOARD

Ottawa, Ontario
Oatway, J. L.

DeHAVILLAND AIRCRAFT OF CANADA, LTD.

Toronto, Ontario
Pounder, D. W.
Warren, H. R.

DIAMOND ORDNANCE FUZE LABORATORIES

Washington, D. C.
Bowles, R.
Brody, P.
Curchack, H.
Dellasanta, O.
Harris, F.
Keto, F.
Van der Linden, R.

DIRECTORATE OF ARMAMENT DEVELOPMENT

Ottawa, Ontario
Snarr, W. B.

DOUGLAS AIRCRAFT COMPANY, INC.

El Segundo, California
Newton, F. C.
Santa Monica, California
Cohen, W. S.
Klein, H.

FIRESTONE TIRE AND RUBBER COMPANY

Akron, Ohio
Lucas, V. E.

FRANKFORD ARSENAL

Philadelphia, Pennsylvania
Brady, J.
Bushey, B.
Cianciosi, A.
Dickey, C.
Halloran, J.
Kymer, J.
Lipinski, H.
Otis, W.
Steinberg, J.
Tanik, L.
Yannuzzi, A.

GENERAL ELECTRIC

Philadelphia, Pennsylvania
Kebely, V.
Peck, R. F.
Powers, J.
Smith, A. M.
Warren, W. R.
Yoler, Y. A.

GENERAL MILLS, INC.
Minneapolis, Minnesota
Hakomaki, R. I.

GLENN L. MARTIN COMPANY
Baltimore, Maryland
Bidwell, J. M.
Coon, M. L.
Jackson, L. L.
Reisert, T.

GRUMMAN AIRCRAFT ENGINEERING CORP.
Bethpage, New York
Gustafson, R. L.
Munier, A. E.
Scheuing, R. A.

HUGHES AIRCRAFT COMPANY
Culver City, California
Naiman, I.
Phillips, W. L.

JET PROPULSION LABORATORY
Pasadena, California
Eimer, M.
Schurmier, H. R.
Wegener, P. P.

LOCKHEED AIRCRAFT CORP.
San Jose, California
Marsh, B. W.
Tucker, M.
Wilson, L. H.
Van Nuys, California
Bershaded, E.
Cannon, E. T.
Swanson, R. S.

MCDONNELL AIRCRAFT CORP.
St. Louis, Missouri
Rohtert, R. E.

MASSACHUSETTS INSTITUTE
OF TECHNOLOGY
Cambridge, Massachusetts
Durgin, F. H.
Wilkie, L. E.

NATIONAL ADVISORY COMMITTEE FOR
AERONAUTICS

Headquarters, Washington, D. C.
Abbott, I. H.
May, R. E.
Ames Laboratory
Moffett Field, California
Allen, H. J.
Canning, T.
Neice, L.

Langley Aeronautical Laboratory
Langley Field, Virginia
Bird, J. D.
Hopko, R.
Huber, P.
Sabol, A.

Lewis Flight Propulsion Laboratory
Cleveland, Ohio
Reshotko, E.

NATIONAL RESEARCH COUNCIL OF CANADA
Ottawa, Ontario
Lukasiewicz, J.
Templin, R. J.

NAVAL AIR MISSILE TEST CENTER
Point Mugu, California
Fitzgerald, M.

NAVAL ORDNANCE LABORATORY
Silver Spring, Maryland
Auld, C. D.
Brady, J. J.
Carter, H.
Chamberlin, A.
Crogan, L. E.
Dawson, V. C.
Diggins, J. L.
Fedenia, J. N.
Gallagher, J. J.
Greenwald, A.
Hall, D.
Jusino, J. B.
Kurzweg, H. H.
Lightfoot, G. R.
Long, J. E.
May, A.
Roberts, J.
Seigal, A. E.

NAVAL ORDNANCE LABORATORY (Cont'd)

Sheppard, B. S.
Slawsky, Z. I.
Thurston, P. A.
White, C. E.
Winkler, E.
Witt, W. R.

NAVAL ORDNANCE TEST STATION

China Lake, California

Allan, W. H.
Dunn, E. L.
Haseltine, W. R.
Mayfield, E. B.
Newkirk, H. L.

NAVAL PROVING GROUND

Dahlgren, Virginia

Anderle, R. J.
Brown, D. R.
Cohen, C. J.
Frick, C. H.
Hubbard, E. C.
Jones, A. L.
Mitchell, J.
Mulligan, J. E.

NAVAL RESEARCH LABORATORY

Washington, D. C.

Atkins, W. W.
Fuller, R. H.

NORTH AMERICAN AVIATION, INC.

Columbus, Ohio

Simon, W. E.
Downey, California
Briggs, E.
Dew, J. K.
Oliver, R. B.

OFFICE ASSISTANT SECRETARY
OF DEFENCE (R&D)

Washington, D. C.
Nestingen, I.

OFFICE OF NAVAL RESEARCH

Washington, D. C.
Sherman, F. S.

PICATINNY ARSENAL

Dover, New Jersey

Carson, W.
Costa, D.
Loeb, A. A.
Pallington, A.
Spector, J.
Trevorrow, D.

RAMO-WOOLDRIDGE CORP.

Los Angeles, California

Ambrosio, A.
Hayes, W. D.

REDSTONE ARSENAL

Huntsville, Alabama

Murphree, W. D.
Newby, D. H.
Northrop, C. L.
Shapiro, N. M.

REPUBLIC AVIATION CORP.

Farmingdale, New York

McIlroy, W.
Rennemann, C.
Sanator, R.
Mineola, New York
Kennedy, R. M.

A. V. ROE CANADA LTD.

Malton, Ontario

Chamberlin, J. A.
Taylor, W.

ROSEMOUNT AERONAUTICAL LABORATORIES

Rosemount, Minnesota

Deleo, R. V.
Herman, R.
Moynihan, F. A.

SANDIA CORPORATION

Albuquerque, New Mexico

Vaughn, H. R.

UNITED AIRCRAFT CORPORATION

East Hartford, Connecticut

Taylor, W.

UNIVERSITY OF SOUTHERN CALIFORNIA
Los Angeles, California
Dailey, C. L.

WATERTOWN ARSENAL
Watertown, Massachusetts
Muldoon, R.

WRIGHT AIR DEVELOPMENT CENTER
Dayton, Ohio
Huber, F. J.
Liu, Tung-Sheng
Shorr, M.

INTENTIONALLY LEFT BLANK.

AGENDA*

Thursday, 24 January 1957

<u>Registration</u>	8:15 - 9:00 am
<u>Welcome</u>	9:00 - 9:15 am
Col. C. L. Register Director, Ballistic Research Laboratories	
<u>Remarks by General Chairman</u>	9:15 - 9:30 am
Mr. C. L. Poor Chief, Exterior Ballistics Laboratory	
<u>Session I</u>	9:30 - 11:10 am
Chairman, Dr. H. H. Kurzweg Associate Technical Director Naval Ordnance Laboratory	
Simulation of the Atmospheric Entry of Ballistic Missiles (CONFIDENTIAL) <u>S. E. Neice and J. A. Carson</u> Ames Aeronautical Laboratory, NACA	
Some Problems Associated with the Determination, from Range Firings, of Dynamic Stability of Ballistic Missile Re-Entry Shapes (CONFIDENTIAL) <u>L. C. MacAllister</u> Ballistic Research Laboratories	
<u>Lunch</u>	At Transonic Range and Officers Club
<u>Session II</u>	1:00 - 4:40 pm
Chairman, Mr. H. Julian Allen Chief, High-Speed Research Division Ames Aeronautical Laboratory, NACA	
A Correlation of Free-Flight Transition Measurements On Various Blunt Nose Shapes by Use of the Momentum- Thickness Reynolds Number <u>W. R. Witt, Jr. and J. Persh</u> Naval Ordnance Laboratory	
Advances in the Dynamic Analysis of Range Data <u>C. H. Murphy</u> Ballistic Research Laboratories	

* Papers were presented by those whose names are underlined.

Survey, Calibration, and Reduction Techniques
Used at the Thompson Aeroballistics Laboratory
W. H. Allan and E. L. Dunn
Naval Ordnance Test Station

Wake Visualization Studies in the Aeroballistics
Range

G. V. Bull, and C. B. Jeffery
Canadian Armament Research and Development
Establishment

The Controlled-Temperature-Pressure Range

F. D. Bennett
Ballistic Research Laboratories

Tour

5:00 - 6:00 pm

Aerodynamics Range
CTP Range and Wind Tunnels

Social Hour and Dinner

Friday, 25 January 1957

Session III

8:30 - 11:20 am

Chairman, Brigadier D. A. G. Waldock
Chief Superintendent
Canadian Armament Research and Development
Establishment

Two Aeroballistic Range Topics:

- (1) Mass Asymmetry*; (2) Dynamic Stability
J. D. Nicolaides
Bureau of Ordnance

Design and Initial Tests of the NOL Shock Gun (CONFIDENTIAL)

V. C. D. Dawson
Naval Ordnance Laboratory

An Application of Aeroballistics Range Techniques
to Models with Digonal Rotational Symmetry

G. H. Tidy and M. E. Thomas
Canadian Armament Research and Development
Establishment

Sabots Used at the Thompson Aeroballistics Laboratory

W. H. Allan
Naval Ordnance Test Station

Lunch

At Transonic Range and Officers Club

* With J. E. Long, U. S. Naval Ordnance Laboratory and G. Parrish,
Bureau of Ordnance.

Chairman, Dr. W. R. Haseltine
Head, Ballistics Division
Naval Ordnance Test Station

Research Investigations in the Ames Supersonic Free-
Flight Facilities (CONFIDENTIAL)

T. N. Canning

Ames Aeronautical Laboratory, NACA

Aeroballistic Range Measurements of the Performance
and Stability of a Supersonic Fighter Aircraft
(CONFIDENTIAL)

H. R. Warren*, R. J. Templin** and B. Cheers

Canadian Armament Research and Development
Establishment

Model Launching Techniques and Other Items Related
to Range Firings

J. E. Long

Naval Ordnance Laboratory

Closing Remarks

3:20 - 3:30 pm

Mr. C. L. Poor

Saturday, 26 January 1957

Tour

10:00 - 1:00 pm

Naval Ordnance Laboratory
Aeroballistic Facilities

* DeHavilland Aircraft of Canada Limited.

** National Aeronautical Establishment.

INTENTIONALLY LEFT BLANK.

SIMULATION OF THE ATMOSPHERIC ENTRY OF BALLISTIC MISSILES II: 13

(CONFIDENTIAL)

S. E. Neice and J. A. Carson
Ames Aeronautical Laboratory, NACA

Abstract is Classified

SOME PROBLEMS ASSOCIATED WITH THE DETERMINATION, FROM RANGE FIRINGS, OF DYNAMIC STABILITY OF BALLISTIC MISSILE RE-ENTRY SHAPES II: 37

(CONFIDENTIAL)

L. C. MacAllister
Ballistic Research Laboratories

In the past, free flight ranges have been useful in the determination of the dynamic stability of bodies of revolution and of symmetric missiles. Recently a considerable amount of work has been devoted to firings of models of war heads. The conditions under which the models are fired and the aerodynamic properties of the shapes make the determination of the dynamic stability of the models quite difficult. The problems that arise and some possible solutions are discussed.

A CORRELATION OF FREE-FLIGHT TRANSITION MEASUREMENTS ON VARIOUS BLUNT NOSE SHAPES BY USE OF THE MOMENTUM-THICKNESS REYNOLDS NUMBER I: 23

W. R. Witt, Jr. and J. Persh
U. S. Naval Ordnance Laboratory

A systematic series of blunt nose shapes has been fired in the Pressurized Ballistics Range for boundary-layer transition studies. The transition of the boundary-layer flow from laminar to turbulent is determined directly from the shadowgraph plates. The nose shapes have all been fired near a Mach number of 3 and the Reynolds number per foot has been varied by changing the pressure (density in the firing range).

The Reynolds number based on momentum thickness, Re_θ , at the observed transition location, was calculated using the laminar boundary-layer calculation method given by Cohen and Reshotko in "The Compressible Laminar Boundary Layer with Heat Transfer and Arbitrary Pressure Gradient" (NACA TN 3326). In general, the results indicate that transition occurs at values of Re_θ which are of the same order of magnitude as the values of minimum critical Reynolds number usually associated with incompressible flow.

ADVANCES IN THE DYNAMIC ANALYSIS OF RANGE DATA

I: 45

C. H. Murphy
Ballistic Research Laboratories

The range technique has been usually restricted to dynamic analysis of the motion of thrustless symmetric missiles acted on by linear aerodynamic forces. In recent years all three of these restrictions have been relaxed.

First, a gun-boosted burning rocket program fired on the Transonic Range is described and the relatively minor alterations to the data analysis procedure are indicated. Next the more difficult problem of a finned missile with bent fins and spin rate varying through resonance is discussed. Finally, the successful treatment of cubic nonlinearities in static and Magnus moments and their associated forces is described.

SURVEY, CALIBRATION, AND REDUCTION TECHNIQUES USED AT THE THOMPSON AEROBALLISTICS LABORATORY

I: 85

W. H. Allan and E. L. Dunn
U. S. Naval Ordnance Test Station

The cameras of the Thompson Aeroballistics Laboratory are calibrated once a year by photographing reference markers in the field of view of each camera. Three wires, anchored to towers at each end of the range, are suspended in space near the range line. The reference markers are 1/8-inch plastic beads located every two feet along the wire. This paper describes the techniques used to measure the coordinates of the cameras and the plastic beads; the mathematical treatment of these coordinates to furnish calibration equations for each camera; the use of the equations in solving for orientation and location of the missile in space; the results obtained through this system; and a discussion of the limitations and advantages of this system.

G. V. Bull and C. B. Jeffery
Canadian Armament Research and
Development Establishment

By the interaction of hydrochloric acid and ammonium hydroxide vapours, a plane sheet of laminar smoke filaments can be produced in the range along the flight trajectory. Models developing lift due to incidence were fired through these planar sheets. Spark and fastax photography was used to record the development of the wake profiles in the plane of the smoke. Wake distortions and vortex formations have been studied for several types of bodies; for a cruciform arrangement of rectangular panels of aspect ratio 1.9 on a cylindrical body, the wake distortion as determined from these tests have been compared with computations based on the assumptions of linear theory.

THE CONTROLLED-TEMPERATURE-PRESSURE RANGE

I:149

F. D. Bennett
Ballistic Research Laboratories

A survey is given of the research and development program which has culminated in operation of the Controlled-Temperature-Pressure Range (CTPR) for production of flows up to Mach 11. Methods of control of temperature and pressure in the 45' working section are described. The instrumentation necessary for (1) measurement of projectile drag coefficient and (2) measurement of density throughout the field of flow is discussed in some detail. The 10" Mach-Zehnder interferometer is a special feature. Various research problems encountered in the development of light sources, projectile launchers and data handling schemes are briefly touched upon.

At low supersonic Mach numbers a problem requiring the full field of the 10" Mach-Zehnder interferometer has recently been completed. Here a study of phenomena in the distant N-wave flow about a small sphere has led to a new and simple experimental criterion for N-wave flow and to information about convergence to N-wave flow with radial distance from the projectile.

J. D. Nicolaides
Bureau of Ordnance

(1) MASS ASYMMETRY

with

J. E. Long, U. S. Naval Ordnance Laboratory
Gene Parrish, Bureau of Ordnance

A simple approximate theory for the free flight motion of ballistic missiles having mass asymmetry is given and proofed by experimental firings in the NOL Pressurized Aeroballistic Range.

(2) DYNAMIC STABILITY

The Epicyclic Theory for the flight dynamics of ballistic missiles has yielded various "Dynamic Stability Criteria" which are often used to evaluate missile performance. Recent misleading uses of the theory and criteria in appraising missile performance require a simple restatement of the theory, its assumptions and its use.

The parameters of Nutation Half-Life, Precession Half-Life and Total Motion Half-Life are suggested as better criteria for missile dynamics than those classically based on the Linear Theory.

Also a summary of important Nonlinear Cases of ballistic missile flight performance is given.

DESIGN AND INITIAL TESTS OF THE NOL SHOCK GUN

II: 61

(CONFIDENTIAL)

V. C. D. Dawson
U. S. Naval Ordnance Laboratory

The design and initial tests of the NOL Shock Gun are described. The operation of this gun, which was conceived by Dr. A. E. Seigel and Dr. Z. I. Slawsky, is based upon a new principle and missiles weighing two grams have been launched from a 0.50-caliber smooth-bore gun at velocities in excess of 13,000 feet per second.

AN APPLICATION OF AEROBALLISTICS RANGE TECHNIQUES
TO MODELS WITH DIGONAL ROTATIONAL SYMMETRY

I: 219

G. H. Tidy and M. E. Thomas
Canadian Armament Research and
Development Establishment

A series of flat plate wings of triangular planforms has been fired at Mach numbers 1.5 and 2 and their trajectories have been measured.

Preliminary manual reduction of the data is presented and the derived values of some aerodynamic coefficients are compared with NACA wind tunnel measurements. The possibility of more complete analysis and of application of the range technique to airplane configurations are considered.

SABOTS USED AT THE THOMPSON AEROBALLISTICS LABORATORY

I: 241

W. H. Allan
U. S. Naval Ordnance Test Station

A review of sabots used at the Thompson Aeroballistics Laboratory from the beginning of operations to the present. The discussion will cover spinner and finner sabots used in guns ranging from 40-mm to 8-inch bore diameter. Follow-thru, breakapart, slug styrofoam, and slow-spin smooth bore sabots will be discussed along with the use of the sabot retarder.

RESEARCH INVESTIGATIONS IN THE AMES
SUPERSONIC FREE-FLIGHT FACILITIES

II: 81

T. N. Canning
Ames Aeronautical Laboratory, NACA

Abstract is classified.

AEROBALLISTIC RANGE MEASUREMENTS OF THE
PERFORMANCE AND STABILITY OF A SUPERSONIC
FIGHTER AIRCRAFT

II: 101

(CONFIDENTIAL)

H. R. Warren*, R. J. Templin**, and B. Cheers
Canadian Armament Research and
Development Establishment

This paper describes a method being developed for measuring aircraft performance and stability characteristics in free flight. Tests have been made firing into the Aeroballistics Ranges small scale models of a current delta wing fighter at a supersonic Mach number and approximately 1/10 its combat Reynolds number. Velocity screens, schlieren and yaw card measurements are used to obtain histories of the models speed, altitude and later motion during flight. From the analysis of these records information is obtained about the aircraft drag, lift, lateral and longitudinal aerodynamic derivatives.

* DeHavilland of Canada, Limited

** National Aeronautical Establishment

MODEL LAUNCHING TECHNIQUES AND OTHER ITEMS
RELATED TO RANGE FIRINGS

I: 273

J. E. Long
U. S. Naval Ordnance Laboratory

A discussion of the variety of methods used to launch scaled models in the free-flight precision ranges at NOL is given. These methods include such items as: (1) launching finned missiles from rifled guns; (2) launching subcaliber spinning models from over-sized sabots; (3) launching spheres as small as 1/32 inch in diameter for drag; and (4) launching model aircraft.

Under related items the discussion will be centered about the following techniques: (1) firing models with a jet exhausting from the model base; (2) investigating the arming of fuzes by X-raying the recovered round; (3) firing spinning models with hot and cold plastics rotating bands; (4) development of the spin sonde; and (5) firing models from powder guns at 10,000 ft/sec.

A CORRELATION OF FREE-FLIGHT TRANSITION
MEASUREMENTS ON VARIOUS BLUNT NOSE SHAPES
BY USE OF THE MOMENTUM-THICKNESS REYNOLDS NUMBER

W. R. Witt, Jr.
J. Persh

U. S. Naval Ordnance Laboratory
White Oak, Silver Spring, Maryland

INTENTIONALLY LEFT BLANK.

A CORRELATION OF FREE-FLIGHT TRANSITION
MEASUREMENTS ON VARIOUS BLUNT NOSE SHAPES
BY USE OF THE MOMENTUM-THICKNESS REYNOLDS NUMBER*

INTRODUCTION

One of the greatest uncertainties in the prediction of the heat transfer to arbitrary body shapes is the location of the transition "point." While laminar boundary-layer theory yields indications of the probable effects of several variables on boundary-layer transition, it does not permit prediction of the transition "point."

For some time we have been investigating boundary-layer transition in the Pressurized Ballistics Range at the Naval Ordnance Laboratory. The transition "point" is determined directly from the shadowgraph plates and is taken as the position at which small eddies first appear in the boundary layer.

Our earlier investigations, sponsored by the U. S. Air Force, have previously been reported (reference a). These firings were made with 10-degree included angle cones that had polished or ground-finished

* Published in report form at NOL as NavOrd 4400. Supported by the U. S. Air Force

surfaces, and sharp or slightly blunted tips. Results of these earlier investigations were as follows:

a. For a highly-polished (1 to 2 microinch) sharp-pointed cone, transition was found to occur at free-stream Reynolds numbers varying from 1 million to 21 million at small angles of attack under similar firing conditions

b. On a rougher cone (8 to 10 microinches) with a slightly blunted tip (0.0625 Dia.) the same maximum Reynolds numbers of transition were obtained as on the polished cone. The low values of Reynolds number of transition, however, observed on the smooth cone were not obtained with the slightly blunted, rougher cone.

The recent tests which are to be described here were also fired in the Pressurized Ballistics Range. This range is well-suited to the investigation of boundary-layer behavior for the following reasons:

- a. The turbulence level is negligible
- b. The air pressure (density) can be varied, permitting a wide range of Reynolds number per foot (much larger than can usually be obtained in wind tunnels)
- c. Numerous spark shadowgraph stations are available permitting both horizontal and vertical observations.

The quality of the results obtained from a boundary-layer study in free flight will depend on how well the following parameters can be controlled or known accurately:

- a. Mach number
- b. Body geometry or pressure distribution

- c. Range pressure (Re/ft)
- d. Surface finish
- e. Angle of attack
- f. Heat transfer (T_w/T_∞)

The present study was made with the models shown on Figure 1 with most of these six parameters held constant. These nose shapes include 20-degree and 40-degree cones with nose-to-base radii of 0.75, 0.500, 0.250, and 0.125 and cone-like noses based on $1/2$ and $1/3$ power curves. For these firings the Mach number has been in the neighborhood of 3 and the range pressure was varied from $1/2$ to $2-1/4$ atmospheres, with one shot at 5 atmospheres.

For the firings discussed herein, the wall temperature of the models was essentially room temperature. However, equipment has been developed which will permit the temperature of 10-degree cones to be raised as high as 1000 degrees Fahrenheit immediately before firing.

Complete control of the angle of attack is impossible in range firings. The models for transition studies are always designed so as to keep these angles small ($0 < \alpha < 4^\circ$). Since the angle of attack cannot be controlled accurately, it can be treated as a correlation parameter (see reference a).

Surface roughness cannot be eliminated but polishing techniques can reproduce a smooth surface rather well. A number of the $1/2$ power and $1/3$ power noses were polished to a 1 to 2 microinch finish. The cones were unpolished (8 - 10 microinches). A detailed account of the polishing technique and of the surface-measuring method can be found in reference (a).

Pressurized Ballistics Range

The Pressurized Ballistics Range (Figure 2) is an enclosed tube three feet in diameter and 300 feet long in which the pressure can be varied from 0.01 to 6 atmospheres. There are twenty-five stations at which spark shadowgraphs can be taken of the model in flight. As the model approaches each station (Figure 3) a spark is initiated by the pulse from a photoelectric pickup unit. At each station the light from the spark falls directly on a vertical photographic plate and is reflected by a mirror onto a horizontal plate. The times at which the sparks flash at any 13 of the 25 stations are recorded on electronic counters.

Symbols and Definitions

M = Mach number

P₀ = free-stream stagnation pressure

Re_θ = Reynolds number based on momentum thickness (θ)

r = local radius of model

R = radius at base of model

s = distance measured along surface of model

T = local static temperature

u = longitudinal velocity component

y = distance perpendicular to surface

θ = boundary-layer momentum thickness = $\int \frac{\rho u}{\rho_e u_e} \left[1 - \frac{u}{u_e} \right] dy$

θ_v = half-angle of cones

μ = viscosity coefficient

ν = kinematic viscosity coefficient

ρ = density

Subscripts:

e = local conditions outside boundary layer
w = wall or surface value
 ∞ = initial or free-stream value

Data Recorded

The two spark shadowgraphs obtained from each station give horizontal and vertical projections of the model and of the flow pattern. The transition is well defined except in the optically distorted region near the front of blunt-nosed bodies. As mentioned before, transition is detected by locating the formation of small eddies or vortices in the boundary layer. From each plate the position of transition is measured both on the windward and sheltered sides of the cone. Thus there are four transition readings at each station. Three typical spark shadowgraph prints are shown as Figures 4, 5, and 6. The true angle of attack is calculated from the horizontal and vertical components of the angle of attack that are read from the plates. Since neither of the shadowgraph plates is, in general, parallel to the plane of the angle of attack, the fully windward and fully sheltered sides are not seen. The fully windward side can be determined and the four transition readings at each station can be related (in azimuth) to the true wind vector.

Since from one shot sixty transition measurements are normally obtained, one representative transition length had to be selected for each shot. This was done by taking an average of the readings from the vertical plates. The vertical plate readings were selected

since these readings are more accurate than the readings from the horizontal plates because the reflected light from the mirror (Figure 3) does not give as good a shadowgraph.

Results

It appears reasonable that any correlation of boundary-layer transition on body shapes with pressure gradients should involve Reynolds numbers based on flow properties outside the boundary layer and some characteristic thickness associated with the boundary layer.

Of the boundary-layer parameters considered (total thickness, displacement thickness, and momentum thickness), the boundary-layer momentum thickness appears most reasonable. The momentum thickness may be defined as the thickness of a layer in the free-stream flow having a momentum equal to the loss of momentum in the boundary layer due to viscous effects. Now for a look at the results and the success of the correlation.

The transition data discussed here were obtained from thirty-one shots including sixteen firings with the $1/2$ and $1/3$ power noses. The data from these firings are listed on Table I. The variation of Re_θ with distance along the surface was calculated up to the observed transition point using the method given by Cohen and Reshotko in reference (b). The use of this method requires a knowledge of the surface pressure and temperature distributions at the edge of the boundary layer in addition to the wall temperature. The pressure distribution was determined by use of the modified Newtonian flow concept (reference c), and the temperature distribution was calculated

using the perfect gas isentropic flow relations. While it is realized that the Newtonian flow calculation procedure is inadequate for the slender cone models, it was felt that for consistency it should be used for all of the configurations investigated. The model wall temperature was assumed to be room temperature and unchanged during the short time of flight (duration of less than 0.1 seconds). This is a reasonable assumption since the calculation scheme utilized is not particularly sensitive to small changes in wall temperature. It is important to mention that the transition "point" Re_0 values obtained are presumably associated with the end of transition even though they are based on the average of numerous readings per shot. Justification for the statement that the first appearance of turbulence on the photographs indicates the end of transition was reported by Grunewald (reference d). In Grunewald's wind-tunnel investigation it was shown by comparisons between surface temperature data and schlieren observations that the end of transition is observed. Effectively, if this is the actual case, this means that the transition region, which may be of appreciable length, is neglected and it is assumed that laminar flow exists in this region. Since the length of the transition region depends on a combination of several parameters, it is not possible to assign a specific adjustment factor to the data which are presented. However, Mr. Persh of NOL has a NavOrd report ready for publication (reference g) in which he describes a technique for calculating the boundary-layer development in the transition region.

Figure 7 shows how the values of $Re_{\theta_{tr}}$, determined as previously described, vary with the incompressible Pohlhausen (reference f) pressure gradient parameter, $Re_{\theta} \frac{\theta}{u_e} \frac{du_e}{ds}$. This pressure gradient parameter was chosen as the abscissa because of its familiarity and apparent suitability as a correlation parameter for compressible flows. Also included in this figure are the subsonic data reported by Persh (reference e). It is important to point out that the subsonic data are for the start of transition and, therefore, represent an earlier part of the transition regime than do the range data. It is seen that all of the experimental values of $Re_{\theta_{tr}}$ lie between 300 and 800, and are reasonably grouped about the theoretical incompressible curve of Tetervin and Levine (reference f). The favorable influence of strong heat transfer and strong pressure gradient on laminar stability is not evident from these data. In fact, the data indicate that neither a cool surface nor favorable pressure gradient appreciably affect the values of Re_{θ} at the end of transition. In general, it appears that transition on these body shapes occurs at Reynolds numbers which are of the same order of magnitude as the values of minimum critical Reynolds number usually associated with incompressible flow.

Conclusions

From a systematic investigation of boundary-layer transition on blunt-nose body shapes in the NOL Pressurized Ballistics Range, the following conclusions may be drawn:

- a. For all the data analyzed, the calculated values of the momentum thickness Reynolds number, Re_{θ} , at the observed transition

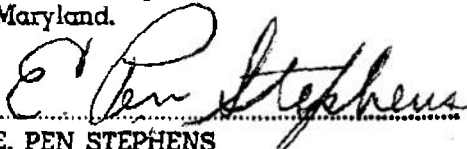
point were never larger than 800 nor less than 300. It appears therefore that transition occurs at values of Re_θ , which are of the same order of magnitude as the values of minimum critical Reynolds number usually associated with incompressible flow

b. Although the data have a "trend" with incompressible pressure gradient parameter $Re_\theta \frac{\theta}{u_e} \frac{du_e}{ds}$ suggestive of that described by incompressible stability theory, it does not appear that a favorable pressure gradient appreciably affects the values of Re_θ at which transition occurs

18 FEB 1957

.....
(Date)

Released by the Commander, U. S. Naval
Ordnance Laboratory, White Oak, Silver
Spring, Maryland.


.....
E. PEN STEPHENS
Technical Information Officer, Acting

References

- (a) Witt, W. R., Jr.: "Free-Flight Boundary-Layer Transition Studies on Cones" Proceedings of the Fourth Midwestern Conference on Fluid Mechanics (1955) Purdue University
- (b) Cohen, Clarence B. and Reshotko, Eli: "The Compressible Laminar Boundary Layer with Heat Transfer and Arbitrary Pressure Gradient" NACA TN 3326 (1955)
- (c) Private communication with L. Lees, California Institute of Technology
- (d) Grunewald, K. H.: "Temperature Recovery Factors in the Transitional and Turbulent Boundary Layer on a 40-degree Cone Cylinder at Mach Number 2.9" NavOrd Report 2742 (July 1953)
- (e) Persh, Jerome: "A Study of Boundary-Layer Transition from Laminar to Turbulent Flow" NavOrd Report 4339
- (f) Tetervin, Neal and Levine, David A.: "A Study of the Laminar Boundary Layer as Affected by Changes in the Boundary Layer Thickness in Regions of Pressure Gradient and Flow Through the Surface: NACA TN 2752 (1952)
- (g) Persh, Jerome: "A Procedure for Calculating the Boundary Layer Development in the Regions of Transition from Laminar to Turbulent Flow" NavOrd Report 4438 (to be published)

TABLE I

Pressurized Ballistics Range Boundary
Layer Transition Results

Shot No.	Body Shape* n	M_∞	P_o atm.	M_{local}	$Re_{\theta_{tr}}$	$Re_\theta \frac{\theta}{u_e} \frac{du_e}{ds}$	Re/ft
1666	1/3	3.07	1	2.006	554.8	0.0242	11.04
1704	1/3	3.35	1	2.151	631.8	0.0235	10.59
1706	1/3	3.26	1/2	2.231	532.1	0.0152	5.00
1707	1/3	3.10	3/4	2.153	591.4	0.0171	7.74
1742	1/3	2.99	1-3/4	1.909	651.1	0.0439	19.86
1679	1/2	3.23	1-1/2	1.639	549.2	0.0250	20.38
1712	1/2	2.95	1/2	1.966	448.9	0.0107	5.53
1711	1/2	3.20	1	1.818	440.9	0.0143	12.37
1708	1/3	3.21	1/2	2.220	530.9	0.009	5.03
1709	1/2	3.47	3/4	1.868	423.0	0.0025	9.35
1680	1/2	3.19	1	1.607	383.8	0.0141	13.70
1664	1/3	2.81	2	1.70	577.8	0.0263	24.57
1681	1/2	3.45	3/4	1.637	346.8	0.0105	10.35
1665	1/3	3.20	1-3/4	1.70	615.0	0.0126	22.20
1743	1/3	2.56	1	1.88	550.0	0.0070	10.72
1682	1/2	3.4	1/2	1.798	314.0	0.0246	6.39

* See Fig. 1

TABLE I (Cont'd)

Pressurized Ballistics Range Boundary
Layer Transition Results

Shot No.	θ_v	Cone Radii (inches)	M	P _o atm.	M _{local}	Re _{ctr}	Re _θ	$\frac{\theta}{u_e}$	$\frac{du_e}{ds}$	Re/ft
1595	10°	0.5	2.47	2	1.75	498.6		0		34.9
1596	↓	0.5	2.58	2	1.95	512.3				36.4
1609		0.25	3.07	1	2.11	651.5				20.8
1613		0.25	2.97	1-1/2	2.03	573.8				29.2
1629		0.25	2.97	2	2.08	487.4				41.1
1461	20°	0.75	2.10	2	1.80	757.2				21.3
1462	↓	0.75	1.99	2	1.49	696.3				20.5
1466		0.75	2.43	2	1.63	752.0				22.85
1616		0.5	2.55	1	1.66	472.9				11.78
1618		0.5	2.24	2	1.57	672.1				22.07
1627		0.5	2.68	2	1.68	596.0				23.89
1620		0.25	2.64	2	1.64	575.4				23.31
1623		0.25	3.18	1	1.77	339.2				12.64
1626		0.25	2.86	2	1.72	335.7				24.60
1628		0.125	2.00	5	1.50	471.5				51.31
1622		0.125	3.09	1	1.76	427.7				12.50
1619	↓	0.125	2.44	2	1.53	493.8				23.05

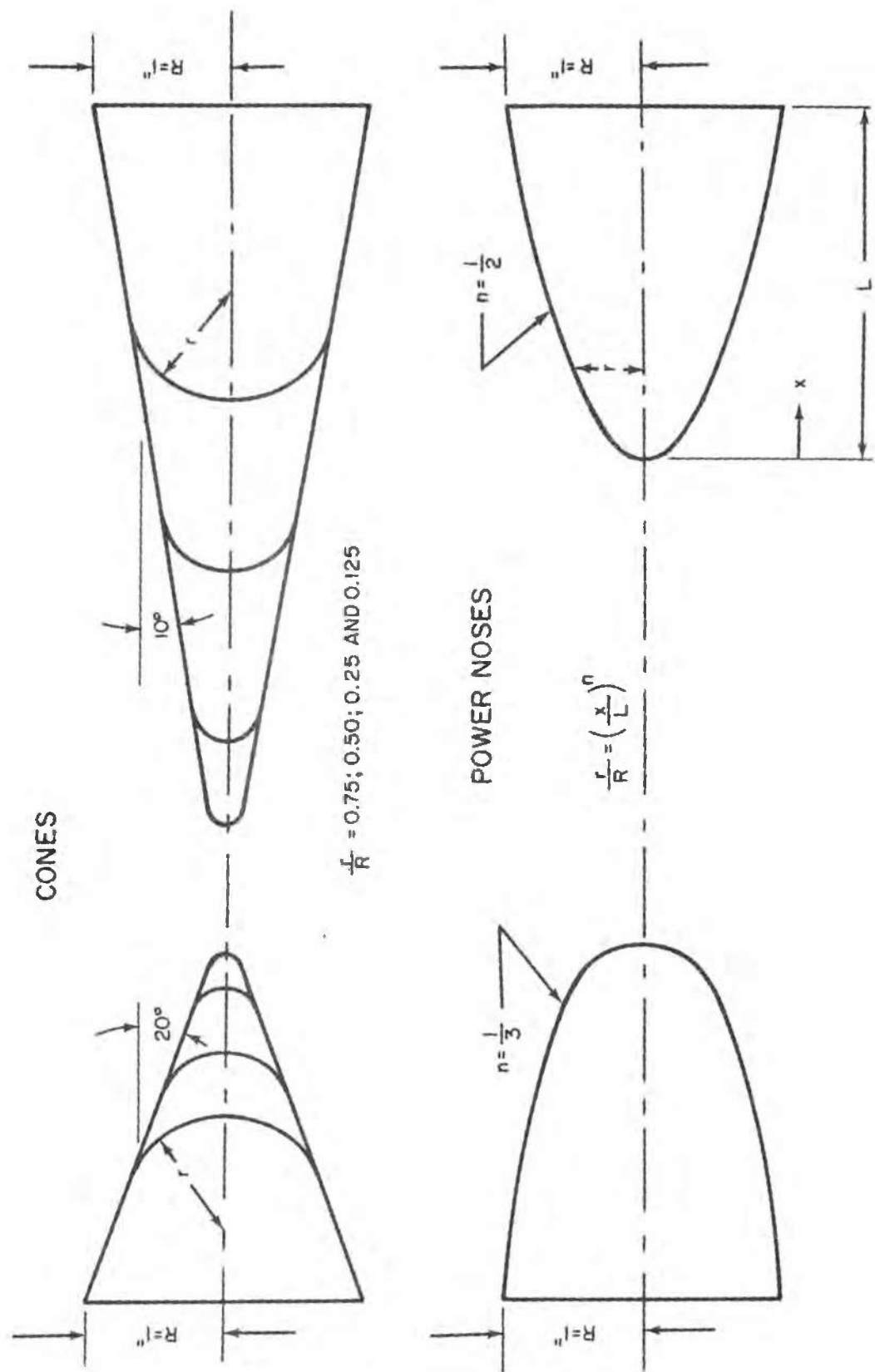


FIG.1 MODELS FOR THE PRESENT INVESTIGATION

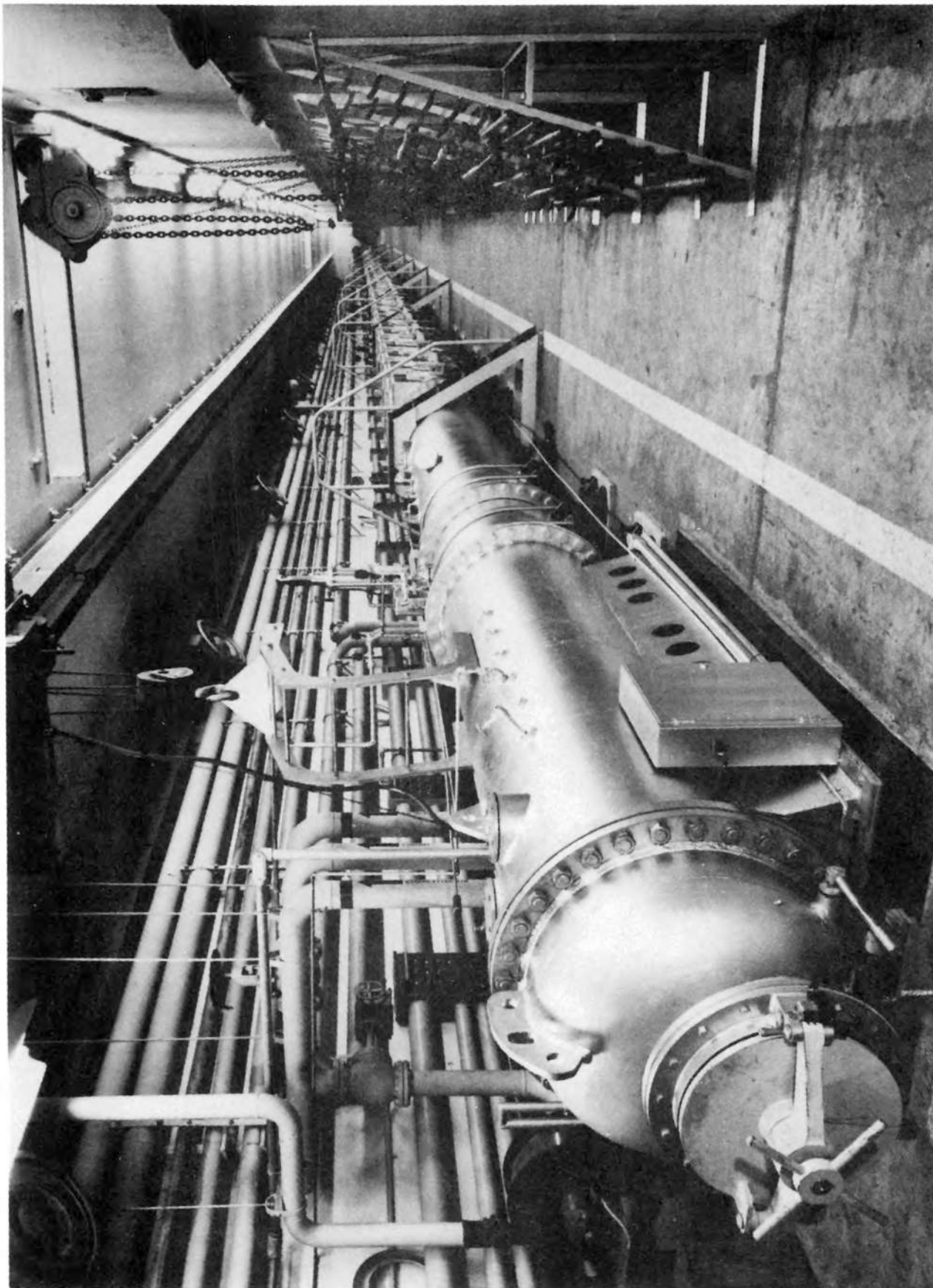


Fig. 2 The NOL Pressurized Ballistics Range

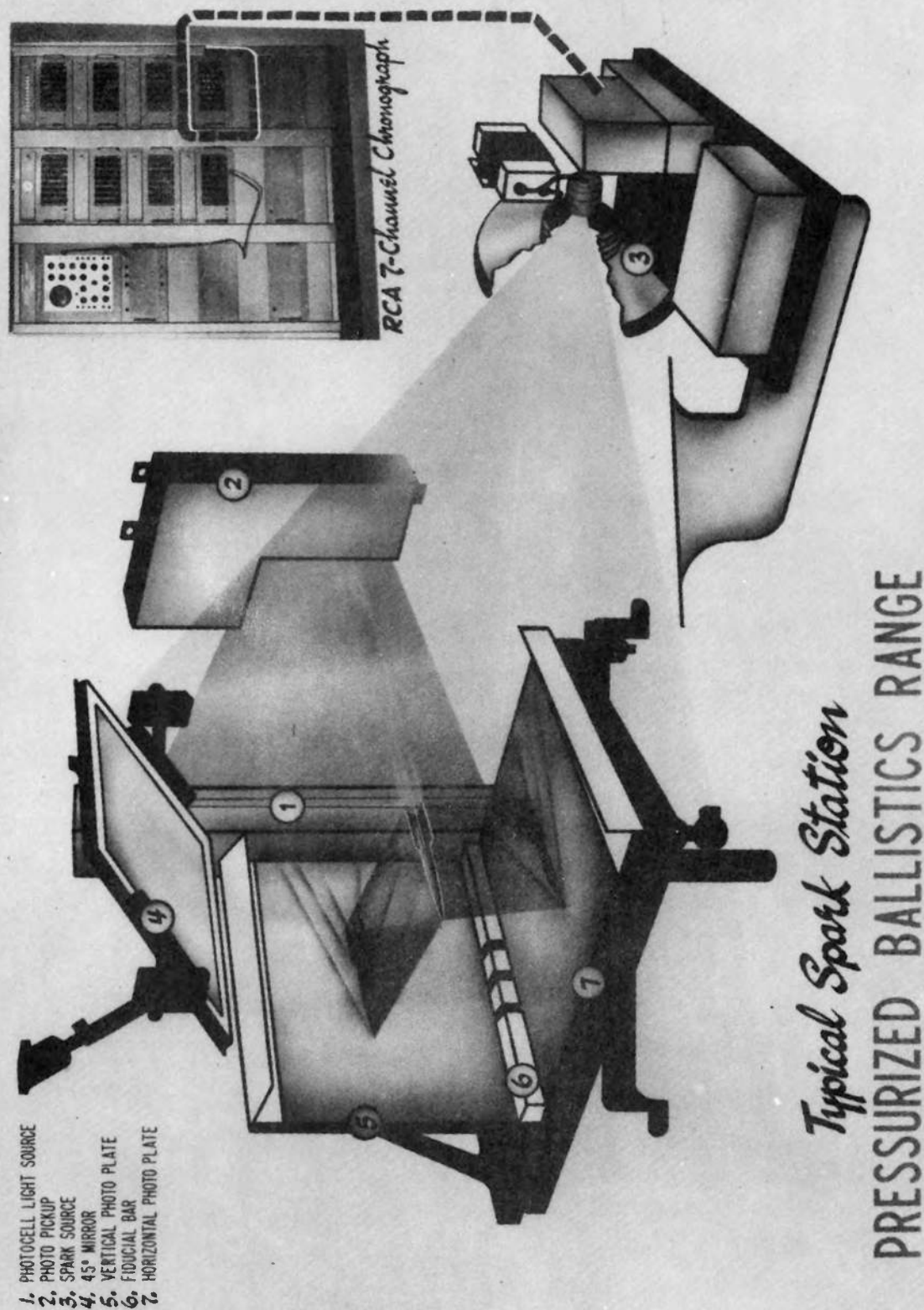


Fig. 3 Typical Spark Station, Pressurized Ballistics Range

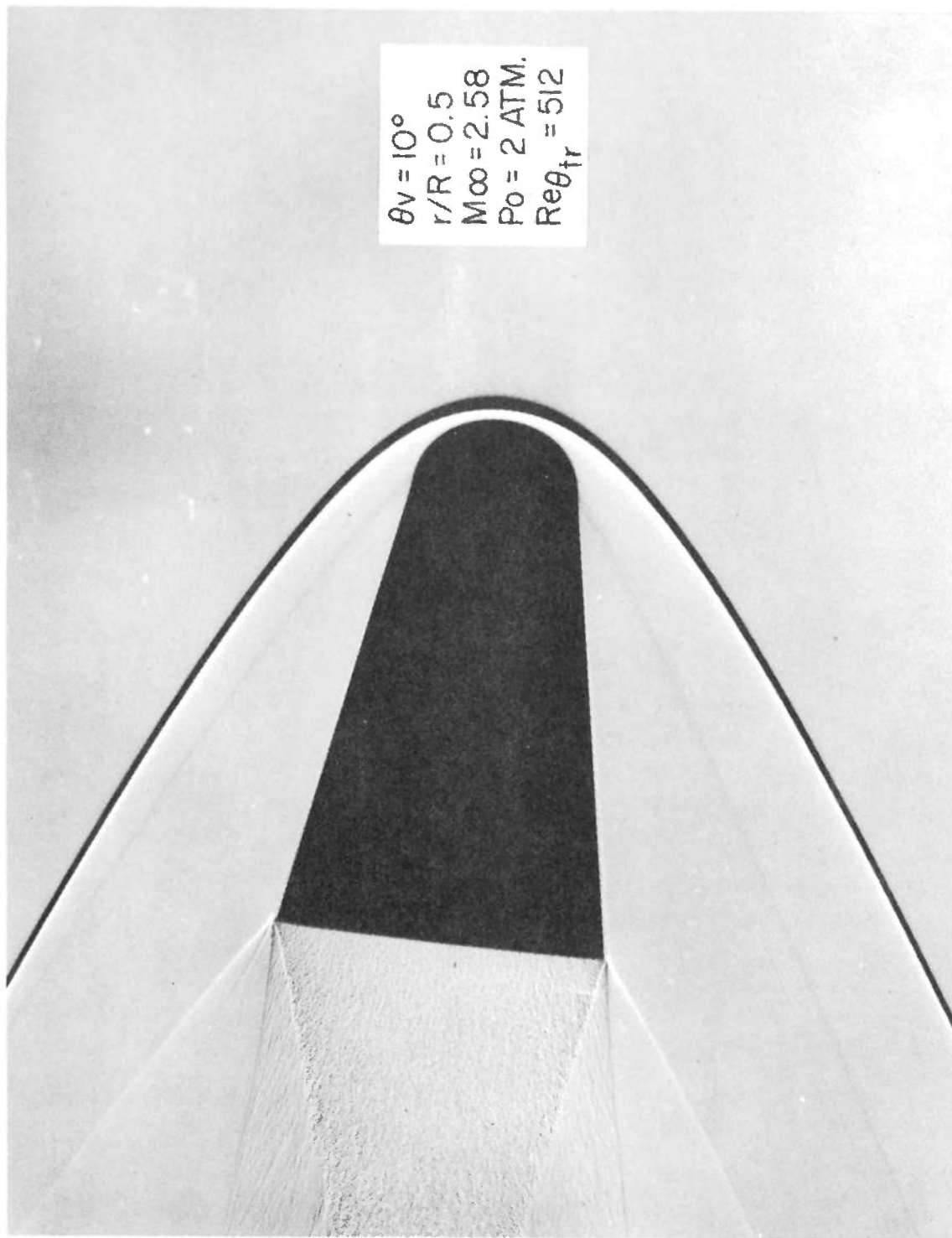


FIG. 4 TYPICAL SPARK SHADOWGRAPH PRINT
SHOT I596

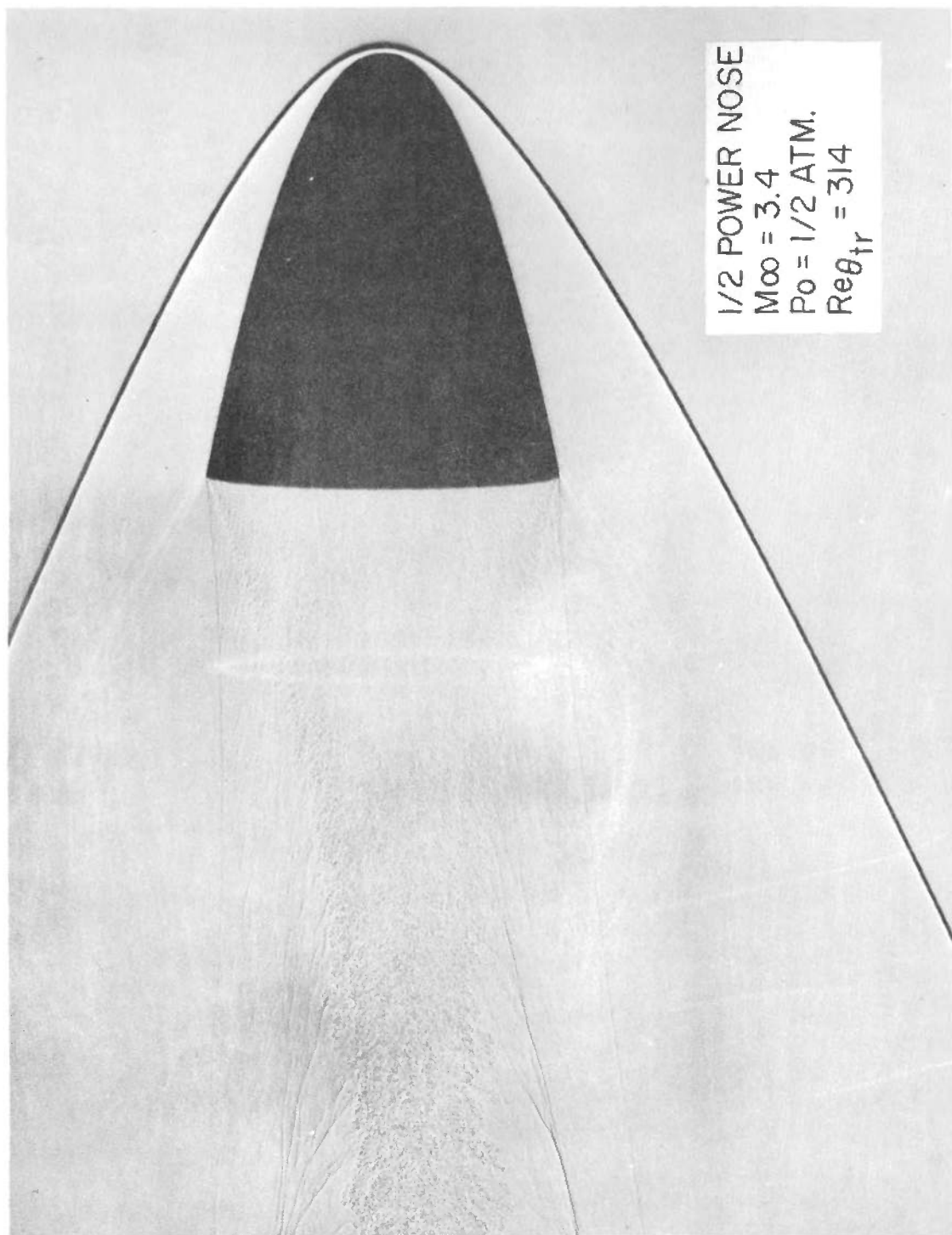


FIG. 5 TYPICAL SPARK SHADOWGRAPH PRINT
SHOT 1682

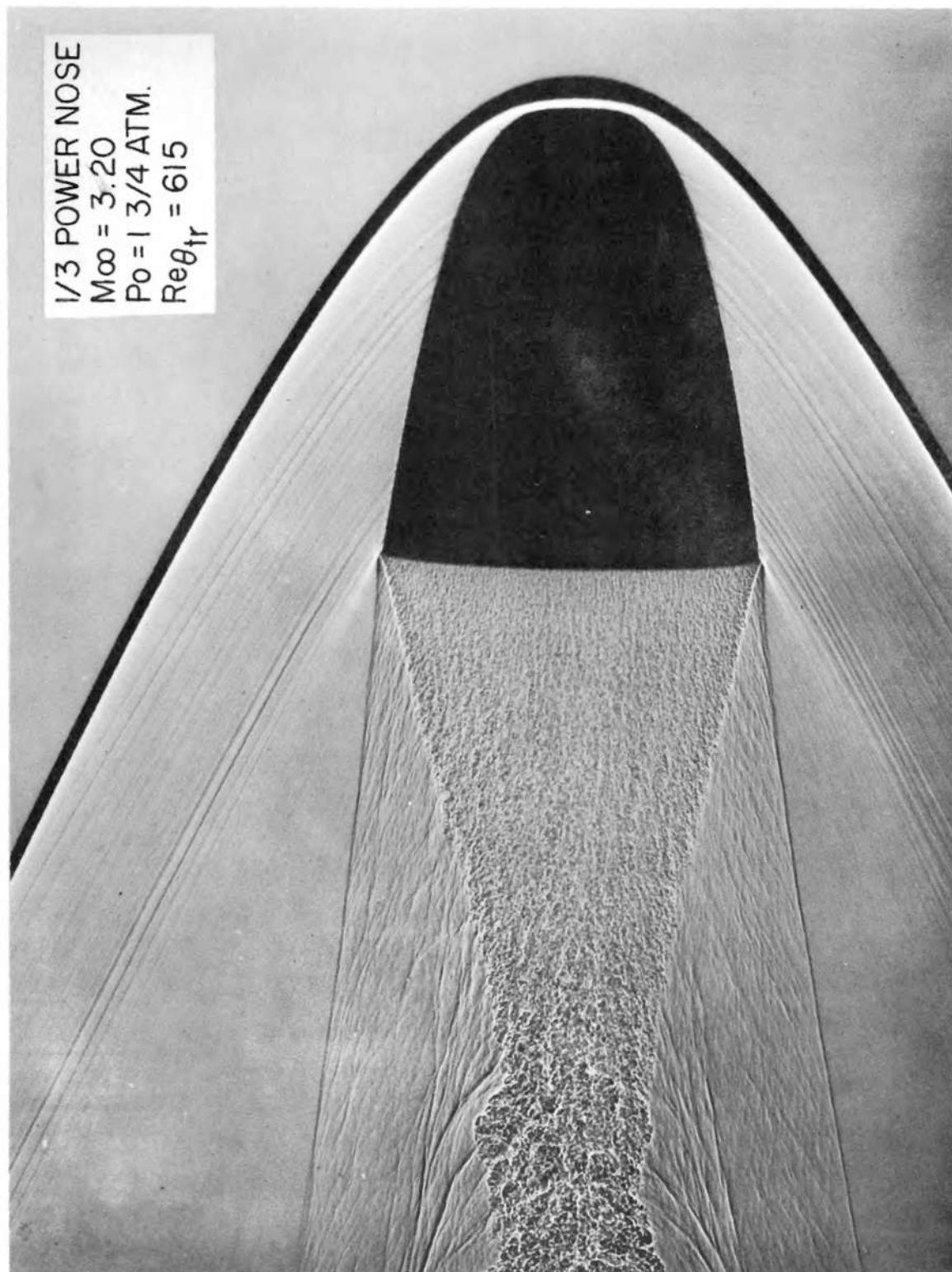


FIG. 6 TYPICAL SPARK SHADOWGRAPH PRINT
SHOT 1665

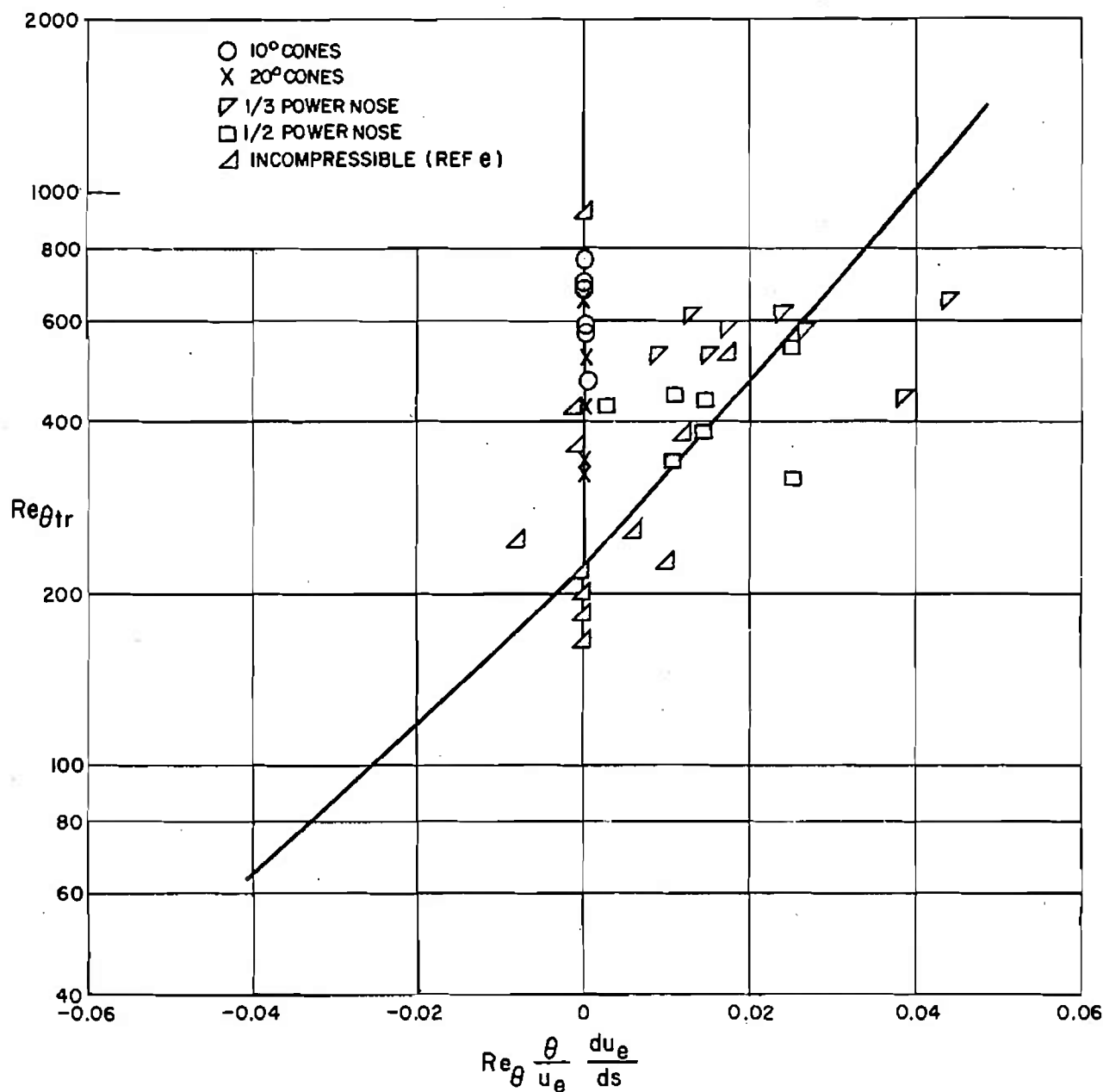


FIG.7 VARIATION OF CALCULATED VALUES OF $Re_{\theta_{tr}}$
WITH THE INCOMPRESSIBLE PRESSURE GRADIENT
PARAMETER, $Re_{\theta} \frac{\theta}{u_e} \frac{du_e}{ds}$

INTENTIONALLY LEFT BLANK.

ADVANCES IN THE DYNAMIC ANALYSIS OF RANGE DATA

Charles H. Murphy

Ballistic Research Laboratories
Aberdeen Proving Ground, Maryland

INTENTIONALLY LEFT BLANK.

Charles H. Murphy
Ballistic Research Laboratories

INTRODUCTION

The first use of aerodynamic ranges was the accurate measurement of the drag coefficients of bullets and shells. As the instrumentation improved in both quantity as well as quality, good measurements of the pitching and yawing motion of projectiles became available. The transverse motion of their centers of mass were also measured with good accuracy. From these data values of various linear aerodynamic coefficients could be computed.¹ Ranges were then used to test symmetric finned missiles. Since finned missiles with angles of rotational symmetry equal to or less than 120° have the same linear aerodynamic force and moment expansion as bodies of revolution, this introduced no new difficulties.

Thus, it can be said that the "classical" use of aerodynamic ranges has been for the dynamic analysis of thrustless symmetric missiles acted on by linear aerodynamic forces and moments. All three of these restrictions arise from the fact that the range method infers the aerodynamic force and moment from the observed motion and, therefore, is usually restricted to problems for which the differential equations have solutions in closed forms. As we shall see these restrictions can be and have been relaxed. Although the swerving motion of the center of mass can be considered, we will limit ourselves in this paper to the pitching and yawing motion and its associated aerodynamic coefficients.

This paper will be divided into four parts. First we will discuss the "classical" case. Then a gun-booster burning rocket program fired on the Transonic Range will be described and the minor alterations to

the data analysis indicated. Next the more difficult problem of an asymmetrical finned missile with roll rate varying through resonance is considered. Finally, the successful treatment of cubic non-linearities in static and Magnus moments and their associated forces is described.

Although the linear expansion of the transverse aerodynamic force and moment in terms of the angles α , β , the angular velocities q , r , and their time derivatives require the use of thirty-two derivatives, the assumed rotational symmetry reduces this number to sixteen. The introduction of a plane of mirror symmetry² reveals that half of these derivatives are odd functions of the roll rate p and, therefore, vanish for zero roll rate. These will be identified by products of second order derivatives and the roll rate and are called Magnus coefficients. The remaining derivatives can be independent of roll rate. This total of eight non-Magnus and eight Magnus derivatives can be reduced to five if only those quantities which usually have a measurable effect on the motion are retained³. (Due to the rotational symmetry the use of complex variables is a convenient shorthand.)

$$\therefore Y + iZ = -\frac{1}{2} \rho V^2 S C_{N_\alpha} (\beta + i\alpha) \quad (1)$$

$$\begin{aligned} M + iN = \frac{1}{2} \rho V^2 S l \left\{ \left[\left(\frac{pl}{V} \right) C_{M_{p\alpha}} - iC_{M_\alpha} \right] [\beta + i\alpha] \right. \\ \left. + C_{M_q} \left[\frac{(q + ir)l}{V} \right] - iC_{M_{\dot{\alpha}}} \left[\frac{(\dot{\beta} + i\dot{\alpha})l}{V} + \frac{ip l (\beta + i\alpha)}{V} \right] \right\} \end{aligned} \quad (2)$$

where ρ is air density
 V is total velocity
 S is reference area
 l is reference length
 p, q, r are components of the angular velocity vector
 α is angle of attack
 β is angle of sideslip

$$C_{N_{\alpha}} \equiv -C_{Y_{\beta}} = -C_{Z_{\alpha}} \quad (\text{Normal force derivative})$$

$$C_{M_{\alpha}} \equiv C_{m_{\alpha}} = -C_{n_{\beta}} \quad (\text{Static moment derivative})$$

$$C_{M_{p\alpha}} \equiv C_{m_{p\beta}} = C_{n_{\alpha}} \quad (\text{Magnus moment derivative})$$

$$\left. \begin{aligned} C_{M_q} &\equiv C_{m_q} = C_{n_r} \\ C_{M_{\dot{\alpha}}} &\equiv C_{m_{\dot{\alpha}}} = -C_{n_{\dot{\beta}}} \end{aligned} \right\} \quad (\text{Damping moment derivatives})$$

(The expression following $C_{M_{\dot{\alpha}}}$ is the derivative of $\beta + i\alpha$ in a non-rolling coordinate system. As has been pointed out by Sacks⁴ and later by Davis⁵ this choice has certain advantages.)

In Eqs. (1-2) both the angles and the angular velocities are measured in missile-fixed coordinates. Since non-rolling coordinates give rise to slightly less complex differential equation, we will make use of a non-rolling coordinate system. Quantities in this coordinate system will be distinguished by tilde superscripts. (Fig. 1)

If the effect of gravity is neglected, the aerodynamic force assumed to be linear, and the mass distribution assumed to be symmetric ($I_y = I_z$), the following differential equation for the complex angle of attack, $\tilde{\xi}$, can be derived:

$$\tilde{\xi}'' + (H - iP) \tilde{\xi}' - (M + iPT) \tilde{\xi} = 0 \quad (3)$$

where $\tilde{\xi} = \tilde{\beta} + i\tilde{\alpha} = (\beta + i\alpha) e^{i \int p \, dt}$

$$H = \frac{\rho S \ell}{2m} \left[C_{N_{\alpha}} - 2C_D - k_t^{-2} (C_{M_q} + C_{M_{\dot{\alpha}}}) \right]$$

$$M = \frac{\rho S \ell}{2m} k_t^{-2} C_{M_{\alpha}}$$

$$T = \frac{\rho S \ell}{2m} \left[C_{N_{\alpha}} - C_D + k_a^{-2} C_{M_{p\alpha}} \right]$$

$$P = \frac{I_x}{I_y} \frac{pl}{V}$$

$$m = \text{mass}$$

$$C_D \quad \text{drag coefficient}$$

$$k_t = \sqrt{\frac{I_y}{ml^2}} \quad \text{transverse radius of gyration}$$

$$k_a = \sqrt{\frac{I_x}{ml^2}} \quad \text{axial radius of gyration}$$

$$I_x \quad \text{axial moment of inertia}$$

$I_y = I_z$ transverse moment of inertia and primes denote differentiation with respect to dimensionless arclength $s = \int \frac{V}{l} dt$. For constant spin to velocity ratio and constant moment coefficients, Eq. (3) can be easily solved:

$$\tilde{\xi} = K_1 e^{i\phi_1} + K_2 e^{i\phi_2} \quad (4)$$

$$\text{where } \phi_j = \phi_{j0} + \phi_j^* s$$

$$K_j = K_{j0} e^{\lambda_j s} \quad \text{and}$$

$$\lambda_j + i\phi_j^* = \frac{1}{2} \left[-H + iP \pm \sqrt{4M + H^2 - P^2 + 2iP(2T - H)} \right]$$

The pitching and yawing motion is described in a complex plane by the sum of two two-dimensional vectors which are exponentially damped in magnitude and rotating with angular velocities ϕ_j^* . (Fig. 2) For a statically stable missile with zero spin ($M < 0$, $P = 0$) the motion is described by a damped ellipse. (Fig. 3) If the missile is allowed to spin, the ellipse will precess and become an epicycle. (Fig. 4) A statically unstable missile which is spin-stabilized, ($M > 0$, $4M - P^2 < 0$), has an epicyclic motion with the nodes on the inside. (Fig. 5)

The basic procedure in range tests is to fit observed pitching and yawing motion by Eq. (4) and to infer from the measured damping factors and frequencies the actual aerodynamic moments which act on the missile. In a similar fashion the center of mass motion can be used for measurements of the normal force derivative $C_{N\alpha}$.

THRUST

The consideration of a burning rocket introduces three modifications of Eq. (3):

- (1) The drag equation, $\frac{V^*}{V} = - \frac{\rho S l}{2m} C_D$, is no longer valid.
- (2) The mass and radii of gyration are not constants.
- (3) A jet damping term*, $\frac{m^* \lambda^*}{m} \left[\left(\frac{r_e}{k_t} \right)^2 - 1 \right]$ where r_e is distance from the c.m. to the nozzle exit, must be added to the right side of Eq. (3).

A further practical handicap to aerodynamic range tests of burning rockets is the large dispersion inherent in conventional rockets.

Live gun-boosted rockets have tolerable dispersions and have been launched in the Transonic Range⁶. Figure 6 is a direct microflash of a burning 2.75 in. rocket while Figure 7 is a shadowgraph of the same rocket. Although the rocket motor does expose part of the shadowgraph, the shadow itself is of good quality.

For this firing the modifications listed above can be easily handled:

- (1) $\frac{V^*}{V}$ was approximately constant and positive. This means that a negative pseudo drag coefficient may be used in Eq. (3)
- (2) The variations in mass and radii of gyration were relatively mild and averages can be estimated to within 10%.
- (3) The jet damping term for the high initial velocities was small and so could be neglected.

The conventional data analysis was then employed to yield values of C_{M_α} ,

* This term arises from the fact that the gases in the jet carry angular momentum from the rocket.

$C_{M_{p\alpha}}$, $C_{M_q} + C_{M_{\dot{\alpha}}}$, and $C_{N_{\alpha}}$. Figure 8 gives a comparison of $C_{M_{\alpha}}$ for burning and non-burning rockets. The jet appears to have little effect on this aerodynamic coefficient.

In 1952, Nicolaides⁷ treated the problem of missiles with slight configurational asymmetry and constant roll rates. This asymmetry can be caused by misaligned fin surfaces or deflected control surfaces and can be described by a constant amplitude aerodynamic force and moment whose directions are constant in missile - fixed coordinates. For this case our basic equation (Eq. (3)) is modified by the introduction of an inhomogeneous term.

$$\ddot{\xi} + (H - iP) \dot{\xi} - (M + iPT) \xi = M_{\epsilon} e^{i(\theta + \theta_{\epsilon})} \quad (5)$$

where $M_{\epsilon} = -\frac{\rho S l}{2m} k_t^{-2} C_{M_{\epsilon}} \epsilon$
 ϵ is magnitude of asymmetry angle
 θ_{ϵ} is its initial orientation and
 $\theta = \int_0^t p dt = \int_0^s \frac{pl}{V} ds.$

For constant $\frac{pl}{V}$ Nicolaides showed that the solution of the pitching and yawing motion assumed the form:

$$\xi = K_1 e^{i\phi_1} + K_2 e^{i\phi_2} + K_3 e^{i(\theta + \phi_{30})} \quad (6)$$

where $K_3 e^{i\phi_{30}} = \frac{-M_{\epsilon} e^{i\theta_{\epsilon}}}{\theta'^2 (1 - \frac{I_x}{I_y}) + M - i\theta'(H - \frac{I_x}{I_y} T)}$
 $\theta' = \frac{pl}{V}$ and the other symbols are defined after Eq. (4).

The third term in Eq. (6) possesses a rather important resonance property for statically stable missiles. This occurs when the roll rate is near the pitching frequency. (More precisely it is when $\theta'^2 (1 - \frac{I_x}{I_y}) + M = 0$.)

For this roll rate K_3 can become quite large. Its size is determined by the aerodynamic damping, $H - \frac{I_x}{I_y} T$. In Figure 9, the amplification of equilibrium yaw, $\frac{K_3(\theta^*)}{K_3(0)}$, is plotted versus the ratio of spin rate to yawing rate for different aerodynamic damping. The resonance peaks can be quite large for reasonable aerodynamic damping.

Naturally, the curves of Figure 9 are of no quantitative value for the variable roll rate problem. For this more difficult data analysis problem of free flight missiles whose roll rates vary through resonance considerable use was made of an analog computer⁸. (Figure 10)

For this method Eq. (5) together with the measured roll history was placed on the computer, and a series of solution curves were drawn. These were compared with actual measurements and the parameters* H , M , M_c and θ_c together with initial conditions ξ_0 , ξ_0' were then varied by trial and error in a curve fitting process. For an experienced operator a good fit could be obtained in two to four hours. Figure 11 shows such a fit for a missile whose roll rate grows to 1.23 times its resonant value.

This approach, however, suffers from a crucial dependence on an experienced operator. If it is possible, it is desirable to have the machine make the necessary decisions. With this in mind it was decided to try to make use of one of BRL's large digital machines. To do this it was necessary to be able to state the solution of Eq. (5) for non-constant $\frac{p\ell}{V}$.

At this point it is important to note that although the particular solution is quite sensitive to roll rates near resonance, the complementary solution is relatively insensitive. This means that we can either neglect $\frac{p\ell}{V}$ on the left side of Eq.(5) or replace it by an average value. The problem is now to find the solution of an inhomogeneous linear equation

* T was neglected in this work.

with constant coefficients. Since we know that the complementary solution is given by Eq. (4), the general solution can be found by the method of variation of parameters.

According to this method the constants K_{jo} , ϕ_{jo} in Eq. (4) are assumed to be functions of s . For convenience we will introduce the quantities $A_j = K_{jo} e^{i\phi_{jo}}$

$$\tilde{\xi}_A = A_1 e^{(\lambda_1 + i\phi_1') s} + A_2 e^{(\lambda_2 + i\phi_2') s} \quad (7)$$

where $\tilde{\xi}_A$ is the particular solution due to asymmetry and A_1, A_2 are complex functions of s .

Differentiating we see that

$$\begin{aligned} \tilde{\xi}_A' &= (\lambda_1 + i\phi_1') A_1 e^{(\lambda_1 + i\phi_1') s} + (\lambda_2 + i\phi_2') A_2 e^{(\lambda_2 + i\phi_2') s} \\ &\quad + A_1' e^{(\lambda_1 + i\phi_1') s} + A_2' e^{(\lambda_2 + i\phi_2') s} \end{aligned} \quad (8)$$

If the last two terms are set equal to zero,

$$A_1' e^{(\lambda_1 + i\phi_1') s} + A_2' e^{(\lambda_2 + i\phi_2') s} = 0 \quad (9)$$

and

$$\tilde{\xi}_A' = (\lambda_1 + i\phi_1') A_1 e^{(\lambda_1 + i\phi_1') s} + (\lambda_2 + i\phi_2') A_2 e^{(\lambda_2 + i\phi_2') s} \quad (10)$$

Differentiating again we obtain the following:

$$\begin{aligned} \tilde{\xi}_A'' &= (\lambda_1 + i\phi_1')^2 A_1 e^{(\lambda_1 + i\phi_1') s} + (\lambda_2 + i\phi_2')^2 A_2 e^{(\lambda_2 + i\phi_2') s} \\ &\quad + (\lambda_1 + i\phi_1') A_1' e^{(\lambda_1 + i\phi_1') s} + (\lambda_2 + i\phi_2') A_2' e^{(\lambda_2 + i\phi_2') s} \end{aligned} \quad (11)$$

If Eqs. (7, 10, 11) are substituted in Eq. (5) and it is recalled that terms without A_j^i come from the solution of the homogeneous equation and must cancel, the following equation can be obtained:

$$(\lambda_1 + i\phi_1^i) A_1^i e^{(\lambda_1 + i\phi_1^i)s} + (\lambda_2 + i\phi_2^i) A_2^i e^{(\lambda_2 + i\phi_2^i)s} = M_\epsilon e^{i(\theta + \theta_\epsilon)} \quad (12)$$

Substituting Eq. (9) in Eq. (12),

$$A_1^i = \frac{M_\epsilon e^{-(\lambda_1 + i\phi_1^i)s} + i(\theta + \theta_\epsilon)}{\lambda_1 - \lambda_2 + i(\phi_1^i - \phi_2^i)} \quad (13)$$

$$A_2^i = \frac{M_\epsilon e^{-(\lambda_2 + i\phi_2^i)s} + i(\theta + \theta_\epsilon)}{\lambda_2 - \lambda_1 + i(\phi_2^i - \phi_1^i)} \quad (14)$$

If Eqs. (13-14) are integrated and the integrals substituted in Eq. (7), the following general solution can be obtained:

$$\tilde{\xi} = K_1 e^{i\phi_1} + K_2 e^{i\phi_2} + \tilde{\xi}_A \quad (15)$$

where

$$\tilde{\xi}_A = \frac{M_\epsilon e^{i\theta_\epsilon} \left[\int_0^s \left[e^{(\lambda_1 + i\phi_1^i)(s-r)} - e^{(\lambda_2 + i\phi_2^i)(s-r)} \right] e^{i\theta(r)} dr \right]}{(\lambda_1 - \lambda_2) + i(\phi_1^i - \phi_2^i)}$$

Eq. (15) can now be fitted by the usual ~~least~~ squares differential corrections method. This process has been coded for the ORDVAC by F. Yonda⁹.

The rounds which had been fitted by the analog computer in Ref. 8 have now been fitted by the ORDVAC and the results are given in Table 1. The standard error σ of the ORDVAC fit is about 60% of the standard error of the analog computer fit. Since the latter work was a trial and error process and the ORDVAC method did not depend on the skill of the machine operator, this superiority of the digital method was not surprising. As can be seen from the other entries in the table, the analog computer operator was, however, very capable.

TABLE I

Rd. No.	$p_{\infty}/p_{\text{Reson}}$	$10^3 \sigma$		% ΔM	% ΔH	% ΔM_{ϵ}
Ref. 8 ORDVAC						
3099	.72	2.0	1.3	3.4	-0.1	-4.8
3088	.91	1.5	1.0	1.4	-6.5	-6.4
3100	1.00	1.8	1.1	6.1	-6.5	+30.3
3098	1.02	2.0	1.1	2.9	-7.1	-3.1
3105	1.08	1.9	1.3	2.6	-1.9	+8.5
3103	1.09	1.3	1.3	3.9	+9.8	+33.3
3090	1.10	1.8	1.5	1.1	-13.3	+14.7
3104	1.11	1.6	1.0	1.2	+3.1	+3.8
3102	1.23	2.0	0.9	0.3	+3.1	+4.8

Where

p_{∞} is steady state roll rate

p_{Reson} is roll rate at resonance

σ standard error of fit

$$\% \Delta M = 100 \left[1 - \frac{M_{\text{Ref 8}}}{M_{\text{ORDVAC}}} \right]$$

$$\% \Delta H = 100 \left[1 - \frac{H_{\text{Ref 8}}}{H_{\text{ORDVAC}}} \right]$$

$$\% \Delta M_{\epsilon} = 100 \left[1 - \frac{M_{\epsilon \text{ Ref 8}}}{M_{\epsilon \text{ ORDVAC}}} \right]$$

Although non-linearities can arise from geometric terms as well as all the aerodynamic terms, we will confine ourselves to angles of attack for which the geometric linearizations are correct and only the static and Magnus moments are non-linear. The more complete problem is treated in References 10-11. We will also limit ourselves to those non-linearities which arise from the angles, $\tilde{\alpha}$, $\tilde{\beta}$, and can occur for bodies of revolution². (For configurations with less symmetry, terms other than these can occur.) Under these assumptions our basic equation assumes the form:

$$\tilde{\xi}'' + (H - iP) \tilde{\xi}' - \left[M(\delta^2) + iPT(\delta^2) \right] \tilde{\xi} = 0 \quad (16)$$

where $\delta^2 = |\tilde{\xi}|^2 = \tilde{\alpha}^2 + \tilde{\beta}^2$

Range tests of missiles which were known to have non-linear aerodynamic coefficients did not reveal pitching and yawing motions which were qualitatively different from those associated with linear forces and moments. In other words, it was not possible to identify non-linearities from the angular motion of individual rounds over the relatively short observed trajectories. On comparing fitted damping exponents and frequencies from different firings of the same configuration at the same Mach number it was found that they varied with the amplitude of the motion. Hence, the non-linear motion over short trajectories can be approximated by the linear epicycles but the epicyclic parameters are functions of some "effective" magnitude of the motion.

In order to obtain quantitative relations we will make use of a perturbation process which is a generalization of the Kryloff-Bogoliuboff method¹² and is similar to the method of variation of parameters. Eq. (16) can be written in the form:

$$\tilde{\xi}'' - iP\tilde{\xi}' - M(0)\tilde{\xi} = -H\tilde{\xi}' + \left[M(\delta^2) - M(0) + iPT(\delta^2) \right] \tilde{\xi}. \quad (17)$$

If the right side of Eq. (17) is neglected, then for a gyroscopically stable missile the solution is an epicycle without damping:

$$\tilde{\xi} = K_{10} e^{i\hat{\phi}_1} + K_{20} e^{i\hat{\phi}_2} \quad (18)$$

where

$$\hat{\phi}_j = \hat{\phi}_{j0} + \hat{\phi}'_j s$$

$$\hat{\phi}'_j = \frac{1}{2} \left[P + \sqrt{P^2 - 4M(0)} \right] \quad \text{and}$$

$$P^2 - 4M(0) > 0.$$

We now assume a solution of the form

$$\tilde{\xi} = K_1 e^{i(\hat{\phi}_1 + \psi_1)} + K_2 e^{i(\hat{\phi}_2 + \psi_2)} \quad (19)$$

where $K_j(s)$ and $\psi_j(s)$ are unknown functions of s . Substituting Eq. (19) in the left side of Eq. (17), and inserting a condition similar to Eq. (9), we can now write equations which are formally equivalent to Eqs. (13-14) for $A_j = K_j e^{i\psi_j}$ and $\lambda_j = 0$.

$$(K'_1 + i\psi'_1 K_1) e^{i\psi_1} = \frac{-H \tilde{\xi}' + \left[\frac{M(\delta^2) - M(0) + iPT(\delta^2)}{i(\hat{\phi}'_1 - \hat{\phi}'_2)} \right] \tilde{\xi}}{i(\hat{\phi}'_1 - \hat{\phi}'_2)} \quad (20)$$

$$(K'_2 + i\psi'_2 K_2) e^{i\psi_2} = \frac{-H \tilde{\xi}' + \left[\frac{M(\delta^2) - M(0) + iPT(\delta^2)}{i(\hat{\phi}'_2 - \hat{\phi}'_1)} \right] \tilde{\xi}}{i(\hat{\phi}'_2 - \hat{\phi}'_1)} \quad (21)$$

We now substitute Eq. (19) on the right side of Eq. (20) and divide by $K_1 e^{i\psi_1}$:

$$\frac{K'_1}{K_1} + i\psi'_1 = \frac{-H \hat{\phi}'_1 \left[1 + \frac{\hat{\phi}'_2 K_2}{\hat{\phi}'_1 K_1} e^{i\phi} \right] + \left[\frac{PT(\delta^2) - i[M(\delta^2) - M(0)]}{\hat{\phi}'_1 - \hat{\phi}'_2} \right] \left[1 + \frac{K_2}{K_1} e^{i\phi} \right]}{\hat{\phi}'_1 - \hat{\phi}'_2} \quad (22)$$

where

$$\phi = \hat{\phi}_2 + \psi_2 - \hat{\phi}_1 - \psi_1 \quad \text{and}$$

$$\delta^2 = |\tilde{\xi}|^2 = K_1^2 + K_2^2 + 2K_1 K_2 \cos \phi.$$

Since effective values of the damping exponents and frequencies as desired, we average Eq. (22) and separate into real and imaginary parts. *

$$\therefore \lambda_1 = \frac{K_1'}{K_1} = \frac{-H\hat{\phi}_1' + \frac{1}{2\pi} \int_0^{2\pi} PT(\delta^2) \left[1 + \frac{K_2}{K_1} \cos \phi \right] d\phi}{\hat{\phi}_1' - \hat{\phi}_2'} \quad (23)$$

$$\phi_1' = \hat{\phi}_1' + \psi_1' = \hat{\phi}_1' - \frac{\int_0^{2\pi} [M(\delta^2) - M(0)] \left[1 + \frac{K_2}{K_1} \cos \phi \right] d\phi}{2\pi (\hat{\phi}_1' - \hat{\phi}_2')} \quad (24)$$

Symmetric expressions apply for the other mode of oscillation.

As an application of this technique we now consider the case of a cubic static moment. The static moment coefficient is quadratic and has the form:

$$C_{M_\alpha} = a_0 + a_2 \delta^2 \quad (25)$$

$$\therefore M(\delta^2) = \frac{\rho l^3}{m} k_t^{-2} [a_0 + a_2 \delta^2] \quad (26)$$

Substituting Eq. (26) in Eqs. (24) and its partner for the other mode, we can obtain the following relations.

$$\phi_1' = \hat{\phi}_1' - \frac{\frac{\rho l^3}{m} k_t^{-2} a_2 (K_1^2 + 2K_2^2)}{\hat{\phi}_1' - \hat{\phi}_2'} \quad (27)$$

* Since T and M are even functions of ϕ , the sine integrals vanish.

$$\phi_2' = \phi_2 - \frac{\frac{\rho l^3}{m} k_t^{-2} a_2 (K_2^2 + 2K_1^2)}{\phi_2 - \phi_1} \quad (28)$$

Multiplying Eq. (27) by Eq. (28), neglecting fourth powers of the K_j 's, and simplifying, we can write our final relation.

$$C \phi_1' \cdot \phi_2' = a_0 + a_2 \delta_e^2 \quad (29)$$

where $C = \frac{m}{\rho l^3} k_t^2 = \frac{I_y}{\rho l^5}$

$$\delta_e^2 = K_1^2 + K_2^2 + \frac{K_1^2 \phi_1' - K_2^2 \phi_2'}{\phi_1' - \phi_2'}$$

If we call the left side of Eq. (29) the "effective" static moment coefficient, this equation states that the pairs of effective static moment coefficients and effective angles of attack squared as obtained from different tests of the same configurations should fall on a line. The slope of this line is a_2 and the intercept is a_0 . Figure 12 shows such a plot for three center of mass locations. Since we could expect the coefficients a_0 , a_2 in the moment expansion to be linear in c.m. position, these values are plotted against c.m. position in Figure 13. Good internal consistency can be seen. The slopes of the lines in Figure 13 are the corresponding normal force coefficient, i.e.

$$C_{N_\alpha} = b_0 + b_2 \delta^2 \quad (30)$$

These values and others have been compared with wind tunnel measurements with good correlations¹⁰.

Since the maximum angles in Figure 12 are about 10° , we consider a large angle of attack program as our final example. (Fig. 14) Here the maximum angle of attack is 35° and a single line does not fit the data*. A pair of lines form a good approximation. Since a line in this

* The geometric non-linearities could not be neglected for this program and the appropriate formulas from Reference 10 have been used.

plot corresponds to a cubic in the moment plane, this means the moment is approximated by a pair of cubics (Fig. 15). These curves have been found to be in good agreement. The discontinuous derivative can be explained by a shadowgraph of the projectile. At about 22° flow separates on the lee side. (Fig. 16)

In addition to a cubic static moment this equivalent linearization method has been successfully used for the measurement of cubic Magnus moments as well as cubic normal and Magnus forces¹⁰. As we can see the limited concept of the aerodynamics range as a tool for the measurement of linear forces and moments is no longer correct.

SUMMARY

In summary it should be noted that the classical use of aerodynamic ranges has been extended in three directions:

- (1) Gun boosted rockets have been successfully handled by the range technique.
- (2) The pitching and yawing motion of an symmetric missile with roll rate varying through resonance has been properly analysed by use of both analog and digital computing machines.
- (3) Accurate measurements have been made of cubic static and Magnus moments together with their associated forces.

REFERENCES

1. Fowler, R. H., Gallop, E. G., Lock, C. N. H., Richmond, H. W., The Aerodynamics of a Spinning Shell, Phil. Trans. Roy. Soc. London (A) 221, 295-387, Dec. 1920.
2. Maple, C. G. Synge, J. L., Aerodynamic Symmetry of Projectiles, Q. A. M. Vol. VI, No. 4, Jan 1949.
3. Murphy, C. H., Nicolaides, J. D., A Generalized Ballistic Force System, BRL Report 933, May 1955.
4. Sacks, A. H., Aerodynamic Forces, Moments, and Stability Derivatives for Slender Bodies of General Cross Section, NACA TN 3283, Nov. 1954.
5. Davis, R. A., The Response of a Bisymmetric Aircraft to Small Combined Pitch, Yaw, and Roll Control Actions, I.A.S. Reprint 684, Jan 1957.
6. MacAllister, L. C., Rogers, W. K., Aerodynamic Properties of the 2.75-inch Rocket T131, BRIM 948, Nov. 1955.
7. Nicolaides, J. D., On the Free Flight Motion of Missiles Having Slight Configurational Asymmetries, BRL Report 858, June 1953.
8. Schmidt, J. A., A Study of the Resonating Yawing Motion of Asymmetrical Missiles by Means of Analog Computer Simulation, BRL Report 922, Nov. 1954.
9. Yonda, A. W., Data Reduction of the Yaw and Sverve of a Fin-Stabilized Missile With a Roll Varying Through Resonance For A High Speed Electronic Digital Computer, BRIM 1042, Oct. 1956.
10. Murphy, C. H., The Measurement of Non-Linear Forces and Moments by Means of Free Flight Tests, BRL Report 974, Feb. 1956.

11. Murphy, C. H., Prediction of the Motion of Missiles Acted on by Non-Linear Forces and Moments, BRL Report 995, Oct. 1956. (Also The Prediction of Non-Linear Pitching and Yawing Motion of Symmetric Missiles, I.A.S. Preprint 677, Jan 1957.)
12. Kryloff, N., and Bogoliuboff, N. B., Introduction to Non-Linear Mechanics, translated by S. Lefschetz, Princeton University Press, 1947.

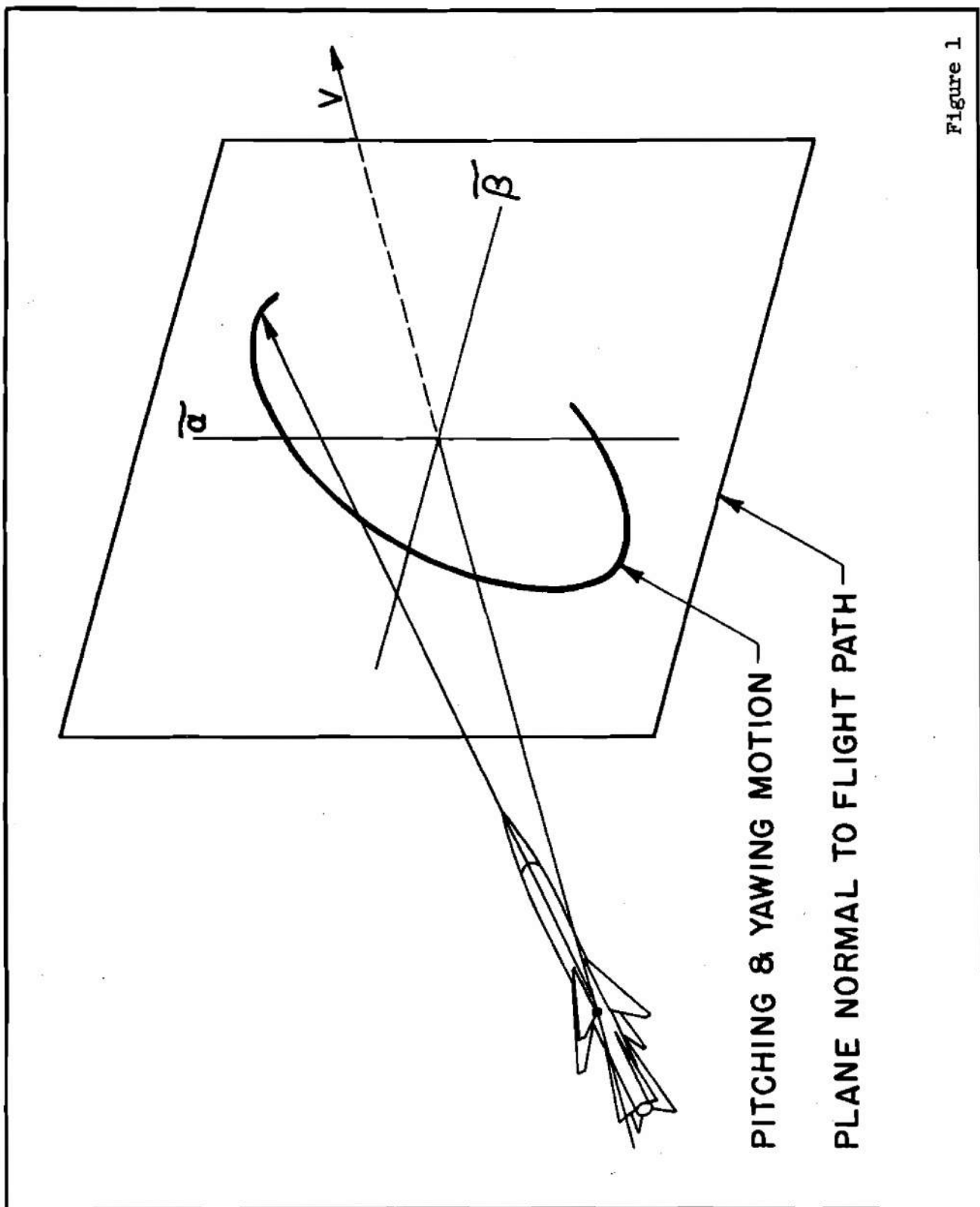
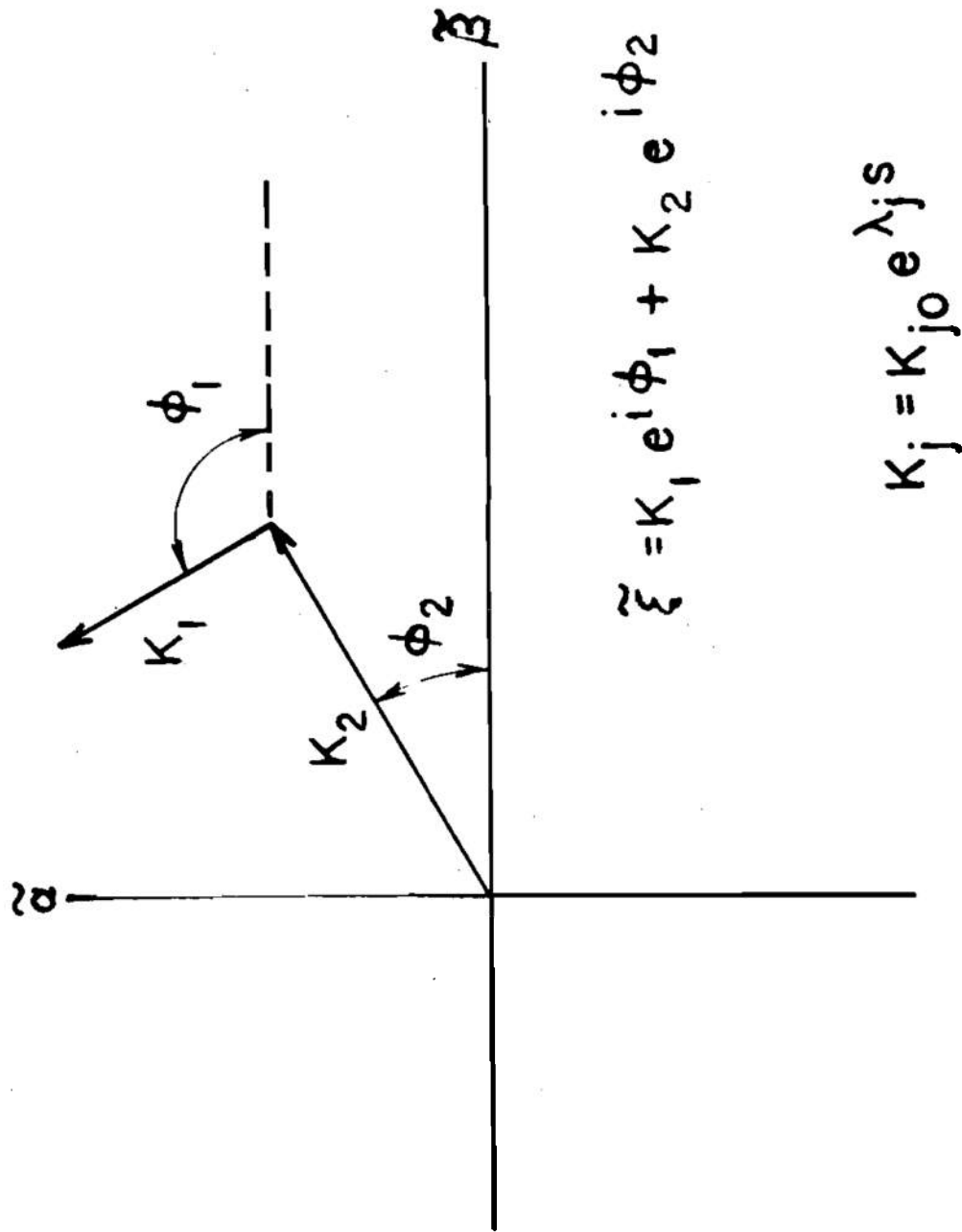


Figure 1



$\phi_j = \phi_{j0} + \phi'_j s$

Figure 2

NON-ROLLING STATICALLY STABLE SYMMETRIC MISSILE

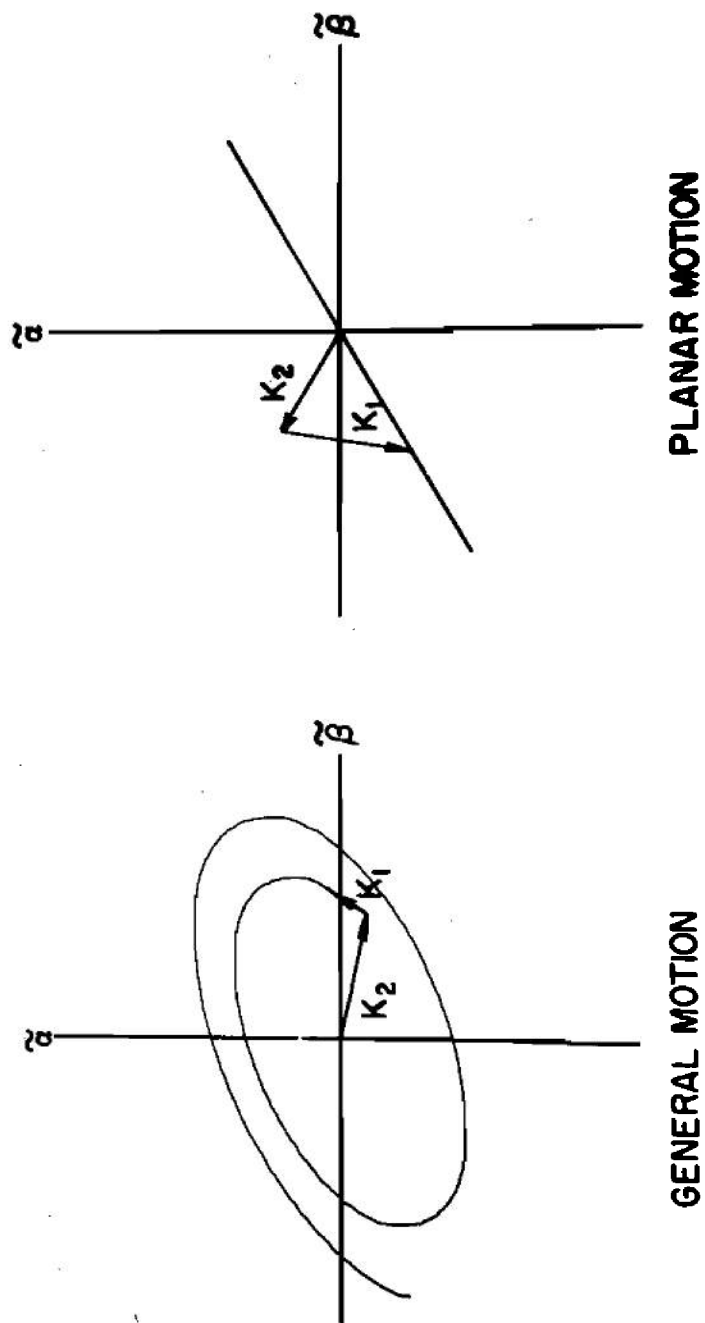


Figure 3

ROLLING STATICALLY STABLE SYMMETRIC MISSILE

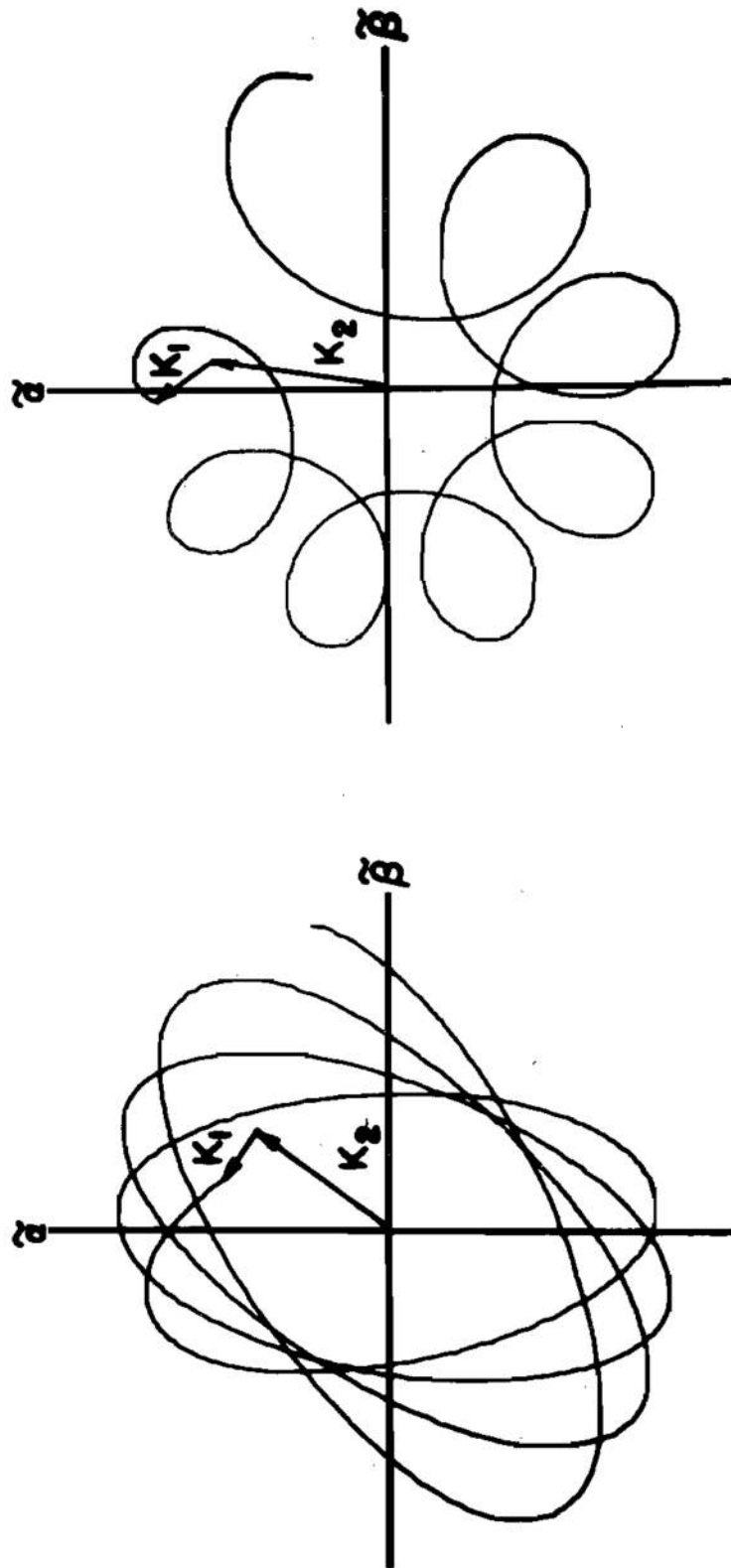


Figure 4

ANGULAR MOTION OF SYMMETRIC
STATICALLY UNSTABLE MISSILE

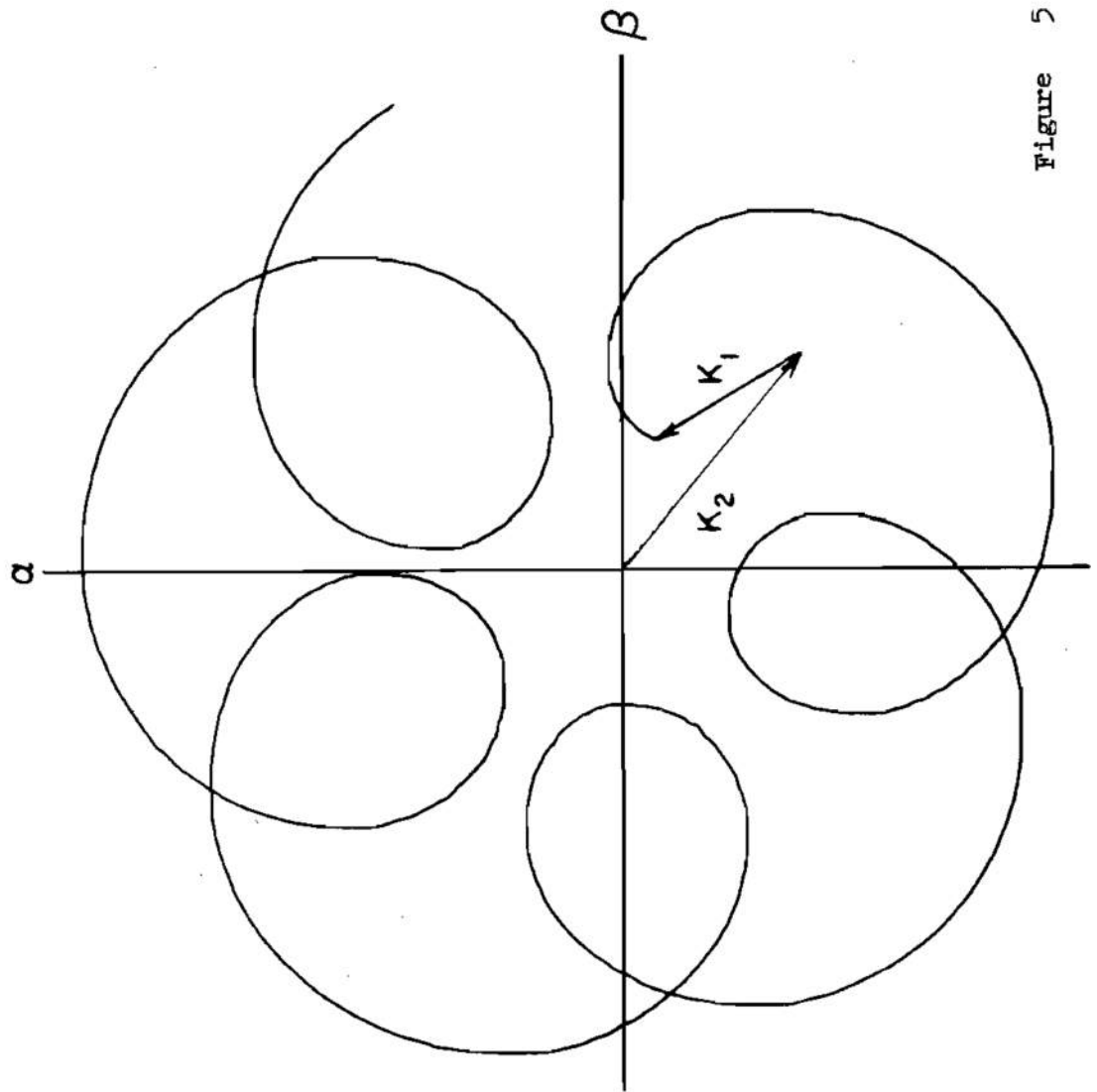


Figure 5

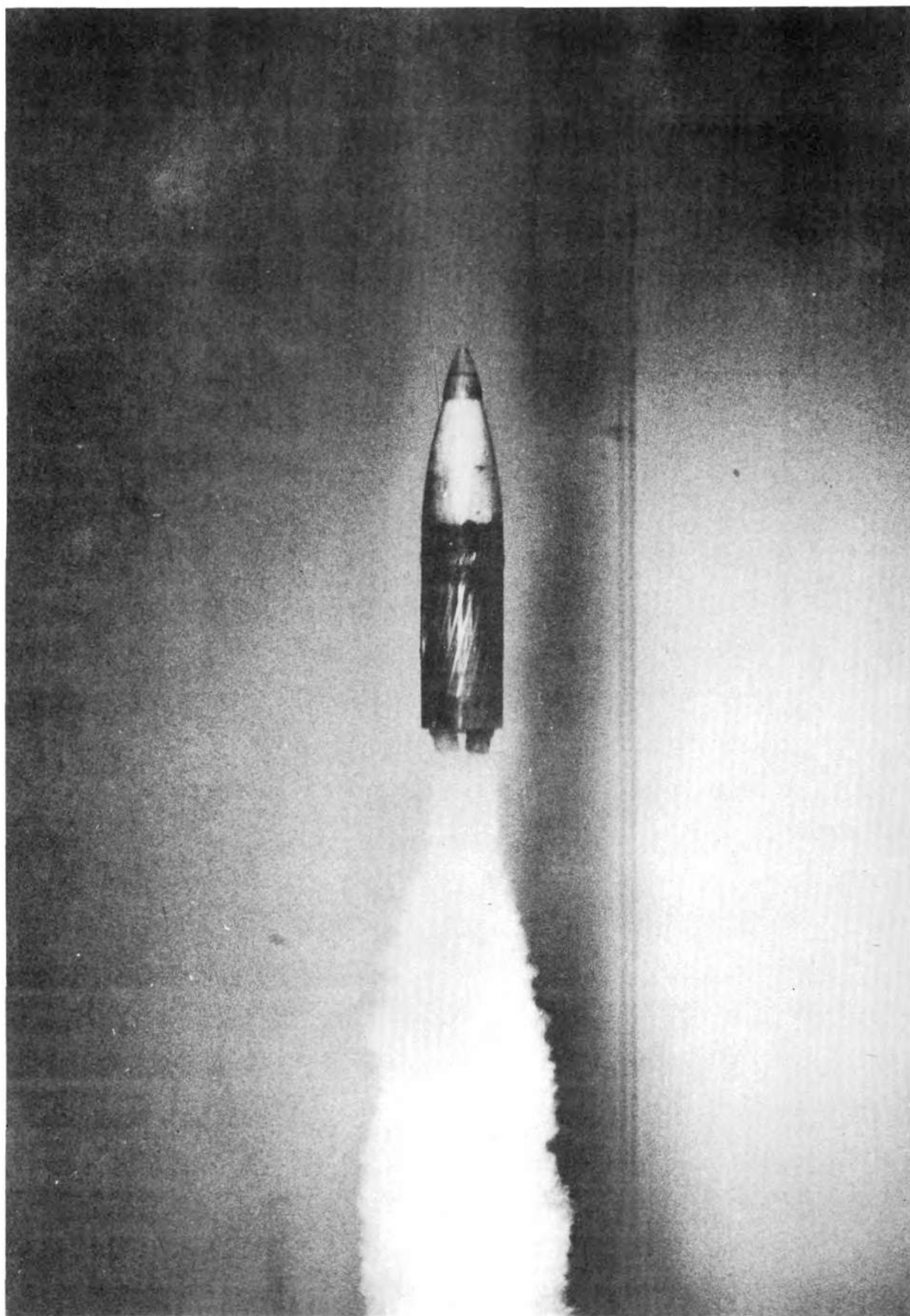


Figure 6

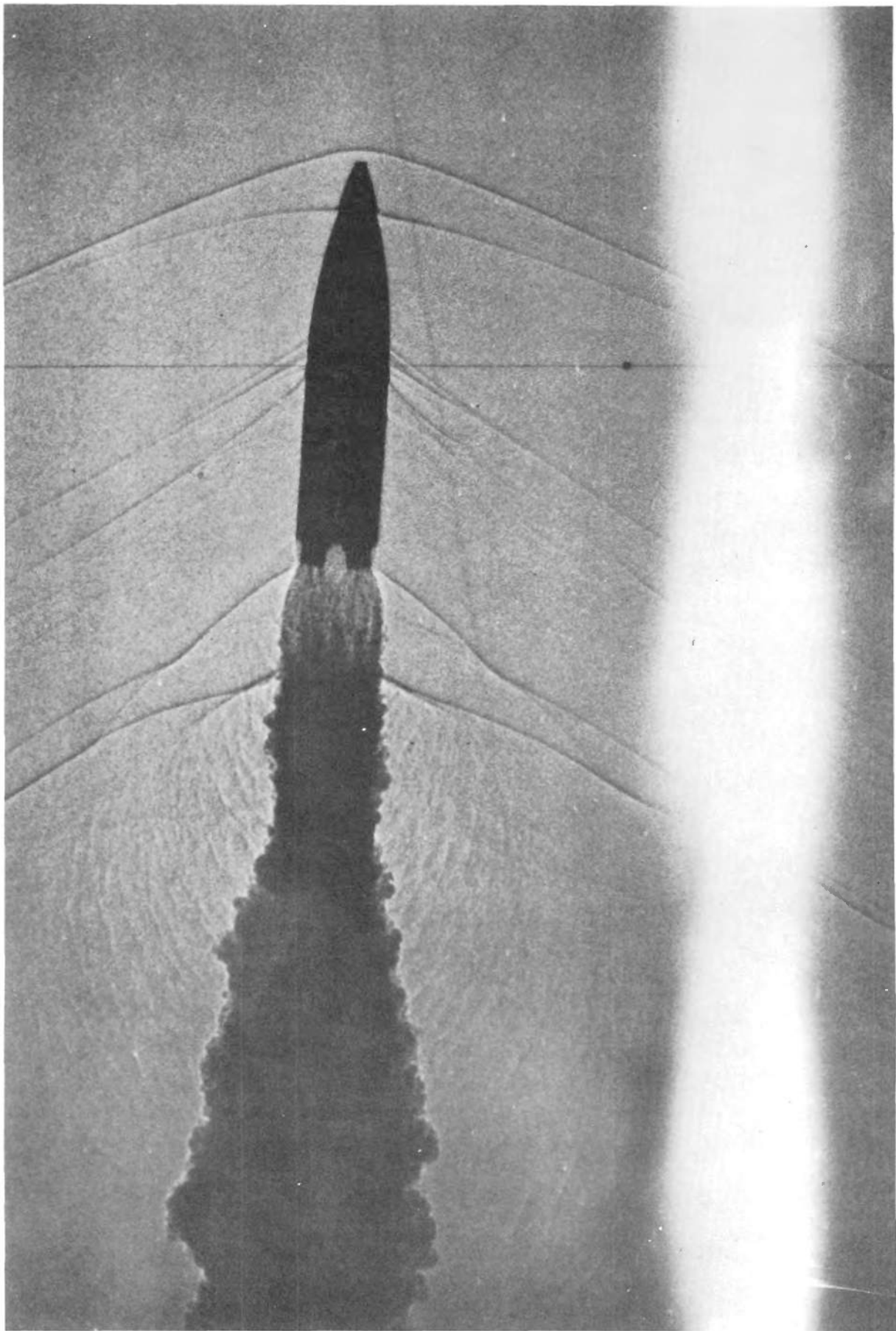


Figure 7

STATIC MOMENT COEFFICIENT vs. MACH NUMBER

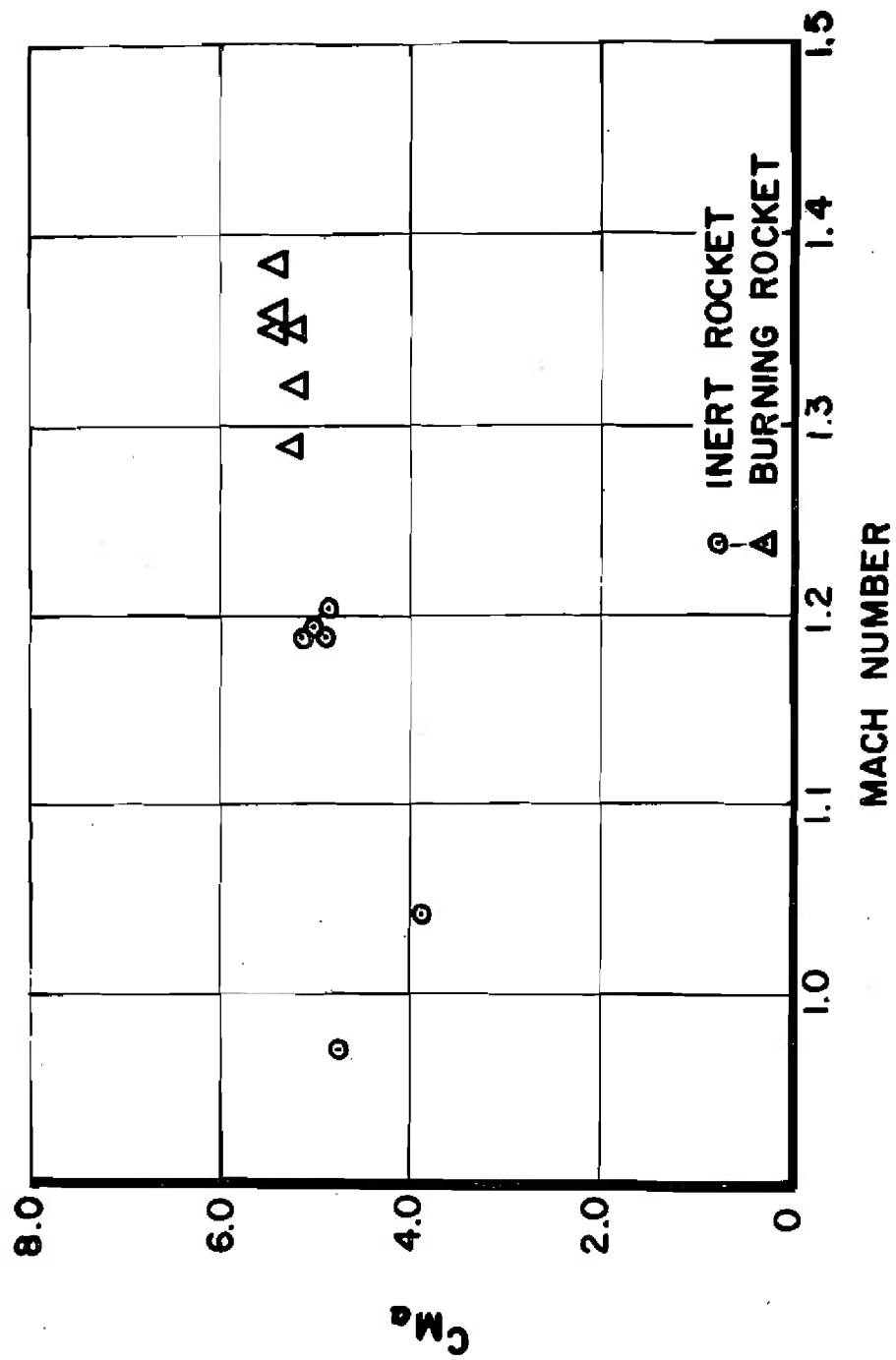


Figure 8

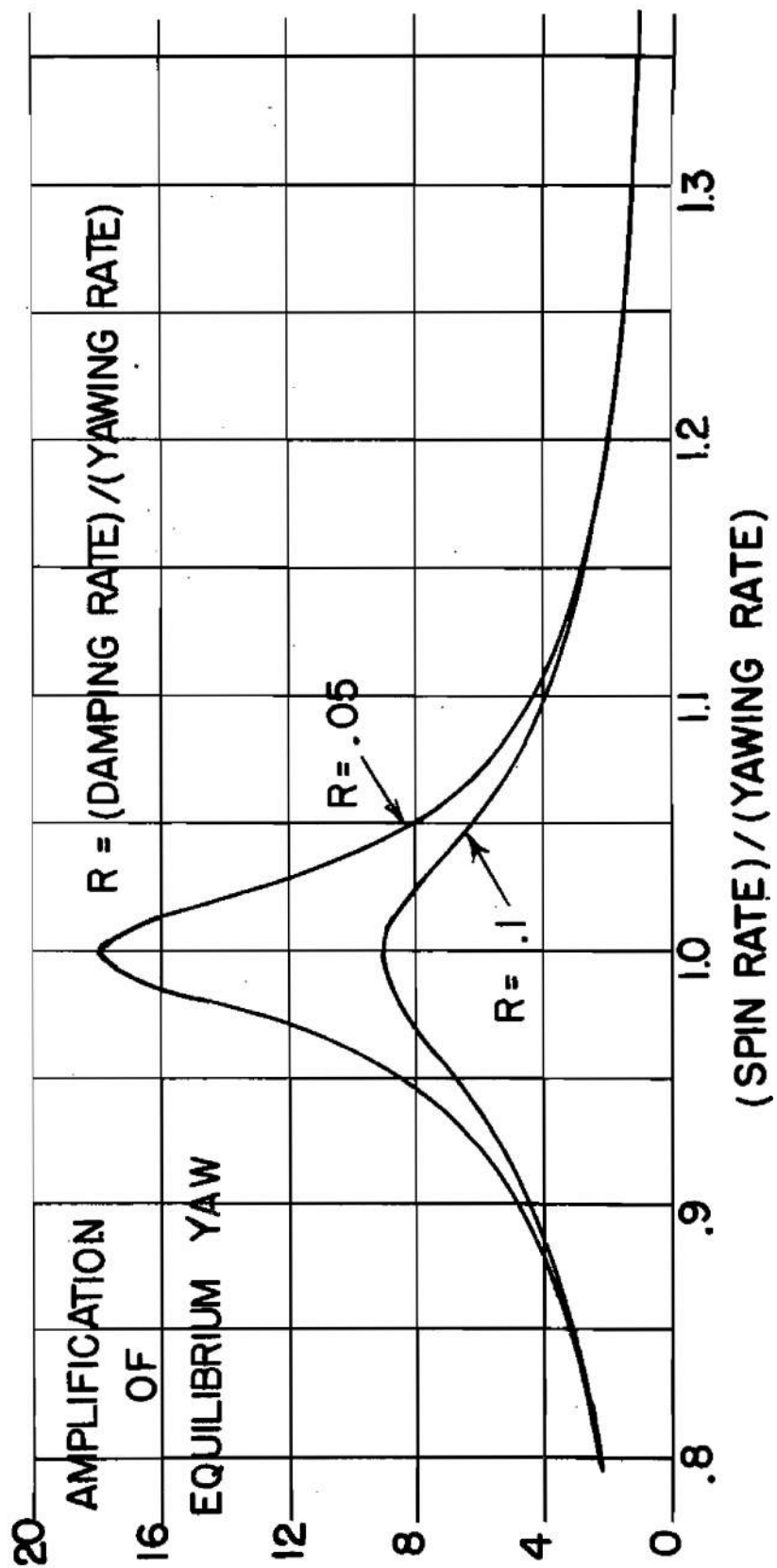


Figure 9

POLAR PLOT FOR YAW OF FINNED SHELL
WITH CANT AND ECCENTRICITY

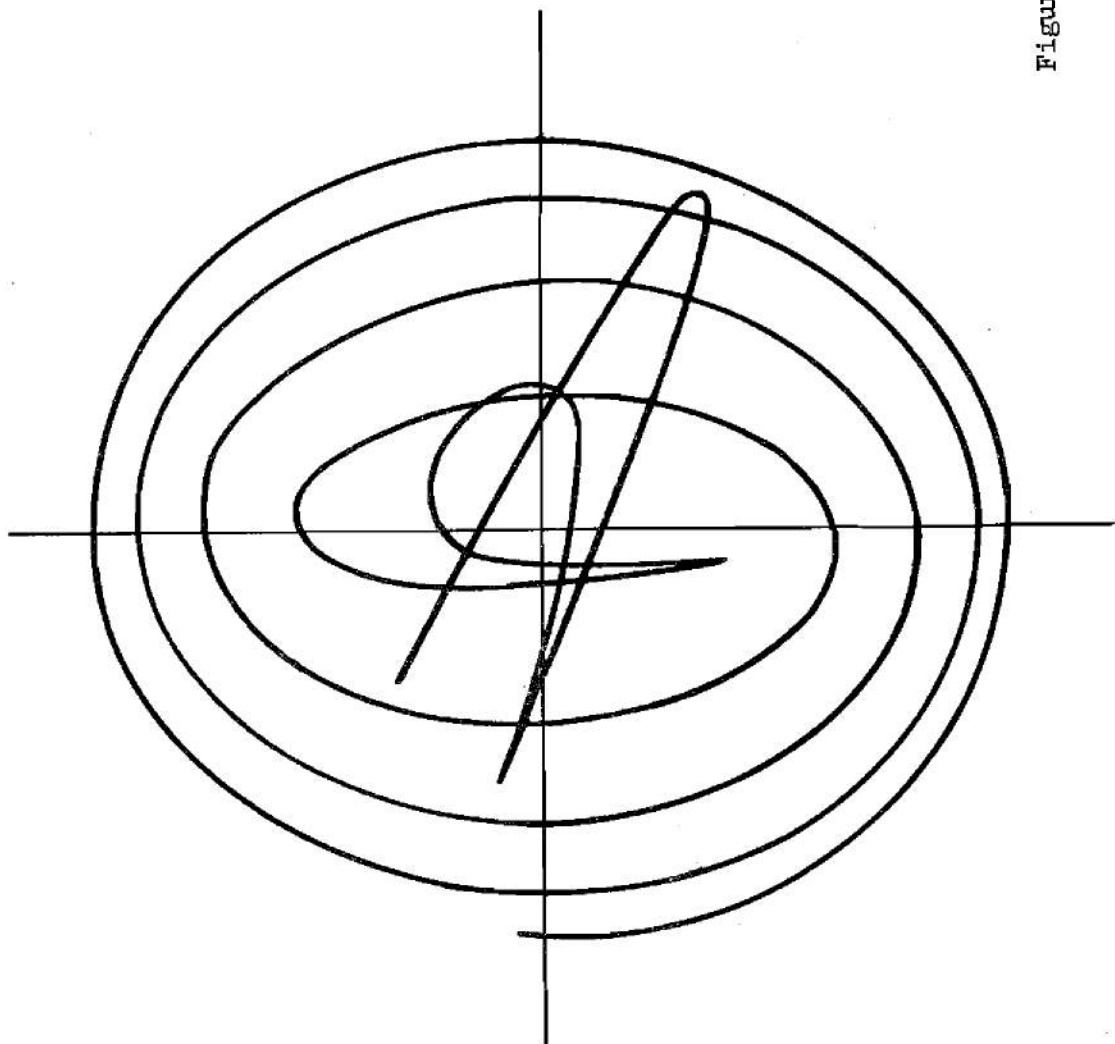


Figure 10

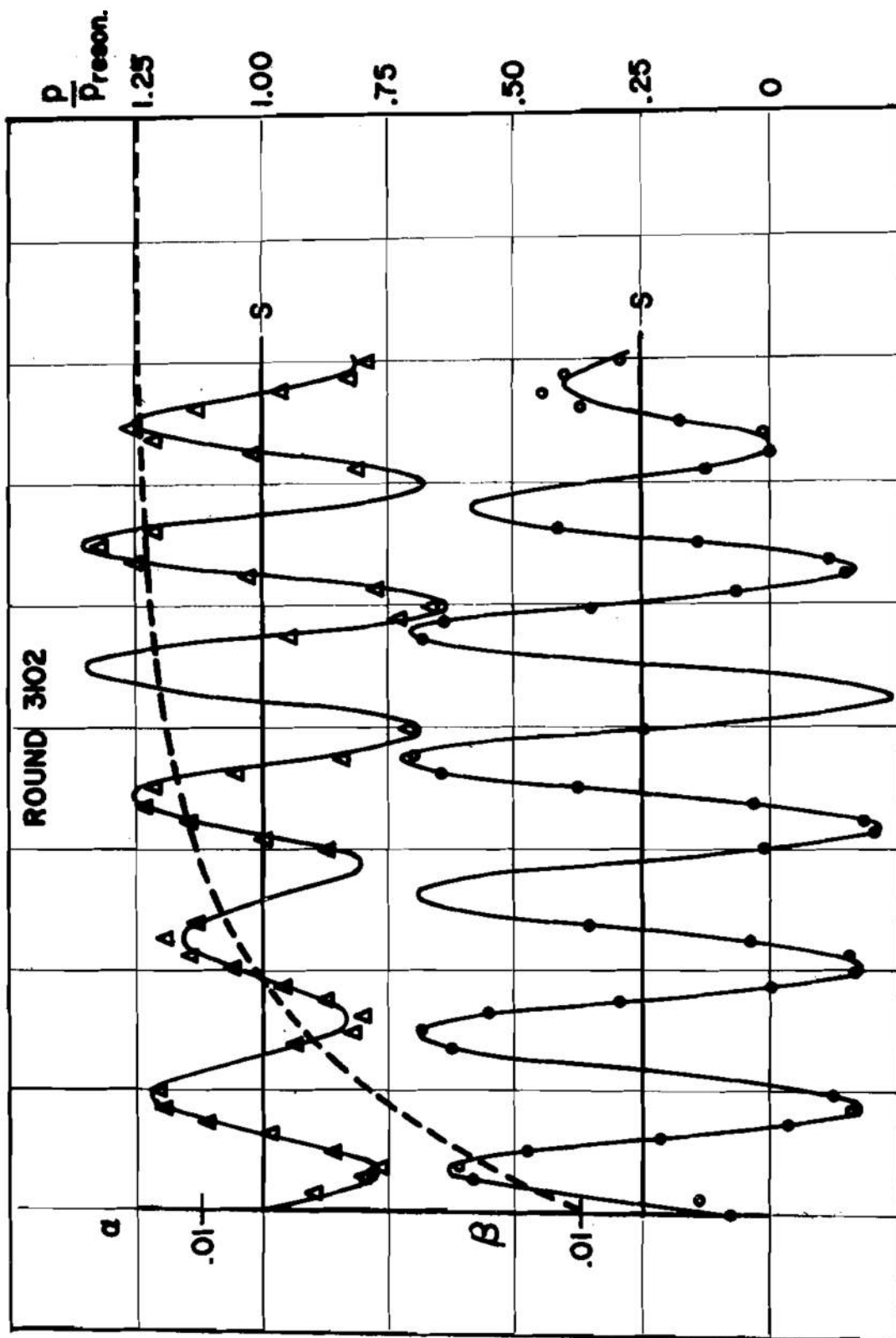
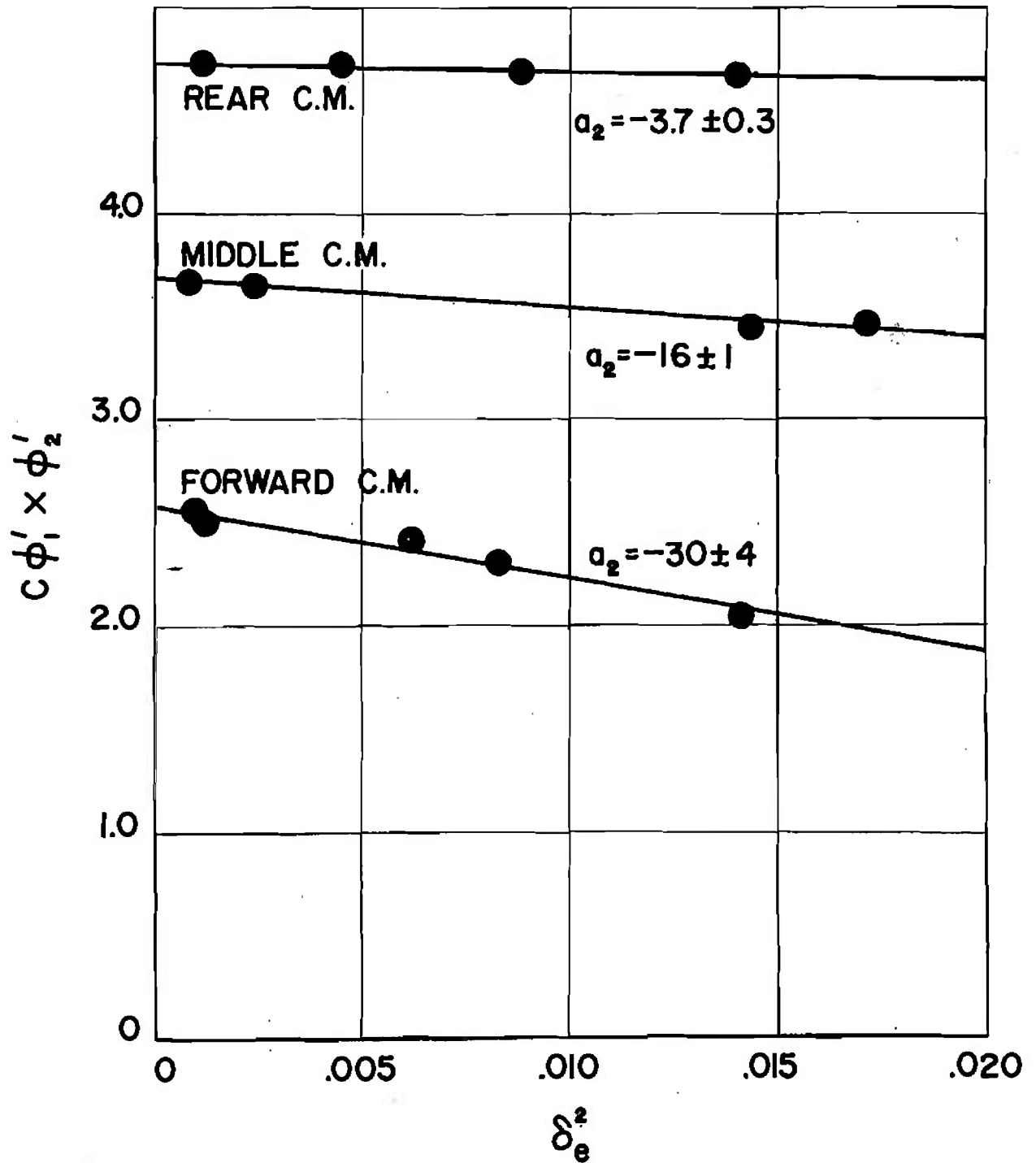


Figure 11

EFFECTIVE STATIC MOMENT COEFFICIENT

vs

EFFECTIVE SQUARED ANGLE OF ATTACK



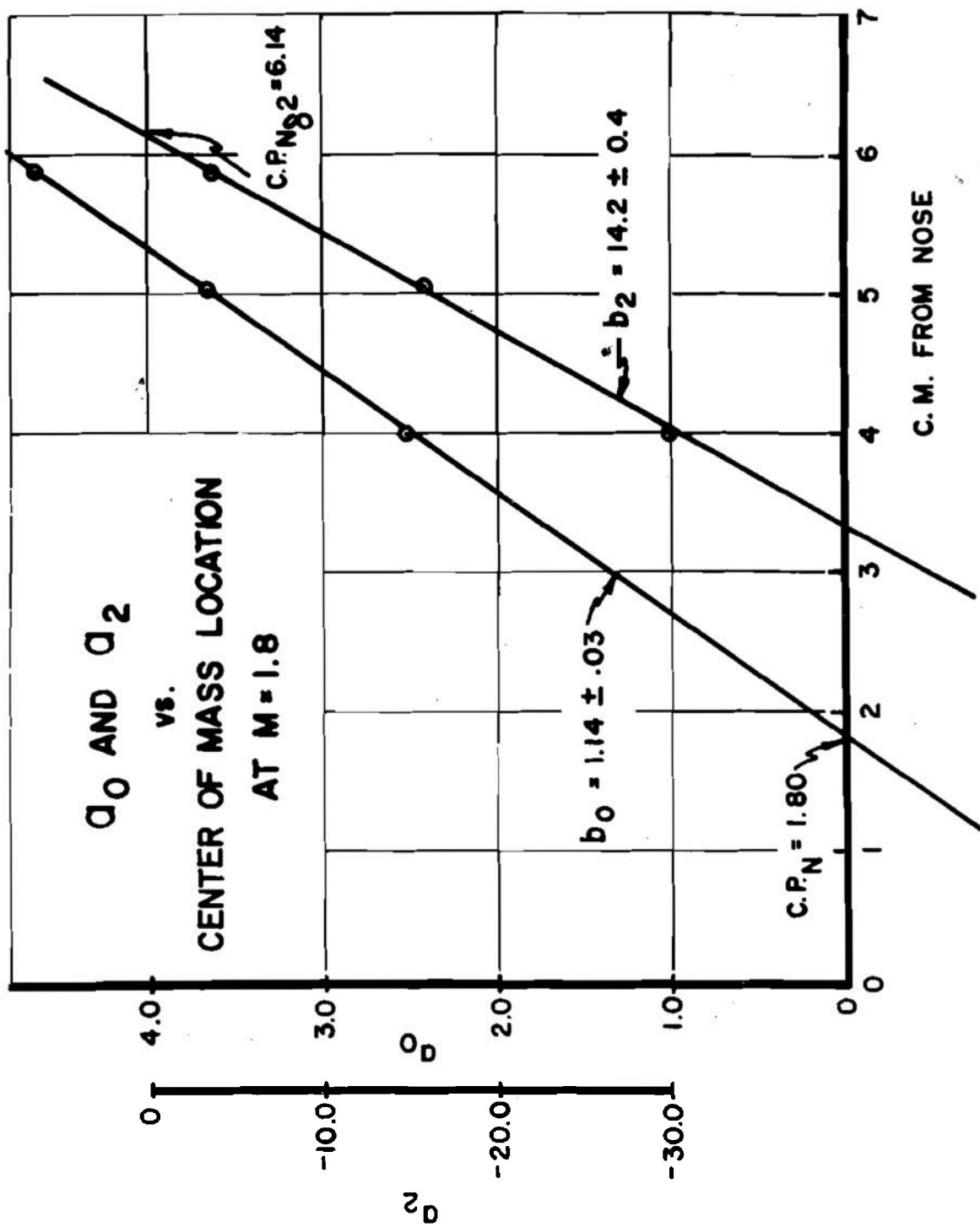


Figure 13

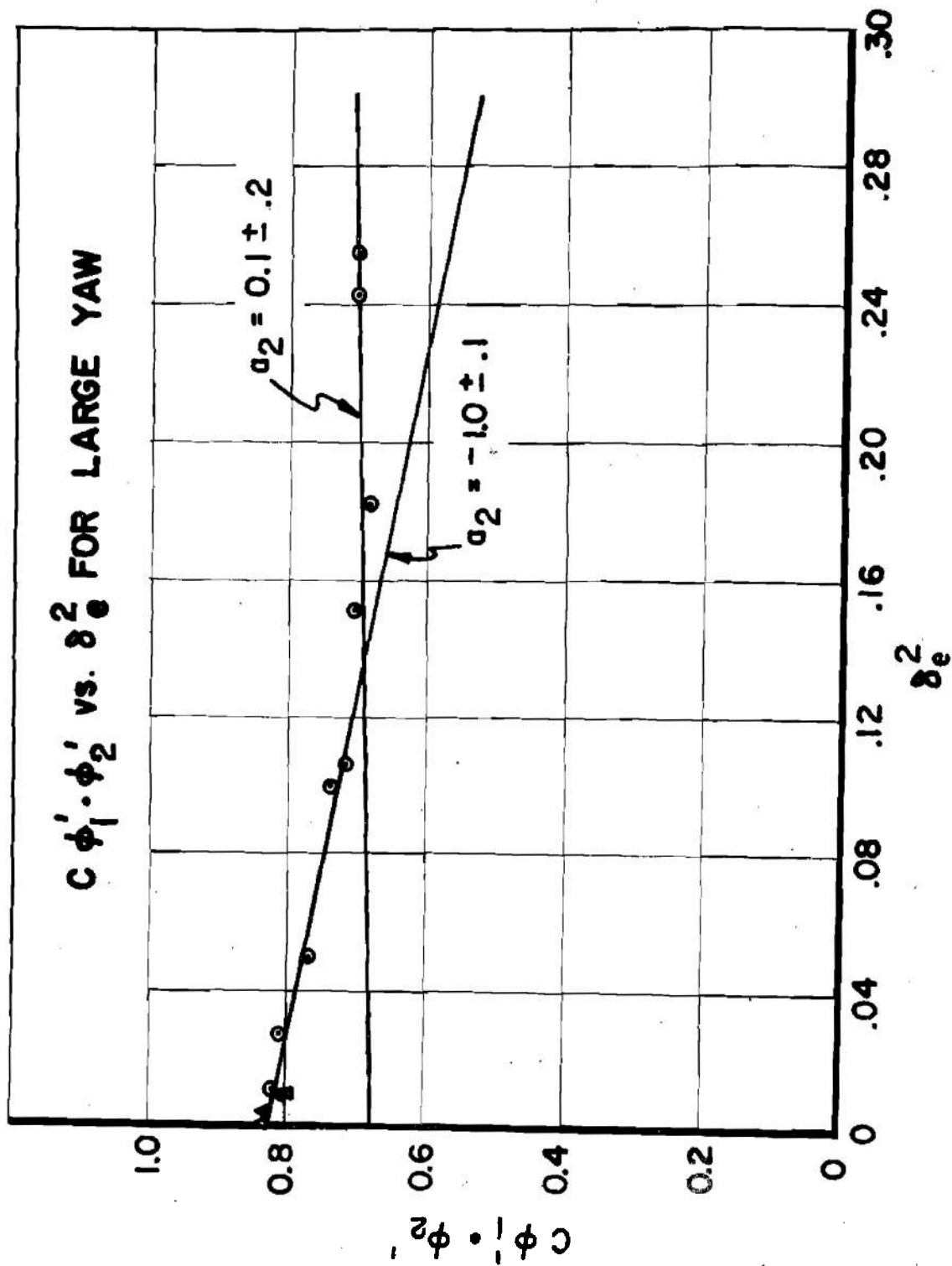


Figure 14

$C_{M_\alpha} \cdot Q$ vs. Q FOR LARGE YAW

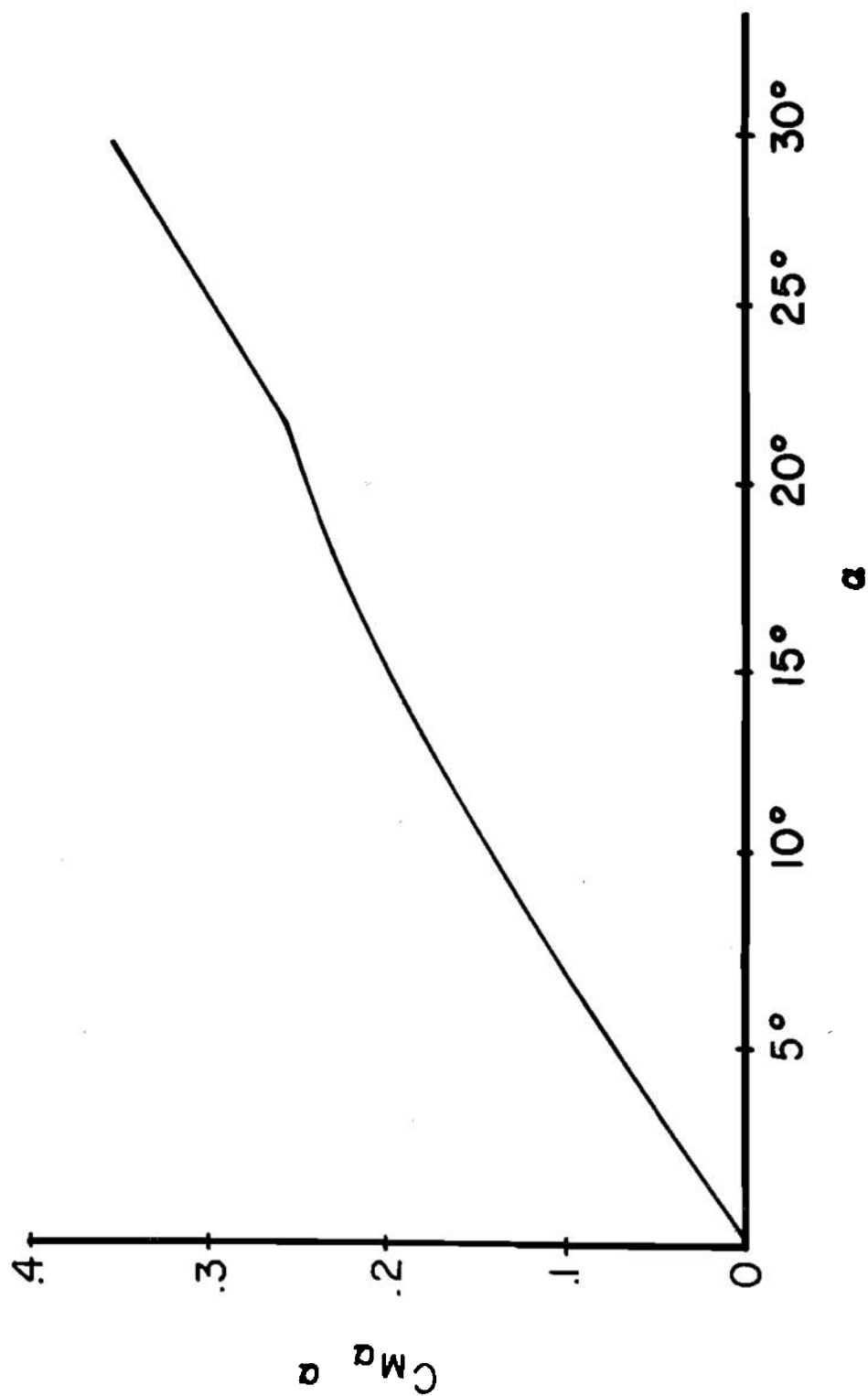
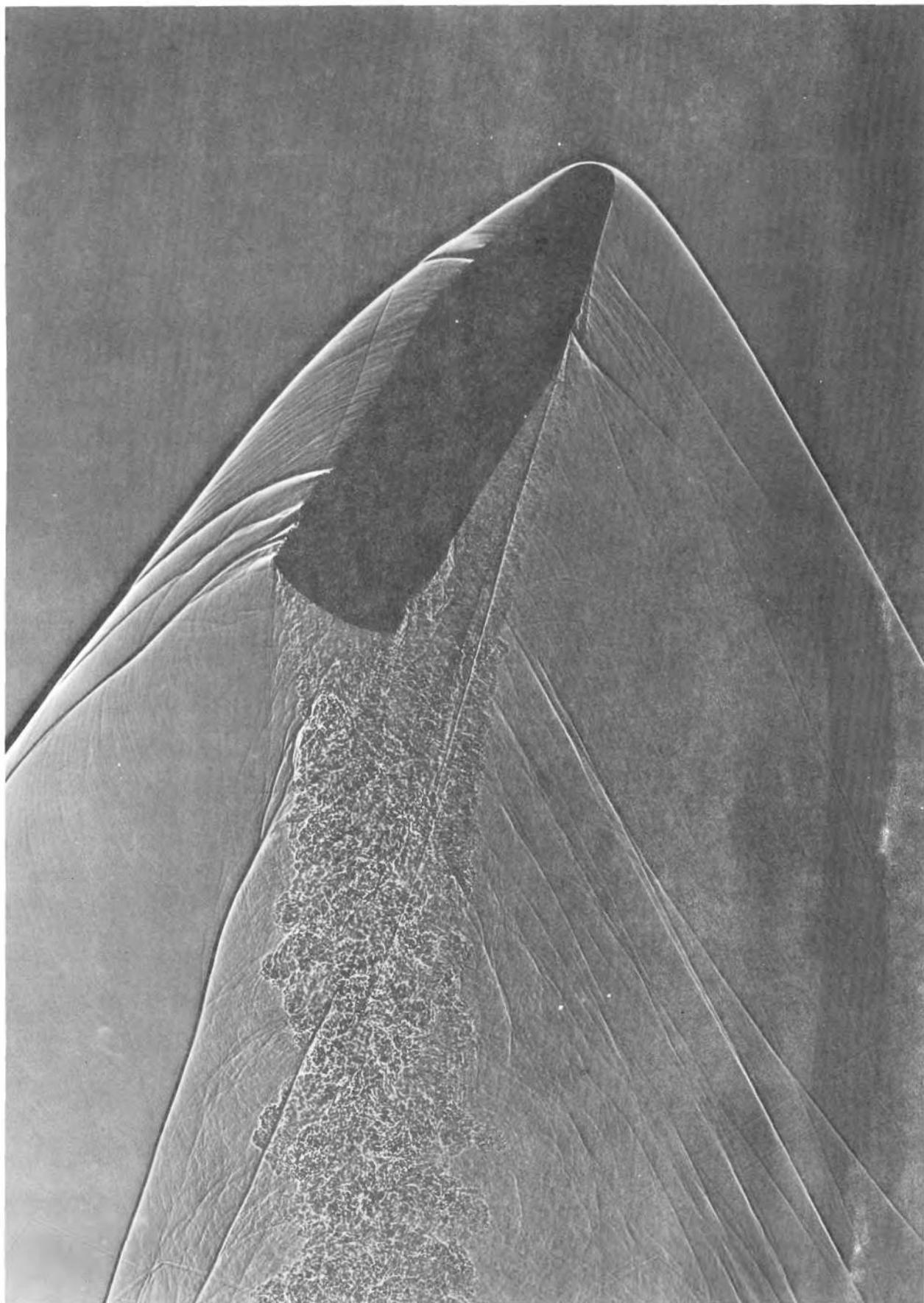


Figure 15



INTENTIONALLY LEFT BLANK.

SURVEY, CALIBRATION, AND REDUCTION TECHNIQUES USED
AT THE THOMPSON AEROBALLISTICS LABORATORY

Wallace H. Allan
Eldon L. Dunn

U. S. Naval Ordnance Test Station
China Lake, California

INTENTIONALLY LEFT BLANK.

SURVEY, CALIBRATION, AND REDUCTION TECHNIQUES USED
AT THE THOMPSON AEROBALLISTICS LABORATORY

Wallace H. Allen
Eldon L. Dunn

U. S. Naval Ordnance Test Station

INTRODUCTION

An essential requirement for free-flight aeroballistics ranges is an accurate means of determining the orientation and position of the missile. This is usually done photographically; it has been done by yaw cards and ideally we would like to do it electronically. For the present, photographic systems are the most popular. This paper is concerned with the photogrammetric problem of reducing data from the Thompson Aeroballistics Laboratory. The paper describes the precise position survey, the photographic calibration of the cameras to furnish transformation equations, the use of the transformation equations to yield position and orientation of the missile, alternate solutions for position and orientation, solutions for roll orientation, and the results of the reduction as applied to several typical rounds. The basic reduction methods were developed by N. S. Hall, formerly of the Naval Ordnance Test Station.

Photographic methods fall into two classes; those used on small ranges where the image is full size or larger, and those used on the larger ranges that work with greatly reduced image sizes. The scale reduction used in the Thompson Aeroballistics Laboratory is $1/40$. Most ranges, small and large, use external reference systems. In these systems the position of the missile is determined by using reference markers in the field of view of the camera. We use an internal reference system in which two fiducial markers inside the camera are used to pinpoint the location of the missile. The accuracy of the external reference system depends upon the long-term stability

of the building or the reference cables. The internal reference system depends upon well built, temperature-compensated cameras and stable camera piers. Once the calibration is completed, the cameras are expected to maintain their positions and orientations for at least a year. Figure 1a illustrates the camera and its mount. The camera is mounted on axes that intersect at the front nodal or perspective point of the lens. The camera may be swung in azimuth or elevation angles without disturbing the location of the front nodal point. The camera may be oriented and securely locked in position. The pier is made of reinforced concrete and is sunk more than 8 ft. underground. Figure 1b is a view of the inside of the camera; the two fiducial lamp projectors may be seen in this view. The six projecting pins are located in the focal plane of the lens and the glass photographic plate is positioned against these pins. The lenses and fiducial projectors are mounted so that as the temperature of the camera changes, the distance between the two fiducial marks and the focal distance change as if the camera were made of glass. This maintains the same scale values, provided the photographic plates are left in the cameras long enough to assume the temperature of the cameras.

PRECISE SURVEY

Our cameras are calibrated once a year by photographing some 30 reference beads in the field of view of each camera. The positions of these beads in space are accurately determined by means of a precise survey, and the positions of the bead images on the plate are used in a least-squares fit yielding the coefficients of the transformation equations for each camera. Figure 2 is a transverse section of the laboratory showing a typical camera station. The beads are fixed at two-foot intervals along each of 3 calibration wires. These wires hang in a tight catenary curve near the range line within the circle entitled "circle of missile model dispersion," in Fig. 2. The wires

are suspended from towers located at each end of the range. Figure 3 is a view of the laboratory looking downrange. The downrange tower may be seen at the extreme end of the range. The catenary wires are made of .030-inch-diameter Ni-Span-C alloy, an invar-type material. The wires are suspended so that their effective coefficient of expansion is approximately $1/40$ of that of invar.

In order to calibrate the cameras, the locations of the beads and cameras must be known to an accuracy of at least a .001 of a foot. (Approximately a $1/100$ of an inch.) Since there are 44 cameras and more than 700 beads used in this system the task is not a simple one. The positions of the beads and cameras are found in a coordinate system in which the X-axis is parallel to the range line and located 1 foot to the left (or west) of the left line of cameras as seen in Fig. 3. The Y-axis is cross-range and located 40 feet up-range from the first camera station and the Z-axis is vertical with its origin 1 foot underground. In laboratory coordinates, X is positive downrange, Y is positive to the right, and Z is positive upward. Thus it is seen that this coordinate system is lefthanded and, barring some catastrophe, all coordinates of each object of interest are positive.

Our survey is accomplished with Swiss surveying instruments. The Wild N-III level is used to determine the level of each camera. Figure 4 illustrates this instrument. All of our camera elevations are nearly the same, so the same rod reading is used between fore and back sights. The elevation differences are measured, using the optical micrometer. This instrument can give differences good to a .001 of an inch between cameras 20 feet apart. The elevation sights are taken on a small rod or scale resting on a bench mark mounted on the camera. Figure 5 illustrates the rod and bench mark. The reference mark on the bench mark is located directly above the front nodal point of the camera at a fixed distance from the nodal point. There are four such bench marks, any one of which may be placed on a camera and when properly leveled will indicate the same

location within several .001 of an inch. Figure 6 illustrates an alternate method of taking levels using a hydraulic micrometer level.

The distance between cameras is determined with an invar tape. We use a 20-foot tape for measuring distances between cameras and a 100-foot tape as a primary standard against which the 20-foot tape is compared. The two tapes agree with each other over the 100-foot distance within a few .001 of an inch. Both were standardized at the Bureau of Standards. Figure 7 illustrates one end of our taping rig. The tape is tensioned by means of a 20 lb. dead weight and the tape read with the magnifying glass. Figure 8 shows the other end of the tape. The spring scale is used as a shock absorber to prevent overstraining the tape while setting the rig up. Only the west or left cameras are taped for distance. The east cameras and all the beads are located by means of theodolite triangulation. Figure 9 shows the Wild T-3 theodolite mounted on the basic bench mark. The bench mark contains a center hole, and a stud on the base of the theodolite plate is positioned in the hole. The theodolite is centered on the base plate by means of a dial indicator referenced against a diameter concentric with the inner stud. The theodolite may be centered to within a .001 of an inch. Figure 10 illustrates the Wild T-3 and an operator observing a bead on the wire. The cameras at station 2 and station 23 are defined as being parallel to the range line and they define the basic camera line. All other cameras in this line are measured as to their cross-range coordinates by the use of the theodolite.

The Wild level is used to give the z or elevation coordinate of the cameras. The tape gives the x or downrange coordinate. The theodolite gives the y or cross-range coordinate of the cameras. Each camera in the west line may be used as a theodolite station to observe the beads or the east line of cameras. Azimuth angles taken to the east cameras serve to fix the xy coordinates of the cameras. The basic equations used in determining the xy coordinates from the

azimuth angles are illustrated in Fig. 11. It may be seen from Fig. 11 that the position of an unknown such as Bead x_3y_3 is determined by measuring the angles α and β , using the basic camera line as a reference line. The coordinates of the theodolites are the same as those of the cameras upon which they are mounted. The two equations have two unknowns x_3y_3 for which they can be solved. The basic equations for determining the z coordinate are illustrated in Fig. 12. The elevations of the beads may be measured by means of the Wild T-3 theodolite. An elevation angle θ to the bead may be measured and the elevation calculated using the elevation z_t of the theodolite and the horizontal distance D from the bead to the theodolite. The elevation of the theodolite is determined by finding its height L over the elevation of the front nodal point of the camera. The height L is measured by finding the elevation z_t ; then $L = z_t - z_2$. z_t is found by observing, with the theodolite, a bench mark on an adjacent station. The dip angle ϵ and distance D to the camera may be used to compute the distance h . This distance plus l , the height of the bench mark above the nodal point of the camera, plus the elevation z_1 of the observed camera may be used to calculate z_t . Then L is determined. L remains constant for a particular theodolite as it is moved from camera to camera.

The horizontal distances between beads on the wires are secured by a process by which each bead is fixed by triangulation in space. Only azimuth angles need to be taken for this measurement. The distances between beads are determined by taking three separate measurements several days apart and using the average of the three measurements. The distances are believed to be accurate to within a few .0001 of a foot. As these distances are added together accumulated errors can become large, so distances are checked every 20 ft. against triangulated data and then corrected if necessary. It is believed that the accumulated

distances are good to within .001 of a foot.

The towers move slightly every day and the wire changes its sag slightly with temperature so that the positions of all beads need to be determined by a method that can be accomplished very quickly. We do this by what we call a speed run. In the speed run all of the coordinates of the beads are measured by a process which takes about an hour and 15 minutes. The speed run is accomplished by a technique that requires two theodolites and two three-man crews plus a supervisor who operates a third theodolite. Advantage is taken of the fact that the three lines are catenaries. If the end beads and midpoint bead position of each wire are known, then the position of the rest of the beads may be calculated provided the distance between beads is known. Actually, to increase accuracy, more data than this is taken. Since the xy coordinates of the beads change slowly only the end beads are observed in azimuth during the speed run and these measurements can be verified against determinations taken hours before and after the speed run. In order to get a good fix on elevation, twelve beads on each wire are observed. The elevation readings are taken from the nearest theodolite station, which means that twelve different theodolite stations are occupied during the speed run. The third theodolite serves only to observe sag to correct the elevation readings of the other theodolites for changes in sag with time. This correction is very small because the theodolite crews start work at the end points and finish at the middle of the wire where the change in sag is largest. No bead changes more than .002 of a foot in sag between its measurement and the taking of the calibration plate and this is accounted for. Now the positions of all the beads may be calculated knowing the distances between beads, the coordinates of the end points, and the elevations of the twelve beads on each wire. As soon as this speed run is completed, a calibration picture is taken of the beads by the precision cameras. The plates are used to find the transformation equations of each camera.

DETERMINATION OF TRANSFORMATION EQUATIONS

The calibration plates are measured in a Mann comparator that is accurate to a few microns. The positions of each of the two fiducial marks and of the individual bead images on each photographic plate are determined with respect to the rectangular coordinate frame of the comparator; the plates do not need to be positioned in the comparator with particular care as far as the angular orientation is concerned. The comparator measurements are made by either one or two readers, and each reader makes N independent measurements of each point. The individual "x" and "y" readings are automatically recorded on IBM cards, along with the necessary identification code. These cards are the input data to an IBM 701 or 704 electronic calculator, both of which are coded to calculate the coefficients of the transformation equations for each camera. From this point on, any arithmetic mentioned is performed by these high-speed computers.

The original N readings of each point are averaged separately for each reader. The orthogonal axes of the comparator coordinate system are then rotated and translated by standard procedures so that the new x-axis passes through the two fiducial marks, with the new origin midway between the fiducial marks. Figure 13 shows the relationship between the two coordinate systems. The positive direction of the y-axis is upward as defined by the image of the photographic background in the laboratory, and the positive direction of the x-axis is directed toward the downrange fiducial mark. It is seen that the plate coordinate system is "left-handed" for the right or east cameras and "right-handed" for the left or west cameras. This rotation and translation of the comparator coordinate system to the camera plate axis is performed separately for the measurements of each reader. If two readings have been made, the two sets of plate coordinates are averaged.

The bead coordinates are used to determine the coefficients of transformation equations relating focal plane positions with positions in space. The positions in space are all located in two space-planes approximately parallel to the focal plane of the camera and located near the range line of the laboratory. Figure 14 shows the space-planes, which are inclined at 45 degrees to the horizontal and are exactly parallel to the x-axis or range line. The coordinates of the beads on the calibration plates are used to give a least-squares determination of the coefficients of two general quadratic functions to fit the known positions of points in the space-plane. The points in the space-plane are determined from the survey by projecting the bead coordinates into the space-plane as seen from the camera. This is simply done by forming the equation of a line through the bead and nodal point of the camera and then solving for the intersection of this line with the space-plane. Figure 15 shows the transformation equations for one camera relating focal-plane positions with space-plane positions. The 10 coefficients are determined by the previously-mentioned least-squares fit. These equations take account of the camera lens distortion and remove the need for the cameras to be exactly aligned to the assumed geometry. All scale factors between plate coordinates and space coordinates are likewise accounted for by the coefficients. If the readings of the beads are now applied to these equations and the positions of the beads in space calculated, then the standard deviation of the bead positions as computed with respect to the actual positions is approximately .001 of a foot.

CENTER OF GRAVITY REDUCTION

When a missile is tested in the range, accurately-timed light flashes of one-microsecond duration are utilized to obtain multiple-image photographs of the missile at each station. Figure 16 shows a typical data record for one of the cameras. The fiducial marks visible at the ends of the plate, in addition

to relating the missile records with those of the calibration, also provide the means for correcting for the difference in plate temperatures at the times of reading the calibration plate and the data plate. The correction factor is equal to the distance between the fiducial marks for the calibration plate divided by the same distance for the missile record. This correction factor is computed separately for each data plate, and is applied to all comparator readings of the missile images.

As in the case of the calibration plates, each photographic record is measured on the Mann comparator by one or two readers, each reader making N independent measurements of each nose, tail and fiducial mark. The comparator coordinate axes are translated and rotated so that the plate coordinates are defined in the same manner as for the calibration plates.

At this time the transformation equations are introduced to convert the plate coordinates of each point to its x and z coordinates in the appropriate space-plane. Figure 14 illustrates the space-planes previously mentioned; from an inspection of the figure it is apparent that

$$y_2'' = 29.2840 - z_2''$$

$$y_2' = z_2' + 1.0000$$

where the prime indicates a right camera, a double prime indicates a left camera, and the subscript 2 indicates the point on the ray from the camera to the point under observation. Since the coordinates of the front nodal point of each camera lens are known and the positions of the points in the space-plane are known from the transformation equations, then two points on each ray are known and the equations of the rays can be written. These equations are displayed in Fig. 17; here the subscript 1 indicates the camera coordinates. The expressions in the denominators are the direction numbers of the rays.

It is unlikely that the two rays will intersect and, hence, the most probable point must be chosen to represent the position of the point under observation. It is felt that neither ray is more accurate; hence the midpoint of the common perpendicular to the rays is chosen. The direction numbers of the common perpendicular may be obtained as the direction numbers of the vector product of the two rays. These numbers are given by the expressions in Fig. 18; this figure also shows two equations of the common perpendicular. In these equations the x 's, y 's, and z 's have the property that they lie both on the perpendicular and on the ray. Since no points on the common perpendicular are known, an arbitrary point $X_0 Y_0 Z_0$ on this line is chosen to write its equation; this equation and the equations of the rays may then be solved simultaneously to yield the points of intersection. The fixed point is chosen in such a way that the numbers appearing in the equations are of reasonable magnitude. To do this it is sufficient to fix the coordinate corresponding to the largest direction number. As the common perpendicular is in all cases nearly parallel to the x -axis, the direction number a will in all cases be largest. Therefore, we set X_0 equal to 20 times the station number, and Y_0 and Z_0 can be determined in terms of y' or y'' as shown in Fig. 19. Here the coefficients are functions of the two sets of direction numbers, the camera coordinates, and X_0 and hence can be calculated.

The solutions of the equations of the rays and the equations of the common perpendicular are given in Fig. 20, where again the coefficients are the same as those used in the equations of Y_0 and Z_0 , and have been determined. The final values of x, y , and z are taken as the average of the x' and x'' , y' and y'' and z' and z'' , respectively.

The differences between x' and x'' , etc. are a direct measure of the miss distance between the rays from opposite cameras. This distance is usually very

small; however, if a camera has changed its orientation since its calibration, then the miss distance becomes significant. Thus we have a measure every round of how well the cameras are maintaining their calibration.

Once the positions of the nose and tail have been determined, the direction cosines of the missile axis may be calculated by standard geometric procedures. Then the position of the center-of-gravity of the missile is given by the expressions in Fig. 21. In these equations l is the distance from the CG to the nose of the round and l' is the distance from the CG to the base. It is seen that the expression for each coordinate of the CG is the average of the values for the coordinate based on the nose and tail points.

CENTER OF GRAVITY REDUCTION FOR BLUNT BODIES

Recently, interest has arisen in determining the aerodynamic characteristics of blunt-nosed re-entry shapes for Intercontinental Ballistic Missiles. Missiles having these shapes are not susceptible to reduction by the method just described, because they have no definite "nose" point that can be seen from all perspectives available to the cameras in the laboratory. However, a method of determining their position and orientation has been devised and will now be described. In case the base of the missile is too large for accurate determination of its center, a slender pin is installed in the center of the base and the tip of this pin is read as the base of the missile; at the same time, another point on the axis of the round near the nose is read. Figure 22 illustrates such a missile and the points read. By the procedure just described, the coordinates of the base are determined, as well as the coordinates x_2 , y_2 , and z_2 in the space-plane of the points on the rays from each camera to each of the two points on the axis. These two points together with the coordinates of the front nodal point of the lens of each camera determine a plane through the axis of the round. There are two of these planes, one for each camera, and they intersect in the

axis of the round. One can use a solution of the equations of the planes analogous to the vector product and obtain the direction numbers and hence the direction cosines of the axis of the missile. Now, knowing the direction cosines of the missile axis and the location of the base, one can find the location of the CG by use of the equations given in Fig. 23, where d is the distance from the CG to the tip of the pin.

ROLL ORIENTATION

The roll orientation of the missile is measured with the aid of spin pins fastened in the base of the missile. These pins are coded by means of their shape; one pin is pointed, and the other pin is blunt. These pins are read in the comparator and their position found in space. The roll orientation of the missile is found by finding the line that goes through the position data for the two pins. The change of orientation of this line gives a measure of the spin.

EXAMPLES

Figure 24 illustrates the yawing and swerving motions of a finned missile plotted against downrange distance. The orientation angles (derived from the direction cosines by use of the small-angle approximations) were converted to yaw angles by correcting for gravity drop and drift due to gun alignment. The damping and frequency terms for this round were well-determined by a digital reduction. Figure 25 shows the yawing motion of a typical spinning missile based on data obtained from the reduction applied to a 5-inch projectile. The data were subjected to an iterative epicyclic yaw reduction on a digital computer using the method of differential corrections, and the standard deviation of the fit was about 3 milliradians.

We believe that by the application of the survey and reduction techniques described in this paper, we are able to achieve excellent accuracy for a range

of this size. One of the principal advantages of this calibration method over some of the methods using external reference systems is that the camera is calibrated over its entire field of view and the data can be assessed with equal accuracy throughout the entire range regardless of where the missile is located along the range line. This permits us to take multiple-image photographs with each camera, thus increasing the frequency of data points. Although our cameras are spaced 20 ft. apart, we are able to secure accurate data every five feet along the trajectory. This feature is very important to us. As an example, the curve presented in Fig. 25 would yield a less accurate determination of turning and damping rates if we used every fourth point in the fit.

Thus accuracy and frequent data points are one of our principal advantages. However, when we speak of accuracy it should be borne in mind that we are referring to the larger type of aeroballistic range. The smaller spark and pressure ranges are capable of obtaining more accurate position data, because they work with full scale or larger images. The principal disadvantage of our range is that we are not able to achieve good orientation data on short missiles. Since we find orientation by locating the position of the nose and tail of a missile, short base lines reduce the accuracy of the orientation data. We do not like to work with missiles shorter than .5 of a foot.

In conclusion, it is felt that the survey, calibration, and position reduction techniques just described render the Thompson Aeroballistics Laboratory a well-equipped tool to assess the aeroballistic characteristics of models or full scale missiles ranging from 1 to 3 feet in length.



FIG. 1a. 4" x 10" CZP-1 PLATE CAMERA AND MOUNT

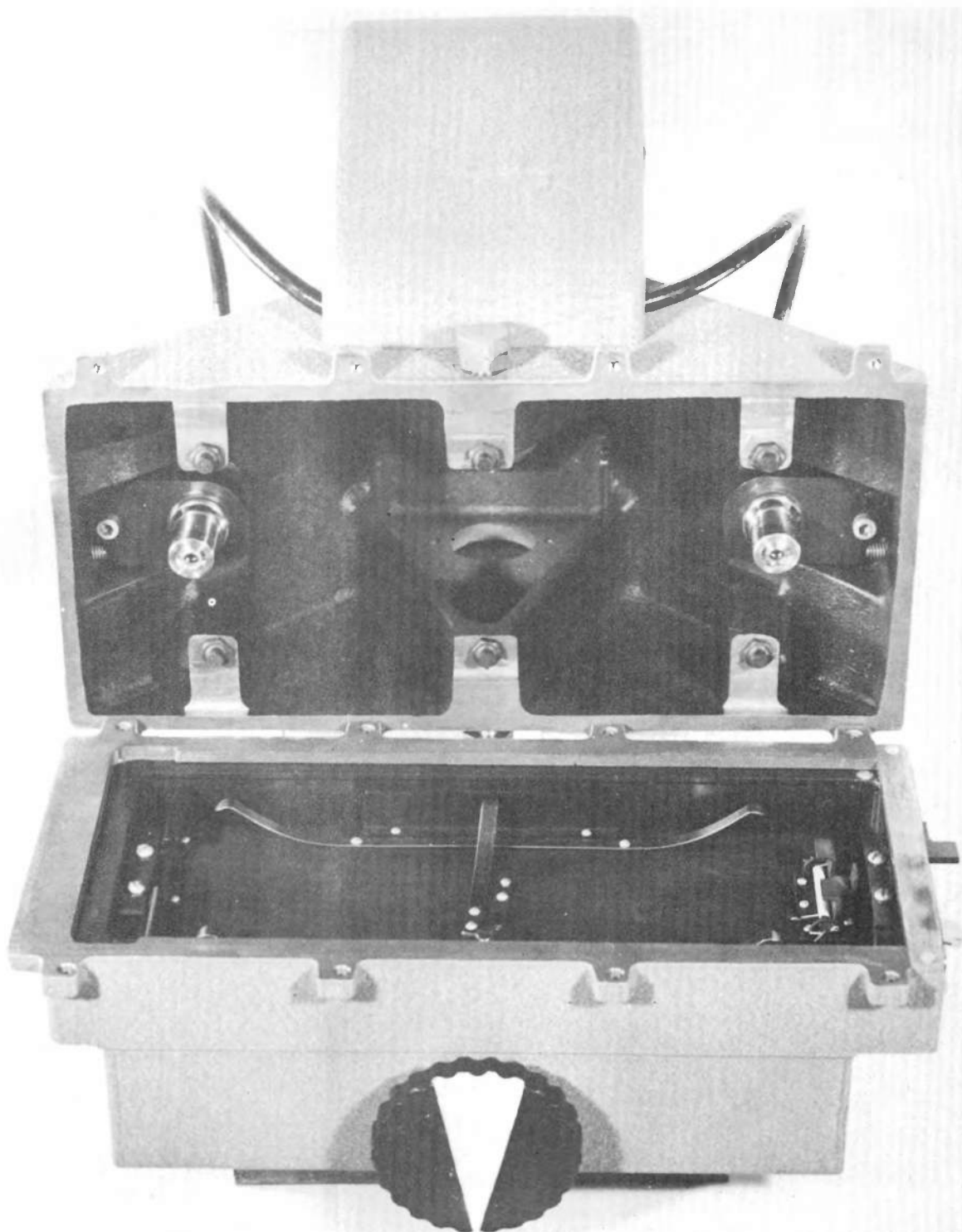


FIG. 1b. 4" x 10" CZP-1 PLATE CAMERA - INTERIOR VIEW

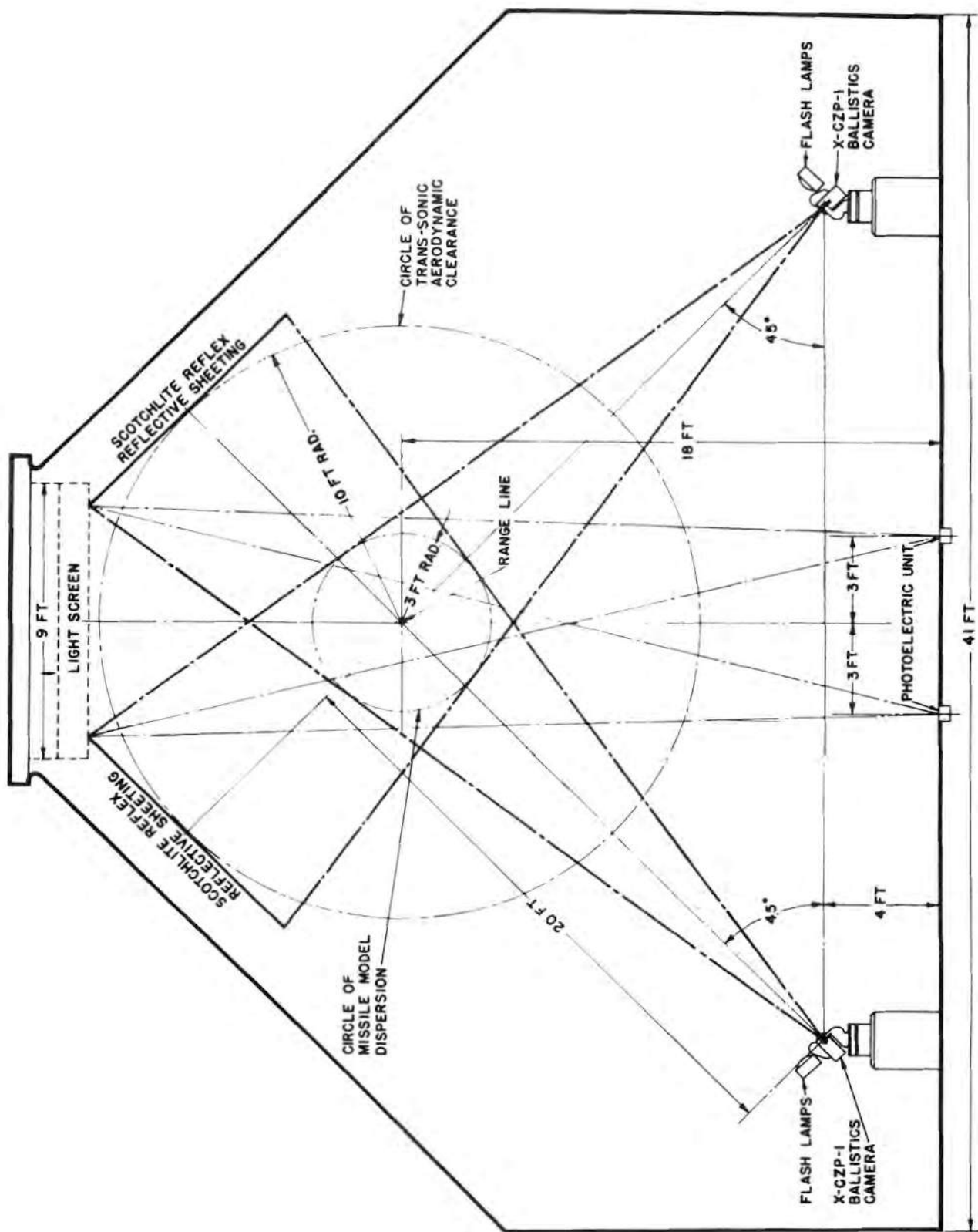


FIG. 2. TRANSVERSE SECTION OF THOMPSON AEROBALLISTICS LABORATORY

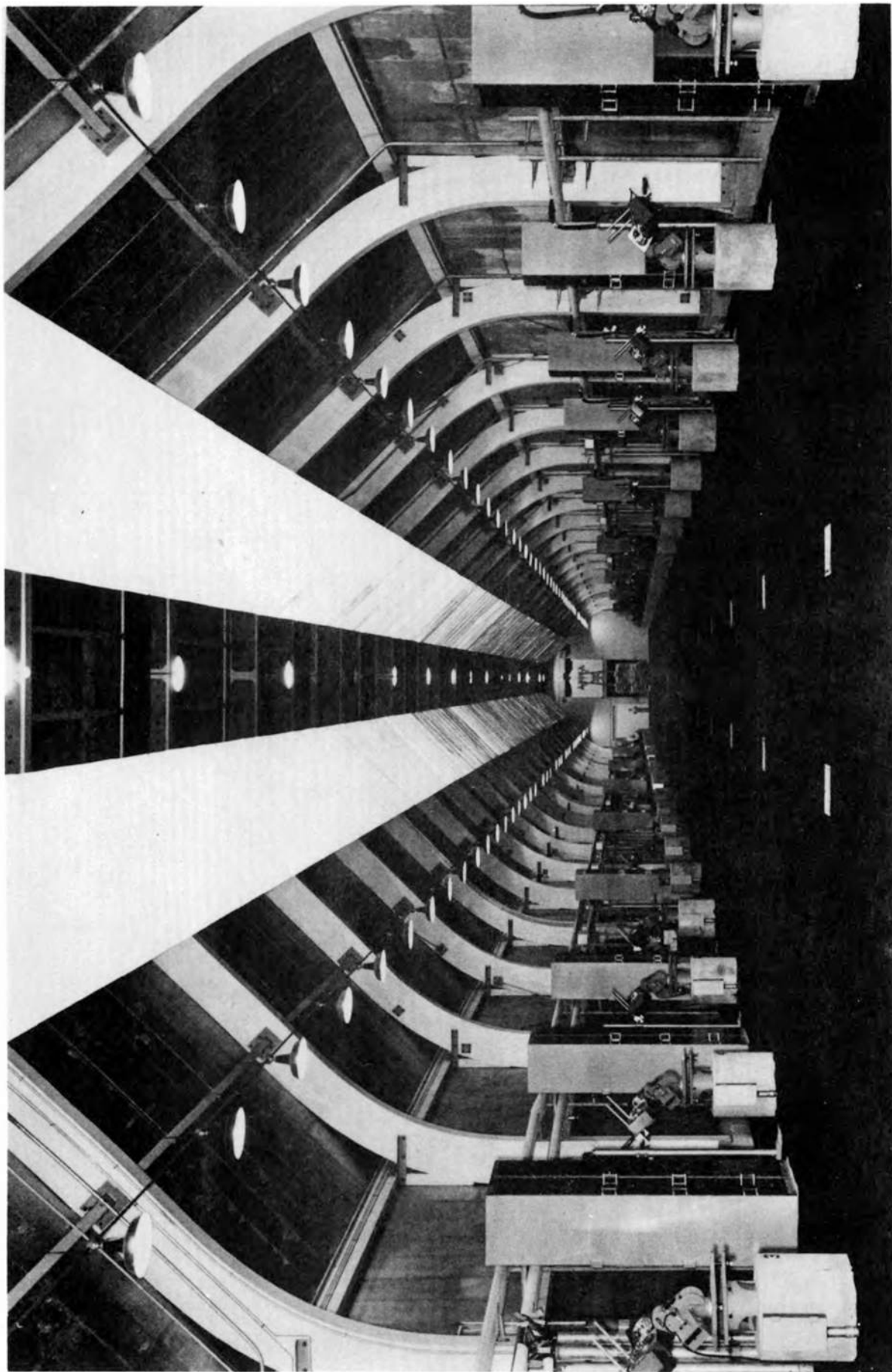


FIG DOWNRANGE VIEW OF THOMPSON AEROBALLISTICS LABORATORY

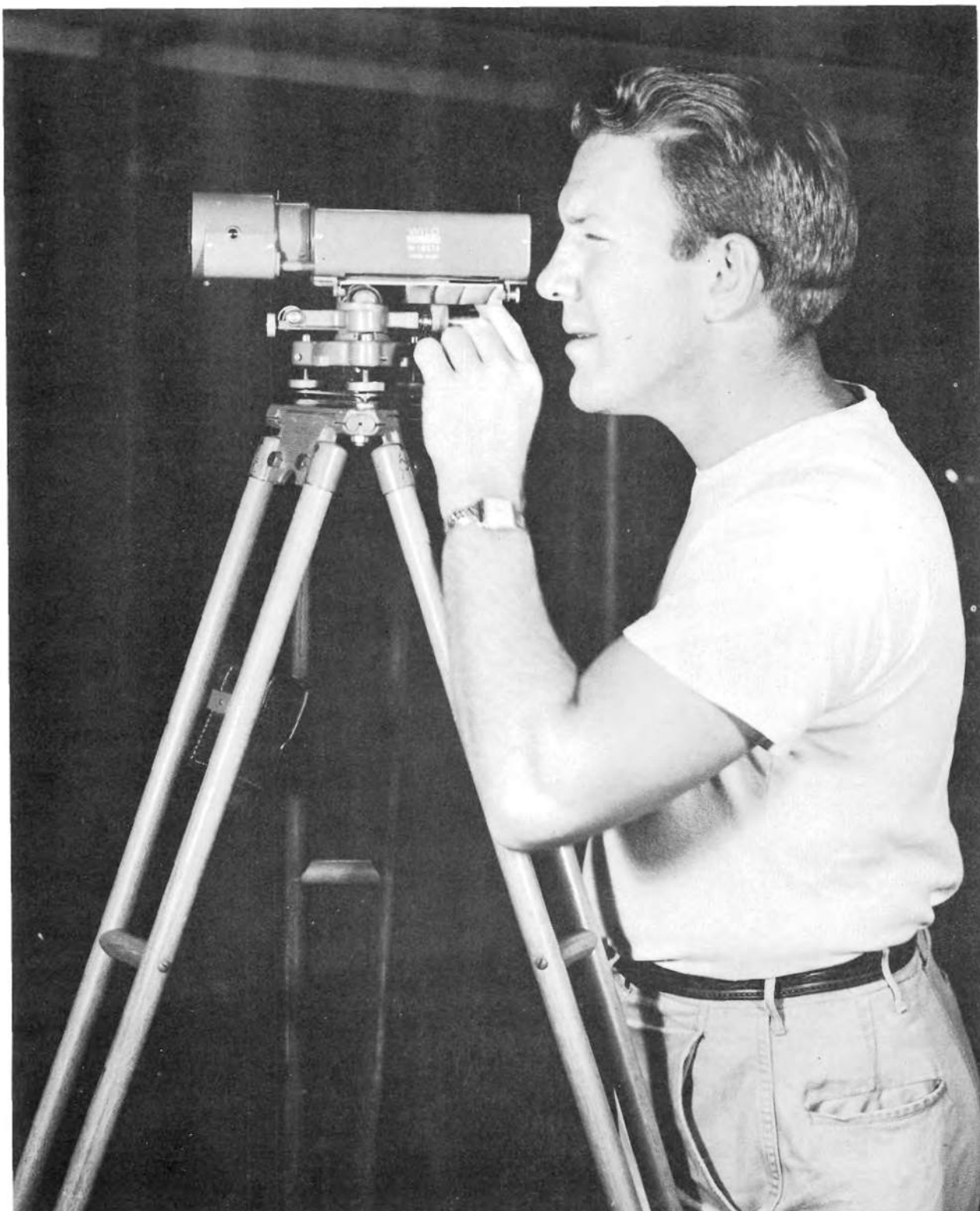


FIG. 4 WILD N-111 LEVEL USED FOR MEASURING ELEVATION OF CALERA BENCH
MARK.

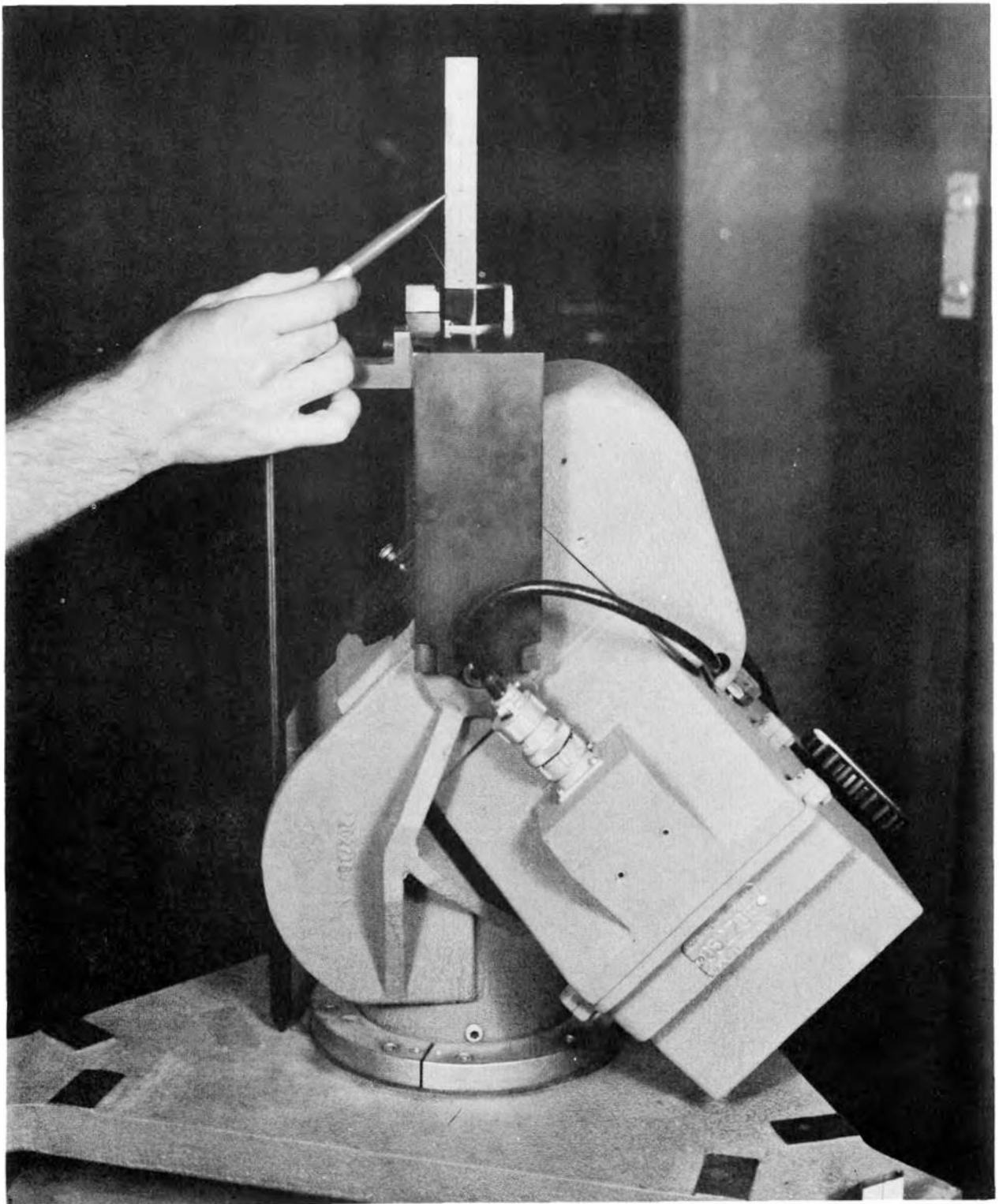


FIG. 5 ELEVATION ROD ON CAMERA BENCH MARK, USED FOR READING ELEVATIONS
WITH THE WILD N-111 LEVEL.

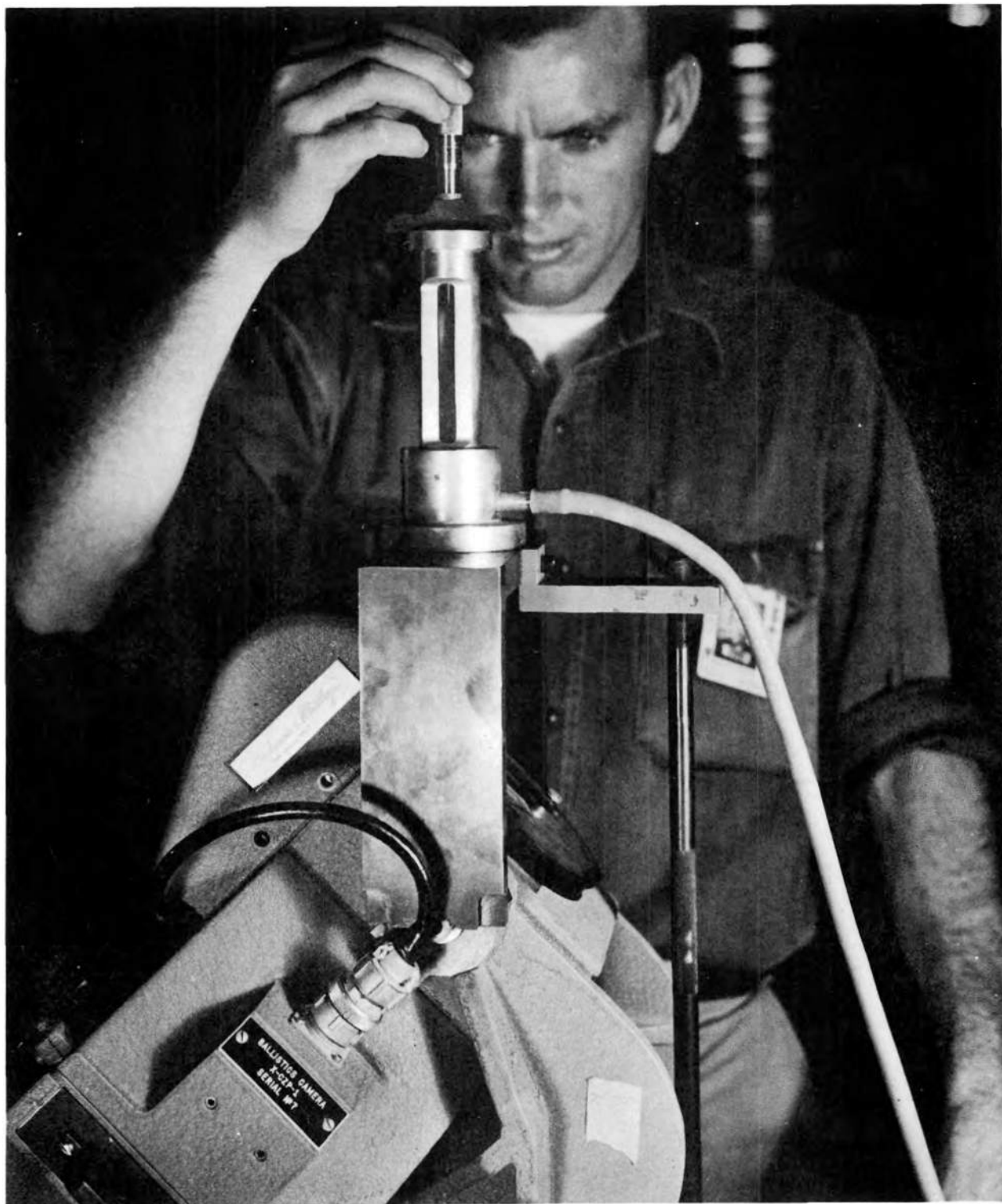


FIG. 6 HYDRAULIC MICROMETER LEVEL USED FOR MEASURING ELEVATION OF
CAMERA BENCH MARKS.

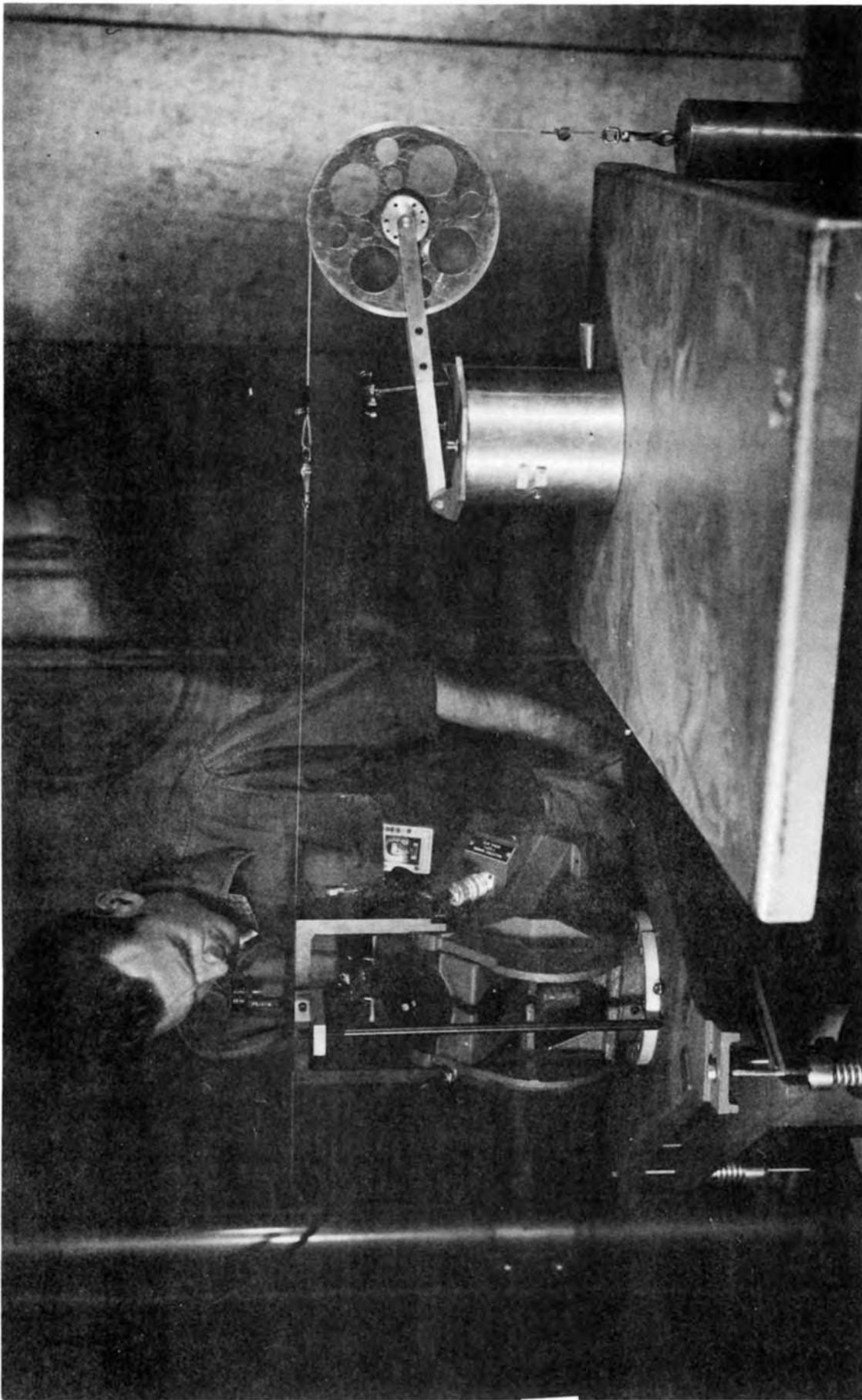


FIG. 7 TAPING STAND EQUIPPED WITH DEAD WEIGHT TENSION CONTROL, USED FOR TAPING DISTANCES BETWEEN CAMERAS.

NP/45-69823, USNOTS, Inyokern, California

August 1953

UNCLASSIFIED

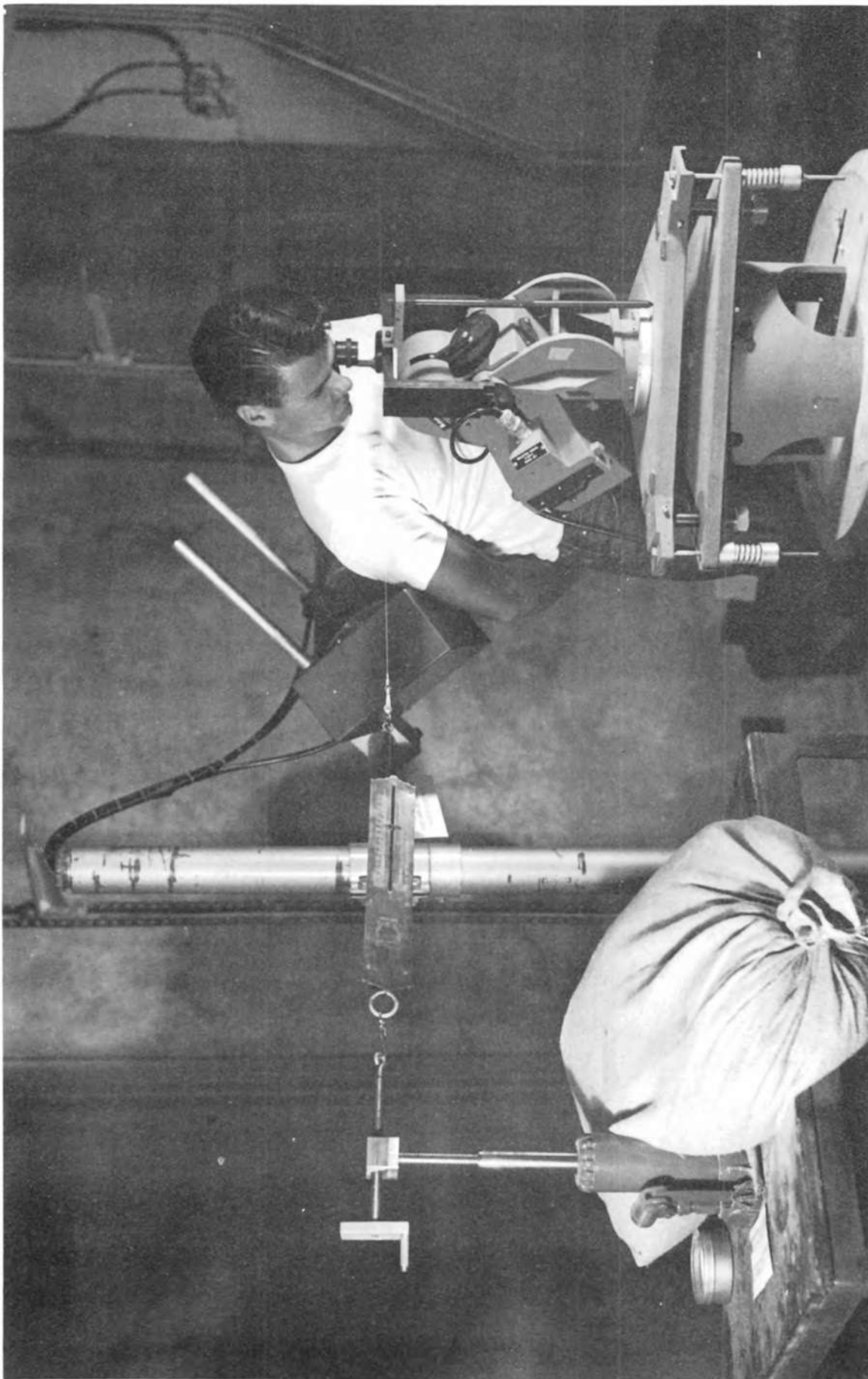


FIG. 8 TAPING STAND EQUIPPED WITH SPRING SHOCK ABSORBER, USED FOR TAPING DISTANCES BETWEEN CAMERAS.

NP/45-69824, USNCTS, Inyokern, California

August 1953

UNCLASSIFIED

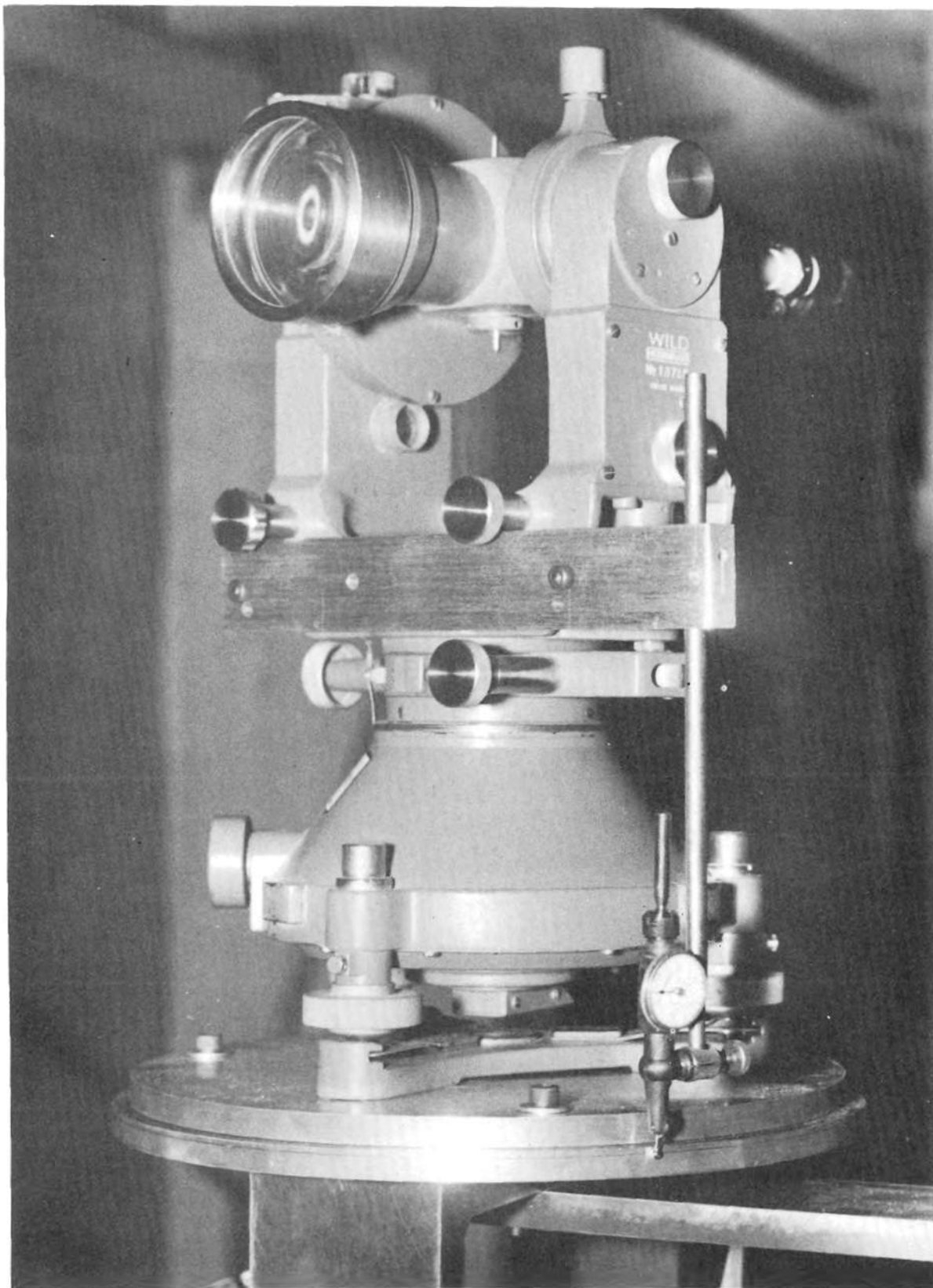


FIG. 9. WILD T-3 THEODOLITE

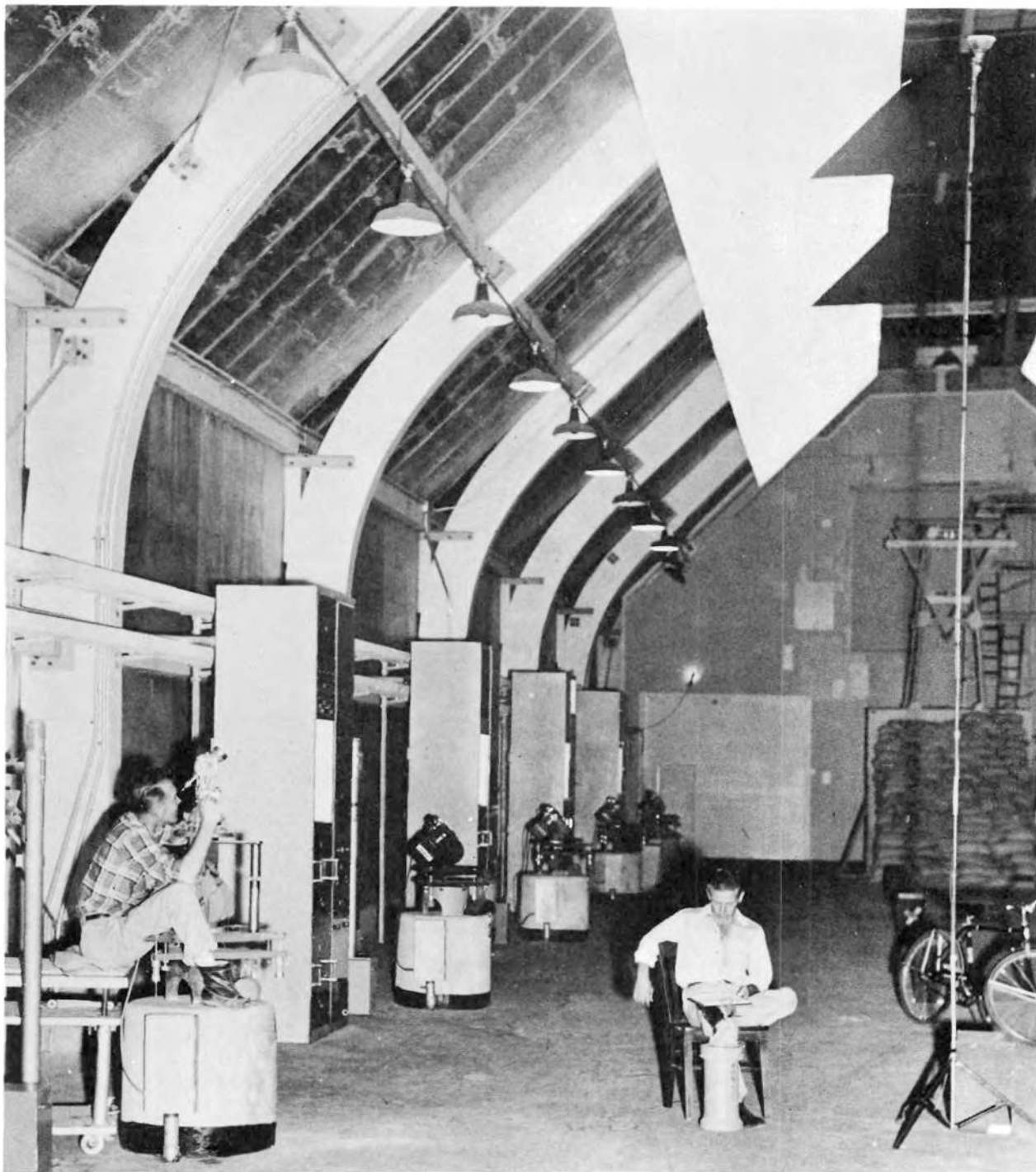
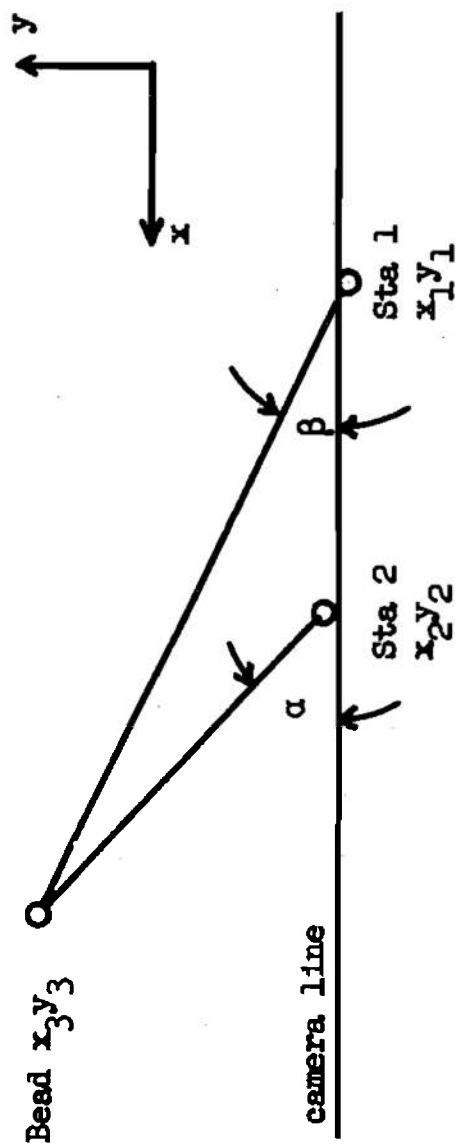


FIG. 10. WILD T-3 CREW OBSERVING BEAD

HORIZONTAL PLAN



$$\tan \alpha = \frac{y_3 - y_2}{x_3 - x_2}$$

$$\tan \beta = \frac{y_3 - y_1}{x_3 - x_1}$$

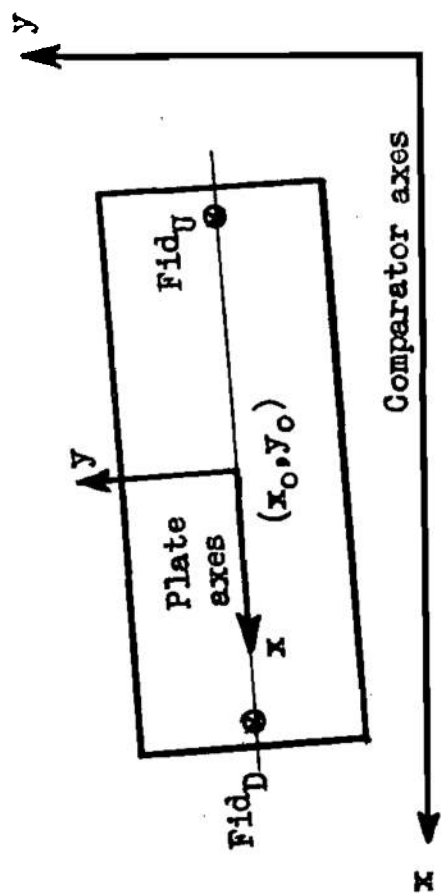
FIG. 11. TRIANGULATION EQUATIONS

The diagram shows a beam of total length L supported at two points, labeled 'Sta 2' and 'Sta 1'. A coordinate system is defined with the x -axis along the beam and the z -axis perpendicular to it. The beam is subjected to a uniformly distributed load H acting downwards. A point load P is applied at a distance d from the right support. The beam has a height h and a thickness t . The distance from the left support to the point load is D . The distance from the point load to the right support is $L - D$. The beam is inclined at an angle θ to the horizontal. The vertical distance from the supports to the top of the beam is z_t . The vertical distance from the supports to the bottom of the beam is z_b . The vertical distance from the supports to the center of the beam is z_c . The vertical distance from the supports to the top of the beam is z_t . The vertical distance from the supports to the bottom of the beam is z_b . The vertical distance from the supports to the center of the beam is z_c .

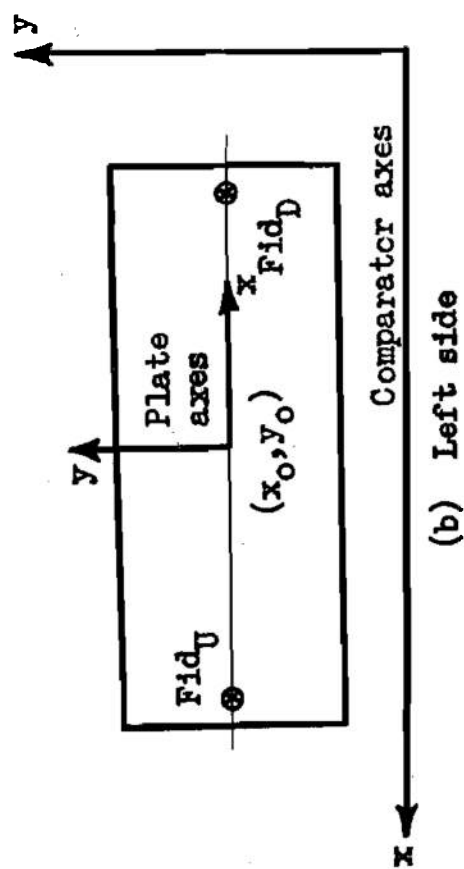
$$z_t = z_1 + l + h$$

$$z_3 = z_2 + H$$

FIG. 12. ELEVATION EQUATIONS



(a) Right side



(b) Left side

FIG. 13. TRANSFORMATION TO PLATE COORDINATES

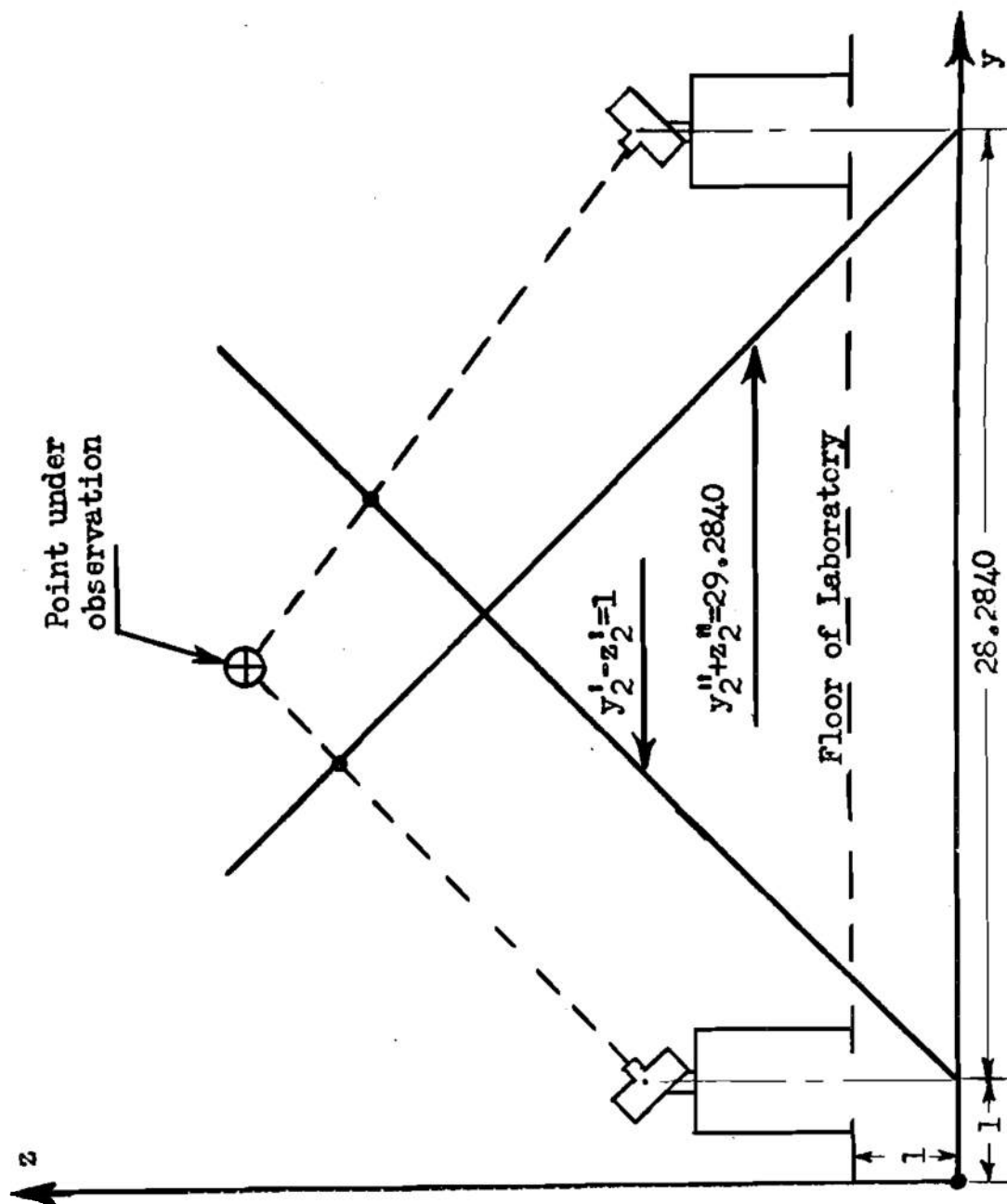


FIG. 14. PROFILE OF LABORATORY SHOWING PROJECTION PLANES

$$x_2 = a_1 x_p + b_1 y_p + c_1 + d_1 x_p^2 + e_1 y_p^2 + f_1 x_p y_p$$

$$z_2 = a_2 x_p + b_2 y_p + c_2 + d_2 x_p^2 + e_2 y_p^2 + f_2 x_p y_p$$

FIG. 15. TRANSFORMATION EQUATIONS

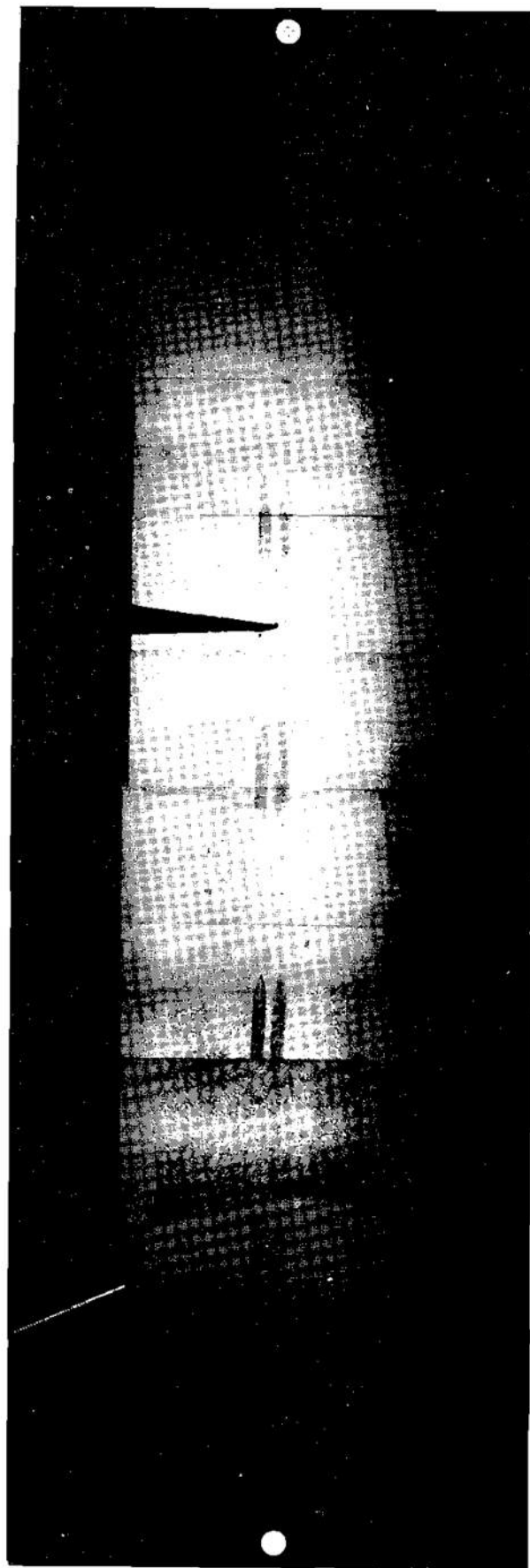


FIG. 16. TYPICAL DATA PLATE

$$\frac{x' - x_1'}{x_2' - x_1'} = \frac{y' - y_1'}{y_2' - y_1'} = \frac{z' - z_1'}{z_2' - z_1'}$$

Right station:

$$\frac{x'' - x_1''}{x_2'' - x_1''} = \frac{y'' - y_1''}{y_2'' - y_1''} = \frac{z'' - z_1''}{z_2'' - z_1''}$$

Left station:

FIG. 17. EQUATIONS OF RAYS

$$\frac{x' - x_0}{\alpha} = \frac{y' - y_0}{\beta} = \frac{z' - z_0}{\gamma}$$

$$\frac{x'' - x_0}{\alpha} = \frac{y'' - y_0}{\beta} = \frac{z'' - z_0}{\gamma}$$

$$\alpha = m_{RL}^n - m_{LR}^n; \quad \beta = l_{LR}^n - l_{RL}^n$$

$$\gamma = l_{RL}^m - l_{LR}^m$$

FIG. 18. EQUATIONS OF COMMON PERPENDICULAR

$$Y_0 = Ky'' + Q = ky' + q$$

$$Z_0 = Iy'' + J = iy' + j$$

$$K = 1 - \frac{\beta l_L}{\alpha m_L} ; Q = \frac{\beta}{\alpha} \frac{l_L}{m_L} y_1'' + x_0 - x_1''$$

FIG. 19. SOLUTIONS FOR Y_0 AND Z_0 .

$$y' = \frac{K(j - J) + I(Q - q)}{Ik - Kl}; \quad y'' = \frac{ky' + q - Q}{K}$$

$$x' = \frac{l_R}{m_R} (y' - y_1') + x_1'; \quad x'' = \frac{l_L}{m_L} (y'' - y_1'') + x_1''$$

$$z' = \frac{n_R}{m_R} (y' - y_1') + z_1'; \quad z'' = \frac{n_L}{m_L} (y'' - y_1'') + z_1''$$

FIG. 20. INTERSECTIONS OF RAYS AND COMMON
PERPENDICULAR

$$\bar{x} = \frac{x_N - l\lambda + x_T + l'\lambda}{2}$$

$$\bar{y} = \frac{y_N - l\mu + y_T + l'\mu}{2}$$

$$\bar{z} = \frac{z_N - l\nu + z_T + l'\nu}{2}$$

FIG. 21. POSITION OF CENTER-OF-GRAVITY

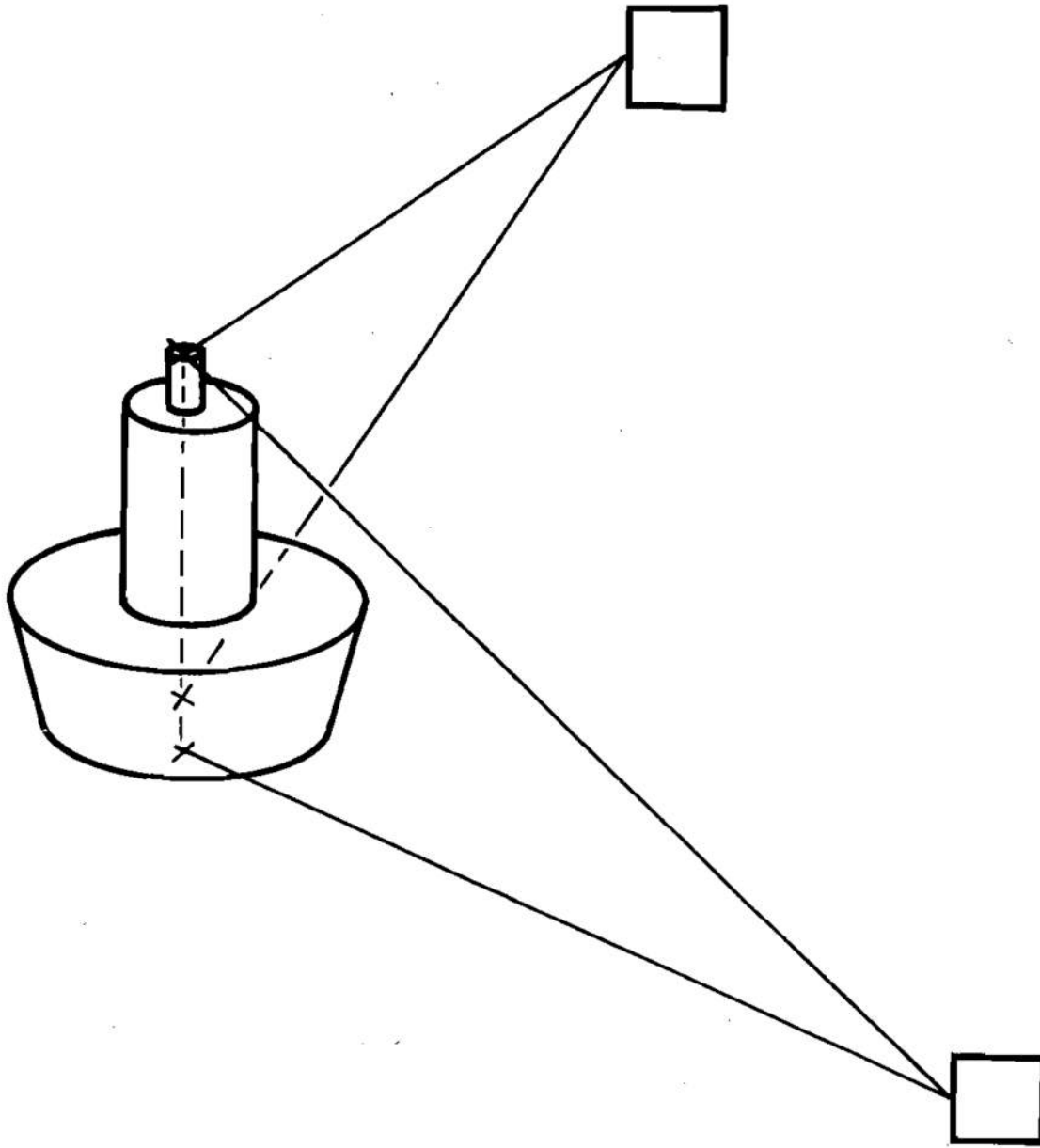


FIG. 22. ORIENTATION OF BLUNT-NOSED MISSILE

$$\bar{x} = x_T + d\lambda$$

$$\bar{y} = y_T + d\mu$$

$$\bar{z} = z_T + d\nu$$

FIG. 23. POSITION OF C.G. OF BLUNT-NOSED MISSILES

ANALOG COMPUTER DETERMINATION OF AERODYNAMIC COEFFICIENTS

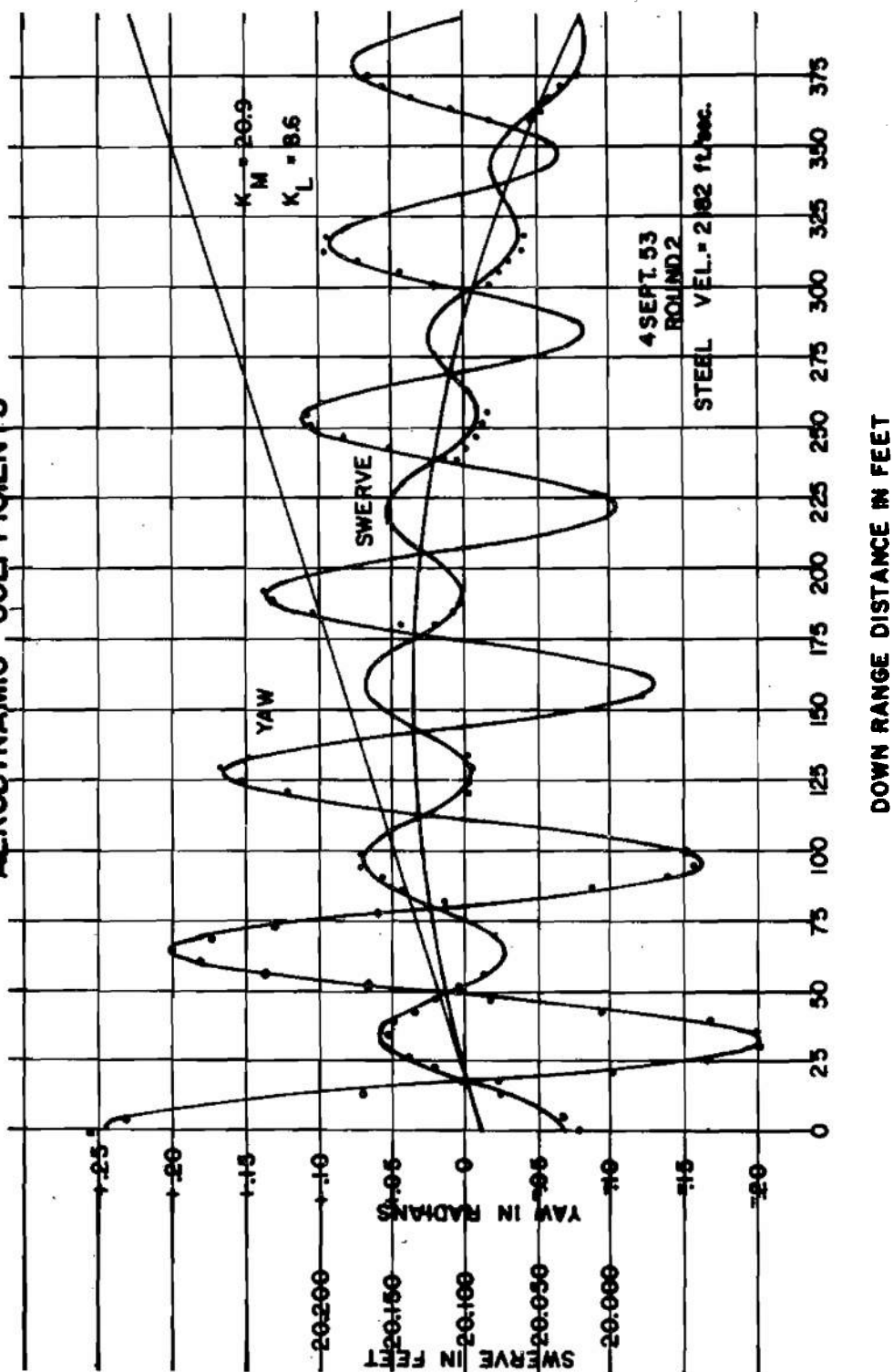


FIG. 24. YAWING AND SWERVING MOTION OF A TYPICAL FIRMER

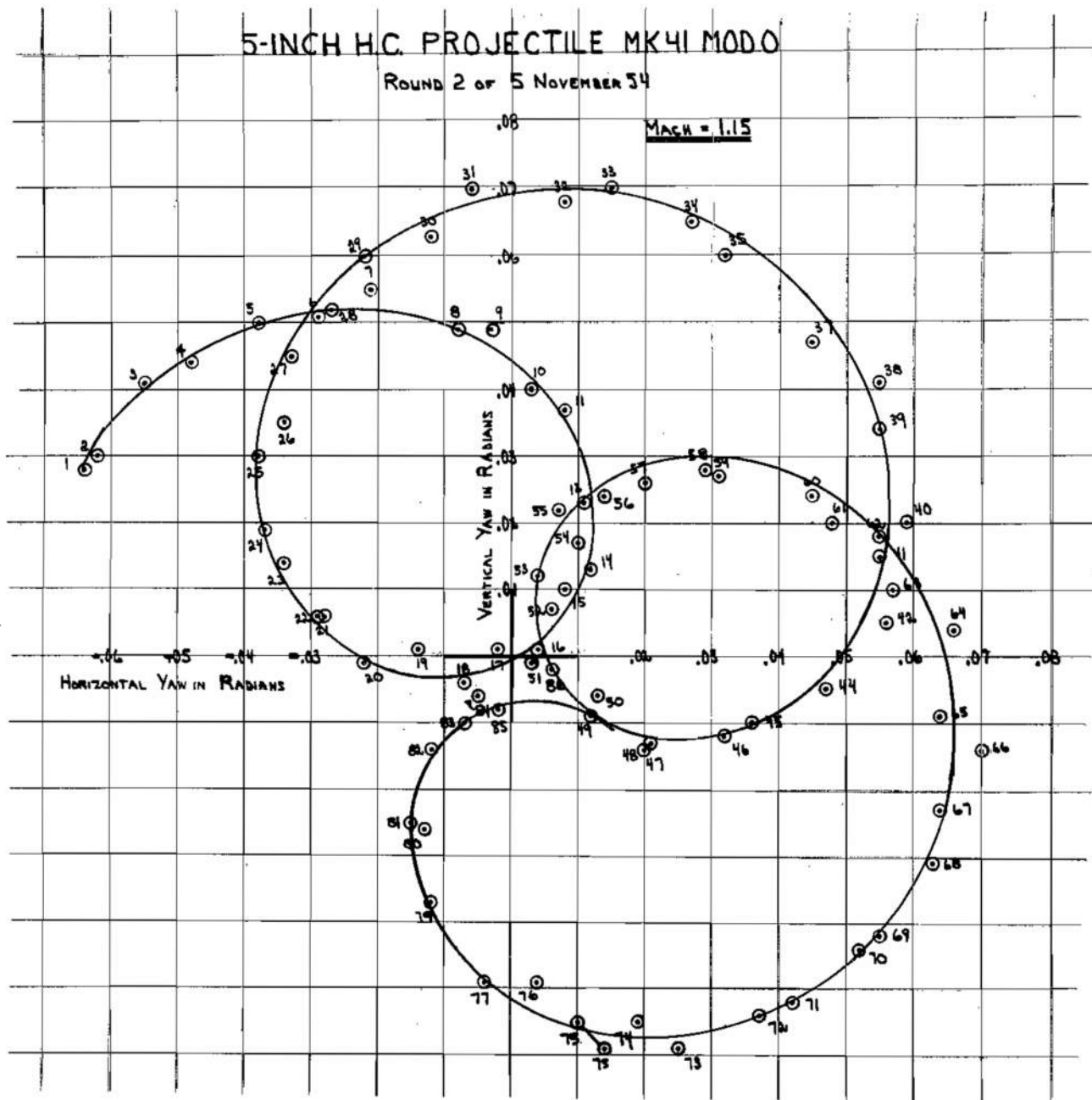


FIG. 25. YAWING MOTION OF A TYPICAL SPINNER

INTENTIONALLY LEFT BLANK.

WAKE VISUALIZATION STUDIES IN THE AEROBALLISTICS RANGE

G. V. Bull

C. B. Jeffery *

Canadian Armament Research and Development
Establishment

* Computing Devices of Canada Ltd.

INTENTIONALLY LEFT BLANK.

WAKE VISUALIZATION STUDIES IN THE AEROBALLISTICS RANGE

G. V. Bull and C. B. Jeffery*
Canadian Armament Research and Development
Establishment

1.0

INTRODUCTION

In the computation of stability and control characteristics of wing-body-tail configurations such as aeroplanes and guided missiles, knowledge of the nature of vortex shedding is essential. Various techniques have been used to date to study vortex shedding phenomena in wind tunnels; for low speed work smoke tunnels and tuft-grid techniques have been used extensively; in the high speed range vapour screen techniques have been developed by the NACA. This present paper will review a technique presently being used and under development in the aeroballistics range of the Canadian Armament Research and Development Establishment.

2.0

EXPERIMENTAL TECHNIQUE

The experimental technique consists of introducing a laminar sheet of smoke filaments normal to the line of fire and obtaining by photographic methods a time history of filament distortion during and after the passage of the model. Photographic observation has been made both by reflected and transmitted light techniques. The rather simple experimental set-up is shown in Figures 1(a) and 1(b). For reflected light observations a microflash unit and simple camera were employed; due to the high speed shutter problem encountered this technique was limited to a single photograph. A high speed drum camera was tried for reflected light photography but was temporarily abandoned due to the amount of development of the technique which appeared necessary for successful results. An on-axis parallel beam shadowgraph system was then set up using a multiple timed spark unit as a light source (Figure 1(c)). Geometrical and diffraction problems with this system led to its modification to

* Computing Devices of Canada, Ltd.

a focussed shadowgraph system using lenses focussed on the plane of the smoke to form an image. This system is similar to the Cranz-Schardin multiple beam system and is shown diagrammatically in Figure 1(b). The spark units are located downstream at a distance of twice the focal length from a 16" diam f/8 paraboloidal mirror. This mirror is centered one diameter off the flight path. The reflected beams pass through the plane of the smoke and focus at lenses opposite the sparks. The lenses are focussed on the plane of the smoke. The whole apparatus is enclosed in a light tight room so that shutters are not needed. This system is essentially a backlighted normal photography technique rather than a shadowgraph technique, and is found to produce rather high quality pictures. The multiple spark unit is started by a trigger pulse obtained from an infra-red screen located just downstream of the smoke and thereafter the sparks automatically discharge consecutively, with time intervals variable as desired between 10 and 100 microseconds approximately. A reference grid of wires is located as shown in Figure 1(b) to allow, by simple geometrical calculations an accurate determination of model position with respect to the smoke. Model velocity is measured by light screens in the normal manner and the flight trajectory and angular orientation are measured using yaw cards.

The production of a laminar sheet of smoke filaments presents a rather difficult problem. In the test procedures employed to date it is necessary for the smoke generator to operate for intervals up to five minutes. The photographic quality of the smoke employed had to be matched to the particular method of observation; for reflected light work ammonium chloride vapour was found to be photographically suitable; at the same time it could be generated easily and gave the most laminar results of any smoke trial.

The simple smoke generator developed for this purpose is shown in Figure 2. In this unit hydrochloric acid and ammonium hydroxide

are allowed to mix by dripping into a common dish and the resulting ammonium-chloride vapour is ejected at very low velocity through a series of glass nozzles by mixing with pressurized air from an air bottle. A chimney is placed above the generator to provide an updraft and assist filament laminarity. With this unit laminar filaments of vapour 10 to 12 inches in length could be obtained quite readily. The ammonium chloride vapour did not prove satisfactory for the backlighting scheme of Figure 1-b, and it was found necessary to use the smoke from oily-rags, ejected through an identical nozzles system.

The experimental set-up described above has been used to study the vortex-shedding from a pitching and yawing body combination. The problem will first be described along with the theoretical background work and then the experimental results will be presented.

3.0

DESCRIPTION OF THE PROBLEM

The specific problem studied to date by this method is associated with the determination of the induced velocity field (downwash and sidewash) behind rectangular plan-form wings located in cruciform on a cylindrical after-body with a conical nose. The particular configuration studied is shown with geometrical details in Figure 3.

Linearized aerodynamic theory has been applied by many authors to the theoretical study of this problem employing an assumed form of the trailing vortex sheet. Lagerstrom and Graham (reference 1) used conical superposition techniques assuming a planar undisturbed sheet of vorticity extending from the wing trailing edge downstream to infinity in the streamwise direction. Other authors have chosen a fully-rolled vortex sheet extending from various positions along the wing-chord downstream to infinity in the streamwise direction. Application of these methods to a variety of configurations shows some rather large discrepancies with experiment primarily associated with the manner of rolling up of the trailing vortex sheet. Spreiter and

Sacks (reference 2) discussed the mutual interaction effects of shed vorticity and used water-tank studies to show experimentally the manner of vortex shedding which could occur. Rogers (reference 3) applied slender body theory to compute the distortion of the wake behind low aspect ratio delta wing-body combinations, in both subsonic and supersonic flows. In the present studies, the method employed by Rogers was applied to cruciform rectangular wings in supersonic flows for which slender body theory could be assumed to hold.

4.0

THEORETICAL WAKE ROLLING UP

The manner of rolling up of the trailing vortex sheet behind lifting surfaces is determined by the spanwise distribution of lift on the surface. For the configuration considered here the wing panel loading was computed by using strip theory and accounting for body upwash lift on the wings by the method of Beskin (reference 4). Within the framework of slender-body theory, changes in the downstream direction are neglected and the governing linearized differential equation becomes two-dimensional in form and independent of Mach number.

Under these assumptions standard line vortex theory may be applied. The lifting surface is then replaced by a distribution of horseshoe vortices leaving the surface at the trailing edge and passing downstream in the streamwise direction. The body effect is taken into account in the normal fashion by distributing inverse vortices corresponding to the external field. For the computational work, the panel loading was approximated by using ten equal strength vortices adjusted slightly from their normal position to give a smooth curve of their divided differences. For small angles, it was assumed that pitch and yaw effects do not couple through the wake, and therefore from the symmetry of the model it is necessary only to compute the case of pure pitch, simple linear superposition yielding the combined case. The induced velocity at each vortex position due to the complete vortex field was computed and the local streamwise direction established. Step by step construction

of the vortex paths downstream was then made using increments in downstream direction of approximately .05 chord lengths. The numerical computations were performed under contract by the Computing Devices of Canada Ltd. on a digital computer. For a pure pitch of 3° , the distortion of the trailing vortex sheet in the downstream direction as computed is shown in Figure 4 for the case of a free stream Mach number of 1.5. From this figure it is seen that the wake tends to roll into two vortex cores, one inboard and one outboard of roughly equal strength.

5.0

EXPERIMENTALLY DETERMINED WAKE DISTORTION

(a) Reflected-Light Technique

Because only a single photograph could be obtained per trial, this method was not extensively used.

A typical result obtained by this method is presented in Figures 5 (a) and (b) which show two views of the model of Figure 3 fired at a Mach number of 1.5 and having a pitch angle of attack of $1/2^{\circ}$ and zero yaw. The side view (Figure 5 (a)) shows the position of the model with respect to the smoke; the smoke plane is 1.25 chord lengths back of the model trailing edge. The back view shows the vorticity pattern in the smoke; careful inspection will show an outboard translation of the filaments above the wing and an inboard translation of those below the wing. The outboard vortex core is in the position to be expected from the calculations; the inboard vortex cannot be detected. Another interesting result obtained from a test round similar but not identical to that of Figure 3 is shown in Figure 6. This projectile had a pitch angle of attack of 1° , a yaw angle of attack of $1/2^{\circ}$ and was fired at a nominal Mach number of 1.5. The photograph is taken about 2 chord lengths aft of the trailing edge. The vortex formation at the tips of the lifting surfaces is plainly visible with no visible inboard vortex formation being detectable. There also appears in this photograph traces of the intersection of the shock waves from the leading edges of the lifting surfaces.

(b) Back Lighting Results

Because of the simplicity of equipment involved and the time-sequence of wake distortion obtainable, the backlighting scheme has been used extensively in the present tests. Figure 7 shows the development of the vorticity pattern in the smoke field, x/c is the distance downstream of the trailing edge in wing chords. The round shown here has identical geometry to that shown in Figure 3 and was fired at a Mach number of 1.41; the model developed an angle of attack in pitch of 1.4° and in yaw of 0.25° . The reference wire grid is visible in this series. In interpreting these photographs, the geometry outlined in Figure 1(b) should be studied since the model appears distorted in the perspective view obtained.

Figure 8 is a single photograph of another series taken with a round fired at a nominal Mach number of 1.41, and again with the geometry depicted in Figure 3. This model has an angle of attack in pitch of 2.25° and in yaw of $.6^\circ$, and is rolled 20° from the vertical (the smoke filaments are flowing vertically). The smoke plane is 3.3 wing chords aft of the wing trailing edge. The tip vortex cores are visible from three of the panels, and lost from the fourth in the turbulent region of the wing cut in the smoke. In this photograph refraction effects enable visualization of the vortex cores; it can be seen readily that the vortex cores in the tip regions leave the wing ahead of the mid-chord point. Again no inner vortex cores can be detected.

6.0

ANALYSIS AND DISCUSSION OF RESULTS

The studies described in this report are still in progress; to illustrate the kind of analysis performed on the experimental data and the results obtained the case of Figure 8 will be considered here. Since within the framework of the slender body theory, conditions in any plane downstream of the trailing edge may be computed on the basis

of two-dimensional incompressible theory, the theoretical distortion of the smoke filaments can be computed readily.

From Figure 8, it would appear that most of the vorticity is concentrated in the tip core; two sets of computations were performed, the first assuming that $1/2$ of the total panel vorticity was concentrated in the tip core, and the second assuming the total panel vorticity to be concentrated in this core. Commencing with a set of planar filaments (stream lines of negligible velocity) the distortion of these stream lines due to the two different strength vortices was computed assuming that the vortices had been flowing for a time equal to the time taken for the model to travel 3.3 wing chord lengths at its velocity of 1500 feet per second. The resultant streamline patterns were then compared to that obtained by measurement from Figure 8 correcting for linear and angular distortions. These results are shown in Figure 9 where the $1/2$ strength and full strength results are plotted to the left and right respectively of the experimental results.

From these computations as shown in Figure 9, the experimental field corresponds closely to the resultant field assuming a total concentration of vorticity in the tip core. The strength of the inner core (See Figure 4) is evidently over-estimated considerably by the theory. Further iterations of the results can be carried out to obtain the exact vortex strength of the tip core; in this case the position of vortex shedding should be corrected from the trailing edge to possibly the mid-chord point. However, for conditions far aft of the trailing edge, such as represented in this result, the correction is small (of the order 10%). From the analysis of the smoke distortions at different stations downstream of the trailing edge, the point of vortex shedding can be determined accurately as well as the core strength. These computations are being conducted for the results shown in Figure 7.

Some interesting observations regarding this technique can be made here. By theoretical fitting methods the observed smoke patterns can be used to determine the vorticity distribution in the wake of lifting surfaces even under more complex cases than the single core problem considered here. The complexity of the fitting problem increases with the number of cores it is necessary to assume. Once having determined the vorticity distribution in the wake, the inverse calculation of circulation (lift) on the surface may be performed. This technique would appear to be peculiar to the aeroballistics range, since it requires the introduction of stream filaments in a plane perpendicular to the air flow.

7.0

CONCLUDING DISCUSSION

The analysis of experimental results already obtained is being continued at CARDE. Other experimental techniques are being investigated: among these two may be mentioned. The first is the development of a multiple exposure reflected light system, since with the backlighting method blanketing of a large portion of the field by the model occurs. This system will be inherently more direct. The second development is being carried on by A. Easson to develop a burning wire smoke generator; preliminary results from this method have been most encouraging.

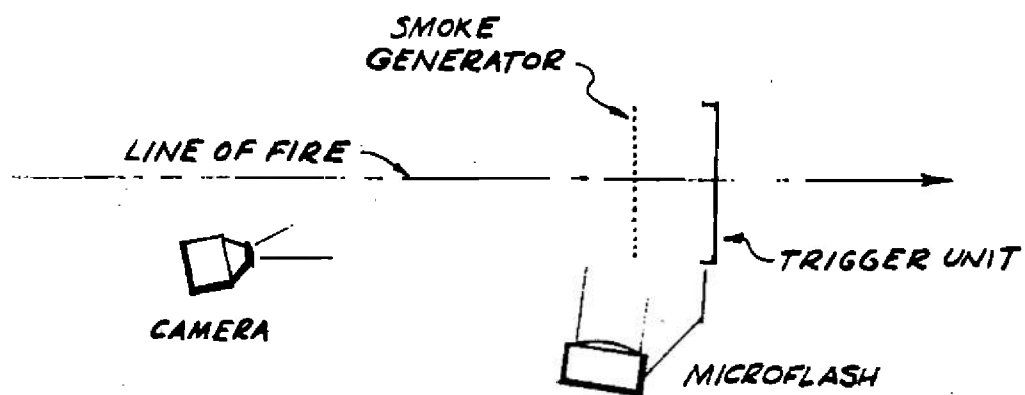
ACKNOWLEDGEMENTS

The active investigation of visualization techniques was commenced after a discussion with Prof. S. M. Bogdonoff of Princeton University, who suggested that such a line of attack might be worthwhile.

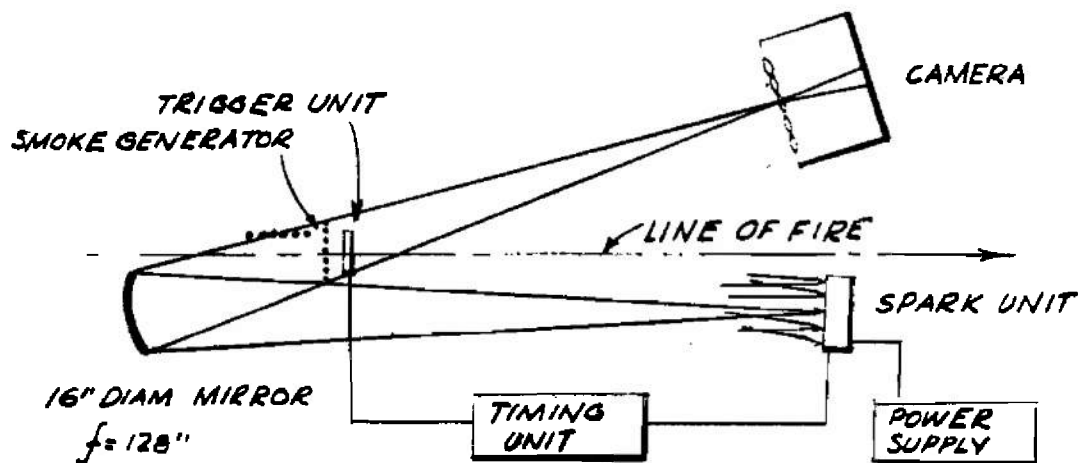
In regard to the experimental work the authors are indebted to Mr. R. Coderre of CARDE for his enthusiastic interest in the problem and in particular for development of the multiple spark system, to Lt. W. Ready for conduct of the numerous test firing under the most adverse conditions, to the CARDE photographic section in general, LAC C. MacKenzie in particular.

REFERENCES

1. Lagerstrom, P. and Graham, M., Downwash and Sidewash Induced by Three-Dimensional Lifting Wings in Supersonic Flow.
2. Spreiter, John R. and Sacks, Alvin, H., The Rolling Up of the Trailing Vortex Sheet and its Effect on the Downwash Behind Wings. Jour. Aero. Sci. Vol 18, No. 1 - Jan. 1951.
Sacks, A. H., Behaviour of Vortex System Behind Cruciform Wings, - Motions of Fully Rolled-up Vortices - NACA TN 2605, 1952.
3. Rogers, Arthur, Application of Two-Dimensional Vortex Theory to The Prediction of Flow Fields Behind Wings of Wing-Body Combinations at Subsonic And Supersonic Speeds NACA TN 3227.
4. Beskin, L., Determination of Upwash Around A Body of Revolution at Supersonic Velocity APL/JHU/CM - 251.

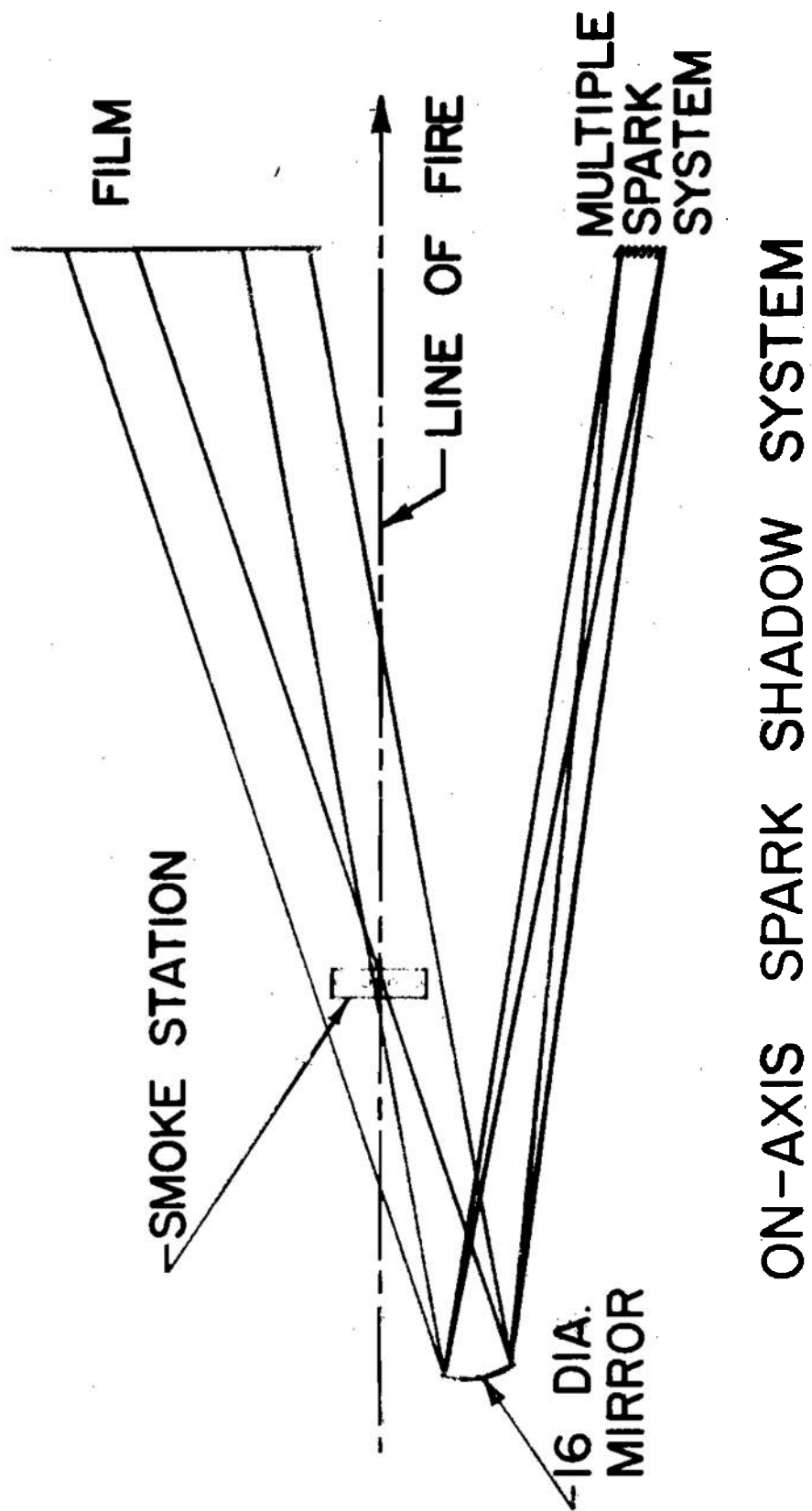


(a) REFLECTED LIGHT SYSTEM



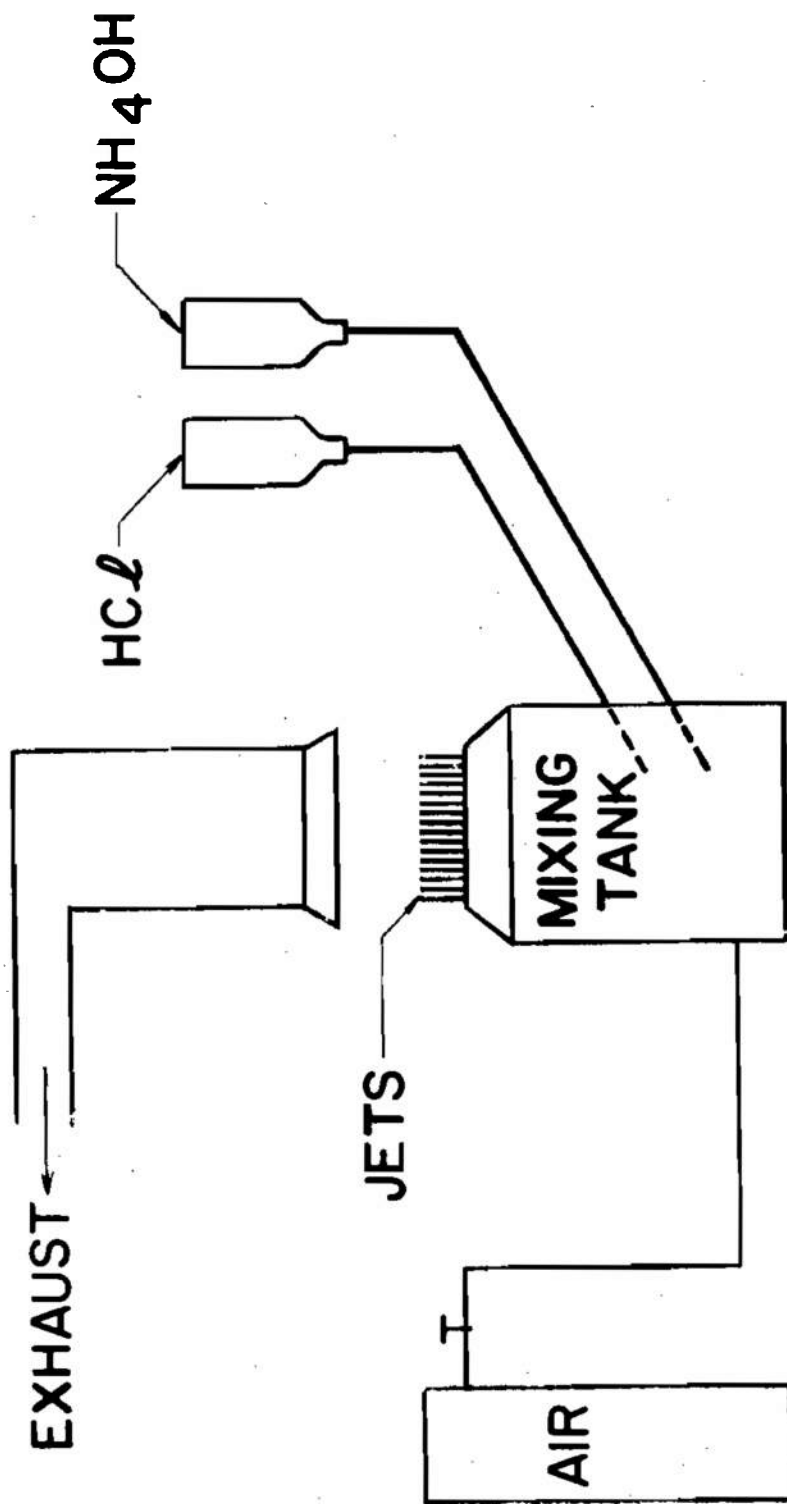
(b) BACK-LIGHTING SYSTEM

FIGURE 1: EXPERIMENTAL SETUP USED FOR
VORTEX SHEDDING STUDIES



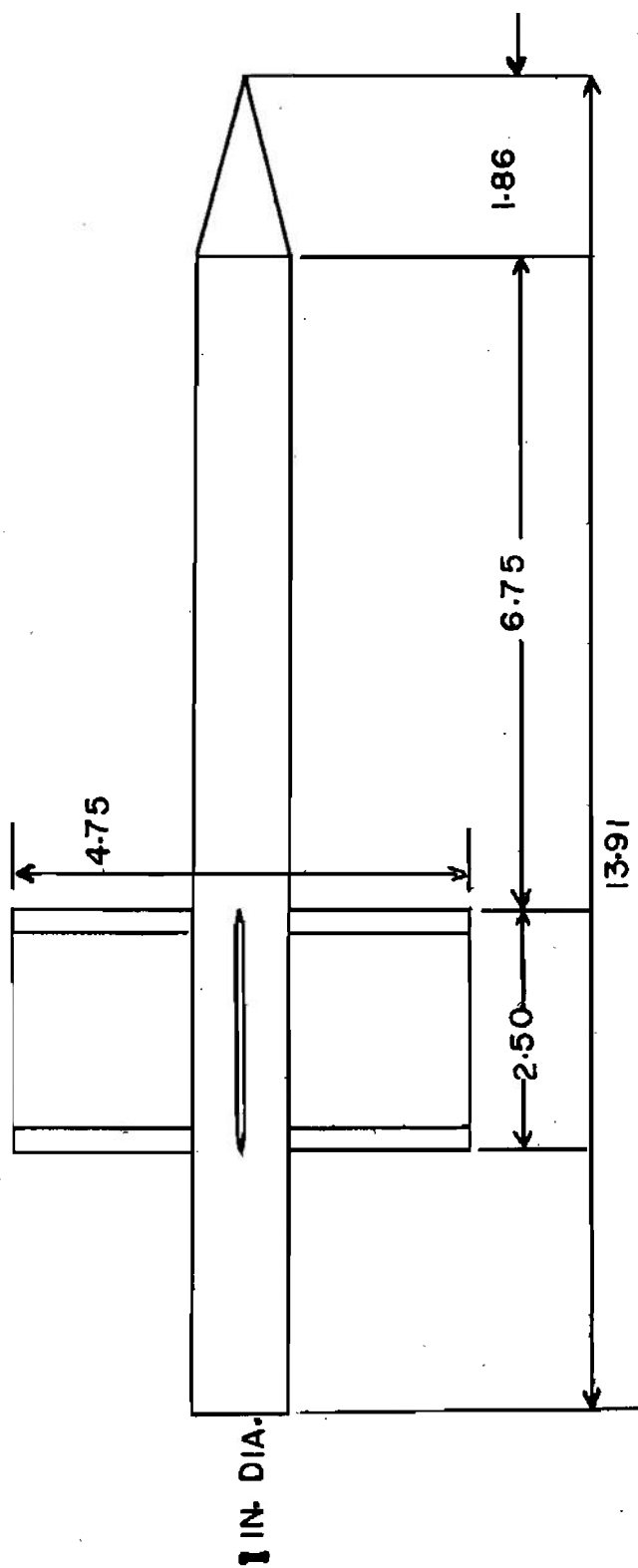
ON-AXIS SPARK SHADOW SYSTEM

FIG 1(C)



SMOKE GENERATING APPARATUS

FIG. 2



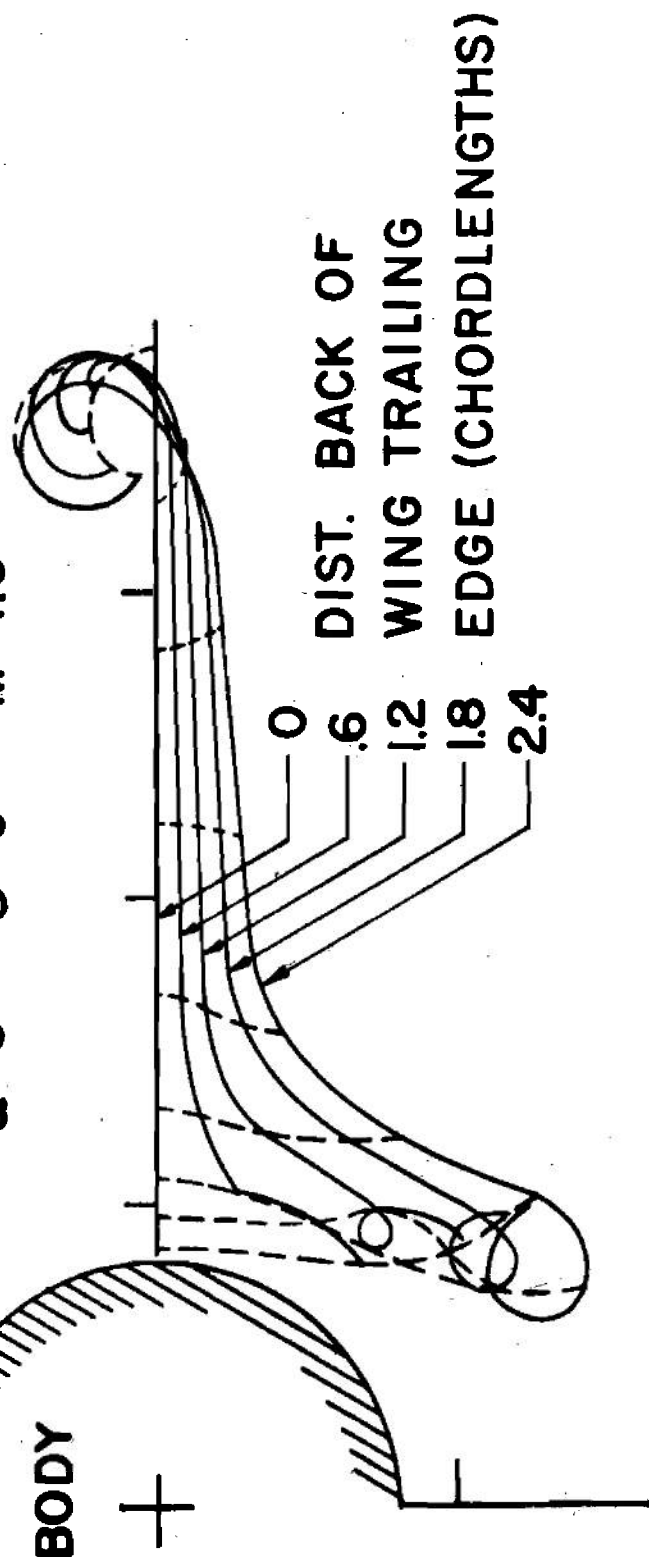
WING BODY ROUND

FIG. 3

COMPUTED ACCORDING TO SLENDER BODY
ASSUMPTIONS FOR RECTANGULAR WING-BODY
COMBINATION

ASPECT RATIO = 1.9 SPAN / DIAM = 4.75

$\alpha = 3^\circ$ $\delta = 0^\circ$ $M = 1.5$



DISTORTION OF TRAILING VORTEX SHEET

FIG. 4

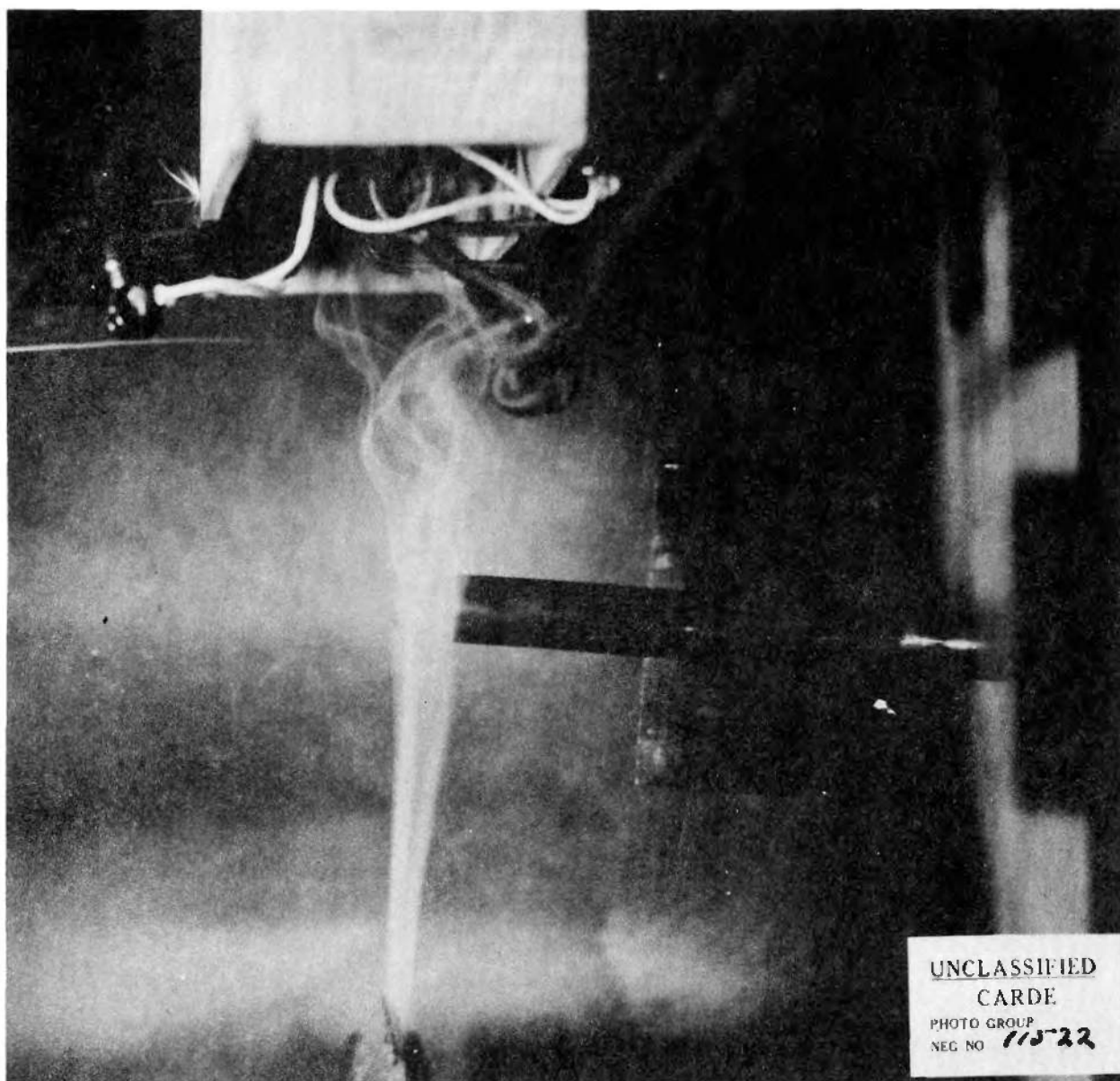


FIG. 5(a)
REFLECTED LIGHT SIDE VIEW OF
MODEL & SMOKE

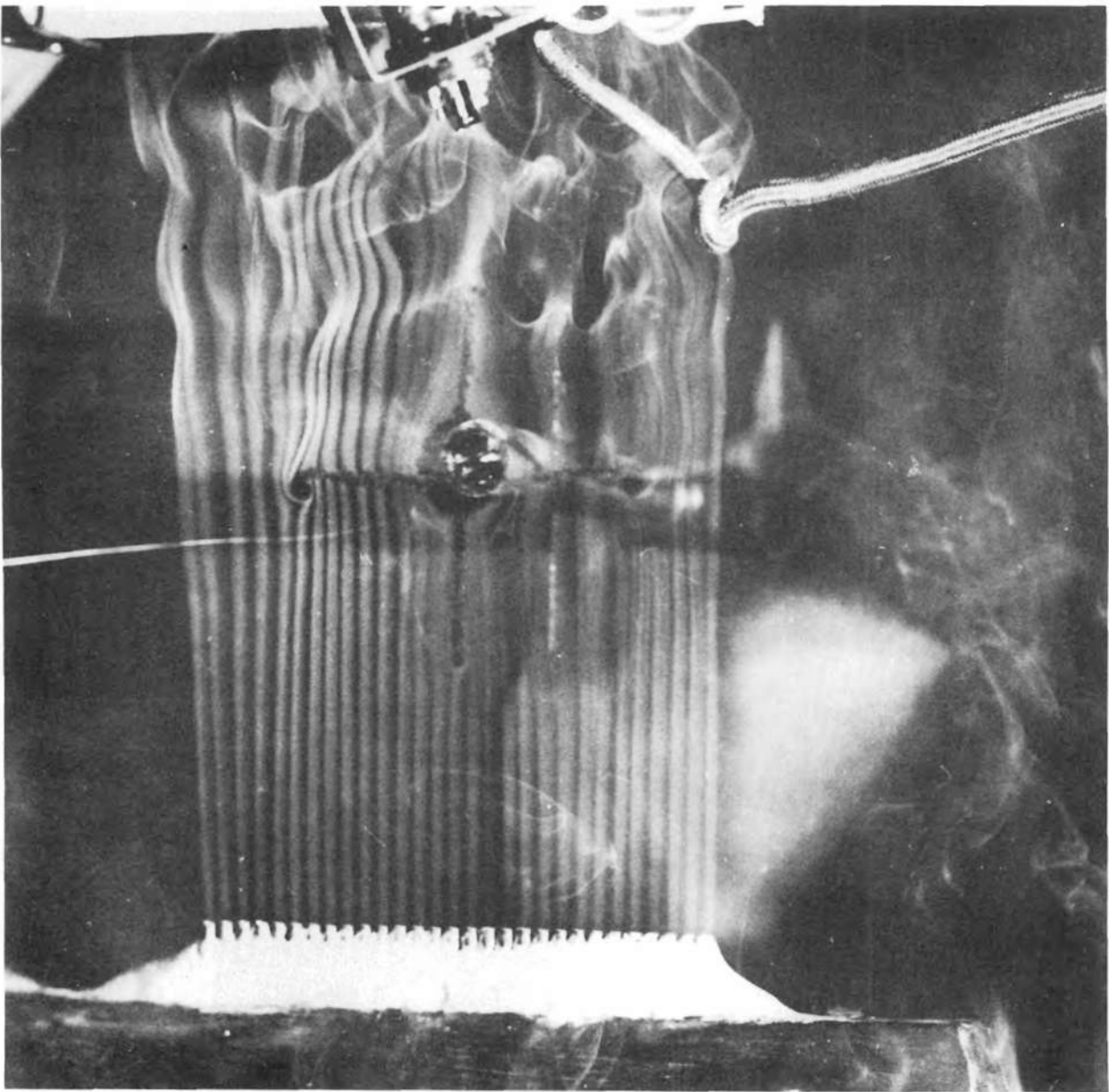


FIG. 5 (b)
REFLECTED LIGHT VIEW OF
SMOKE DISTORTION

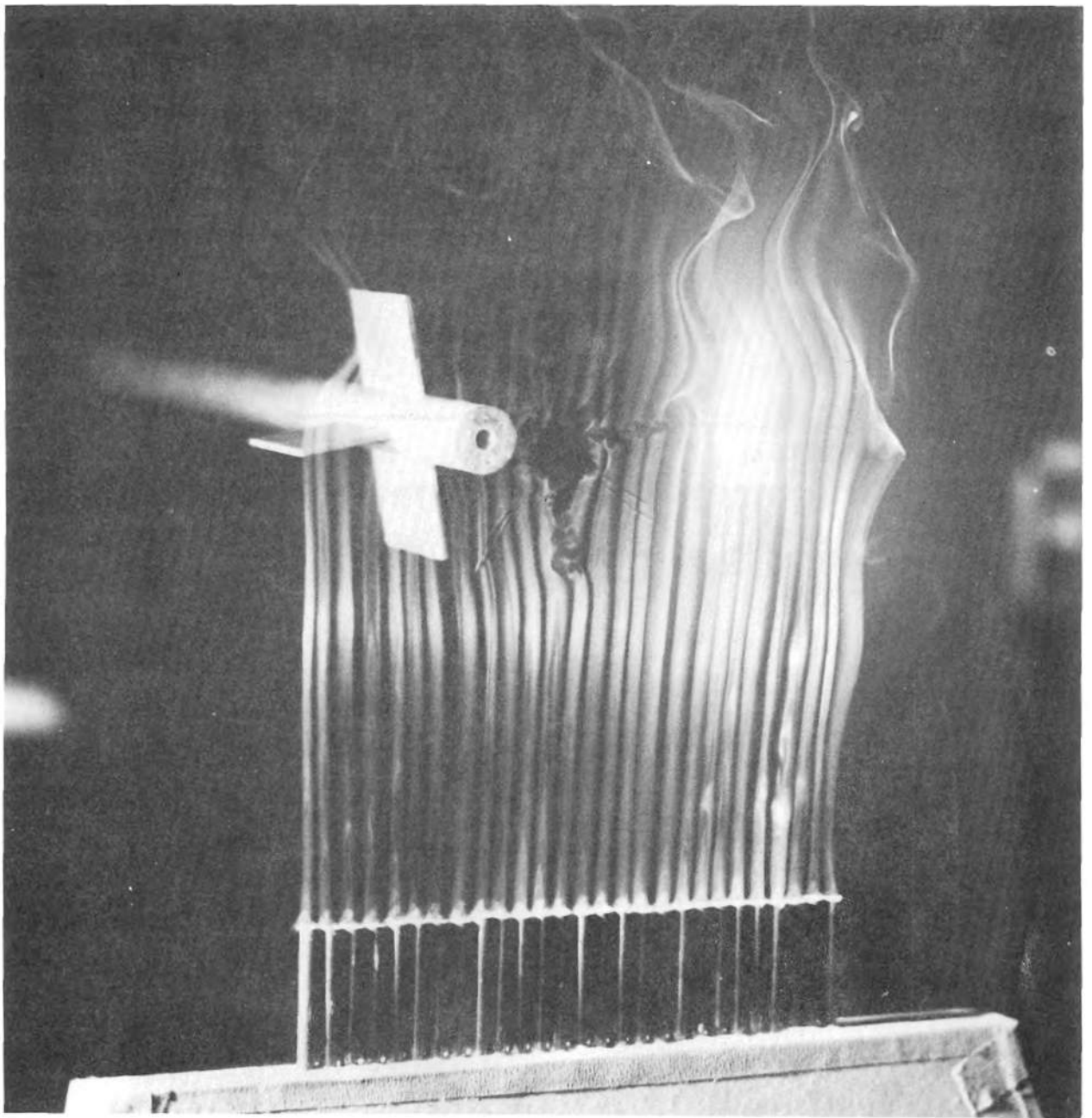


FIG. 6
REFLECTED LIGHT PHOTO
OF SMOKE SHOWING SHOCK
WAVE INTERSECTION.

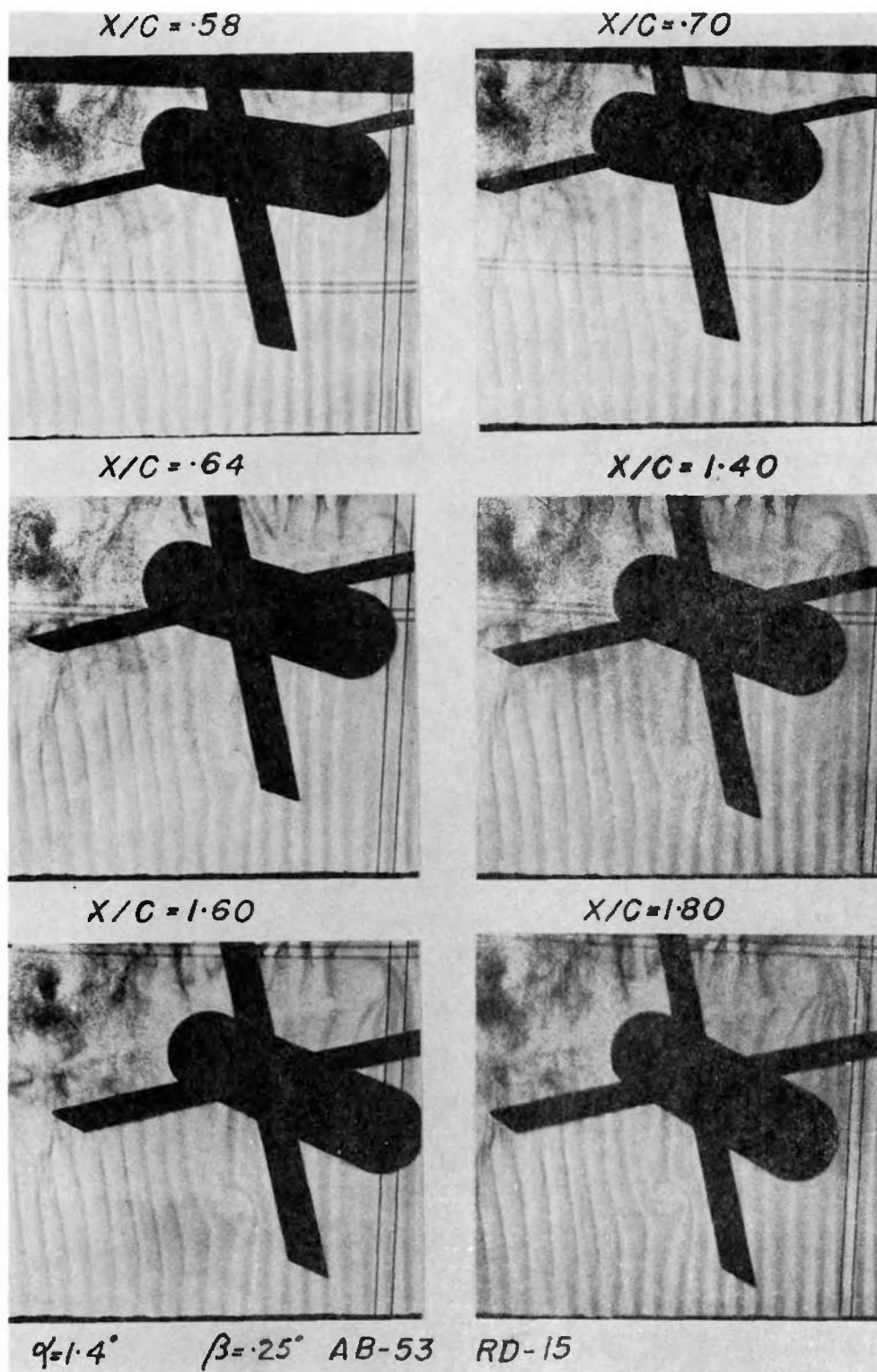


FIG. 7
 DEVELOPMENT OF VORTEX
 PATTERN IN SMOKE



FIGURE 8 : SMOKE PATTERN

$$M = 1.41 \quad \frac{x}{c} = 3.3 \quad \alpha = 2.25^\circ \quad \beta = 0.6^\circ$$

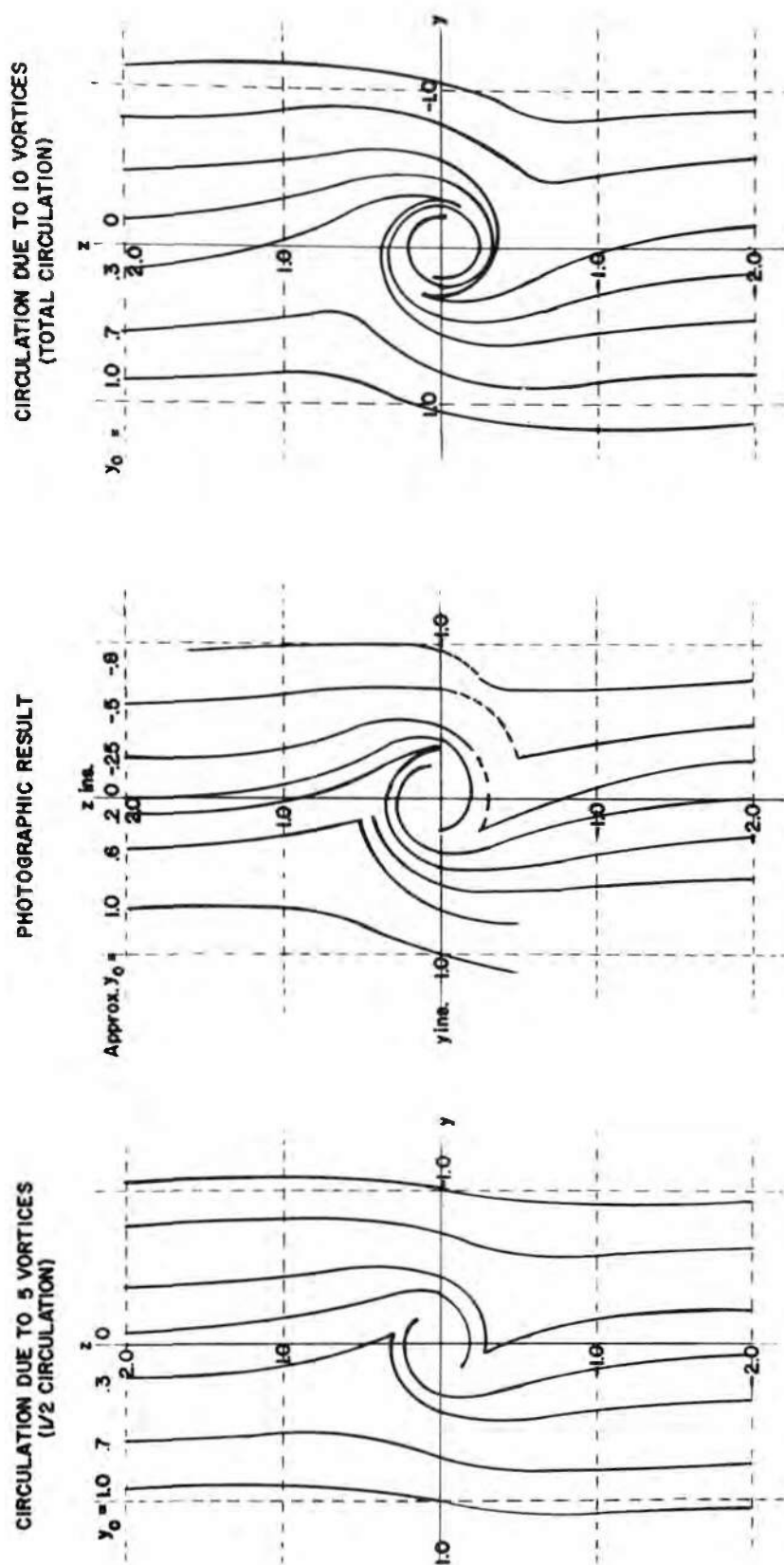


FIG. 9 COMPUTED AND EXPERIMENTAL SMOKE FILAMENT DISTORTION

THE CONTROLLED-TEMPERATURE-PRESSURE RANGE:
SPECIFICATION, PROBLEMS OF MEASUREMENT,
AND RECENT PROGRAMS

F. D. Bennett

Ballistic Research Laboratories
Aberdeen Proving Ground, Maryland

INTENTIONALLY LEFT BLANK.

THE CONTROLLED-TEMPERATURE-PRESSURE RANGE:
SPECIFICATION, PROBLEMS OF MEASUREMENT,
AND RECENT PROGRAMS

by

F. D. Bennett

Ballistic Research Laboratories
Aberdeen Proving Ground, Maryland

INTRODUCTION

1.1 Historical Survey

The development program which has culminated in the high Mach number instrument called the Controlled-Temperature-Pressure Range, abbreviated CTPR, had its first beginnings in the period from 1944-1946. During this interval Col. Paul Libessart, of the French Army, Drs. R. F. Clippinger, I. E. Segal and R. N. Thomas in various conferences and memoranda evolved the idea of an enclosed firing range in which the working fluid could be maintained at closely controlled pressure and temperature. While the earliest record is in the form of a typewritten memo dated June 1944 from Col. Libessart to the late Dr. Edwin P. Hubble who was then director of the Exterior Ballistics Laboratory, the final design is the conception of its principal architect Dr. R. F. Clippinger. Subsequently many people have participated in the construction, modification and operation of the CTP Range. Some of their contributions appear as items in the bibliography to this paper and will be indicated by bracketted [] numbers in the text.

From the beginning it was clearly recognized that control of temperature, particularly through use of refrigerants such as liquefied gases, offered the possibility of choosing the ambient velocity of sound so as to obtain high Mach number flows about freely moving supersonic projectiles. Through use of refined optical techniques offered by the Mach-Zehnder interferometer it was hoped that comparisons could be drawn between experimentally produced and theoretically calculated fields of flow.

The seemingly easier objective of high Mach numbers has been realized only recently while the apparently more complex comparisons of experimental and calculated flows [1,2] could be carried out earlier. Certain simple cases were studied in a prototype Model Range with pressure control only. This prototype which is now in its Mark II design, was constructed expressly to provide experience with an enclosed, pressurized range. Many valuable results have been obtained from it and lessons have been learned which could be applied to problems of instrumentation for the CTPR. The Model Range remains a useful tool for studies requiring variable density only, but has been superseded by the CTPR where high Mach numbers are desired.

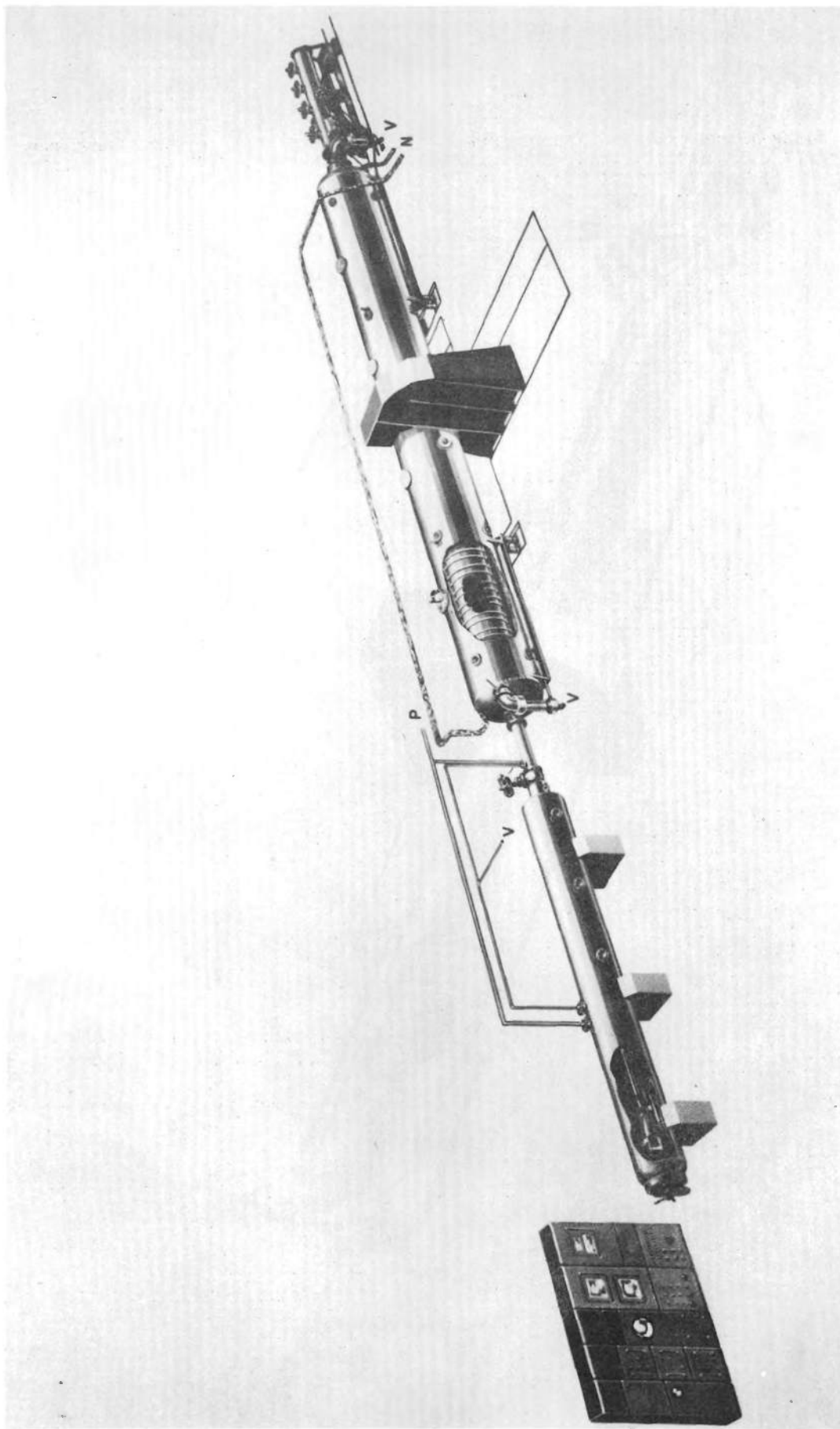


Figure 1. Artist's conception of the Controlled - Temperature - Pressure Range and its associated controls.

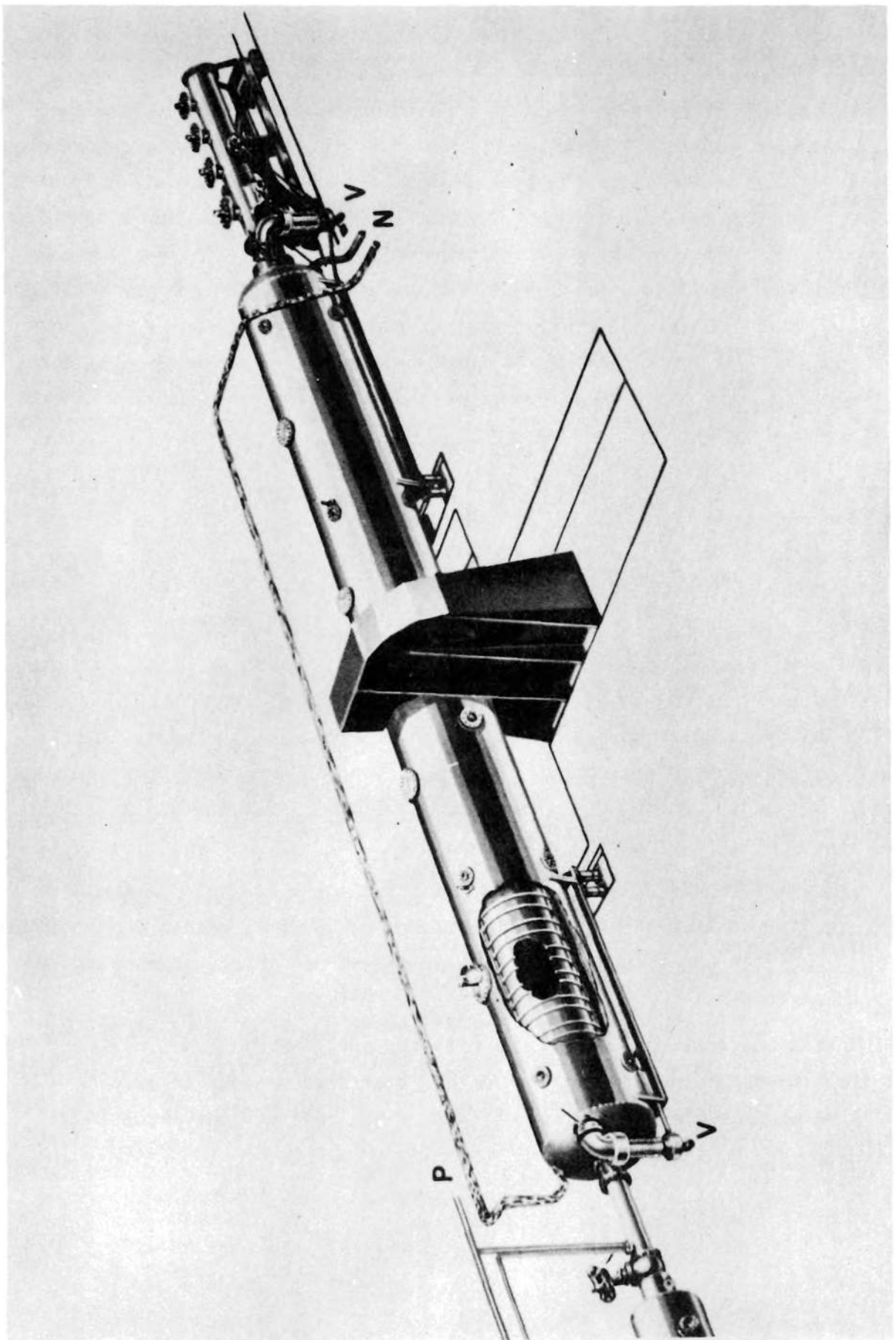


Figure 2. Enlarged view of central working section seen in Figure 1.

II RANGE DEVELOPMENT

2.1 Control of Pressure and Temperature

In Figure 1 is given an artist's conception of the CTPR in schematized form. The main outlines of the three principal parts, viz., the gun chamber, central working section, and stopping section can be seen. The oil-diffusion vacuum pumps, and the pressure and nitrogen lines are indicated by V, P and N respectively. Figure 2 shows an enlarged view of the working section and stopping tube. The dark frame in the center represents the external housing of the 10" Mach-Zehnder interferometer. At the cutaway section may be discerned both the annular evacuated space between inner and outer cylinders, and the cooling and heating coils wrapped around the inner chamber.

Both the type and density of the working fluid can be controlled in the CTPR; thus γ and ρ_1 may be chosen as desired throughout the gamut of available gases and continuously in the domain of pressures $0 \leq p \leq 10$ atm. For most room-temperature experiments dry air, dew point $t_s \leq -70^\circ\text{F}$, from the Wind Tunnel sphere is used both as working fluid and as a rinse for the gun section after firings. Since the combined volumes of the CTPR sections do not exceed 600 cu. ft. and ordinarily only about one-third of this volume is changed per firing, the demands on the sphere supply are not high. At the extreme low temperature $T \doteq 80^\circ\text{K}$, only permanent gases may be used. The choice so far has been dry nitrogen, mainly because of its similarity to air, secondarily because it can be conveniently introduced from the piping system carrying the refrigerant.

Control of temperature is achieved by circulating liquids or gases in two sets of cooling coils, with top and bottom headers, placed as uniformly as possible around the 45', stainless-steel, inner cylinder of the working section.

For low temperature runs, liquid nitrogen supplied by tank truck and centrifugally pumped through one set of coils at pressures up to 30 psi provides a minimum temperature near 85°K over the entire observation

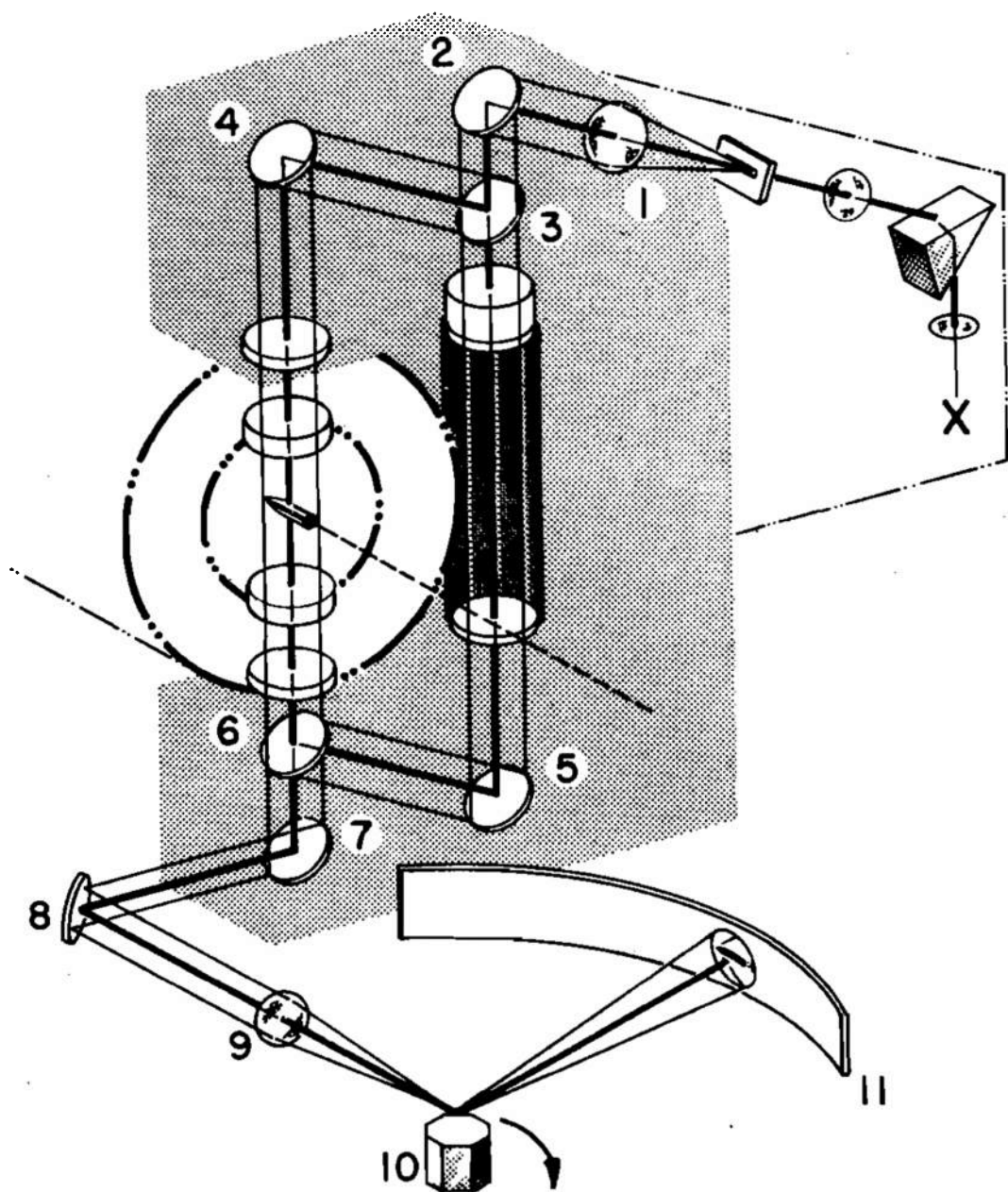


Figure 3. Schematic Diagram of the 10" Mach-Zehnder interferometer. Spark source and liquid-prism monochromator appear at the upper extreme right. One beam passes through the CTPR, the other through a cylindrical compensating chamber. Components may be identified as follows: x - light source; 1, 9 - lenses; 3, 6 - divider plates; 2, 4, 5, 7, 8 - plane mirrors; 10 - rotating mirror; 11 - film holder.

chamber. Heat gains from the outside shell are minimized by maintaining the intervening annular space at high vacuum, $p \leq .05$ micron, and insulating the inner evacuated wall with several layers of aluminum-foil radiation-shield.

Temperatures higher than ambient are obtained by circulating electrically heated oil from an insulated tank through the other set of coils. The upper temperature limit $T = 400^\circ\text{K}$ is set by the efficiency of the oil heating system and the chemical stability of the oil.

2.2 Instrumentation

The working section of the CTPR has five sets of paired crossed windows with 6" diameter apertures separated by 9' intervals. Each is instrumented for spark shadowgraph records except at the center station. Here a horizontal window pair for shadowgraph and triggering beam apparatus precedes by about two feet a vertical station with 10" diameter, optical glass windows accurately aligned for the 10" Mach-Zehnder interferometer.

Reference marks in the shadowgraph stations are surveyed to an accuracy of .001' on the centerline and the stations are rendered perpendicular to the centerline to within a few seconds of arc by means of a precision telescope and optical square.

Time of flight intervals between shadowgraph stations are measured to within ± 0.1 microsecond by means of Hewlett-Packard 10 Mc counters.

The 10" Mach-Zehnder interferometer, one of the largest of its kind used for full-field flow surveys, is equipped with an exploding-wire light-source [3], a liquid-prism monochromator [4] and rotating-mirror camera. The instrument itself is arranged as shown in Figure 3 with its 10" elements at the vertices of a $60^\circ - 120^\circ$ parallelogram oriented perpendicular to the range centerline. Fringes parallel to the centerline fulfill both the condition for optimum light source [5] and the requirements for precision measurement of fringe shift in the field of flow [2, Sec IV].

2.3 Projectile Launchers

The absolute velocity attainable in a free flight range is set by the types of projectile launchers available. Until recently cal .30 and cal .50 smoothbore and rifled guns were the principal means of launching projectiles. Full size spin-stabilized missiles with driving bands and sub-caliber missiles with separating sabots have been extensively used for experimental firings. With cal .30 fixed ammunition and special powder loads velocities up to 5000 fps can be reliably obtained. With the cal .50 smoothbore velocities up to 6000 fps have been achieved in a number of programs.

Quite recently a cal .75 smoothbore gun [6] with detachable chamber and detached ammunition has been used to fire sub-caliber, non-spinning statically-stable rounds in separating sabots. Velocities up to 7000 fps at the muzzle have been attained.

2.4 Mach and Reynolds Number Bounds

Since a principal feature of the CTPR is its potential to utilize cooled gases in which the velocity of sound is low, one expects the span of accessible Mach numbers to be considerably enlarged. Assuming a perfect gas law dependence of sound velocity on absolute temperature we find that at the lowest temperature of the CTPR Mach number can be increased by a factor of approximately $[300/85]^{1/2} \approx 1.9$. Thus with the cal .75 projectile launcher the highest Mach number attainable is slightly less than 12. On the lower side, firings below $M = 1$ have been made on occasion, but routine studies much below $M = 1.2$ are complicated by interference from reflected shock waves. We may then say that with its present instrumentation the Mach number scale of the CTPR satisfies the inequality $1.2 \leq M \leq 12$.

Since density may be controlled directly in the CTPR, it is possible to make Reynolds number Re vary over a considerable range of values. With standard values of the physical constants for the density, viscosity and molecular weight of air we can find for $Re = (\rho VL/\mu)$ the value

$Re = .55 \times 10^6$ per inch, per Mach number per atmosphere at $T = 300^\circ K$. Since at constant pressure density varies inversely with temperature, this specific Reynolds number Re increases with decreasing temperature and at our low temperature limit would be larger by nearly four times.

To illustrate the possible span of Reynolds number values, we note that since the CTPR can be evacuated to pressures below 1 mm Hg, the lower bound is zero and may be approached as closely as we like. For a representative projectile, say 0.5" in diameter, a room temperature study could be carried out at $M = 6$ over the full pressure range $0 \leq p \leq 10$ atm. and the corresponding Reynolds numbers would be $0 \leq Re \leq 1.5 \times 10^7$.

Since the boiling point of oxygen is $90^\circ K$, air cannot be used at the extreme low temperature. Nitrogen which boils about $77^\circ K$ has been used successfully at pressures less than 1 atm. Here the maximum Re for our example would be smaller by a factor of about three.

At the maximum Mach number and pressure, a room temperature study could be made at about $Re = 3 \times 10^7$ - at least in principle. Actually at densities above that characteristic of air at room temperature i.e. $\rho_1 = 1.2 \text{ gm/l}$, a number of difficult problems of measurement appear which severely limit the accuracy possible. To cite a few of these: 1) a high velocity missile decelerates an appreciable fraction of its velocity in 50' of travel when air densities in excess of $3\rho_1$ are used, 2) shadowgraph and interferometer records are complicated by very large refraction effects and 3) refraction may cause important portions of the optical record i. e. large bundles of light rays, to miss the rotating mirror entirely and fail to show on the photographic plate, 4) stability of the projectile if spin stabilized may be adversely affected.

While the potentiality for specification of Re through a considerable range of values is a feature of the CTPR, practical limitations, which can eventually be removed or minimized, have confined variable Reynolds number studies so far to Mach numbers less than six ($M \leq 6$) and densities less than 3.2 gms/l ($\rho \leq 3\rho_1$).

It is clear that Reynolds number cannot be controlled independently of Mach number unless compensating changes are made in one of the other variables such as density, projectile size or type of gas. It is found experimentally that quantities such as drag coefficient K_D depend only weakly on Re over considerable ranges of M . Thus in presenting K_D vs M data the variation of Re from point to point is frequently ignored.

3.1 Space and Time

Measurements of projectile center-of-mass positions relative to some reference starting point and of the corresponding time intervals are among the simplest and most fundamental that can be made in a firing range. From these may be derived values of ballistic drag coefficient K_D .

The effect on drag coefficient of random errors in time has been studied, for ballistic ranges, by Karpov [7] and, for range windtunnel combinations, by Charters [8] who applies Karpov's results. These are based on the following assumptions: 1) time t can be accurately represented as a function of distance Z by a cubic polynomial $t = \sum_0^3 a_i Z^i$, which is fitted by the method of least squares to the set $\{Z_j, t_j\}$ of station data, 2) the times t_j are subject to random errors of measurement satisfying independent normal distributions each of which has the same variance σ_t^2 and 3) the range has an odd number of stations. The effect of random errors in the Z_j is accounted for heuristically by supposing the existence of an equivalent timing error $\sigma_e = \sigma_Z/\bar{V}$, where σ_Z is the standard deviation of Z , assumed the same for each station, and \bar{V} is the average velocity of the projectile. The total variance in time is then taken to be $\sigma_T^2 = (\sigma_t^2 + \sigma_e^2)$.

Karpov then finds that the principal source of error in K_D , aside from constants of the projectile and atmosphere, arises from the quadratic coefficient a_2 . With the number of stations fixed this error varies inversely as the square of range length.

The significance of this result for the CTPR may be seen from the following consideration. In a study of the bounds on errors in K_D encountered in the five station, 20' Model Range, the author and J. M. Bartos [9] established under representative assumptions the maximum limits $\pm 4.6\%$ and $\pm 0.9\%$ for firings of a blunt cone-cylinder at pressures of 1 and 5 atmospheres respectively. Since the base line of the CTPR is 45' long and the number of stations 5, K_D for the same projectile will be

more accurately determined by a factor of more than 4. Since that writing, timing accuracy has been increased by a factor of 6 through adoption of 10 mc. counters. Thus errors of the order of 1% or less in K_D may be regarded as optimum for the CTPR. In point of fact unavoidable uncertainties in the gas density ρ_1 which enters the K_D calculation are sometimes severe enough to mask all other sources of error. This type of error is important only at temperatures near the extreme lower limit, 85°K. Temperature gradients in the Range and uncertainties in pressure and temperature determinations combine to contribute errors in excess of 1% but probably less than 3% for representative high-drag projectiles.

Two points regarding the error study remain to be mentioned. A recent re-examination of the problem by G. D. Kahl and the author shows with range length constant the error in a_2 diminishes as the inverse square root of number of stations when this number is large. Furthermore the equivalent timing error a_e attributed to errors in Z is just that obtained by assuming that the normal equations define the coefficients a_1 as functions of t and Z . With this assumption the variances of the set $\{a_1\}$ may be now calculated directly in terms of the rms errors σ_Z and σ_t . Thus while the prospect of minimizing squared error with respect to both t and Z is explicitly given up, the introduction of the equivalent timing error to account for distance error, increases the variances in a manner which is both strictly in accord with the most convenient assumption of functional relation between t and Z , and in agreement with intuition as to the likely ratio of errors in t and Z .

3.2 Optical Effects

A minute examination of errors in time measurement for the CTPR is relatively unprofitable for the reason that with the introduction of counters capable of discriminating 0.1 μ sec intervals, the rms error σ_t is below the equivalent timing error σ_Z/\bar{V} by a factor of five for $\bar{V} = 10,000$ ft per sec. Thus improvement in distance measurement has a clear priority at the present time. One of the major sources of error in distance measurement is uncertainty inherent in the optical methods employed. This topic will be discussed under three headings, viz.,

1) ideal geometrical shadowgraphs, 2) refraction effects, and 3) diffraction effects.

In the CTPR, measurement of distance reduces in essence to determination of the interval on a photographic film or plate between the shadowgraph images of a fiducial mark and the projectile.

An ideal shadowgraph consists of rectilinear, conical projection of the projectile image onto a plane. Under these conditions a perfectly sharp, enlarged image of the body is obtained.

If geometrical optics is assumed and the refracting medium is uniform, then only the size of the source would affect image sharpness. If we call the source diameter S , the distance along the normal to the film from source to projectile d_1 and from projectile to film d_2 , then the angle subtended by source at projectile is $\alpha = S/d_1$ and the width of penumbra around the projectile is $W = \alpha d_2 = Sd_2/d_1$. The magnification of the shadowgraph is $m = (d_1 + d_2)/d_1$. For the CTPR, sparks with $S = .03"$ are in routine use with $d_1 = 36"$ and $d_2 = 32"$. These dimensions are fixed by the size of the outer shell of the range. Thus the penumbral region of partial shadow and consequent edge uncertainty will be $.027"$ on an image about twice normal size ($m = 1.9$). Estimation of the shadow center can reduce the edge uncertainty perhaps by a factor of 2, but cannot eliminate it entirely. Smaller magnifications and sharper shadowgraphs can be obtained by using a camera lens to focus a plane nearer the projectile onto the photographic plate. These "focussed shadowgraphs" are preferred whenever possible for these reasons and others to be explained presently. Nevertheless installation at each station of a large diameter lens of good quality is a considerable complication and introduces uncertainties of its own.

From the standpoint of flow studies the most valuable portion of a shadowgraph arises not from its approximation to an accurate conical

projection, but from the deviations from this ideal caused by inhomogeneities in the refracting medium.

Conventional treatments of these refraction effects [11, 12] start from the assertion that the curvature of a light ray is equal to the magnitude of the vector product of the ray tangent with the gradient of refractive index [Cf. 13]. In a one-dimensional situation with a weakly refracting medium like air, $|\nabla n| = \partial n / \partial x$ and rays crossing transversely a region of constant gradient will become and remain circular arcs so long as the angle between rays and ∇n does not appreciably change. Under these conditions the beam will be uniformly deflected by the disturbance and no changes in light intensity are to be expected on the photographic plane. The conclusion is then drawn that shadowgraph effects are connected with variable density gradients - in the one-dimensional case with non-zero values of $\partial^2 n / \partial x^2$. With a rounded-step or S-curve density function such as would correspond to a one-dimensional shock wave, the initial region where $\partial^2 n / \partial x^2 > 0$ as $\partial n / \partial x$ increases will correspond to increasingly deflected rays and give rise to lowered illumination, that is a "shadow", on the photographic record; while the final portion where $\partial^2 n / \partial x^2 < 0$ with $\partial n / \partial x$ decreasing will give rise to decreasingly deflected rays. Rays from the front and rear portions intersect to cause a double mapping or region of brightness on the plate.

By this reasoning we thus expect a shock wave to be represented by a shadow followed by a bright line just inside. The outer boundary of the shock where normal intensity ends is an accurate projection since the bounding rays pass through the uniform medium preceding the shock and are not deflected. Observe that we are still neglecting diffraction effects.

The foregoing discussion does not exhaust the conditions under which shadows and bright lines may be obtained. If a sharp boundary separates a region of constant index n from one of constant gradient ∇n , the boundary should be marked by a shadow separating the undeflected linear rays from the deflected circular arcs. The shock shadow followed by a bright region has been found by Sedney and Gerber [14] in a raytracing

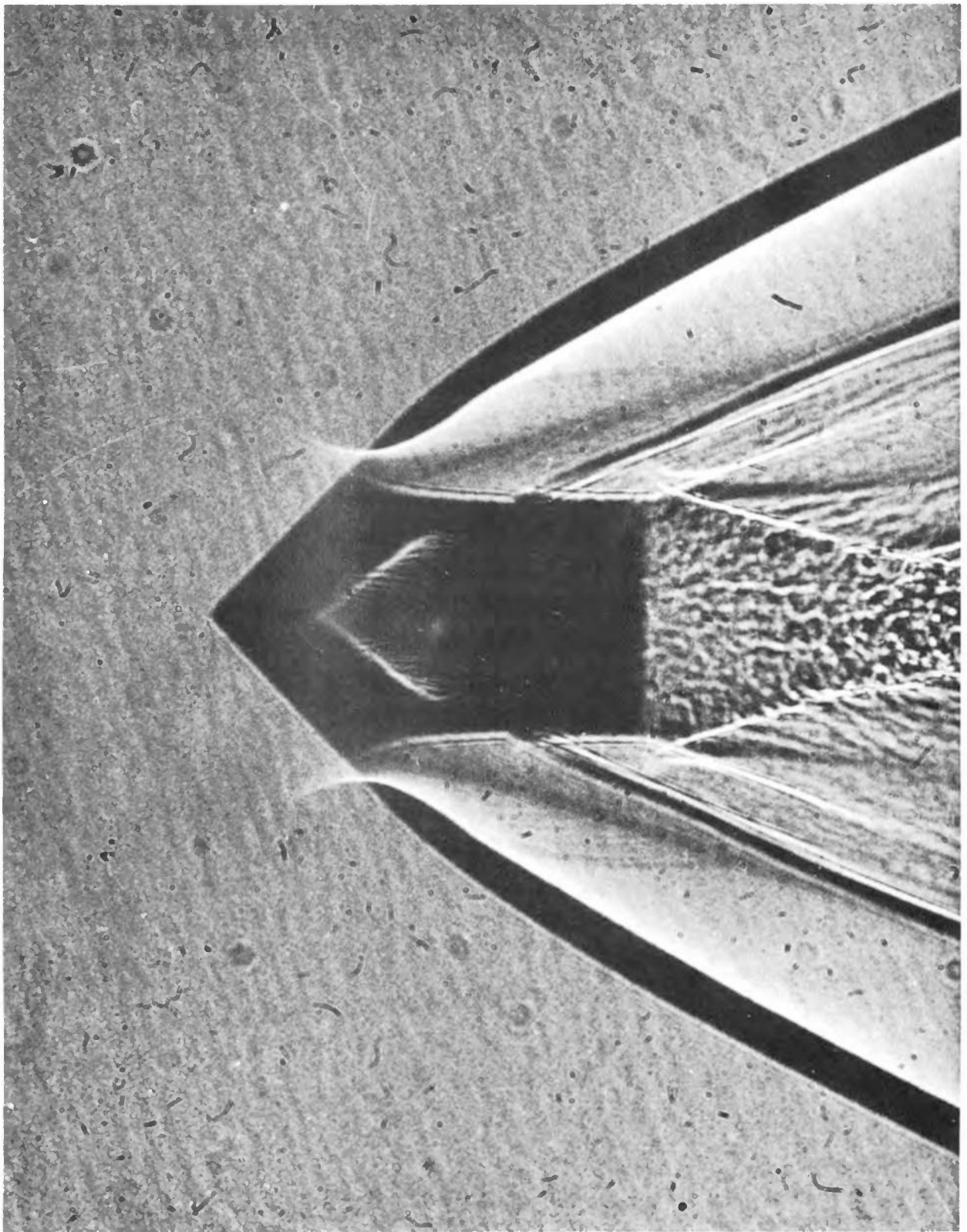


Figure 4. Shadowgraph of blunt (35° half-angle) cone-cylinder at $M = 2.9$ and $p_1 = 5$ atm. The horns of light penetrating the shock wave represent rays refracted by the expansion fans at the corners where the cone and cylinder join.

investigation of refraction by a cone of constant index. Here the conical flow about a supersonic conical body is represented by an equivalent cone of constant refractive index chosen to match the jump at the shock wave but to ignore the slight increase in density as the projectile cone is approached. The cone is assumed to be illuminated by parallel light which travels perpendicular to the axis of the cone -- a case which corresponds to a shadowgraph source at infinity. Rays lying in planes normal to the cone axis are plotted. Traces in the image space of these planes instead of being vertical lines are hooked curves, like inverted skew parabolas, which bend into the geometrical shadow of the refracting cone leaving the region just behind the shock in shadow and doubly mapping a flow region further inside the shadow. The envelope of these curves is a curve of theoretically infinite intensity which corresponds to the bright inside boundary of the shadowgraph shock. The major center portion of each trace is obscured by the solid projectile body leaving only the more refracted rays to illuminate the flow. For cases in which the projectile-to-film distance d_2 is large compared to cone length and refraction displacements correspondingly large as seen in Figure 4, the entire flow region may appear as shadow with illumination from the most refracted rays appearing only inside the body shadow and tracing out two nappes of a luminous cone.

The small interior shocks caused by body roughness have been traced also and found to correspond to curves lying within the body shadow. In a shadowgraph taken at 5 normal densities (Figure 4) these curves are plainly visible as hairy, luminous processes of approximately the shape expected from calculations.

These results, while interesting for flow interpretation, do not bear significantly on problems of position measurement. As already noted, the shock outline is accurate if diffraction effects can be ignored. Thus the forward tip of the usual projectile shadowgraph may be measured with some confidence providing spark duration is small. On the other hand, base position would appear to be more in doubt; for a qualitative ray-

tracing (no quantitative results have been obtained) just behind the base of a cone-cylinder projectile indicates that the grazing rays should be displaced by a small but undetermined amount. Whether forward or backward will depend on the relative strengths of the shock wave and the expansion at the base, and, upon the angles made by the rays with the density gradients at these places. Since the two regions tend to compensate one might assume the effect to be negligible. Measurements of shadowgraph projectile lengths at pressures up to 5 atm when corrected for magnification agree with direct length measurements to within .02", or about 2%.

Diffraction effects, while ordinarily not noticeable in shadowgraphs, are nevertheless present and should be considered when position or angle measurements of highest precision are desired. Diffraction effects are usually not noticeable in range shadowgraphs because 1) spark source duration tends to blur out systems of fringes not parallel to the line of flight, 2) source size tends to blur any system of fringes through superposition of overlapping systems, and 3) spectral breadth of source tends to blur all but the zeroth order interference.

When rotating mirror techniques are used to minimize blur in shadowgraphs of moving projectile taken with spark sources of the type now in use on CTPR, systems of fringes both inside and outside the shock wave may be seen and elsewhere around the projectile. The persistence of a large, bright fringe clearly seen in Figure 4 around the body outline into the turbulent mixing region as a kind of encasement may conceivably be interpreted as evidence of a laminar superlayer anteriorly, between the body and the potential flow; and posteriorly, between the mixing region and the outside potential flow.

Because the ray tracing calculation [14] indicates a double mapping inside the shock, here then is another place where interference may occur if the phase difference between coherent rays is appropriate. A calculation of fringe positions inside the shock has been made [15] on the

basis of the geometrical ray tracing alone and a system found whose maxima and minima lie within about 20 per cent of the measured positions. One would not expect a calculation based on geometrical optics to represent very accurately a situation where diffraction is important; for it is well known that geometrical optics fails to predict phenomena accurately in the neighborhood of focal points or caustic curves - that is to say near ray envelopes such as we encounter behind a shock wave.

A thoroughgoing analysis of diffraction by shock wave boundaries from the point of view of wave optics has not been made to the author's knowledge probably because such a calculation would be very difficult and because diffraction phenomena are not ordinarily enough in evidence to demand attention. Nevertheless, when high precision measurements of unfocussed shadowgraphs are required for the detailed examination of flow phenomena mapped by large refraction effects, account of diffraction effects will have to be rendered and new definitions of apparent shock wave and projectile boundaries will naturally arise from these studies.

3.3 Measurement of Density Fields

The interferometric technique of measuring density throughout an entire axisymmetric field of flow is relatively well understood [2] and can be carried out in representative flows produced at room temperature to an accuracy of about $\pm 2\%$ save near the axis of flow. Various studies of the effects of refraction on interferometric accuracy have been made [16, 2] and some are still in progress [17]. These indicate that largest errors will occur near shock wave boundaries. Experimental studies with the 10" Mach-Zehnder instrument of the CTPR already show that at densities corresponding to one normal atmosphere and above, appreciable regions of an interferogram near the shock wave will be lost because the rays mapping these regions are refracted off the rotating mirror face. Thus the rotating mirror acts like a symmetrical schlieren stop and schlieren effects on high density interferograms are very noticeable indeed. This particular difficulty is easily remedied by use of larger mirror faces; yet it is clear that a limitation exists here for mirrors with 8 faces

2" x 2" in size are rather large objects and to achieve rotational speeds higher than the 6-8000 rpm required by high velocity rounds necessitates turbine motors, or other drives, capable of producing several horsepower. I do not wish to enter the complexities of the light source, rotating-mirror, camera problem for interferometric work, but rather will focus attention briefly on another problem encountered because of the low temperatures used in the CTPR.

As is well known, air or other working fluid must be exceedingly stable and free of variable density, convection currents in order for interferometric techniques to be successful. This requirement has been one of the most difficult to satisfy in the design of the CTPR. In the original plans, the interferometer window cells of the inside stainless steel cylinder were joined to those of the outside mild steel chamber by expansible, stainless steel bellows. On these were attached thermocouples, calrod heating elements and liquid nitrogen cooling coils, the idea being that precise metering of electrical heat and of liquid coolant would keep the outer optical glass windows at room temperature while minimizing heat flow from outer to inner window cells. It was planned to reduce radiated heat losses from outer to inner windows by coating the inner facing surfaces with a thin layer of evaporated gold.

Subsequent tests have shown the need to modify the original designs in almost every detail. Heat conduction through the bellows could not be controlled either rapidly or accurately. They have been removed entirely. Gold coatings thick enough to reflect infra-red radiation were found to be too absorptive of all frequencies to permit their use. They have been replaced by two pairs of solenoid-operated, polished-aluminum shutters in the vacuum space between inner and outer windows. Annular baffles made of cardboard or thin plastic materials such as teflon have been placed between stations inside the working section to stabilize the working fluid and minimize longitudinal temperature gradients. Finally a cylindrical enclosure of cardboard or plastic sheet perforated with 12" horizontal holes to permit passage of the projectile has been used between upper and lower

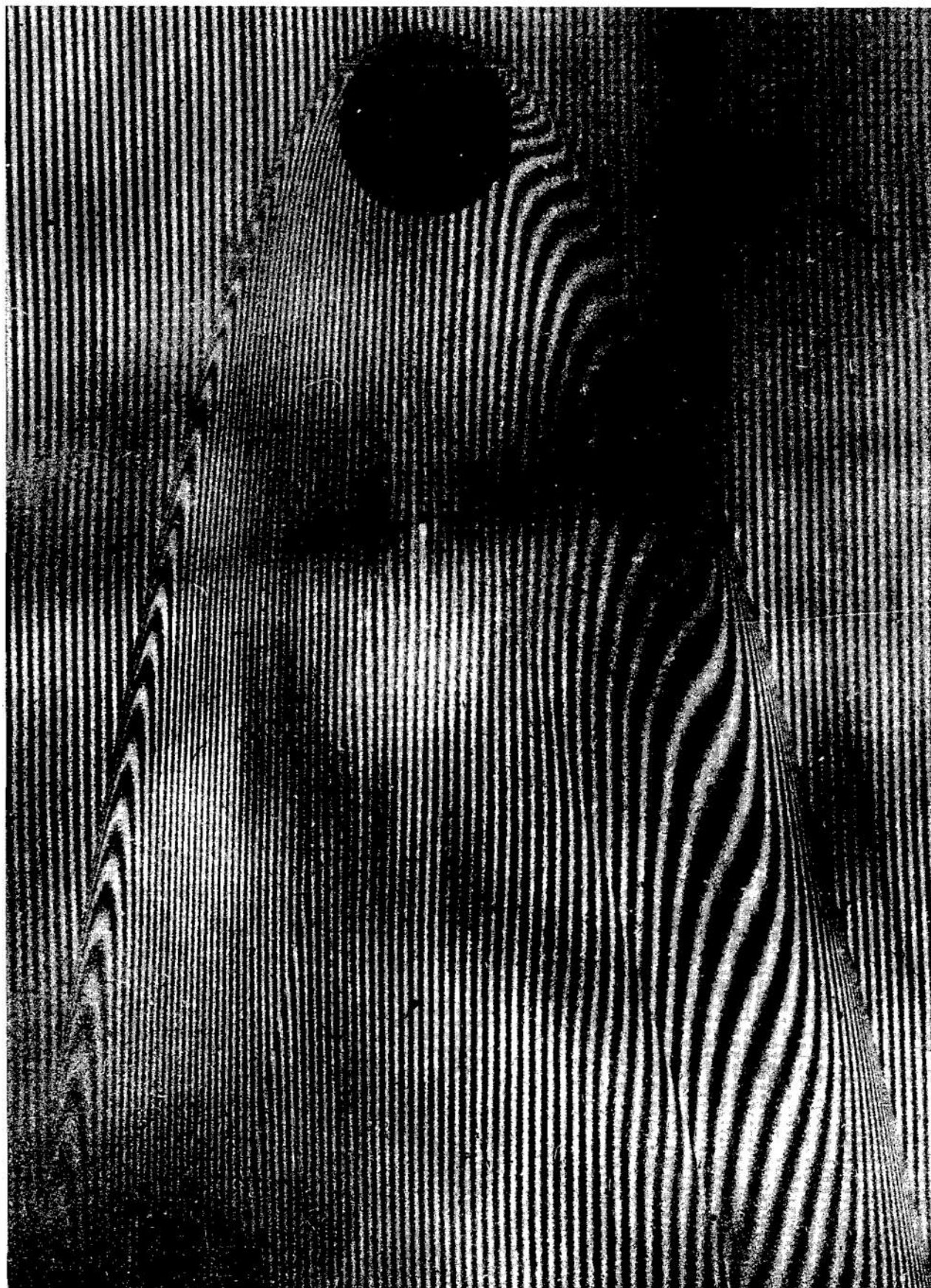


Figure 5. Interferogram of $1/2''$ sphere at $M \doteq 9.3$ in nitrogen at $T \doteq 97^{\circ}\text{K}$ and $p_1 = 3.63''$ Hg.

interferometer windows inside the working section.

All these measures together, plus improved techniques of coolant circulation have resulted in sufficient stability of the cooled gas so that reducible interferograms, of which Figure 5 is an example, can be obtained. These are not of as high quality as those taken at room temperature because slight, local density fluctuations are still present and drift through the interferometric field; nevertheless, these local variations cause only fractional fringe shifts which are small compared to the shifts caused by the flow itself. Achievement of reasonably uniform undisturbed fields at the extreme low temperatures is so recent an accomplishment that complete flow reductions have not yet been made; nevertheless interferograms already in hand show all the essential features of those obtained at room temperature and should yield density fields less accurate by only a few percent.

Since the discovery that the zone method of interferogram reduction deteriorates in accuracy toward the axis of flow [2], a continuing study [18, 19] has been made of various reduction methods which involve least squares procedures of fitting consecutive segments of the fringe shift data with polynomials. The advantages of least squares methods are twofold: 1) hand plotting and smoothing can be avoided and 2) random errors in density values on the axis of flow appear to be no greater than elsewhere. The principal disadvantages encountered so far include 1) spurious discontinuities in density at tie-points of adjacent polynomials and 2) propagation of errors in the fit through the tie points of successively fitted polynomial segments until all accuracy is lost. These difficulties arise because the usual fringe shift curve is not readily fitted by polynomials of degree low enough to be convenient i.e. degree three or four, and so must be approximated over short sections. Electronic computing machine programs for the zone method (ENIAC) and least squares schemes (ORDVAC) have been devised and tested, but the reduction problem is not yet solved in a completely satisfactory manner. A combination of the

two methods, i.e. approximating the fringe shift by the zone method at intermediate and large distances and by a tied, least-squares cubic near the axis, may turn out to be the optimum choice where highest accuracy is desired.

4.1 K_D and Wake Angle Measurements

An account is given, in a companion paper [20] of this symposium, of application of the CTPR to investigate observable properties of the flows about proposed nose models for the ICBM program. The studies made so far represent attempts to simulate normal density flows for the Mach number span $4 \leq M \leq 10$. The demand of this program for data at higher Mach numbers has greatly stimulated development at EBL of high-velocity missile launchers. This Laboratory has under procurement at the present time two guns of the type developed by Drs. Slawsky and Seigel of NOL. When these have been obtained and proven, extension of the present Mach number range by a factor of two is to be expected. This should make accessible to study flows with an appreciable degree of ionization. Whether the interferometric techniques discussed here can be used to explore the properties of a self-luminous, highly excited medium remains open to question.

4.2 K_D vs M for a Blunt Cone-Cylinder

In any discussion of an instrument such as the CTPR the question naturally arises as to how well flows produced by models at low temperatures and high Mach numbers simulate those produced by models or full scale objects at the same Mach numbers and "ordinary" temperatures. To provide a partial answer to this complex question, studies of K_D vs M for a blunt cone-cylinder i.e. a 35° half-angle, cone-cylinder have been made at 300° , 105° and 85° Kelvin. Before discussing some of these results a few theoretical remarks will be interpolated to clarify the situation.

If the equations governing the conservation of mass, momentum and energy for a viscous, heat-conducting, compressible fluid be rendered dimensionless through the introduction of suitable transformations on the dependent and independent variables, then a set of partial differential equations emerges which is not only free of dimensions but also exhibits certain dimensionless functional coefficients which appear as multipliers of the various derivatives.

These coefficients are: $\gamma = C_p/C_v$, $M = V/a$, $Fr = V^2/gL$, $Re_1 = \rho VL/\mu$, $Re_2 = \rho VL/\lambda$ and $W = k\theta/\mu V^2$. Here γ , M and Fr represent specific heat ratio, Mach number and Froude number respectively; while μ and λ stand for the first and second coefficients of viscosity and Re_1 , Re_2 the corresponding Reynolds numbers. The quantity W in which heat conductivity k and a characteristic temperature difference θ occur, has no conventional name but is discussed by Dryden [30] and is recognizable as the ratio of heat flow to energy dissipated by viscous friction. Depending upon assumptions defining relative orders of magnitude of heat flow, viscous dissipation, kinetic energy, other dimensionless quantities such as Nusselt number or Prandtl number may enter through the boundary conditions of a given problem.

If flows about two similar objects of different size, say two spheres in an infinite medium, are to have the same dimensionless solution to the flow equations, then the six coefficients just listed must be preserved without change in the two situations. In addition, initial conditions and conditions at the boundaries must be rendered in dimensionless form and dimensionless coefficients preserved.

In supersonic flow problems encountered in firing ranges it is customary to regard gravitational effects as negligible. Thus Froude number may be disregarded. If heat flow were small compared to viscous dissipation W might be neglected. On the other hand, it has long been understood that conditions on the heat transfer at the flow boundaries determine whether W , Nusselt and/or Prandtl numbers will be of importance. In some range experiments missiles are heated or cooled in order to control these modelling parameters. In experiments to date with the CTPR this has not been done. Comparisons among various drag data are made simply ignoring the fact that W , Pr and Nu have not been controlled in the modelling. As for second coefficient of viscosity the view is taken that either the Stokes' relation $\lambda + 2/3\mu = 0$ holds or the effects of λ can be ignored or if not ignored are strictly proportional to those of μ . Under any of these conditions Re_2 can either be ignored or lumped with Re_1 . This leaves then three coefficients to preserve in the preliminary modelling experiments viz. γ , M , and Re_1 .

The first of these, γ , is usually regarded as constant. Tables of this ratio for air or nitrogen [21] show deviations from $\gamma = 1.40$ of slightly more than 1% in the temperature range $100 \leq T \leq 300^\circ\text{K}$. As the boiling point of air or nitrogen is approached the deviations become larger. The data for nitrogen at one normal density i.e. approximately $1/3$ atm suggest that at $T = 85^\circ\text{K}$ the 1% limit may not be exceeded. For these reasons γ is assumed to be the same constant in both the room and low temperature experiments.

Mach number is chosen to be the independent variable in both experiments. While clearly the room temperature tests cannot reach the high Mach numbers accessible at low temperatures, a considerable overlap in the range of values $4 \leq M \leq 6$ is possible where K_D values ought to be directly comparable. $Re_1 = \rho V L / \mu$ is the one remaining coefficient whose value must be preserved in the two experiments. Because velocity of sound variation with absolute temperature is the essential factor in attainment of the high Mach number data, the dependence of Re_1 on M is shown by writing $Re_1 = \rho L M a / \mu$ where $V = aM$.

If it were true that the temperature dependence of a and μ were the same, then the problem would simplify to that of maintaining $\rho L = \text{const.}$ for a given Mach number. Simple kinetic theory predicts that both a and μ should be proportional to $T^{1/2}$. In the present study of the blunt cone-cylinder it is assumed that the temperature effects of a and μ do cancel. For constant missile size ρ is merely adjusted to have the same value at low temperature as at room temperature. This means working at something less than $1/3$ atm when $T \approx 85^\circ\text{K}$. The further assumption is made that in the non-overlapping region of M , i.e. for $M \geq 6$, the increased Re_1 has little effect on K_D or other flow parameters being studied.

The assumption that the temperature effects of a and μ cancel is not strictly valid. For velocity of sound in nitrogen or air, the relation

$a = CT^{1/2}$ holds within about 3% for temperatures $100 \leq T \leq 300^\circ\text{K}$ at 1 atm. pressure. Viscosity of air or nitrogen varies closely as T raised to the $8/9$ power for the same range of temperature. Thus the simplifying assumption is only a crude representation of the facts. For a fixed projectile size L , to render $Re_1 = \text{const.}$ precisely, one would have to adjust density so that $\rho = \text{const.} \times \mu/Ma$. The measurements of K_D vs M made for comparison purposes at $T = 300^\circ$, (105°) and 85°K for the blunt cone-cylinder [10] show K_D values at all temperatures falling quite well on a continuous curve. As K_D is relatively insensitive to Re_1 , minor variations in this quantity appear to have no significance even up to a five-fold variation in Re_1 [10]. This is in contradiction to preliminary measurements made before precise determinations of ambient density could be made [22].

The relatively small failures indicated above to model γ and Re_1 accurately are often completely masked by experimental difficulties indicative of the crude approach followed during these early uses of the CTPR. Until recently, temperature gradients in the range introduced uncertainty to the interpretation of thermocouple measurements and, as a consequence, into the calculation of the ambient density ρ_1 . Some of the discrepancy between early groups of measurements can be traced to erroneous ρ_1 values used to calculate K_D . Improvements in temperature control and uniformity have brought better agreement between recent series of K_D values.

Among other sources of error at room temperatures are the unaccounted for variations in γ and mol. wt. of the working fluid caused by contaminants from the burnt powder gases. In spite of multiple baffle systems some contamination can hardly be avoided — and cannot at present be detected until a system of chemical analysis of the medium or precise measurement of its characteristic sound speed allows continuous monitoring of the composition of the medium. At the low temperatures contamination from powder gases constitutes a two-fold problem. If the gases are condensible they immediately appear either on walls and window surfaces as "snow" or

"frost" of various kinds or as a fog presumably made up of fine crystals of unknown composition. The fog does not settle out during moderate lengths of time; so the result is a working medium with poorly known physical constants which is also optically of poor quality. During recent firings at low temperatures, the baffle systems plus improved techniques of flushing the gun chamber after firing have minimized problems caused by frost or fog; nevertheless after 10 rounds have been fired from the cal .75 launcher some frost can be observed at the station windows and fog though slight, is easily detectable.

An interesting result in the K_D vs M curves for the blunt cone-cylinder has emerged as improved techniques have provided smoother data. In the region near $M = 4$ a slight bump appears which extends over about half a Mach number. This phenomenon was first noted in the data obtained from firings through nitrogen at low temperatures [10]. More recently firings at room temperature through argon-sulfurhexafluoride mixtures [23] have revealed the same hump in the curve. So far no explanation for its presence can be given.

4.3 Interferometric Properties of the N-Wave

A shadowgraph or interferogram of an axisymmetric flow presents an enormous amount of data in visual form. Attempts to reduce this data to quantitative results emphasize the desirability of principles which correlate whole areas of flow under a single unifying law.

Some years ago the discovery was made [24] that conical flows demonstrate an unusual and simplifying symmetry for interferometric purposes. The gist of this principle is that fringe shift δ , divided by axial distance z is a unique function of r/z throughout the entire conical flow. Here r denotes distance in the radial direction. Plots of δ/z vs r/z yield a single curve in conical flows and may be used as "test gauges" to determine whether a flow is conical and where it departs from conicity. This conical

flow principle has been used successfully as a tool in studying other related flows [25, 26].

Recently a similar principle has been found to hold in the distant flow between the front and rear shocks caused by an axisymmetric, supersonic projectile. Along a trace parallel to the axis, this region is characterized by a vertical pressure rise at the front shock followed by a linear decrease to below ambient levels and finally another vertical pressure rise at the rear shock. Because of the N-shaped pressure curve the region has been called "the N-wave".

Theoretical studies by G. B. Whitham [27] have given approximate expressions for the pressure in the N-wave region. Working to the same approximation D. H. Steininger [28] and the author [29] have derived expressions for the interferometric fringe shift in the N-wave and compared these to data from cone-cylinders and spheres. When suitable approximations are applied, a simple mapping function is obtained which characterizes N-wave flow. If ξ represents the fractional distance between front and rear shocks along a trace at constant radial distance r , then it can be shown that $\delta r^{1/8} G' = \xi^{1/2} (1 - 4\xi/3)$; thus by plotting $\delta r^{1/8} G'$ versus ξ , experimental data can be compared with the function $\xi^{1/2} (1 - 4\xi/3)$. G' is a function which depends upon Mach number, body shape, the wavelength of light used and physical constants of the medium. Convergence to N-wave flow has been examined for a cone-cylinder of 7.5° half-angle and for small spheres. At 70 diameters from the axis of the sphere the agreement between plotted fringe shifts and the mapping function is excellent and one concludes that N-wave flow is obtained.

Not only may fringe shifts within a given region of flow be compared by means of this principle, but also fringe shifts from flows about similar bodies at different Mach numbers and under different conditions of ambient density. This latter is a direct consequence of the fact that the function G' accounts for differences in Mach number, density, etc. It is perhaps apparent that interesting studies of N-wave flow as a function of Reynolds number might now be undertaken.

The N-wave mapping law yields a principle which permits study and comparison of axisymmetric flow data over a large region of the flow. It holds this property in common with the conical flow principle. Reasoning by analogy one may expect that the N-wave property will eventually become useful as a diagnostic criterion and standard of comparison in the same way that the conical flow test already has done.

BIBLIOGRAPHY

1. R. F. Clippinger, J. H. Giese, and W. C. Carter; "Tables of Supersonic Flows about Cone Cylinders", Parts I and II. BRL Report 729 and 730, (July 1950).
2. F. D. Bennett, W. C. Carter, and V. E. Bergdolt; "Interferometric Analysis of Airflow about Projectiles in Free Flight", BRL Report 797 (March 1952) or J. Appl. Phys. 23, 453, (1952).
3. M. R. Lewis and D. B. Sleator; "Exploding Wire Light Source for High Speed Interferometry", BRIM Report 975 (Feb. 1956).
4. D. B. Sleator, V. E. Bergdolt and F. D. Bennett; "Monochromatic Light Source for Interferometry of High Speed Gas Flows", BRIM Report 594. See also J. Appl. Phys. 22, 776, (1951).
5. a) F. D. Bennett; "Optimum Source Size for the Mach-Zehnder Interferometer", BRL Report 731 (Sept. 1950) or J. Appl. Phys. 22, 184 (1951).
 b) F. D. Bennett and G. D. Kahl; "A Generalized Vector Theory of the Mach-Zehnder Interferometer". BRL Report 801 (April 1952) or J.O. S. A., 43, 71, (1953).
6. G. D. Kahl; "Design and Performance of a Cal .75 Smoothbore Missile Launcher". BRL Report to be published.
7. B. Karpov, "The Accuracy of Drag Measurements as a Function of Number of Timing Stations". BRL Report No. 658 (February 1948).
8. A. C. Charters, "Accuracy of Drag Measurements in a Combination Firing Range - Wind Tunnel". BRL TN No. 228 (May 1950).
9. F. D. Bennett and J. M. Bartos, "Bounds on Errors in K_D Caused by Random Errors of Measurement in a Five Station Range". BRIM Report 780 (April 1954).
10. G. D. Kahl, "Drag Characteristics of a Blunt Cone-Cylinder from Transonic to Hypersonic Flow". BRL Report to be published.
11. H. W. Liepmann and A. E. Puckett, "~~Aerodynamics~~ of a Compressible Fluid", John Wiley and Sons, Inc., New York (1947).
12. W. A. Mair, "The Sensitivity and Range Required in a Toepler Schlieren Apparatus for Photography of High Speed Flow", Aero. Quar. 4, 19 (1952).
13. S. Gorn, "Series Expansions of Rays in Isotropic, Non-homogeneous Media", Q. Appl. Math 11, 355, (1953).

BIBLIOGRAPHY

14. R. Sedney and N. Gerber, "Refraction of Light Traversing a Conical Shock Wave", Part I BRL Report No. 946 (August 1955).
15. N. Gerber and J. M. Bartos, "Interference Fringes Behind Shock Wave Shadows", BRLM Report No. 991 (April 1956).
16. R. F. Clippinger, "Comparison Between the Jamin-Mach Interferometer and the Williams Interferometer". BRL Report No. 576 (Sept. 1945).
17. R. Sedney and N. Gerber, "Refraction of Light Traversing a Conical Shock Wave", Part II, BRL Report to be published.
18. F. D. Bennett and J. M. Bartos, "A Statistical Comparison of Two Methods of Interferogram Reduction" BRLM Report No. 748 (Jan. 1954).
19. F. D. Bennett and J. M. Bartos, "Comparison of Least Squares Methods Adapted to Reduction of Mach Zehnder Interferograms". BRL Report to be published.
20. L. C. McAllister, "Some Problems Associated with the Determination from Range Firings of Dynamic Stability of Ballistic Missile Re-Entry Shapes". Proceedings of the Aerodynamic Range Symposium: Confidential Paper, BRL Report 1005, Part II (1957).
21. "Tables of Thermal Properties of Gases", National Bureau of Standards Circular 564, U.S. Gov't Printing Office, Washington (1955).
22. V. E. Bergdolt, "Preliminary Drag Measurements in a 12" Pressurized Range". BRLM Report No. 741.
23. M. R. Lewis and D. B. Sleator, "Measurements of K_D in Argon-Sulfur-hexafluoride Mixtures of $\gamma = 1.4$ ", BRLM Report No. 1047 - in press.
24. J. H. Giese, F. D. Bennett and V. E. Bergdolt, "A Simple Interferometric Test for Conical Flow". J. Appl. Phys. 21, 1226, (1950).
25. J. H. Giese and V. E. Bergdolt, "Interferometric Studies of Supersonic Flows about Truncated Cones". BRL Report No. 830; J. Appl. Phys. 24, 1389 (1953).
26. V. E. Bergdolt, "Air Flow About Cone Cylinders with Curved Shock Waves". BRL Report No. 832; J. Aero. Sci. 20, 751, (1953).
27. G.B. Whitham, "The Flow Pattern of a Supersonic Projectile ". Comm. Pure and Appl. Math. 5, 301, (1952).
28. D. H. Steininger, "Interferometric Analysis of the N-Wave of a Supersonic Projectile". Dissertation, The Pennsylvania State University, University Park, (Jan. 1957).

BIBLIOGRAPHY

29. D. H. Steininger and F. D. Bennett, "An Interferometric Test for N-Wave Flow". J. Fluid Mech. (1957) in press.
30. H. L. Dryden, "Aerodynamic Theory", Vol. VI, Div. T, p. 253, Durand Reprinting Committee, GALCIT, (1943).

TWO AEROBALLISTIC RANGE TOPICS

John D. Nicolaides
Bureau of Ordnance
Department of the Navy

INTENTIONALLY LEFT BLANK.

Part One

MASS ASYMMETRY

J. E. Long, G. Parrish, and John D. Nicolaides

U. S. Naval Ordnance Laboratory, White Oak
and the Bureau of Ordnance

Department of the Navy

ABSTRACT

A simple approximate theory for the free flight motion of ballistic missiles having mass asymmetry is given and proofed by experimental firings in the NOL Pressurized Aeroballistic Range.

INTRODUCTION

A simple theory for the free flight motion of ballistic missiles having mass asymmetry appears to be unavailable in spite of classical treatments in Dynamics^{1,2} and the excellent work of Rankin.³ In Ref. 4 a theory for pure angular mass asymmetries was given, and in Ref. 5 an experimental program to proof this theory was reported. Difficulties arising during this experimental program stimulated Ref. 6, where the theory is extended to include linear mass asymmetry (C.G. laterally displaced from missile axis of configurational asymmetry), and where the importance and contributions of various dynamical and aerodynamical terms are evaluated.

In this note the treatments of Refs. 4, 5, and 6 are combined to yield a simple tested theory for the free flight motion of ballistic missiles having slight mass asymmetry.

The general equations for the free flight motion of a missile having mass asymmetry may be written as

$$\begin{aligned}
 m \left[\dot{u} - vr + wq - x(q^2 + r^2) + y(pq - \dot{r}) + z(pr + \dot{q}) \right] &= X_B \\
 m \left[\dot{v} - wp + ur - y(r^2 + p^2) + z(qr - \dot{p}) + x(qp + \dot{r}) \right] &= Y_B \\
 m \left[\dot{w} - uq + vp - z(p^2 + q^2) + x(rp - \dot{q}) + y(rq + \dot{p}) \right] &= Z_B \\
 I_{xx}\dot{p} + (I_z - I_y)qr - I_{xz}(\dot{r} + pq) + I_{yz}(r^2 - q^2) + I_{xy}(pr - \dot{q}) \\
 m \left[y(\dot{w} - uq + vp) - z(\dot{v} - wp + ur) \right] &= L_B \\
 I_{yy}\dot{q} + (I_x - I_z)rp - I_{xy}(\dot{p} + qr) + I_{xz}(p^2 - r^2) + I_{yz}(qp - \dot{r}) \\
 m \left[z(\dot{u} - vr + wq) - x(\dot{w} - uq + vp) \right] &= M_B \\
 I_{zz}\dot{r} + (I_y - I_x)pq - I_{yz}(\dot{q} + rp) + I_{xy}(q^2 - p^2) + I_{xz}(rq - \dot{p}) \\
 m \left[x(\dot{v} - wp + ur) - y(\dot{u} - vr + wq) \right] &= N_B
 \end{aligned} \tag{1}$$

where x, y, z are the coordinates of the center of gravity location in the $(XYZ)_B$ system.*

By the usual linear assumptions of small normal velocities, linear and angular, and by assuming constant axial velocity and spin, these equations reduce to **

$$\begin{aligned}
 m(\dot{v} - wp + ur - yp^2) &= Y_B \\
 m(\dot{w} - uq + vp - zp^2) &= Z_B \\
 I_{xx}\dot{p} - (I - I_x)pr + p^2 I_{xz} &= M_B \\
 I_{zz}\dot{r} + (I - I_x)pq - p^2 I_{xy} &= N_B
 \end{aligned} \tag{2}$$

*Written in "Body Axes" coordinate system which is fixed in the missile (Fig.1).
 **We have also assumed that the origin and orientation of the XYZ Body Axes are so selected that $x = 0$ $I_y = I_z$ $I_{yz} \approx 0$

For the Aeroballistic Axes, which are tied to the missile but do not roll with it, these equations may be written⁴ as*

$$\begin{aligned}
 m(\dot{v} + ru) - mp^2 S_{M_0} \cos \phi_M &= Y \\
 m(\dot{w} - qu) - mp^2 S_{M_0} \sin \phi_M &= Z \\
 I\dot{q} + pr I_X + p^2 \delta_{m_0} \cos \phi_m (I_X - I) &= M \\
 I\dot{r} - pq I_X + p^2 \delta_{m_0} \sin \phi_m (I_X - I) &= N
 \end{aligned} \tag{3}$$

where

$$\begin{aligned}
 |S_{m_0}| &= \frac{|I_{XY} - i I_{XZ}|}{I - I_X} = \frac{\sqrt{I_{XY}^2 - I_{XZ}^2}}{I - I_Y} \\
 \phi_m &= \phi_0 + \tan^{-1} \left(\frac{I_{XY}}{-I_{XZ}} \right)
 \end{aligned} \tag{4}$$

The physical significance of these equations may be noted from Fig. 1, where S_{M_0} is seen to be the lateral displacement of the center of gravity of the missile and where δ_{m_0} is seen to be the angle between the X-axes and the X' - axis which is one of the three Principal Axes located at the center of gravity of the missile. (It may be shown that if the equations for the motion of the missile are first written in this Principal Axis System and then translated by S_{M_0} and rotated by both δ_{m_0} and ϕ , the aeroballistic equations above would be obtained.**)

* We have assumed that $I_Y \approx I_Z$ for all roll orientations of the Aeroballistic Axes and the Body Axes.

** It is assumed that the mass asymmetry is slight and thus that S_{M_0} and δ_{m_0} are small. It follows that $I_Y \approx I_Z$ and $I_{YZ} \approx 0$.

The aerodynamic force and moment system is given by

$$Y = Y_{vv} + Y_{rr} + Y_{\dot{v}\dot{v}} + Y_{\dot{r}\dot{r}} + Y_{pw}pw + Y_{pq}pq + Y_{p\dot{w}}p\dot{w} + Y_{p\dot{q}}p\dot{q} \\ + Y_{\delta_E} \delta_E \cos \phi - Z_{\delta_E} \delta_E \sin \phi$$

$$Z = Z_{ww} + Z_{qq} + Z_{\dot{w}\dot{w}} + Z_{\dot{q}\dot{q}} + Z_{pv}pv + Z_{pr}pr + Z_{p\dot{v}}p\dot{v} + Z_{p\dot{r}}p\dot{r} \\ + Z_{\delta_E} \delta_E \cos \phi + Y_{\delta_R} \delta_R \sin \phi$$

(5)

$$M = M_{ww} + M_{qq} + M_{\dot{w}\dot{w}} + M_{\dot{q}\dot{q}} + M_{pv}pv + M_{pr}pr + M_{p\dot{v}}p\dot{v} + M_{p\dot{r}}p\dot{r} \\ + M_{\delta_E} \delta_E \cos \phi - N_{\delta_R} \delta_R \sin \phi$$

$$N = N_{vv} + N_{rr} + N_{\dot{v}\dot{v}} + N_{\dot{r}\dot{r}} + N_{pw}pw + M_{pq}pq + M_{p\dot{w}}p\dot{w} + M_{p\dot{q}}p\dot{q} \\ + N_{\delta_E} \delta_E \cos \phi + M_{\delta_R} \delta_R \sin \phi$$

Following the development of Ref. 8 Eqs. (3) and (5) may be combined to yield*

$$\ddot{\vec{w}} + N_1 \dot{\vec{w}} + N_2 \vec{w} = N_3 e^{ipt}$$

$$N_1 \approx - \frac{Z_w}{m} - \frac{(M_q + u M_{\dot{w}})}{I} - ip \left(\frac{Z_{pw}}{m} + \frac{I_y}{I} \right)$$

(6)

$$N_2 \approx - \frac{u M_{w^2}}{I} + p \left(\frac{-i I_y Z_w}{I m} - \frac{i u M_{pv}}{I} - \frac{p_x I Z_{pw}}{I m} \right)$$

$$N_3 \approx \frac{+ipe^*}{mV} \left(1 - \frac{I_x}{I} \right) + i \frac{E^*}{I}$$

where

$$e^* \approx e \delta_E + p^2 m S_M \quad \vec{w} \equiv v + i\omega$$

$$E^* \approx E \delta_E - p^2 m (I_x - I)$$

(7)

and where

$$e = Z_{\delta_E}$$

$$E = -i M_{\delta_E}$$

(8)

Equalities of the Rotary Derivatives^{9,4} are obtained by the assumption that the missile configuration has basic trigonal or greater rotational symmetry and mirror symmetry.

The general solution for the complex angle of attack is found to be Tricyclic Motion*

$$\vec{\alpha} = \frac{\vec{w}}{u} = K_1 e^{\phi_1 t} + K_2 e^{\phi_2 t} + K_3 e^{i p t} \quad (9)$$

where

$$\phi_{1,2} = \lambda_{1,2} + i \omega_{1,2} = -\frac{N_1}{2} \pm \frac{1}{2} \sqrt{N_1^2 - 4N_2}$$

$$\lambda_{1,2} = \left\{ \frac{\omega Z_{\omega}}{2 m V} (1 \mp \tau) + \frac{(M_g + \omega M_{\dot{\omega}})}{2 I} (1 \pm \tau) \pm \frac{\omega M_{p \omega} \tau}{I_x} \right\}$$

$$\omega_{1,2} = \frac{p I_x}{2 I} (1 \pm \frac{1}{\tau})$$

$$K_{1,2} = \frac{\vec{\alpha}_0 - (\lambda_{2,1} - i \omega_{2,1}) \vec{\alpha}_0 + K_3 (\lambda_{2,1} + i \omega_{2,1} - i p)}{(\lambda_{1,2} - \lambda_{2,1}) - i (\omega_{1,2} - \omega_{2,1})}$$

$$K_3 = \frac{N_3}{[i(p - \omega_1) - \lambda_1][i(p - \omega_2) - \lambda_2]} \quad (10)$$

$$S = \frac{p^2 \left(\frac{I_x}{I} \right)^2}{4 \frac{\omega M_{\dot{\omega}}}{I}}$$

$$\tau = \frac{1}{\sqrt{1 - \frac{1}{S}}}$$

* The general solution for the transverse displacement is also of the Tricyclic form and is given by

$$\vec{s} = y + iz = k_1 e^{\phi_1 t} + k_2 e^{\phi_2 t} + k_3 e^{i p t} + k_4 t + k_5$$

The characteristics of Tricyclic type motion are discussed in Ref. 8.

These equations are alleged to enable the computation of the detailed free flight motion of a missile having slight mass asymmetry, or, conversely, to enable the reduction of observed free flight motions for the determination of the aerodynamic coefficients. In order to proof their accuracy an experimental program was undertaken in the Pressurized Aeroballistic Range at the Naval Ordnance Laboratory.

EXPERIMENT

The configuration and the three model designs used in the experiment program are illustrated in Fig. 2. The configuration is a simple cone-cylinder of a fineness ratio of five. The three model designs, Basic, One Hole, and Two Hole, represent three values for δ_{m_0} (0° , $.30^\circ$, and $.42^\circ$), and S_{M_0} ($0.43 \cdot 10^3$, and $0.41 \cdot 10^3$). Table I gives additional physical data on the models tested in the program. (Basic, Rounds, 1912-1915; One Hole, Rds. 1372-1375; Two Hole, Rds. 1586-1592).

The models were gun-launched in the NOL Pressurized Aeroballistic Range (Photo 1), and their free flight motion was observed (Photo 2). A typical history of the observed complex angle of attack is illustrated in Fig. 3.

The complex angle of attack and the lateral displacement were reduced, using both an Epicyclic Reduction and a Tricyclic Reduction. The values of the "fit" (i.e. P.E. α and P.E. β) are given in Table II. It should be noted that the use of the Tricyclic reduction improves the complex angle of attack "fit" by 30.7% (One Hole) and 42.6% (Two Hole).

The aerodynamic coefficients*obtained from the reductions are given with their Probable Errors in Table III. ***

Values for the Third Arm, which exists only because of the Mass Asymmetry, were obtained from the experimental tests and were also computed from the measured physical parameters using the Tricyclic Theory of this note. These theoretical and experimental values for K_3 are given in Table IV.

* The variation in the values of the coefficients from the three model designs should be noted, but no analysis is given herein.

It should be noted that although the size of the Third Arms are of the same order of magnitude as the values for the Tricyclic "fit" (Table II), the probable errors for the Third Arms are small and thus indicate an accurate determination. The consistency of the determination of K_3 round to round appear good except for Rd. 1375 and Rd. 1587.

In Table V the agreement between theory and experiment is given. The values in parentheses are obtained by omitting Rds. 1375 and 1587.

** It should be noted that the Probable Errors of the aerodynamic coefficients are improved by the order of 50% by using the Tricyclic Theory.

CONCLUDING REMARKS

The data from the experimental program indicates that the Tricyclic Theory for mass asymmetry accurately represents the free flight motion of the models tested and that the various static and dynamic aerodynamic coefficients are well determined from the motion using this theory.

The theoretically predicted values for the Third Arm arising from mass asymmetry are in good agreement with the values obtained from the experimental firings. For the One Hole models, this difference of experiment from theory is 11.1%, and for the Two Hole models, the difference is 1.5% (Table V).

An alternate evaluation of the Tricyclic Theory for mass asymmetry might be obtained by comparison of this approximate theory with numerical integrations of the exact equations, Eq. (1), on an advanced computing machine using representative values of S_M and S_m .

REFERENCES

1. Gray, A., Gyrostatics and Rotational Motion, Macmillan and Co., 1918.
2. Routh, Advanced Dynamics, p. 164, sixth edition.
3. Rankin, R. A., The Mathematical Theory of the Motion of Rotated and Unrotated Rockets, Phil. Trans. Roy. Soc. London, No. 837, Vol. 241, March 1949.
4. Nicolaides, J. D., and MacAllister, L. C., A Review of Aeroballistic Range Research on Winged and/or Finned Missiles, Technical Note No. 5, BuOrd, 1955.
5. Long, J. E., The Effects of Mass Asymmetry on the Motion of Missiles, NOL NavOrd Rpt. No. 4433, 1957.
6. Parrish, G. B., An Examination of the Motion Through Air of a Rigid Body with Mass Asymmetry, Technical Note No. 32, BuOrd, 1956.
7. Parrish, G. B., Chapter 8, BOHAC Hydroballistics Design Handbook, BuOrd NavOrd No. 3533, 1955.
8. Nicolaides, J. D., On the Free Flight Motion of Missiles Having Slight Configurational Asymmetries, B.R.L.Rpt. No. 858 and I.A.S. Preprint No. 395, 1952.
9. Bryan, G. H., Stability in Aviation, Macmillan and Co., 1911

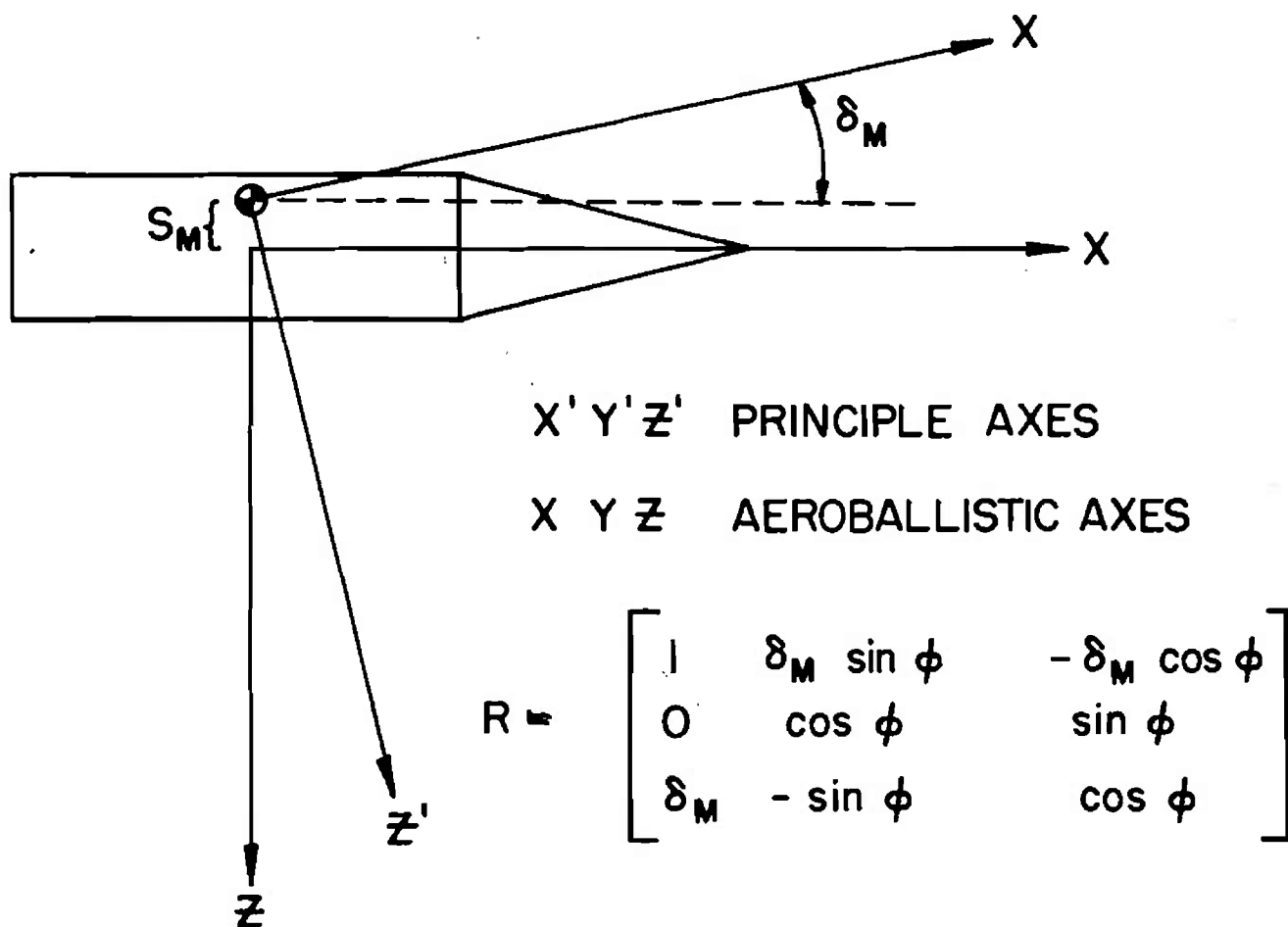
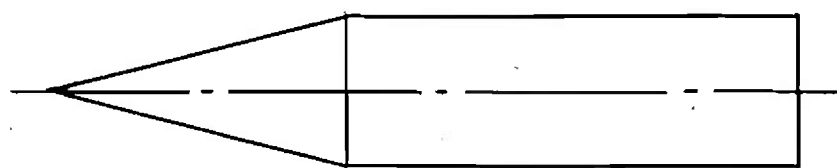
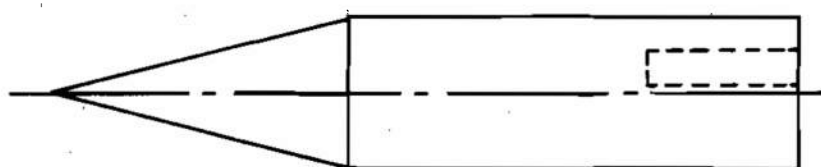
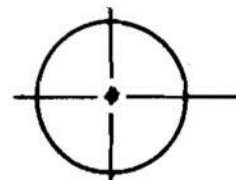


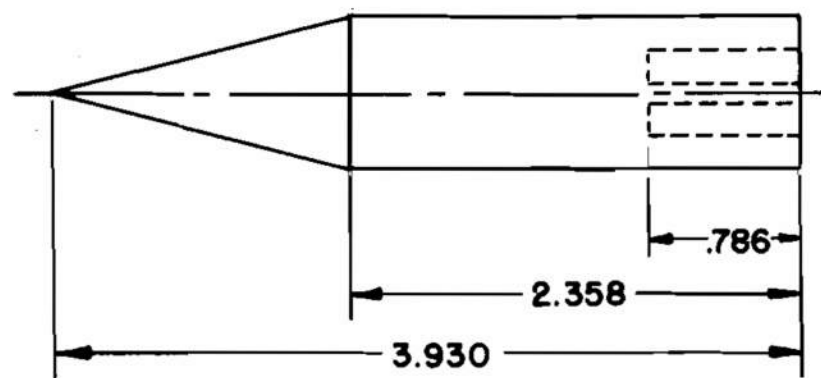
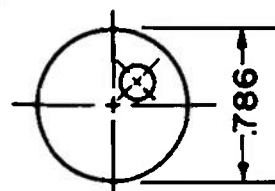
FIG. 1



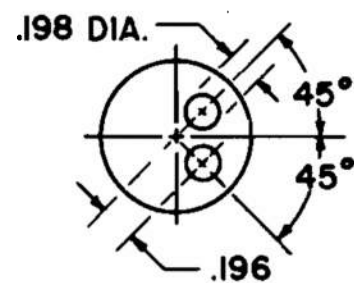
BASIC MODEL



ONE HOLE MODEL



TWO HOLE MODEL



ALL DIMENSIONS ARE
IN INCHES

DESIGN OF MISSILES USED IN EXPERIMENTAL TESTS

FIG.2

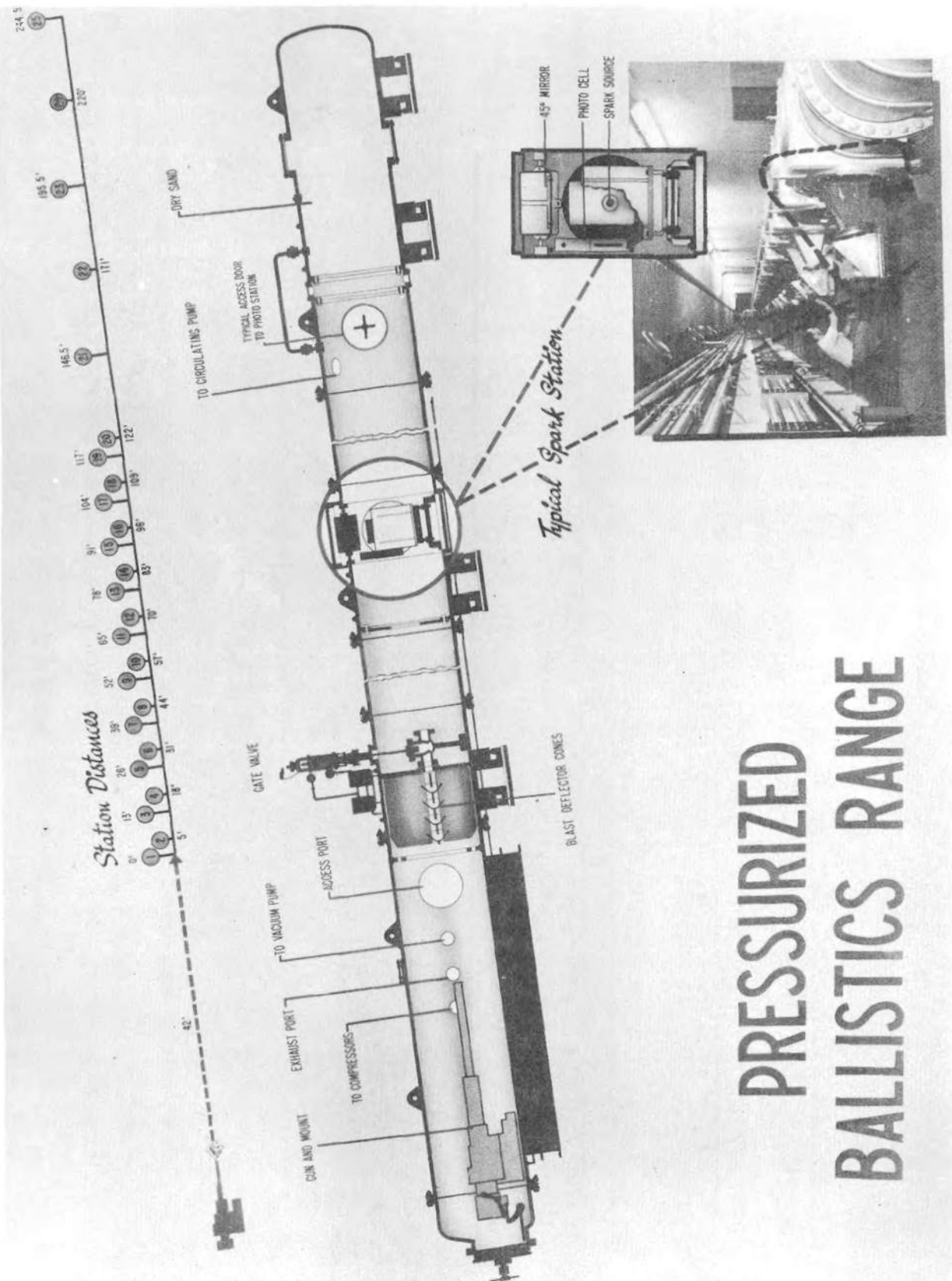
Table I

round	Dx10 ² ft.	L ft.	W ft.	I _{x2}	I _{z2}	I _{x'2}	I _{z'2}	C.G. from base, ft.
basic model								
1912	6.54	0.327	0.392	4.05	46.67			0.122
1913	6.54	0.327	0.392	4.06	47.11			0.122
1914	6.54	0.327	0.392	4.07	47.47			0.122
1915	6.54	0.327	0.392	4.06	46.68			0.122
one hole model								
1372	6.55	0.328	0.387			4.06	38.981	0.125
1373	6.55	0.328	0.387			4.08	39.17	0.125
1374	6.55	0.328	0.387			4.07	39.25	0.125
1375	6.55	0.328	0.388			4.04	39.17	0.125
two hole model								
1586	6.54	0.328	0.373			3.96	42.143	0.126
1587	6.55	0.328	0.373			4.00	42.19	0.126
1589	6.55	0.328	0.373			3.97	42.27	0.126
1590	6.55	0.327	0.373			4.00	42.31	0.125
1591	6.55	0.327	0.373			3.99	42.32	0.125
1592	6.54	0.327	0.372			3.98	41.84	0.126

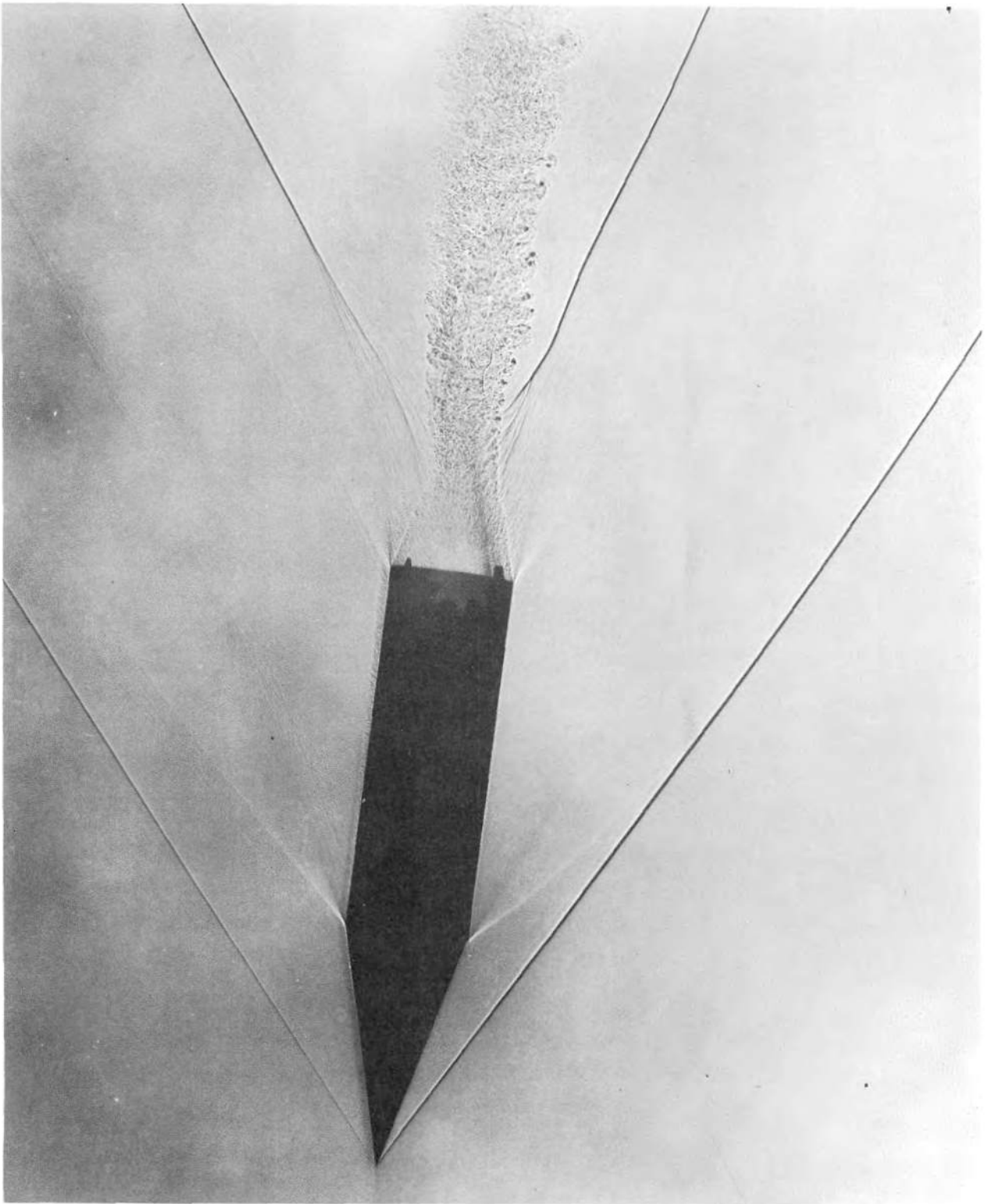
Physical dimensions

- 1 - models measured with hole in 12 o'clock position viewed from base
 2 - models measured with hole in 9 o'clock position viewed from base
 3 - models measured with one hole at 12 o'clock and one hole at 3 o'clock
 positions viewed from base
 4 - models measured with one hole at 10:30 o'clock and one hole at 1:30
 o'clock positions viewed from base

$$\frac{I}{(144)^2} \rightarrow \# - ft^2$$

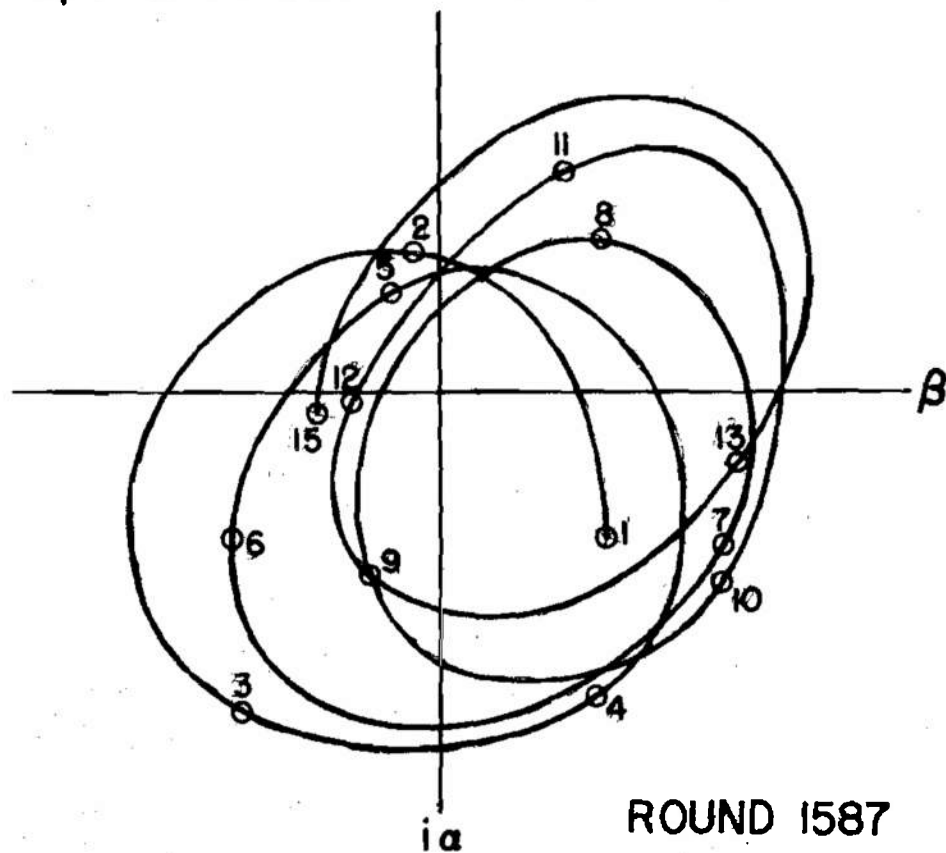


PRESSURIZED BALLISTICS RANGE



INTENTIONALLY LEFT BLANK.

MODEL WITH 2 HOLES
 $\frac{1}{4}$ CAL. IN DIA. 1 CAL. LONG



ROUND 1587

PITCHING AND YAWING MOTION OF MASS ASYMETRICAL

FIG. 3

Table II

Round	EPICYCLIC P.E. ϕ rad.	TRICYCLIC P.E. ϕ rad.	EPICYCLIC P.E. ϕ in.	TRICYCLIC P.E. ϕ in.	ω_1 deg./ft.	ω_2 deg./ft.	ω_3 deg./ft.
1912	0.0020	0.0022	0.0145	0.0158	17.14	2.42	215.6
1913	0.0016	0.0018	0.0156	0.0165	17.00	2.42	213.8
1914	0.0020	0.0022	0.0160	0.0174	17.22	2.34	215.6
1915	0.0012	0.0013	0.0189	0.0204	17.21	2.33	217.1
1372	0.0046	0.0013	0.0162	0.0160	17.92	2.32	216.6
1373	0.0045	0.0014	0.0112	0.0113	17.87	2.28	215.8
1374	0.0054	0.0054	0.0275	0.0244	17.69	2.19	217.4
1375	0.0063	0.0063	0.0102	0.0110	17.54	2.29	216.3
1586	0.0068	0.0042	0.0170	0.0159	18.01	2.22	216.7
1587	0.0089	0.0050	0.0274	0.0234	18.05	2.17	217.3
1589	0.0067	0.0026	0.0131	0.0119	18.02	2.19	217.2
1590	0.0076	0.0050	0.0204	0.0245	18.16	2.16	217.9
1591	0.0069	0.0034	0.0123	0.0116	18.08	2.15	216.2
1592	0.0074	0.0052	0.0160	0.0171	18.21	2.20	217.2

P.E. of yaw and swerve reductions, angular velocities

Table III

BASIC

round	M	C _D	P.E. %	
1912	2.00	0.3736	0.4	
1913	1.95	0.3800	0.6	
1914	1.99	0.3742	0.3	
1915	1.98	0.3785	0.1	
basic model				
	EPICYCLIC		TRICYCLIC	
round	C _{Mα}	P.E. %	C _{Mα}	P.E. %
1912	3.50	3.0	3.49	3.3
1913	3.53	0.7	3.53	0.7
1914	3.54	1.3	3.53	1.3
1915	3.45	0.5	3.44	0.6
	C _{Nα}	P.E. %	C _{Nα}	P.E. %
1912	-	-	-	-
1913	-2.98	2.4	-2.97	2.5
1914	-2.97	3.5	-2.96	3.9
1915	-3.05	2.4	-3.04	2.7
	C _{M_q} + C _{Mα}	P.E. %	C _{M_q} + C _{Mα}	P.E. %
1912	-44.6	30.4	-44.0	33.8
1913	-30.0	23.7	-30.1	26.3
1914	-42.5	19.8	-42.4	20.6
1915	-34.6	10.1	-33.9	11.3
	C _{M_{pα}}	P.E. %	C _{M_{pα}}	P.E. %
1912	1.52	49.4	1.44	51.0
1913	0.96	48.4	0.91	56.2
1914	1.41	65.6	1.35	63.0
1915	1.19	27.1	1.11	30.7

Aerodynamic coefficients

where $C_{Nα} = u C_{Z_{ar}}$ $C_{Mpα} = u C_{m_{pr}}$
 $C_{Mα} = u C_{m_{ar}}$ $C_{Mα} = u C_{m_{in}}$

Table III (cont'd)

ONE HOLE

round	M	C_D	P.E. %	
1372	1.93	0.3826	0.2	
1373	1.96	0.3699	1.5	
1374	1.97	0.3790	0.2	
1375	1.97	0.3765	0.4	
one hole model				
	EPICYCLIC		TRICYCLIC	
round	C_{M_α}	P.E. %	C_{M_α}	P.E. %
1372	3.16	1.1	3.16	0.4
1373	3.16	1.2	3.15	0.4
1374	3.13	0.8	3.13	0.6
1375	3.08	1.6	3.09	0.9
	C_{N_α}	P.E. %	C_{N_α}	P.E. %
1372	-3.10	2.2	-3.00	1.1
1373	-3.02	2.3	-2.88	1.1
1374	-3.11	1.7	-3.00	1.4
1375	-3.16	2.9	-3.05	1.8
	$C_{M_q} + C_{M_\alpha}$	P.E. %	$C_{M_q} + C_{M_\alpha}$	P.E. %
1372	-28.7	21.7	-25.6	7.1
1373	-30.3	25.3	-26.7	7.8
1374	-30.3	16.6	-26.9	11.9
1375	-32.4	29.4	-29.1	16.9
	$C_{M_{p\alpha}}$	P.E. %	$C_{M_{p\alpha}}$	P.E. %
1372	1.15	47.8	0.64	18.0
1373	1.45	42.2	0.80	15.8
1374	1.35	43.0	0.78	23.6
1375	1.58	45.4	0.98	29.9

Aerodynamic coefficients

Table III (cont'd)

TWO HOLE

round	M	C _D	P.E. %	
1586	1.96	0.3894	0.5	
1587	1.97	0.3893	0.6	
1589	1.97	0.3792	0.2	
1590	1.95	0.3918	0.2	
1591	1.99	0.3838	0.2	
1592	1.96	0.3735	0.3	
two hole model				
	EPICYCLIC		TRICYCLIC	
round	C _{Mα}	P.E. %	C _{Mα}	P.E. %
1586	3.06	1.8	3.07	1.1
1587	3.07	1.6	3.05	0.9
1589	3.06	1.8	3.07	0.8
1590	3.05	1.7	3.09	1.1
1591	3.05	1.8	3.08	0.9
1592	3.09	2.5	3.13	1.8
	C _{Nα}	P.E. %	C _{Nα}	P.E. %
1586	-3.27	3.2	-3.24	2.1
1587	-3.24	3.0	-3.21	1.9
1589	-3.14	2.3	-3.12	1.5
1590	-3.28	3.2	-3.29	2.4
1591	-3.18	3.1	-3.15	1.6
1592	-3.22	4.5	-3.17	3.5
	C _{M_q} +C _{Mα}	P.E. %	C _{M_q} +C _{Mα}	P.E. %
1586	-33.5	24.9	-31.7	15.8
1587	-33.1	28.5	-32.1	15.8
1589	-43.2	19.7	-34.7	10.4
1590	-38.2	22.9	-34.1	17.0
1591	-39.6	23.8	-33.2	14.6
1592	-37.5	40.4	-31.3	36.0
	C _{M_{pα}}	P.E. %	C _{M_{pα}}	P.E. %
1586	0.95	58.8	1.17	31.2
1587	0.87	92.7	1.22	36.0
1589	1.69	29.0	1.39	18.4
1591	1.48	37.0	1.32	29.0
1590	1.27	43.1	1.26	38.0
1592	1.32	69.8	1.01	117.7

Table IV

round	* K_3 rad.	* K_3 rad.	* P.E. K_3 rad.
	theoretical	experimental	
basic model			
1912		.00043	.00055
1913		.00052	.00043
1914		.00068	.00051
1915		.00022	.00033
one hole model			
1372	.00599	.00521	.00034
1373	.00597	.00500	.00036
1374	.00594	.00501	.00092
1375	.00596	.00601	.00085
two hole model			
1586	.00783	.00686	.00096
1587	.00782	.00970	.00102
1589	.00779	.00758	.00072
1590	.00776	.00738	.00120
1591	.00769	.00768	.00082
1592	.00788	.00684	.00144

Third Arm, K_3^* , theoretical and experimental

TABLE V

<u>MODEL</u>	<u>FIT</u>	<u>RDS.</u>	<u>K₃</u>		<u>COMPARISON</u>
			EXP.	TH.	
BASIC	.107°	4	.0263°	0°	
ONE HOLE	.206°	4	.303° (11.6%)	.341°	11.1 % (14.9)
TWO HOLE	.263°	6	.439° (13.6%)	.446°	1.5 % (6.7)

COMPARISON OF THEORY & EXPERIMENT

Part Two

DYNAMIC STABILITY*

John D. Nicolaides

Bureau of Ordnance

ABSTRACT

The Epicyclic Theory for the flight dynamics of ballistic missiles has yielded various "Dynamic Stability Criteria" which are often used to evaluate missile performance. Recent misleading uses of the theory and criteria in appraising missile performance require a simple restatement of the theory, its assumptions, and its use.

The parameters of Nutation Half-Life, Precession Half-Life, and Total Motion Half-Life are suggested as better criteria for missile dynamics than those classically based on the Linear Theory.

Also a summary of important Non-Linear Cases of ballistic missile flight performance is given.

*The study in this Technical Note was suggested by A. Wertheimer.

The complex angle of attack is given by:

$$\vec{\alpha} = K_N e^{(\lambda_N + i\omega_N)t} + K_P e^{(\lambda_P + i\omega_P)t} \quad (1)$$

and represents two rotating arms, the nutation and the precession, which can increase or decrease in size. The arms rotate at the rates ω_N and ω_P , and damp or expand at the rates λ_N and λ_P .

This solution for the complex angle of attack was obtained by making the following assumptions:

1. constant missile velocity
2. constant missile rolling velocity
3. constant missile mass and moments of inertia (symmetrical transverse mass distribution and symmetrical axis mass distribution)
4. no gravity attraction
5. linear aerodynamic force and moment system
6. trigonal or greater missile rotational symmetry
7. mirror symmetry of missile
8. small angular displacements and velocities, except roll

These are the assumptions of the Basic Linear Theory. The Theory can be extended by relaxing some of these assumptions, however, for our purposes here we need only consider the Basic Theory.

The requirement for "Dynamic Stability" is that both the Nutation and the Precession Arms damp or*

$$\lambda_{N,P} < 0 \quad (2)$$

This condition is the basic definition of Dynamic Stability as generally used and it insures that eventually all initial motion will fade away. The dynamic stability criteria of Refs. 3 and 5 are other more complicated ways of stating this same simple condition. These criteria and the simple expression above all fail to indicate "how fast" the motion dies out. In order to overcome this shortcoming, the concepts of Nutation Half-Life and Precession Half-Life are introduced as

*See Ref. 6 for definition of all symbols used and a derivation of Eqs. (1), (2),...

$$\text{Nutation Half-Life} = \frac{V}{d \lambda_N} \ln(\frac{1}{2}) \quad (\text{calibers}) \quad (3)$$

$$\text{Precession Half-Life} = \frac{V}{d \lambda_P} \ln(\frac{1}{2}) \quad (\text{calibers}) \quad (4)$$

These relations reveal how far the missile flies in missile diameters until the initial Nutation size is reduced by one-half and how far the missile flies until the Precession is reduced by one-half. Except for a non-rolling fin stabilized missile, these distances are never the same, and as a result the reduction of the total initial motion to one-half size must lie somewhere in between.

The distance between these two distances that Total Motion is reduced to one-half its original size will depend on the relative size of the Nutation and Precession arms initially and their damping rates. This critical distance that the missiles travels in order for the Total Motion to damp one-half its initial value may be calculated from Eq.(5) using Eq. (6). (See Fig. 1.)

$$\text{TOTAL MOTION HALF-LIFE} = \frac{V t_{1/2}}{d} \quad (\text{calibers}) \quad (5)$$

The time of one-half life, $t_{1/2}$, is obtained from

$$\frac{|\vec{\alpha}_0|}{2} = |K_N| e^{\lambda_N t_{1/2}} + |K_P| e^{\lambda_P t_{1/2}} \quad (6)$$

where

$$|\vec{\alpha}_0| \equiv |K_N| + |K_P| \quad (7)$$

Some discussion of this Total Motion is in order. The damping rates λ_N and λ_P are independent of the initial conditions of motion and are determined from the aerodynamic coefficients and the physical parameters of the missile.

$$\lambda_{N,P} \approx \frac{\frac{1}{2}\rho V^2 S}{m} \left\{ C_{Z_w} (1 \mp \tau) + \frac{m d^2}{2 I_V} (C_{m_q} + u C_{m_{\dot{w}}}) (1 \pm \tau) \pm \frac{m d^2}{I_x} C_{m_{\dot{w}}} \tau \right\} \quad (8)$$

The values of K_N and K_P depend on the initial conditions of motion given by

$$K_{N,P} = \frac{\vec{\dot{\alpha}}_0 - \phi_{P,N} \vec{\alpha}_0}{\phi_{N,P} - \phi_{P,N}} \quad (9)$$

where

$$\phi_{N,P} = \lambda_{N,P} + i \omega_{N,P} \quad \omega_{N,P} \approx \frac{V}{2d} \left\{ \left(\frac{\rho d}{2V} \right)^2 \frac{I_x}{I} (1 \pm \tau) \right\} \quad (10)$$

Thus it is clear that the distance of Total Motion Half-Life will depend quite critically on the initial complex angle of attack, $\vec{\alpha}_0$, and the initial complex rate of change of angle of attack, $\vec{\dot{\alpha}}_0$.

For the "Dynamically Stable" missile, $\lambda_{N,P} < 0$, the calculation and interpretation of the Total Motion Half-Life may be carried out in a routine manner using Eq. (5). However, for the case where λ_N or $\lambda_P > 0$ the picture is not so simple and the indiscriminate use of the usual term "Dynamically Unstable" may be downright misleading.

To point up this often misunderstood and misapplied flight condition, it is instructive to consider the special case where K_N is small, K_P is large, $\lambda_N > 0$, and $\lambda_P < 0$. Here we have a case where $\lambda_N > 0$; but is the missile "actually dynamically unstable? Consider the pictorial representation in Fig. 1 (Dashed lines).

Here we note that the Total Motion may at first damp down in an excellent manner yielding a good value for Half-Life;

ultimately, however, the Total Motion will undamp. If the missile has reached its destination before the Total Motion begins to undamp to a significant degree, then "all is well" in spite of the fact that the classical criterion for "dynamic stability" is not satisfied.

Although we have considered a special case, the argument and basic idea is sound in general and thus should be contained in any evaluation criteria for missile performance. This concept can be easily included by calculating the two values for Total Motion Half-Life which such a missile may have from Eq. (5), or by computing the Total Motion Double-Life from Eq. (11).

$$\text{TOTAL MOTION DOUBLE-LIFE} \equiv \frac{V t_2}{d} \quad (\text{caliber}) \quad (11)$$

where the time of double-life, t_2 is obtained from

$$2|\bar{\alpha}_0| = |K_N| e^{\lambda_N t_2} + |K_P| e^{\lambda_P t_2} \quad (12)$$

It should be clear from the above discussion that the indiscriminate use of the terms "Dynamic Instability" without consideration of the missile performance requirements should be carefully avoided. Constructive evaluation of the performance of "Dynamically Unstable" missiles may be presented by using the parameters of Total Motion Half-Life and Double-Life.

SOME NON-LINEAR CASES

The preceding discussion is based entirely on the Linear Theory and its assumptions. There are, however, a number of significant flight cases where the assumptions of the Linear Theory fail and thus the theory cannot be used or must be used with great care. Since these cases may not be generally known and since they seem to be occurring with greater frequency, it seems reasonable to enumerate them below.

Case 1. - Changing Velocity

Ballistic missiles in flight may not have constant velocity. When the dynamic stability criterion is evaluated as a function of Mach number, it is not unusual to find that many missiles have λ_N or $\lambda_P > 0$ over some range of Mach numbers. For example, many fin stabilized missiles and bodies of revolution are unstable at transonic speeds. Also some fin stabilized missiles are unstable at very high Mach numbers. Going strictly by the criterion, these missiles may be adjudged to be dynamically unstable and thus unacceptable. However, the time during which the missile flies in this critical region may be small, and thus the increase in yaw during that increment of time may be small, and may have negligible effect on the retardation and accuracy of the missile. In other words, local flight instabilities may not mean a bad missile. What is important is the integrated effect of missile dynamics over the entire flight of the missile. Dr. Kent, in Reference 7, has suggested such an approach. The seriousness of the local Mach number instability will clearly depend upon the magnitude of the instability, λ_N and λ_P , and the size of the nutation and precession arms, K_N and K_P at the point where the instability begins. Qualitative estimates of the effect can be obtained by using the linear aeroballistic theory.

Case 2. - Non-Linear Moments

Non-linearities in the aerodynamic coefficients can cause serious failures in prediction by the Linear Aeroballistic Theory. It has occurred in a number of cases in the recent past that missiles which were predicted to be dynamically stable were later found to be unstable due to a non-linear increase in the Magnus moment due to angle of attack. This instability was such that at small angles of attack the missiles were stable; however, at large angles

of attack the missiles went unstable. The achievement of stable or unstable flight simply depended on the initial launching conditions. For large cross-wind launchings and/or large muzzle blasts and bore clearance, unstable flights were obtained; whereas for small cross-wind effects and small initial launching conditions, good flights were obtained. It is clearly necessary, then, that the aerodynamic stability derivatives be obtained over the entire range of angle of attack in which the missile may be flying under realistic launching conditions. Reference 8 suggests that the linear aeroballistic theory might be modified to employ these non-linear data and thus yield a criterion for performance of a missile being acted upon by non-linear aerodynamic forces and moments systems. In the cases tested the Quasi-Linear Aeroballistic Theory has yielded results consistent with exact numerical integrations and actual performance.

Case 3. - Non-Linear Moments

Non-linearities in the Aerodynamic coefficients and particularly in the Magnus moment may go in the opposite direction as in the previous case. In other words, the linear criterion has predicted $\lambda_N \approx \lambda_C > 0$ for many bodies of revolution, bullets, shells, etc., at small angles of attack; however, these missiles have become dynamically stable at ~~large~~ values of the angle of attack. The non-linearities, here, were such as to make the missiles dynamically stable at angles of attack other than zero, yet dynamically unstable at angles of attack near zero. (The air drag resulting from this small yawing motion may not be important compared to the other drag sources on the projectile.)

Case 4. - Non-Linearities and Asymmetries

As indicated in Case 1, the seriousness of the dynamic stability depends upon the integrated effect over the entire flight of a missile, and thus upon the magnitude of the instability and the relative size of the nutation and precession arms. The random introduction of configurations asymmetries can lead to larger nutation and precession arms and thus larger complex angles of attack than normally encountered due to initial launching conditions, and thus the flight instabilities of Case 2 and Case 3 can be seriously affected and worsened by any random configurational asymmetries which might exist. One obvious example is the case where the rolling velocity of a missile and the nutation rate are equal and thus we have maximum amplification of the "TRIM" due to any configurational asymmetries which exist. This leads to large angles of attack for which instability of the type mentioned in Case 2 would lead to trouble, where otherwise the flight of the missile would be completely satisfactory.

Case 5. - Roll Lock-In

In addition to the non-linearities in the forces and moments considered in the linear theory, there may be forces and moments entirely left out of the theory which must be considered. One of these neglected moments is the roll moment due to complex angle of attack and missile roll orientation. This roll moment is such as to prohibit the canted fin missile from picking up its intended rolling velocity. This induced roll moment causes Roll Lock-In, which means that the rolling velocity and the yaw rate are the same. One effect of this phenomenon is to force the missile to remain in a condition of resonance instability. (Other situations are discussed in Reference 8.) This failure of the missile to roll in the designed manner clearly negates any evaluation of its performance based on assumed satisfactory roll and the linear theory. Missiles prone to Roll Lock-In may be evaluated using the methods of Reference 8.

Case 6.-Roll Speed-Up

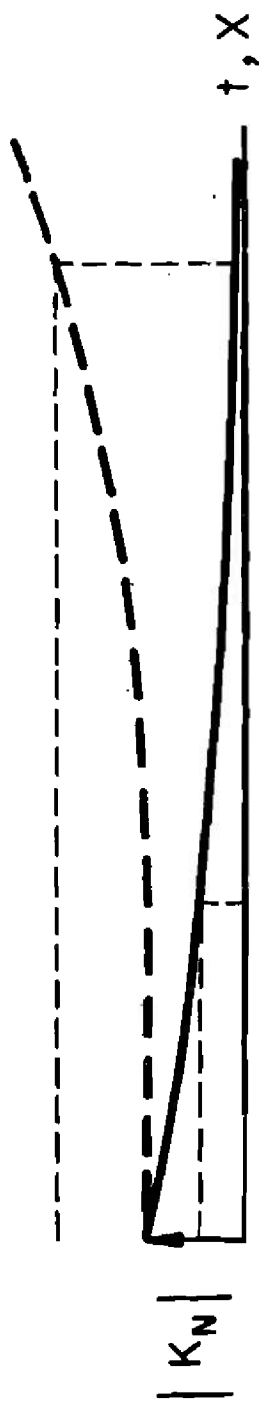
It has been observed that additional non-linear roll moments act on finned missiles in flight. One of the effects of these neglected moments is to cause a marked increase in the steady state rolling velocity of the missile as a function of angle of attack. This Roll Speed-up phenomenon can lead to poor flight performance. For example: for the designed roll rate, the missile might be dynamically stable; however, due to the roll speed-up phenomenon, the increase in rolling velocity with angle of attack may yield a Magnus type instability. A more critical case would be a combination of this roll speed-up with Case 2 (non-linear magnus instability). This type of instability is believed to be the key problem in the short ranges of mortar shells.

Case 7. - Catastrophic Yaw

In addition to the roll moments neglected in Cases 5 and 6, side force and side moments are also left out of the linear aeroballistic theory. This neglected side moment, when coupled with the roll lock-in of Case 5, can yield a magnus type non-linear dynamic instability. In Reference 8 a Modified Quasi-Linear Theory is suggested for approximately evaluating this phenomenon. The application of this theory to a few cases appears encouraging.

REFERENCES

1. Fowler, R. H., Gallop, E. G., Lock, C. N. H., and Richmond, H. W., The Aerodynamics of a Spinning Shell, Phil. Trans. Roy. Soc., London, 1920.
2. Nielson, K. L., and Synge, J. L., On the Motion of a Spinning Shell, Quarterly of Applied Mathematics, Vol. IV, No. 3, Oct., 1946.
3. Kelly, J. L., McShane, E. J., and Reno, F., Exterior Ballistics, Denver Press, 1953.
4. Nicolaides, J. D., On the Free Flight Motion of Missiles Having Slight Configurational Asymmetries, BRL Report No. 858, 1953, and I. A. S. Preprint No. 395, 1952.
5. Murphy, C. H., Data Reduction for the Free Flight Spark Ranges, BRL Report No. 900, 1954.
6. Nicolaides, J. D., and MacAllister, L. C., A Review of Aeroballistic Range Research on Winged and/or Finned Missiles, BuOrd Ballistic Technical Note No. 5, 1953.
7. Kent, R. H., Notes on a Theory of Spinning Shell, BRL Report 898, Feb., 1954.
Kent, R. H., Two-Score Years in Ordnance, Ballistic Research Laboratories, 1956.
8. Nicolaides, J. D., On the Flight of Ballistic Missiles, BuOrd Ballistic Technical Note No. 21, 13 Feb 1956.



$$[\text{HALF LIFE}]_{N,P} = \frac{V}{d \lambda_{N,P}} \ln(1/2) \quad (\text{calibers})$$

$$[\text{DOUBLE LIFE}]_{N,P} = \frac{V}{d \lambda_{N,P}} \ln(2) \quad (\text{calibers})$$



$$[\text{HALF LIFE}]_{\text{TOTAL}} = \frac{V t^{1/2}}{d}$$

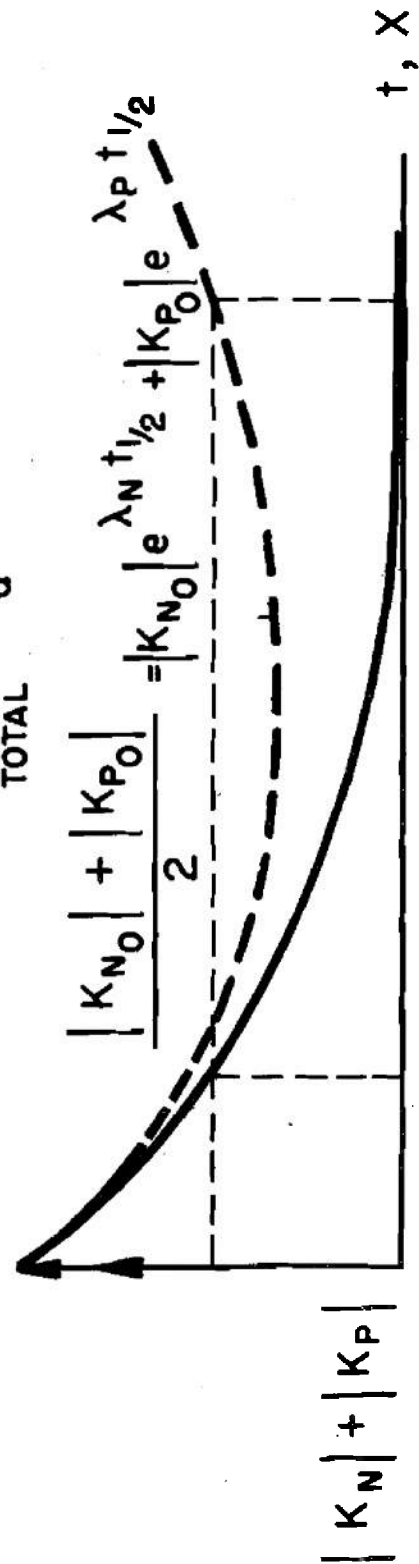


FIG. 1

AN APPLICATION OF AEROBALLISTICS RANGE TECHNIQUES
TO MODELS WITH DIGONAL ROTATIONAL SYMMETRY

G. H. Tidy

Miss M. E. Thomas

Canadian Armament Research and Development
Establishment

INTENTIONALLY LEFT BLANK.

An Application of Aeroballistics Range Techniques
to Models with Digonal Rotational Symmetry

By

G.R. Tidy & Miss M.E. Thomas
Canadian Armament Research and Development
Establishment

SUMMARY

A series of flat plate wings of triangular planform have been fired at Mach Numbers 1.5 and 2. A few trajectories have been measured. Preliminary manual reduction of the data is presented and the derived values of some aerodynamic stability coefficients are compared with linear theory. The possibility of more complete analysis and of application to airplane configurations are considered briefly.

INTRODUCTION

The history of the free flight range as a technique for aeroballistics measurements has been one of steady increase in range of applicability to aerodynamic problems. The measurement of characteristics of spinning shells and of winged missiles with trigonal or greater symmetry has been highly developed on the basis of linear theory. Recent extensions of reduction methods to handle certain non linear aerodynamic coefficients, within the same limits of symmetry, have greatly increased the scope of the technique.

The possibility of applying aeroballistics range methods to measurements on aerodynamic configurations falling outside this category of symmetry is of great interest. This particularly applies to airplane like shapes, as the development of modern supersonic aircraft have increased the need for experimentally determined dynamic stability derivatives.

Though such measurements can be obtained from rocket propelled telemetered vehicles and though wind tunnel dynamic balance methods have become available, there is no doubt that all possible techniques should be exploited. The aeroballistics range offers certain advantages as well, in that the atmosphere is uniform and non turbulent, and a fairly high Reynold's Number is obtainable.

With the expectation that extension of range methods to configurations of one and two plane symmetry would thus be of considerable value, we have begun at CARDE programmes of firings of aircraft models and of simple flat plate triangular wings. The latter program forms the subject of this report. This study was instituted to explore possible methods of data reduction for mirror symmetry and digonal rotational symmetry configurations, and in the event of a successful solution of the problem, to obtain experimental verification of some theoretical dynamic derivatives of wings alone, free of body interference.

This programme is by no means complete and important problems remain to be solved before a successful data analysis method can be assured. This paper should be considered as a progress report only, on a continuing programme of study.

Seventeen wings have been fired to the present date, of which 13 were of aspect ratio one, and the remainder aspect ratio 2. The majority have been fired at a Mach number of about 1.5, although two have been launched at Mach 2.

The models are of simple construction, as shown in figure 1. Centre of gravity adjustments were made by cutting out part of the rear, filling the slots with balsa wood, and attaching aluminum coverplates. The leading edges were wedge shaped, with a total wedge angle of about 50 degrees.

The thickness to root chord ratio was approximately 6 percent. Little effort was expended on surface finish since the main purpose of these preliminary rounds was to investigate analysis procedures, rather than to obtain accurate data. Schlieren photographs of a model in flight appear in figure 3.

Due to a launching problem which developed a large number of these rounds have been failures in that only very small deviations from a straight line trajectory developed. Insufficient measurement stations were employed for some of the earlier models, so that of the total number fired, trajectory measurements in sufficient detail have been obtained for three models of aspect ratio one at Mach 1.5, and for one at Mach 2. Analysis has been concentrated on two of these at Mach 1.5.

RANGE TECHNIQUE

Before further discussion of the present problem, a brief description of the instrumentation employed at CARDE is in order. The measurement apparatus differs from photographic ranges, and analysis methods must be tailored in some degree to suit our instrumentation.

The models are sabot launched into the range from a 5.9 inch calibre smooth bore gun fitted with a hi-lo device for pressure equalization. Light screens at 50' intervals measure velocity and deceleration. Plane sheets of paper, called "Yaw Cards", are surveyed into the range at 5 foot intervals along the firing line. Their normals are set parallel to the fore and aft axis of the range, very nearly that of the line of fire. Horizontal and vertical reference lines are surveyed on each sheet.

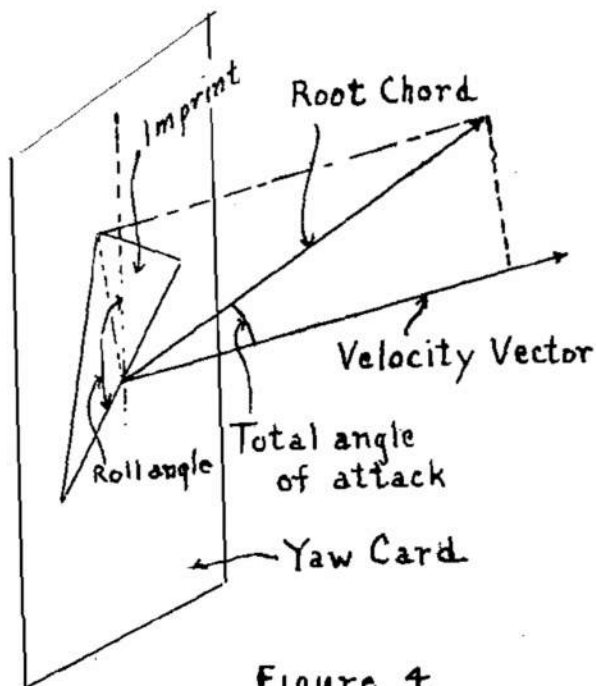


Figure 4.

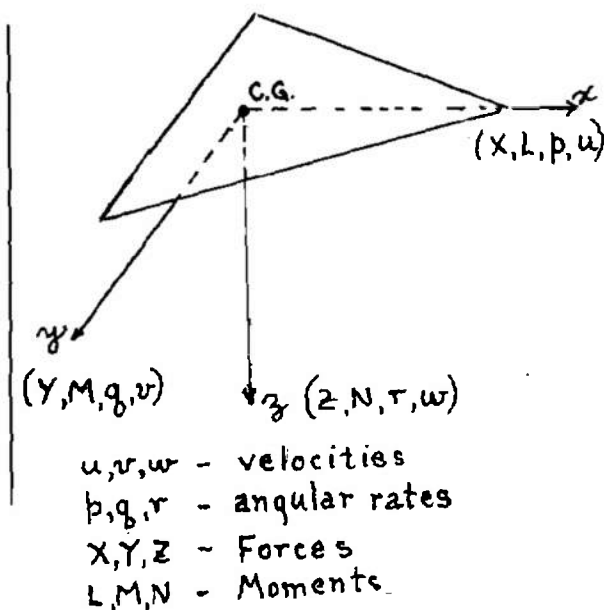


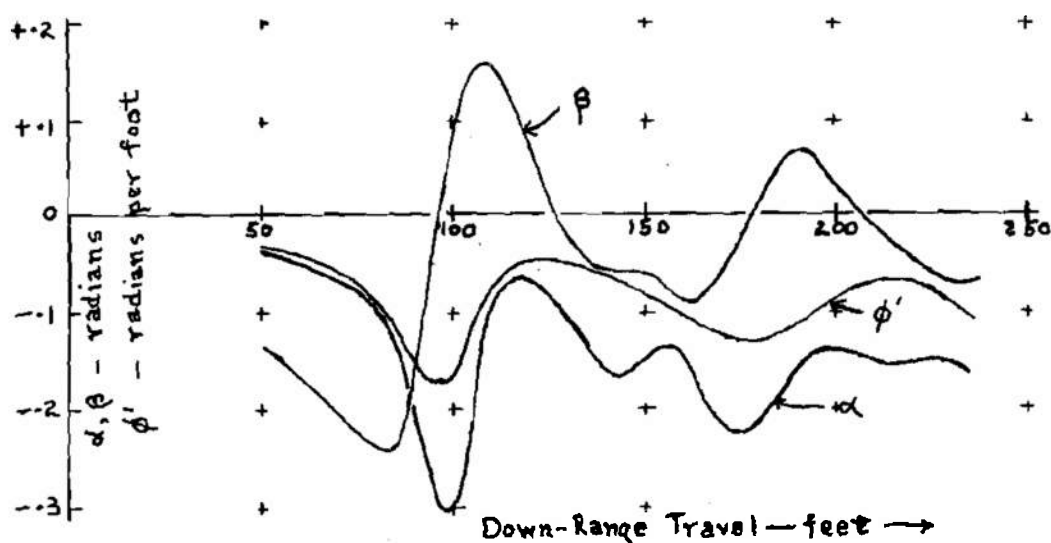
Figure 5

The model leaves a clear impression of the apex and the base on each card. (See Figure 4). The angle of roll is measured directly as the angle between the base line and the vertical. The distance from the centre of the base line to the apex imprint, divided by the root chord, is equal to the tangent of the total angle of attack. The total angle of attack can be resolved into angles of pitch and sideslip in body fixed coordinates, as used for this report. (See Figure 5). Since $\frac{y}{V}$, $\frac{w}{V}$ are the tangents of α, β the card imprints measure these velocity ratios directly. At angles of attack greater than ten degrees or so small projection corrections must be applied. Further corrections are required for rotation of the body axes during the interval between passage of the nose and of the base through the card. Independent measurements of angle of attack agree normally to within 1/10 degree and roll to about 1/4 degree.

The position of the centre of gravity may also be measured with respect to the survey references. It has not been possible as yet to set the references to better than 1/4 in. on a majority of the measurement stations, so that data on CG displacement are not reliable for accurate work.

DESCRIPTION OF TRAJECTORIES

The motion of the wings is interesting because of its ^unusual character. Figure 6 shows the history of roll rate and angles of attack and sideslip in body fixed axes.



This is a typical history for rounds launched at zero pitch. It is seen that a gradual increase in β occurs, until a small angle α is sufficient to produce an appreciable rolling moment. The roll rate induced is such as to increase angle of attack and produce a high acceleration in roll rate. The roll rate oscillates about a quite well defined constant value.

α and β also oscillate about an equilibrium value, though in general the steady α_0 and β_0 cannot be so accurately determined as the steady roll rate, because of the complex form of the oscillation. The equilibrium motion can be most simply described in terms of the total angular velocity vector which tends to line up with the displacement velocity .

The steady initial increase of β under equilibrium launch conditions is due to lack of strong restoring moments in sideslip, in fact it was because of the unknown effects of such low restoring moments that the models were originally launched with a low initial angular rates. Though our first half dozen models quite readily entered the rolling condition, it was gradually found that the initial condition of low angle of attack, yaw and roll rate could persist through most of the instrumented range, the resultant histories being useless for analysis. The launching problem which has thus arisen is being investigated in two ways of which one is to set the model at an initial angle of attack in the sabot. This method appears to stabilize the wing in a dutch roll like trajectory and appears promising for obtaining aerodynamic data near zero angles of attack. Initial angles of attack of up to 10 degrees, combined with yaw are to be tried in the near future. The other consists in attempting to induce the rolling trajectory by causing an initial yaw rate. The rolling trajectory appears of interest because measurements can then be made at high angles of attack.

THE EQUATIONS OF MOTION FOR A WING IN FREE FLIGHT

We may now pass on to a discussion of the equations of motion, in order to explain the observed trajectories and to form a mathematical basis for deriving aerodynamic coefficients.

$$\dot{\alpha} - q \frac{u}{V} + p\beta = \frac{\rho S V}{2m} \cdot \alpha \cdot C_{z\alpha}$$

$$\dot{\beta} + r \frac{u}{V} - p\alpha = \frac{\rho S V}{2m} \cdot \beta \cdot C_{y\beta}$$

$$\dot{p} + \frac{k_z^2 - k_y^2}{k_x^2} \cdot q r = \frac{\rho S}{2m} \cdot \frac{V^2}{c k_x^2} \left[C_{Lp} \cdot \alpha \beta + \frac{c}{2V} (C_{Lp} \cdot \dot{\beta} + C_{Lra} \cdot r \alpha) \right]$$

$$\dot{q} - \frac{k_z^2 - k_x^2}{k_y^2} \cdot p r = \frac{\rho S}{2m} \cdot \frac{V^2}{c k_y^2} \left[C_{Mq} \alpha + \frac{c}{2V} (C_{Mq} \cdot \dot{q} + C_{Ma} \cdot \dot{\alpha}) \right]$$

$$\dot{r} + \frac{k_y^2 - k_x^2}{k_z^2} \cdot p q = \frac{\rho S}{2m} \cdot \frac{V^2}{c k_z^2} \cdot C_{Nr} \beta$$

$$\alpha \equiv \frac{u}{V} ; \quad \beta \equiv \frac{v}{V} \quad \frac{u}{V} \approx 1 - \frac{1}{2}(\alpha^2 + \beta^2)$$

In the above equations α and β symbolize the tangents of angles of pitch and sideslip. The variation of $\frac{u}{V}$ with α and β , normally negligible, can be as great as 4% at peak angles of attack reached in these experiments. Only those aerodynamic coefficients were retained which were thought likely to be of measurable size in the preliminary work. All non linearities in coefficients except in rolling moment have been ignored. The quantities $C_{y\beta}$, C_{Nr} were retained in the hope they could be measured though they were expected to be very small. They are caused by differential friction and leading edge effects. The equations can be generalized if necessary to account for observable non linearities in the aerodynamics.

A simple steady state solution to the equations is possible by setting the time derivatives equal to zero and ignoring the small moments and forces due to sideslip.

$$C_{M\alpha} = -\phi_0'^2 \cdot \frac{2m}{\rho S} \cdot c(k_z^2 - k_x^2)$$

$$C_{z\alpha} = \frac{\beta_0 \phi_0'}{\alpha_0} \cdot \frac{2m}{\rho S}$$

$$C_{Lr\alpha} \alpha_0^2 + C_{Lp} + \frac{2}{c} C_{L\beta} \beta_0 \alpha_0 = 0$$

The equations are shown here in a form suitable for deriving aerodynamic coefficients. The prime sign refers to differentiation with distance along the trajectory. The solution for ϕ_0' shows two possible values, zero and one determined by $C_{M\alpha}$ as written. The zero roll rate condition is only neutrally stable, due to low restoring moments in sideslip.

It appears that if the rolling trajectory can be induced, useful data may be obtained from the steady state. The values of $C_{M\alpha}$ obtained to date appear reasonably accurate, but $C_{z\alpha}$ and C_{Lp} depend upon the measurement of β_0 which is usually small, therefore these data may not prove very reliable. The term $C_{Lr\alpha} \alpha_0^2$ is small compared with C_{Lp} at least for the wings tested to date and has been ignored.

SOLUTION OF THE GENERAL EQUATIONS

When a solution to the differential equations of motion is known, as in the case of shells or cruciform winged missiles, a first approximation to the stability derivatives can usually be found by measuring overall characteristics of the trajectories, such as frequencies and damping rates.

If required, a set of differential corrections may be obtained in some way such as the following. A Taylor's Series expansion of the equation of motion in α , β etc. is obtained in terms of increments of the stability derivatives and initial conditions. The zero order term of the Taylor's series is the solution of the differential equation using the approximate values of the aerodynamics. This term is computed for each station and compared with the observed values.

$$\begin{aligned}\alpha_o &= \alpha_o(A_1, \dots, I_1, \dots) \\ &= \alpha_c(A_{1o}, \dots, I_{1o}, \dots) + \left(\frac{\partial \alpha}{\partial A_1}\right)_o \Delta A_1 + \dots + \left(\frac{\partial \alpha}{\partial I_1}\right)_o \Delta I_1 + \dots \\ \alpha_o - \alpha_c &= \left(\frac{\partial \alpha}{\partial A_1}\right)_o \Delta A_1 + \dots + \left(\frac{\partial \alpha}{\partial I_1}\right)_o \Delta I_1 + \dots\end{aligned}$$

The difference between observation and computation equals the sum of the remainder of the Taylor series terms. A set of linear equation in the differential corrections is thus set up, and a least squares solution can be obtained.

When one turns to the present situation an analytic solution to the equations does not appear very likely. Pitch and yaw modes are intercoupled, even in the general motion at zero steady roll rate. Moreover non-linear terms such as rolling moment due to sideslip and non-linear dynamic terms are very important.

Therefore we plan to employ a machine solution of the differential equations. Some scheme of variation of initial conditions and stability derivatives to produce a set of differential corrections is contemplated, somewhat as in the method just discussed for the trigonal symmetry case, but as yet very little time has been available to investigate this phase of the analysis. The method requires an approximate set of values for the stability derivatives and initial conditions, and our analysis effort up to now has been spent on checking the suitability of one way of finding such approximations.

The method used is the obvious one of treating the differential equations of motion as linear equations in the stability derivatives. The functions of pitch, sideslip, roll, and their derivatives which occur in the differential equations may be measured at each station, from the trajectories. A set of linear equations in the stability derivatives, one for each measurement station is thus obtainable, and can be solved by least squares. The original equations contain the angular velocities q , r and their derivatives, and these quantities are not accurately measurable with the present CARDE instrumentation, because accurate data in lateral C.G. displacement are required for their determination. The equations must therefore be combined to eliminate q , and r , three equations resulting. We call these the pitch, yaw and roll equations, from the main aerodynamic derivatives contained in each.

THE EQUATION IN PITCH

The equation in pitch is shown below. The derivatives now expressed with respect to distance down range, rather than to time.

$$\frac{\rho S}{2m} \left[\left(-C_{Z\alpha} - \frac{1}{2k_y^2} C_{M\dot{\alpha}} - \frac{1}{2k_y^2} C_{M\ddot{\alpha}} \right) \alpha' - \frac{1}{2k_y^2} C_{M\dot{\phi}} \beta \phi' - \frac{1}{c k_y^2} C_{M\alpha} \alpha \left(1 - \frac{\alpha^2 + \beta^2}{2} \right) \right]$$

$$= -\alpha'' + \frac{k_z^2 - k_x^2}{k_y^2} \alpha \phi'^2 - \left(1 + \frac{k_z^2 - k_x^2}{k_y^2} \right) \beta \phi' - \beta \phi''$$

k_x etc: ratio of the radius of gyration (about x axis) to reference length

m = mass

ρ = air density

S = reference area (wing area)

c = " length (root chord)

The quantities on the right hand side contain no aerodynamic coefficients and may be lumped together as the "dynamic variable". If the dynamic variable can be derived together with the "dynamic factors" α , α' and so on, then at each measurement station we have a linear equation in $C_{M\alpha}$, the damping derivatives and the small quantity $C_{Y\beta}$. The group of equations for all stations are then solved by a least squares procedure.

EQUATION IN YAW

The equation in yaw appears below. It will be observed that for the flying wing, the largest aerodynamic derivative is $C_{z\alpha}$.

$$\frac{\rho S}{2m} \left[-\frac{k_y^2 - k_x^2}{k_z^2} \cdot C_{z\alpha} \cdot \alpha \phi' - \frac{1}{ck_z^2} \cdot C_{N\beta} \cdot \beta \right]$$
$$= \beta'' - \frac{k_y^2 - k_x^2}{k_z^2} \cdot \beta \phi'^2 - \alpha' \phi' \left(1 + \frac{k_y^2 - k_x^2}{k_z^2} \right) - \alpha \phi''$$

However if the method were applied to the general airplane motion, yawing and damping derivatives would be of significance and measurable by means of this equation.

EQUATION IN ROLL

The equation in roll is as follows.

$$\frac{\rho S}{2m} \left[\frac{1}{ck_x^2} \cdot C_{L\beta} \cdot \alpha \beta + \frac{1}{2k_x^2} C_{Lp} \cdot \phi' + \left(\frac{1}{2k_x^2} C_{Lr} + \frac{k_z^2 - k_y^2}{k_x^2} \cdot C_{z\alpha} \right) \cdot \alpha (\alpha \phi' - \beta') \right]$$
$$= \phi'' + \frac{k_z^2 - k_y^2}{k_x^2} \cdot (\alpha' + \beta \phi') (\alpha \phi' - \beta')$$

From this equation one can derive the coefficient of rolling moment due to sideslip, and rolling moment due to roll rate.

MEASUREMENT OF FIRST & SECOND DERIVATIVES

First and second derivatives, and the functions α , β and ϕ themselves, have been calculated at points midway between stations by expressing them in terms of first, second and third differences in the observed data. Measurement errors are thus carried down to the dynamic variables of the differential equations. The accumulation of errors due to differencing is probably the chief reason why this method yields only approximate results. Application of data smoothing methods would result in partial elimination of significant variation in the trajectory functions, with the present number of data points per oscillation wave length.

LIMITATIONS OF THE METHOD

One of the limitations of the direct application of this method of analysis is that indeterminate values of aerodynamic derivatives are liable to be obtained, if the derivatives have dynamic factors which are nearly proportional to one another. For instance the factors of C_{Lp} and $C_{L\dot{\alpha}}$ in the roll equation have proven to be proportional for the rounds measured to date. Fortunately here the quantity $C_{L\dot{\alpha}} \alpha (\alpha \phi' - \phi')$ turns out to be small compared with $C_{Lp} \phi'$ and $C_{2\alpha}$ can be obtained by some other means, so that C_{Lp} at least is derivable.

RESULTS

This approximate analysis has been applied to two rounds of aspect ratio one, at approximately Mach 1.45. One round was of aluminum, the other of steel, the ratio of weights about 2 to 1.

Both assumed the steady state roll mode, the lighter model rotating at about 0.14 rad/ft as compared with 0.098 rad/ft. for the steel wing.

Derivatives calculated on the basis of flat plate linear theory for zero angle of attack and sideslip, using the methods of NACA Report 971 by Malvestuto and Margolis, are presented for comparison (see table I).

PITCHING MOMENT & LIFT DUE TO ANGLE OF ATTACK

The internal agreement between dynamic and steady state measurements is 2% in both cases for pitching moment. It had been intended to vary $C_{M\alpha}$ by changing CG position in order to find $C_{z\alpha}$ and the centre of pressure but all rounds with forward CG were failures. These wings had CG's at 60.4 and 61.4% root chord, - too near one another to give good results for cp position. The cp as calculated is 65% root chord but a change of one percent in both rounds can alter the cp to 67%. On this basis the common $C_{z\alpha}$ for both rounds is as shown. The result is somewhat high compared with linear theory. The values of $C_{z\alpha}$ calculated from the yaw equation show variations which may be due to omission of terms in the equation for asymmetry moments caused by model roughness and errors in construction. The steady state values of $C_{z\alpha}$ are of poor dependability since the steady sideslip angle is small compared with its variation.

ROLLING MOMENT DUE TO YAW

There is no steady state solution for this quantity. The roll equation has been solved, by using the linear theory value for $C_{z\alpha}$, appearing in the equation.

S - From Steady State Equations D - From Dynamic Equations

Stability Derivative AR = 1, M = 1.45	Linear Theory Flat Plate	Wing 4 - 2		Wing 5 - 3		Experiment. Average
		S	D	S	D	
$C_{m\alpha}$	-	-0.103	-0.103 \pm 2%	-0.123	-0.126	
$C_{Z\alpha}$	From Moments	-	-1.90	-	-1.88	-1.89
	From yaw equation	-2.25	-	-1.6	-	
$C_{L\theta\alpha}$	-0.48	-	-0.49 \pm 4%	-	-0.37	-0.43
C_{Lp}	-0.052	-0.037	-0.033 \pm 20%	-0.02	-0.032	-0.32
$C_{Z\alpha} + \frac{1}{2k_y}(C_{m\dot{y}} + C_{n\dot{z}})$	-8.7	-	\pm 4	-	-18	-11
$\frac{1}{2k_y} C_{m\dot{y}}$	-4.7	-	\pm 0.8	-	-9	-5

TABLE I - STABILITY DERIVATIVES

The resulting term is so small that the inaccuracy of this value will not appreciably affect the result. The individual rounds differ from the average by about 14% and the average is 10% lower than linear theory would indicate.

DAMPING COEFFICIENTS IN PITCH

A large variation is evident. Even signs are wrong in some cases. One possible reason for this result is that the dynamic factor multiplying $(C_{2\alpha} + \frac{1}{2}k_y^2(C_{mq} + C_{m\dot{q}}))$ is nearly 180° out of phase with and proportional to the dynamic factor of C_{mq} in the pitch equation, over most of the trajectories. The results may therefore be somewhat indeterminate and the coefficients subject to considerable error.

DAMPING IN ROLL

The dynamic damping in roll values agree fairly well with each other and with theory. However the steady state results are unreliable, again due to the difficulty of measuring steady state sideslip.

No correlation of the sideslip dynamic variable with β has been found, indicating that the effects of yawing moment due to sideslip are less than experimental errors.

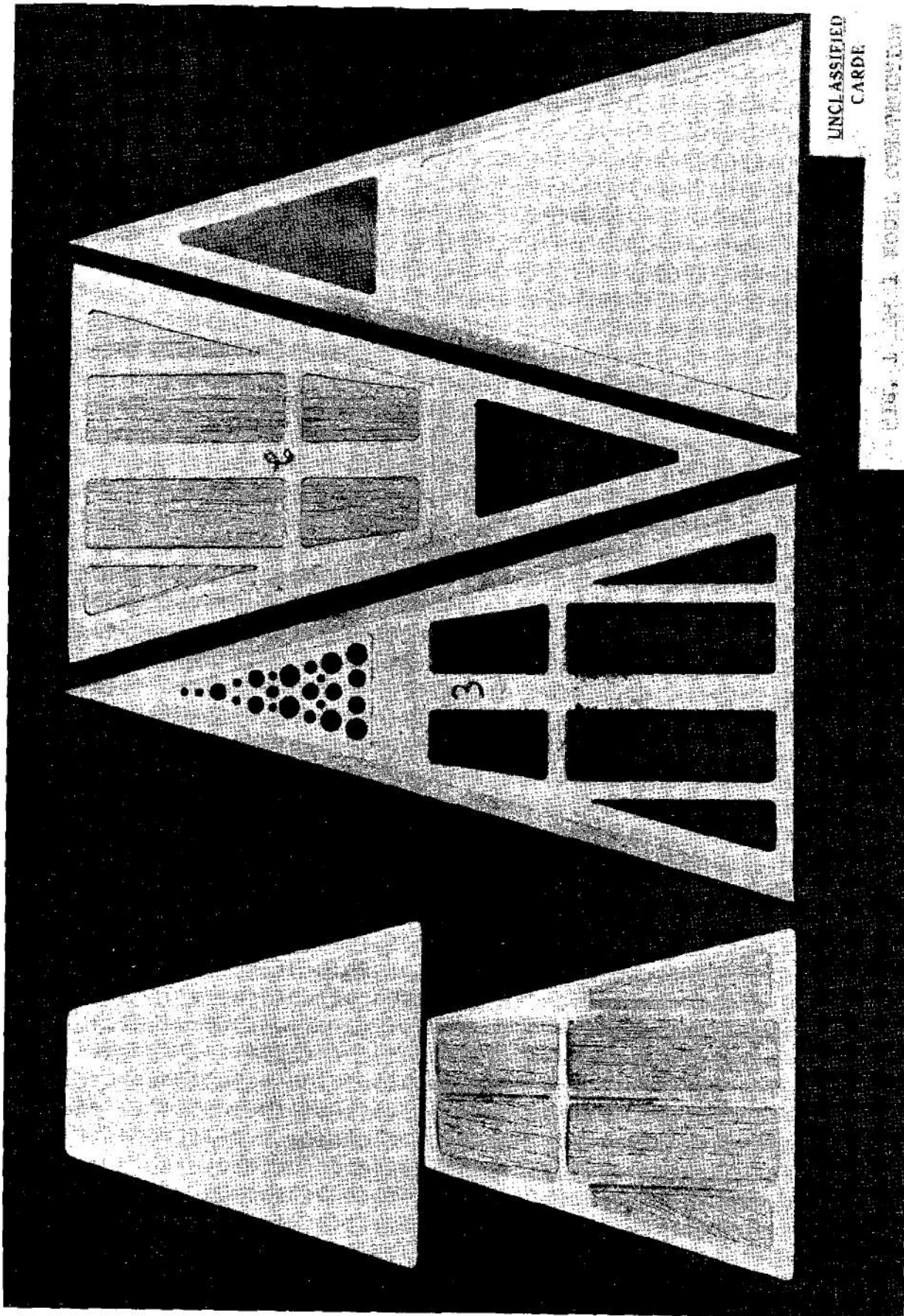
CONCLUSIONS

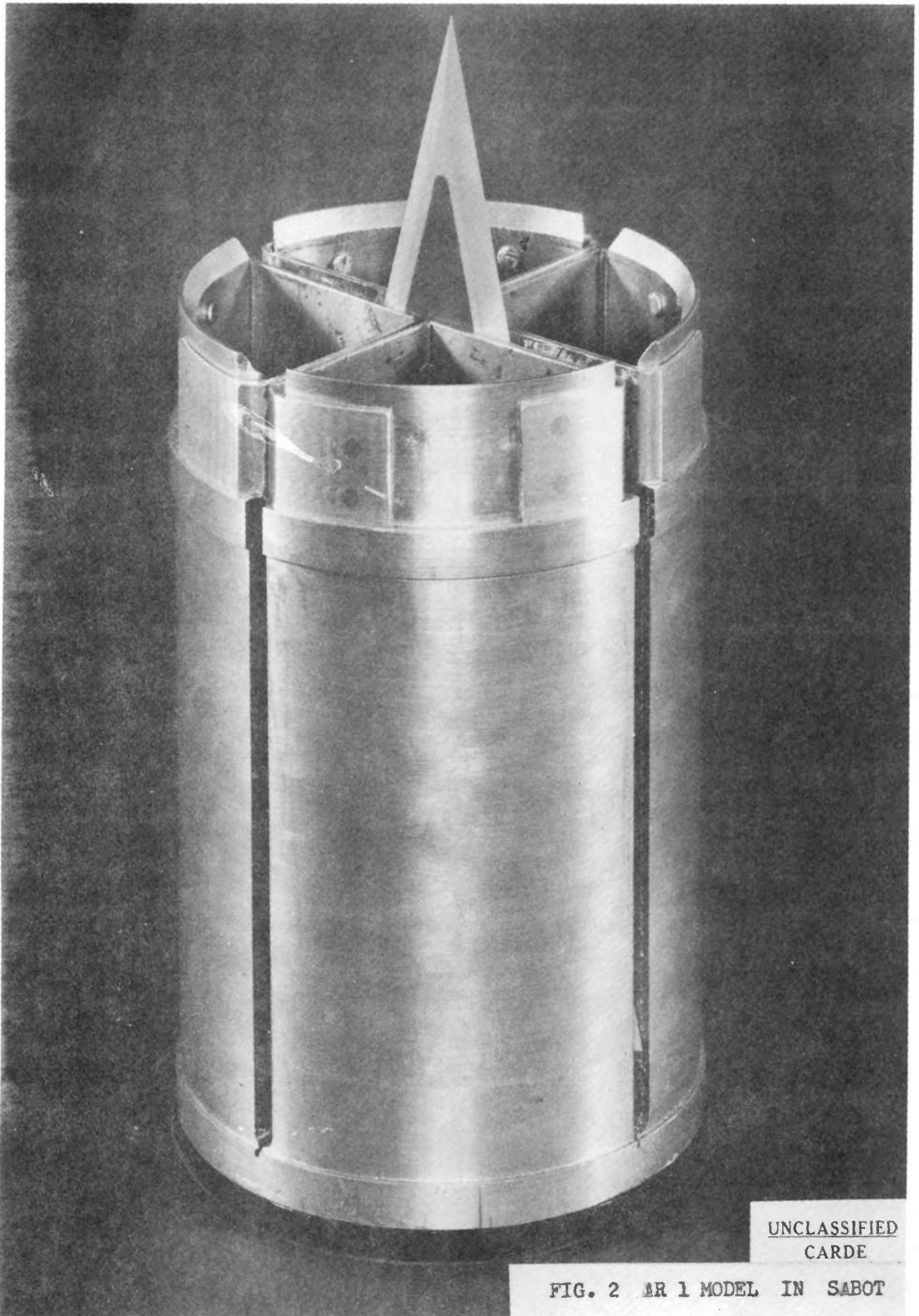
The quantity of data obtained to date is too scanty to determine the accuracy of the approximate results. In any case the final test must be the application of the data to a computer solution for differential coefficients. However the results at least for the larger stability derivatives appear promising enough to warrant further work on the problem.

A difficulty has arisen in the indeterminate solutions for damping derivatives in pitch, which will apply to any machine solution as well. One possible means of overcoming this indeterminacy is to fire the rounds with high initial angles of attack and the minimum of sideslip angle and rate, so

that the early part of the trajectory will consist of oscillations in pitch with low roll rate. The damping term in rate of change of angle of attack will then be predominant.

The present results do not permit one to predict with confidence whether the analysis method will be applicable to airplane-like, low roll rate trajectories. This type of trajectory will produce lower peak amplitudes in total angle of attack resulting in higher percentage errors associated with the dynamic variables. However the approximate stability derivatives so derived may still be sufficiently accurate for application to differential correction methods. It is hoped that further tests with emphasis on trajectories with low roll rate, will help to clarify this situation.

[illegible]



UNCLASSIFIED
CARDE

FIG. 2 AR 1 MODEL IN SABOT

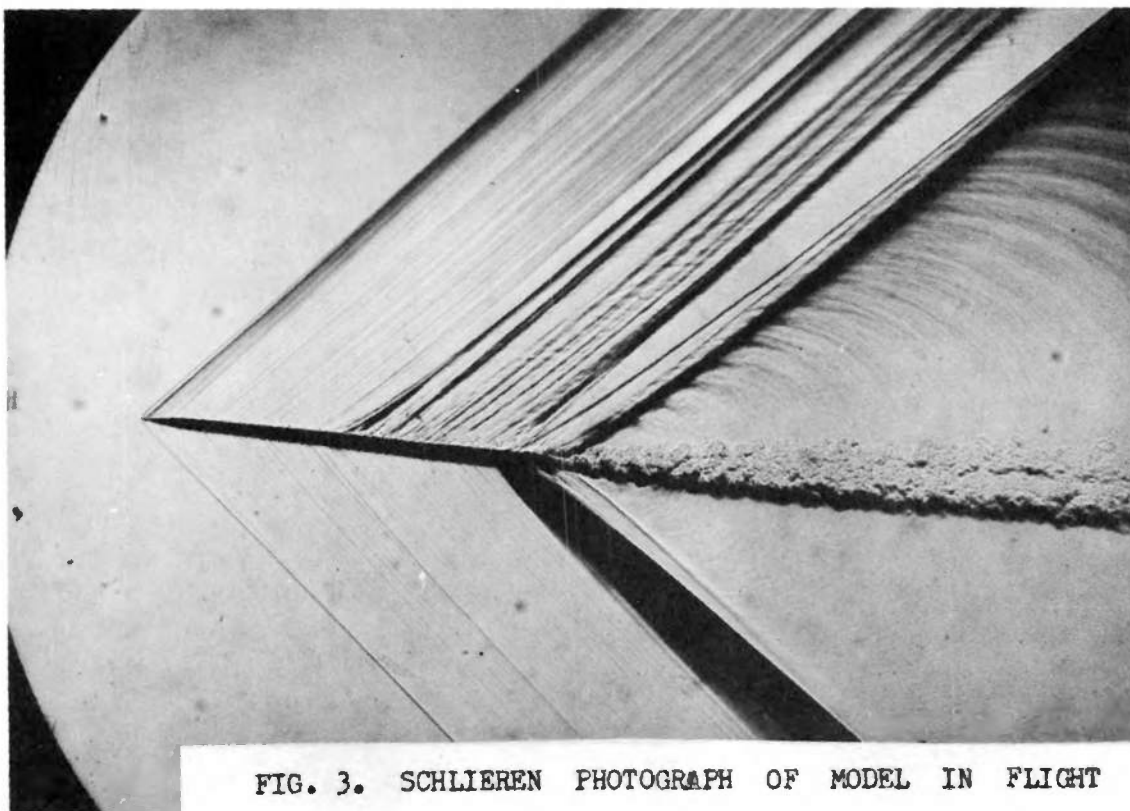
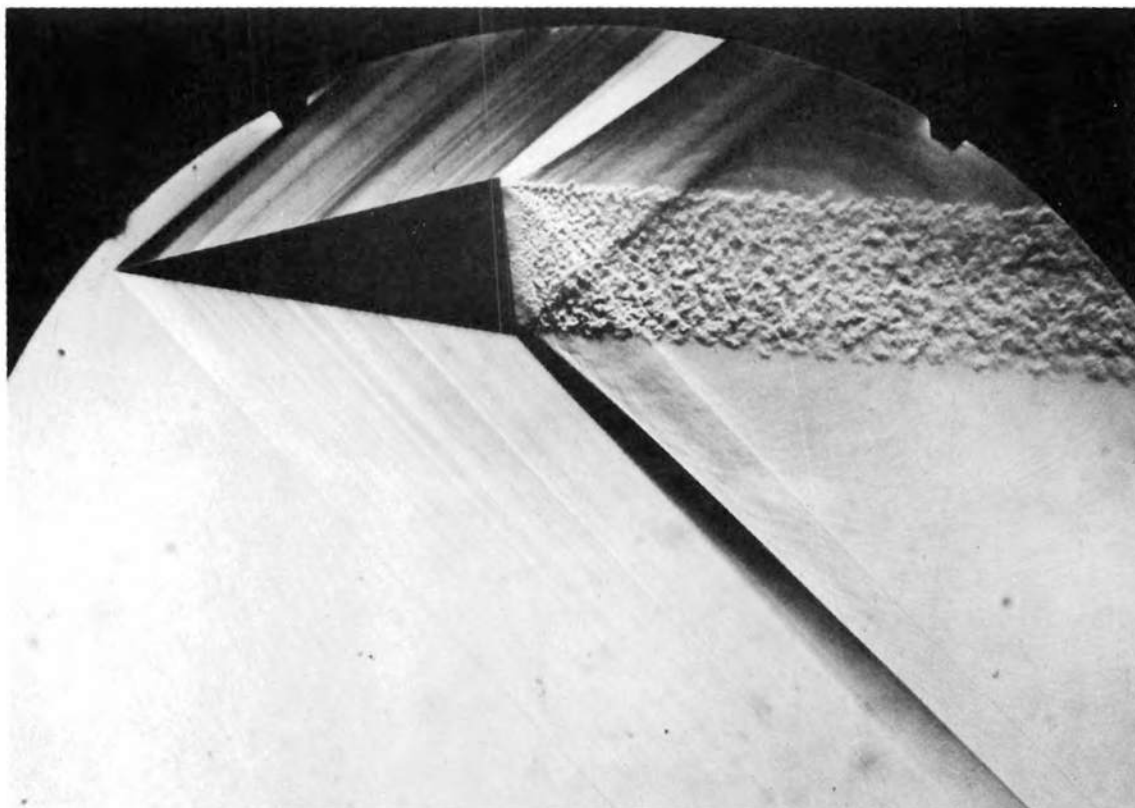


FIG. 3. SCHLIEREN PHOTOGRAPH OF MODEL IN FLIGHT

SABOTS USED AT THE THOMPSON AEROBALLISTICS LABORATORY

Wallace H. Allan

U. S. Naval Ordnance Test Station
China Lake, California

INTENTIONALLY LEFT BLANK.

SABOTS USED AT THE THOMPSON AEROBALLISTICS LABORATORY

Wallace H. Allan

U. S. Naval Ordnance Test Station

INTRODUCTION

Aeroballistic range work requires some means for projecting the missile through the range; the accepted standard for this work is a gun. The use of a gun entails the use of a sabot in almost all cases, the principal exceptions being projectiles designed for guns. The sabot is usually a piston that holds and pushes the missile and seals the bore against the propelling gases. Sabots used at the Thompson Aeroballistics Laboratory fall into two classes: those intended for smooth-bore guns, usually referred to as finner sabots, and those intended for rifled guns, referred to as spinner sabots. These two classes fall into two more classifications: those that "break apart" after leaving the gun, and those that "follow thru" the range after the missile; and, of course, there are those that do a little bit of both.

The Thompson Aeroballistics Laboratory has no systematic program of sabot development. Years ago we did, principally to give us a feeling for the problems involved. Now, each missile and sabot combination is treated as a separate problem. The sabot is designed on the basis of past experience and the first attempt at the design is usually fired through the Laboratory for data, although an outdoor range is available for sabot development work. If the first firings are successful, then the program can be completed in the minimum of time and expense. If the firing is unsuccessful then the problem is reappraised, the sabot redesigned, the laboratory repaired, and the program resumed. The cost of sabots and models, firing time, and the time scale of the program lead us to believe that this is the inexpensive way to conduct

our programs. Damage due to errant rounds has been small compared to the cost of good rounds that would have been lost under a more conservative program.

SPINNER SABOTS

Let us first consider spinning projectiles. We have available the following twist barrels: 40mm 1-30 twist; 3"/50 1-10, 1-15, 1-20, 1-25, and 1-32 twist; 3 7/10 1-22 twist; 5"/54 1-10, and 1-25 twist. The 3" diameter spinning projectile is considered optimum for our range. 40mm projectiles are usually too short for accurate orientation readings and the 5" projectiles react so slowly to external forces that only limited portions of the damping arms can be observed.

Many of the spinning projectiles fired through our laboratory do not require sabots since they are designed for gun launching. For instance, Fig. 1 is a picture of a full-scale 5"/54 projectile and two subcaliber models of this projectile. The models can be fired from the 3"/50 and 40mm guns, and of course the 5" projectile is fired from the standard 5"/54 gun. In the case of the 40mm model, our only available barrel for the 40mm gun did not have enough twist to stabilize the model by spin; therefore, a subcaliber sabot was designed to allow firing the 40mm model from a 3" 1-10 twist barrel giving the barrel an effective twist of 1-18. This is a very effective way of obtaining odd twist ratios not readily available in our stock of gun barrels. Figure 2 illustrates this type of subcaliber sabot. This particular sabot consists of a driving piston containing a pre-engraved rotating band and an expanded foam-plastic body (styrofoam) to support the round before firing. The base of the missile is fitted with pins used to observe by photographic means the spin rate of the missile. These pins fit into holes in the piston portion of the sabot, and the torque to spin the missile is applied through the pins. Not all of the torque is applied through the pins, since the coefficient of friction between the base of the missile and the piston is almost sufficient to drive the missile

in torque in most cases. Spin and air drag separates the foam plastic and piston from the missile after leaving the gun. This type of sabot is also used when high velocity firings are required, since many bore size rocket models are very heavy, limiting the maximum velocity at which they can be fired. This type of sabot has been useful but is not 100% reliable. Often missiles are mallaunched with this sabot. Our next attempt at this type of sabot will eliminate the foam plastic and replace it with nylon plastic. Subcaliber sabots are frequently driven at excess spin rates. Quite often the copper obturating band or the aluminum or copper rotating bands burst under the high spin rates. In this case the sabot parts are caught by a blast shield in front of the gun. Figure 3 illustrates this shield. The large circle of impact marks was made by the driving bands fired from the 3" 1-10 twist barrel. The circle diameter is independent of velocity but depends mainly upon the twist ratio of the gun. If a sabot is apt to break apart because of high spin, then the driving band is deliberately weakened by partially cutting the rotating band. Care has to be taken that the driving pins on the base of the missile are not damaged by the breaking of rotating bands. The inner portion of the sabot is usually made of 75 ST aluminum and it usually "follows thru" the laboratory after the missile. Figure 4 illustrates another sabot of this form. This particular sabot was designed by the Aerojet-General Corporation. In this case the missile is held to the piston by three pins that fly out under centrifugal force, and the barrel prevents the pins from withdrawing until the missile leaves the barrel. The front support ring riding on the ogive is cut almost in half so that centrifugal force will break it apart. In fact, there is only .020 of an inch of metal on the inside diameter holding it together. The sabot is blown from the missile by trapping propelling gases in a chamber between the sabot and missile.

An earlier version of this sabot had a copper obturating ring located in the forward groove and the front support ring was held together on the outside diameter by $1/16$ inch of metal. Figure 5 is a synchro-ballistic picture of the earlier version of this sabot in action. First we see that the front support did not break apart. Next the forward obturating ring expanded under centrifugal force to a point where it was not discarded when the sabot blew back. Corrections made to this combination were simple and effective. The forward seal was discarded completely and the slot in the front support was cut to only .020 of an inch. The sabot worked fairly well then.

Bore-diameter-spinning rocket models generally need a sabot to impart the correct spin to the missile. Figure 6 illustrates a piston sabot we have used for many years. In this sabot the center piston fits in a cylindrical hole in the base of the round. A small hole through the sabot permits pressure to build up in a gas chamber located at the end of the piston. Upon leaving the barrel the gas reacts against the piston and blows the sabot free of the missile. The small gas hole in the sabot is drilled through a steel insert to prevent gas erosion from enlarging and filling the gas chamber with molten metal which tends to jam the piston in the hole. The driving torque is applied from the rotating band through the spin pins that are used for spin measurements. Copper rotating bands are preferred because of their very effective obturating actions; however, the spin rates are usually too high for copper so that 75 ST aluminum rotating bands are used with a small copper or nylon obturating band. Another version of this type of sabot is illustrated in Fig. 7. Here spherical balls are used to drive the missile in spin and then upon leaving the barrel centrifugal force acts upon the balls wedging the round and sabot apart. The balls are caught by the blast shield in front of the gun. The principal advantage of this sabot over the earlier style is that a center pin may be used in the tail of the missile without interference with the blow-off system.

This type of sabot is less susceptible to sticking than the piston sabots. A variation of this system is displayed in Fig. 8. This system uses discs instead of balls. There seems to be no essential difference between the two schemes in performance. Figure 9 shows a yaw-inducing spinner sabot. Yaw can be induced in these sabots by stepping the base. The mass eccentricity and the reaction of the muzzle blast on the step both serve to induce yaw.

In spinner sabots one major consideration is whether a pre-engraved rotating band should be used. I personally prefer this style, but it is expensive to produce. At high pressures there seems to be no appreciable difference between the pre-engraved and engraving style of sabot; however, at low pressures the action of the engraving type can be erratic and in many cases the projectile has stuck in the barrel only partially engraved. One major problem which has arisen in the use of engraving-type sabots is the separation of the sabot and the missile in the barrel. This is caused by the sabot accelerating the missile for a very short distance, contacting the engraving band, then stopping for an instant while the pressure builds up to the engraving pressure. The projectile during this instant separates from the sabot and later when the sabot contacts the missile again it will frequently damage the base of the projectile or the spin pins. An effective way of eliminating this difficulty is to pin the missile and sabot together as previously illustrated. Our usual way of overcoming this difficulty is to take great care that the sabot is properly seated in the barrel with no clearance between the engraving band and the lands of the barrel. Figure 10 illustrates another form of spinner sabot. This sabot was designed by Aerojet-General Corporation. The missile fits the 3" gun and the pre-engraved band on the missile fits the gun rifling. This rotating band would not take gun accelerations unassisted. The sabot actually furnishes the main driving torque through its frictional contact with the base. The sabot is built so that any slippage between the

sabot and the missile does not harm the spin pins. This sabot and model combination was quite successful.

FINNER SABOTS

Let us now consider finned projectiles. We have available the following smooth-bore barrels: 1"1-208, 42mm, 3"1-48, 3"2-65, 5"1-37, and 8"25-53. The 1"1 and 42mm guns are considered undersize for our range. Most missiles are fired through the 3" or 5" gun, with the 8" gun rapidly becoming very popular.

We have used a standard style of "follow-thru" sabot for years. Figure 11 shows the general configuration. In this sabot the missile is held by fingers in correct alignment with the bore before firing and under acceleration. The sabot is very stable in its flight and usually is more accurate than the missile. The holes in the tail of the sabot not only serve to lighten the tail but they prevent the tail from shearing in the bore under the expansion due to chamber pressure. The obturating ring is quite far forward in this design. Yaw can be induced with this sabot by leaving a few of the gas-relief holes located near the tail undrilled. The muzzle pressure can then give the tail a kick as the missile leaves the muzzle. This sabot is somewhat expensive to make but very reliable in action in guns of 40mm and 3". 5" sabots in this design have failed quite badly. The after tail section usually blows up completely. If there is a complete blowup, the rocket model is usually launched fairly well; but many times the blowup is not complete and the missile is mallaunched. Our first attempt at curing this mallaunch was a completely new sabot called the slug-styrofoam follow-thru. Figure 12 illustrates this sabot. This sabot is the simplest we have ever made. The slug is usually made of aluminum for use in 5" guns and micarta-aluminum for the 8" gun. The missile sits on its tail under acceleration and the styrofoam is used only to support the missile in bore alignment before firing. The styrofoam blows apart upon leaving the muzzle

and the slug separates from the missile because of its greater aerodynamic drag. This sabot has launched some missiles very well and it has apparently failed in other cases. At the present time we hesitate to recommend it. Figure 13 shows a slug follow-thru which has worked quite successfully in the case of a missile which failed to fly well with the slug-styrofoam sabot. This sabot is essentially the front half of the original follow-thru. It looks quite a bit out of a balance but remember that the sabot is of 8" diameter and the model only weighs 4.5 lbs.

The original break-apart sabot used in our laboratory is shown in Fig. 14. This style of "break apart" has been used at up to 3" diameter, but has caused barrel scoring at velocities of over Mach 3. This sabot is expensive to make and it is moderately heavy when made of aluminum. Figure 15 is an example of a break-apart sabot for a cone fired from the 40mm gun. This sabot was successful at Mach 3. Figure 16 shows a break-apart sabot for a rather odd object. The sabot is for a 5" gun and is made of nylon with a rubber obturating disc. The sabot is sawed almost completely into quarters and just a few tabs are left to hold it together during the loading process. This particular design feature was shown to us by Dr. Bull of CARDE. This sabot has been quite successful. Figure 17 shows another variation of this style. This sabot is for the 3" gun. Figure 18 illustrates the design in which a base plate was felt to be necessary. This is a sabot for a 5" gun and the ball is a solid 2.5-inch-diameter sphere made of steel. The spherical surface prevents the use of a sabot which completely breaks apart, since under acceleration the spherical surface would tend to wedge the sabot quarters in the barrel. This sabot breaks into four quarters and a base plate. We were able to drive these balls at up to Mach 5 with this type of sabot. The acceleration was so great that an early model of this sabot failed because the ball was driven completely through the aluminum base of the sabot during the initial acceleration phase.

Figure 19 illustrates a rather unusual sabot for an unusual model. The model has a tungsten head and a body consisting of aluminum tubing .010 of an inch thick. The body is quite fragile, making it necessary to push the model at the base of the tungsten head. The sabot therefore has a rather long rod in order to push the missile. Unfortunately the missile has a rather high drag so that the sabot cannot be expected to pull free; therefore, the sabot was pulled from the missile by a device that is called the sabot stopper. Figure 20 shows this device. A tapered steel tube is fastened onto a muzzle attachment that aligns the tube with the bore. Clearance between the muzzle and the entrance to the tube is maintained so that gases in the barrel may escape. The tapered tube is smaller than the sabot diameter so the sabot is retarded passing through the tube. The missile is of a still smaller diameter and passes through the "sabot stopper" unhindered, the retardation of the sabot separating it from the missile. In this particular case no attempt was made to capture the sabot but only to slow it down. In other cases, complete captures have been made at velocities of the order of 1000 ft/sec. The steel tube is given a very low velocity during the retardation process and it pulls free of the gun. The sabot in this particular case proved to fly stably through the range. Another interesting sabot is illustrated in Fig. 21. This sabot is driven in spin by a turbine drive. Escaping gases react to impart spin to the sabot. Mr. Hitchcock of APG wrote a paper on this technique with reference to imparting spin to a mortar shell. We fired four models of this type of sabot and found that we could impart slow spin to the missile. Twist rates of 1-200 were achieved in the case of the many-fluted model. The slugs were never adapted to any actual model studies by us.

We use the 3", 5", and 8" smooth-bore guns often in our work. The 5" is the favorite gun because the missiles are about optimum for accurate work in our laboratory. The 8" gun is used particularly for problems involving models

that are structurally weak. The great length of the barrel permits low accelerations. The 5" and especially the 8" gun are regarded as one of our most important tools allowing us to fire programs considered impractical elsewhere. Sabot design is considered an important factor in the successful completion of a program. Unfortunately, the design of a sabot is still in the stages of an art rather than a science because the designer has to work with small numbers of widely varying missile configurations usually under pressure to make the first round fly properly.

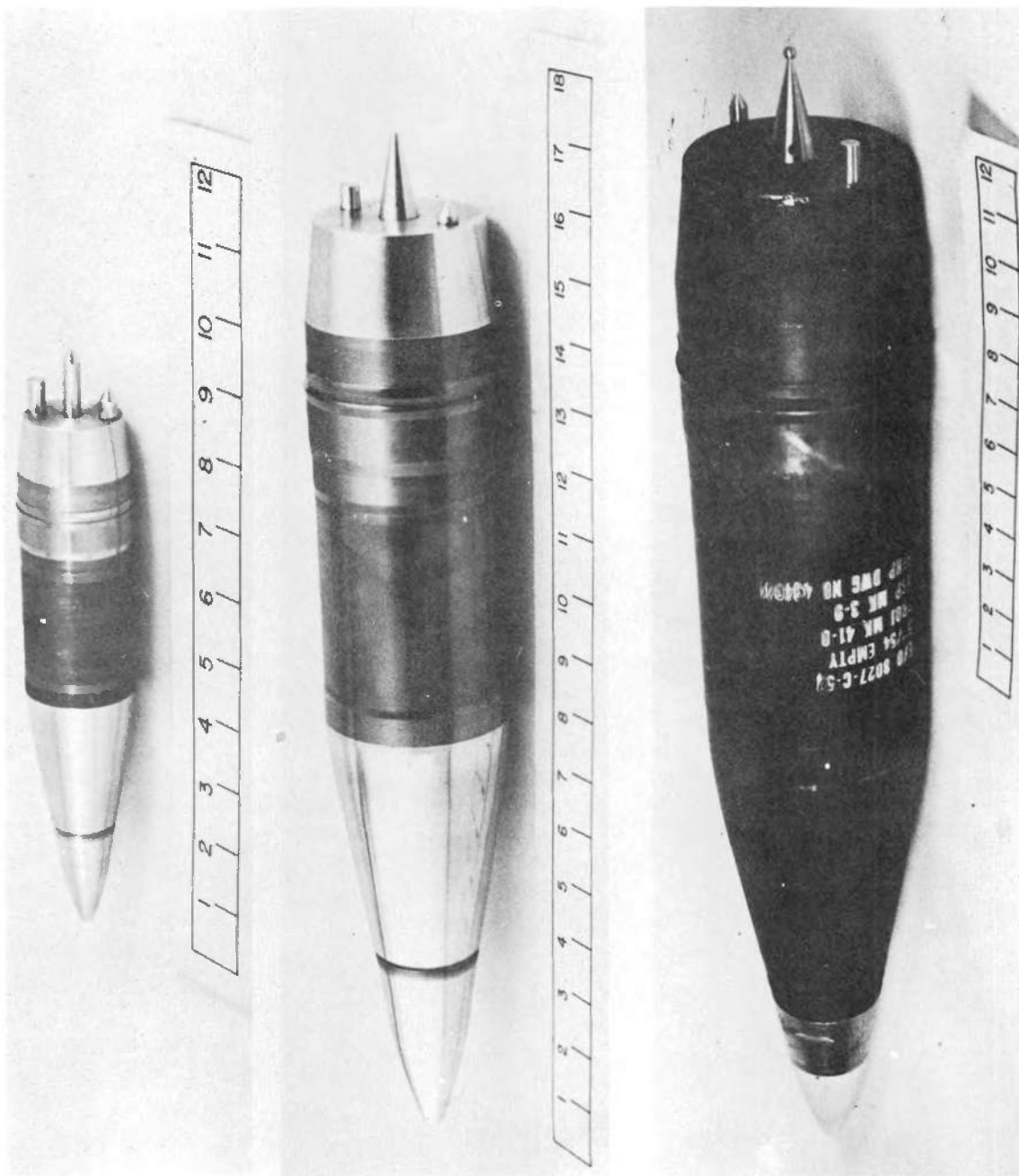


FIG. 1. 40mm AND 3-INCH MODELS, AND 5-INCH PROJECTILE MK 41 MOD 0

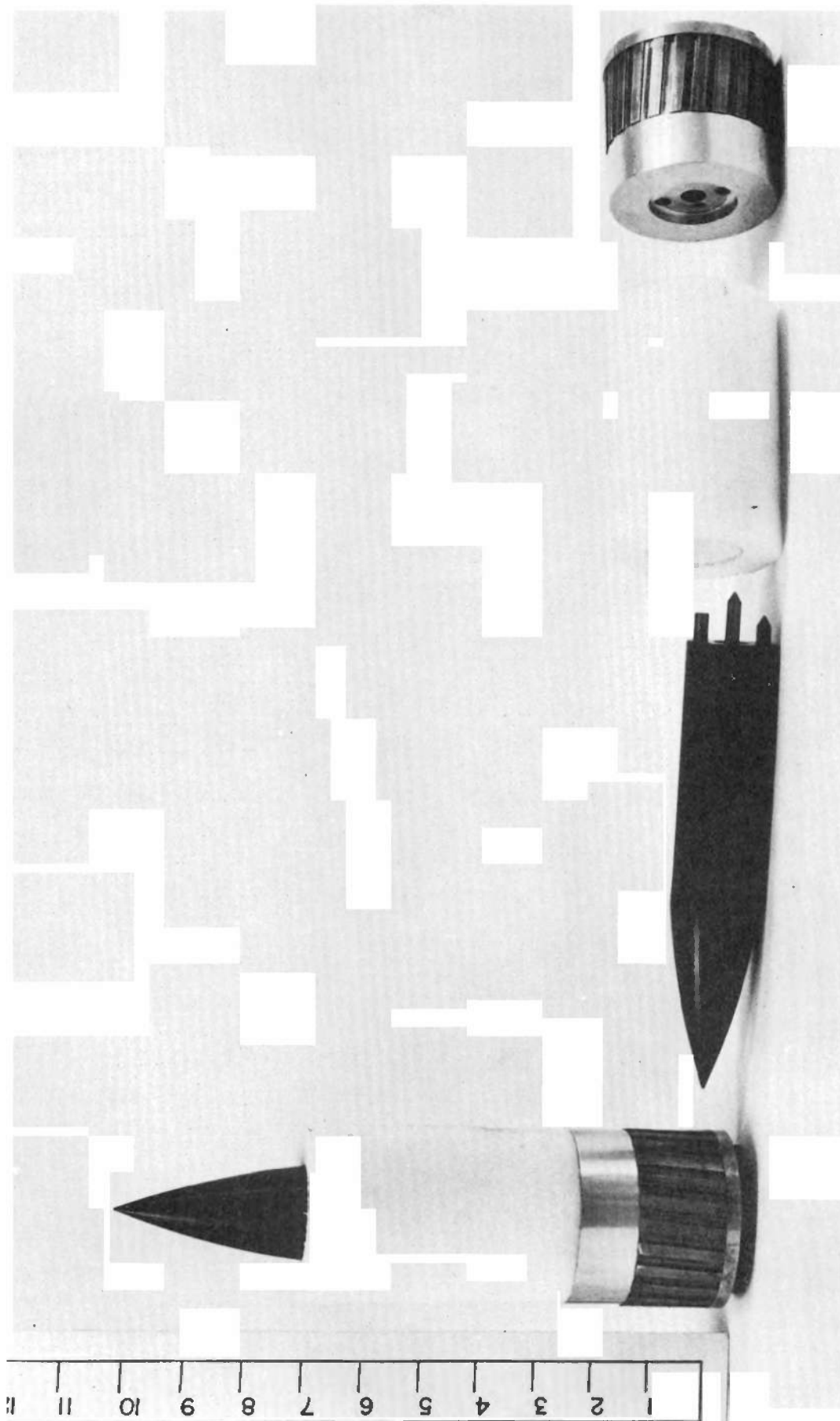


FIG. 2. 3-INCH SUBCALIBER SABOT FOR 40mm MODEL

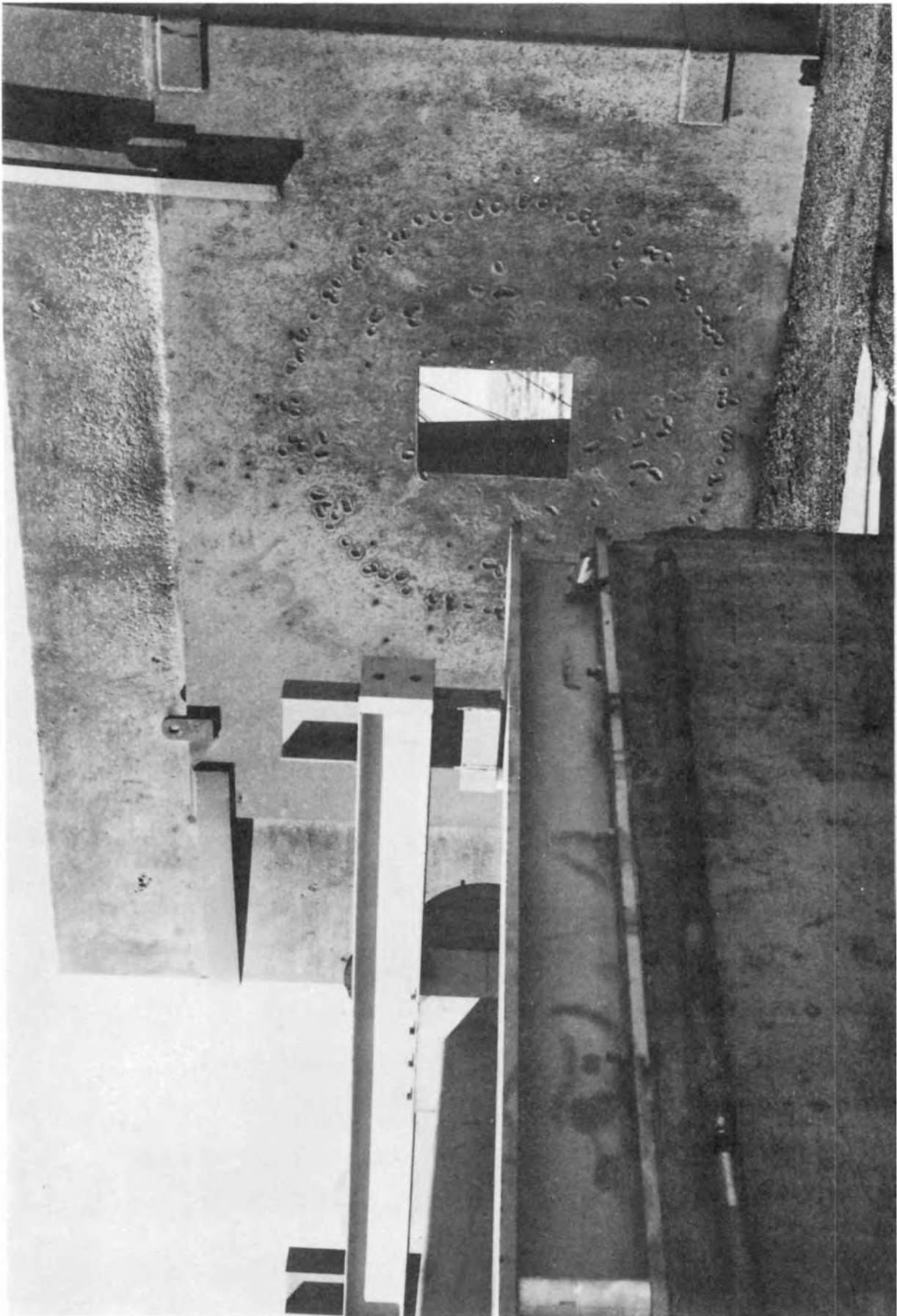


FIG. 3. BLAST SHIELD LOCATED NEAR GUN MUZZLE

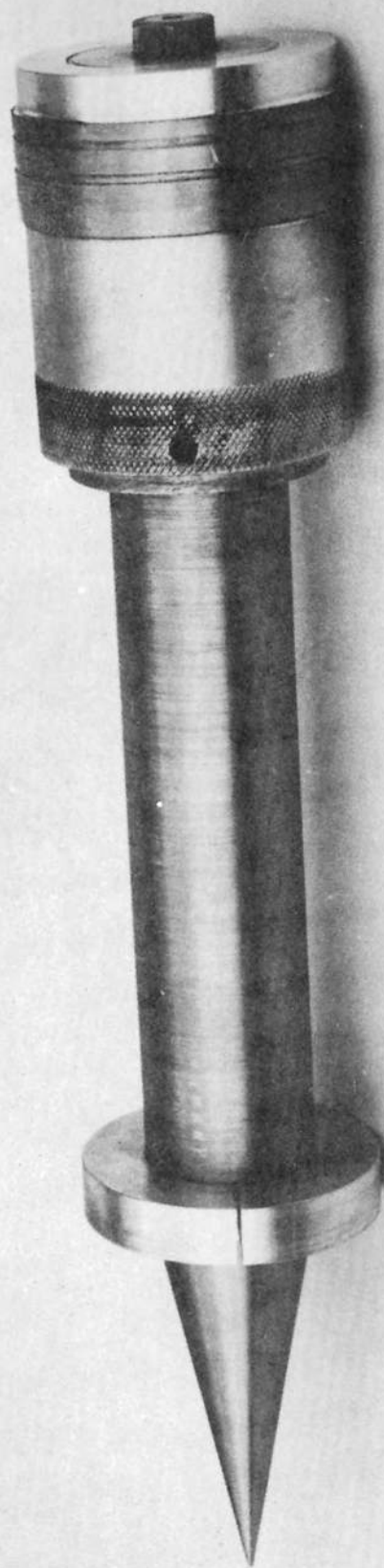


FIG. 4. 3-INCH SUBCALIBER SABOT

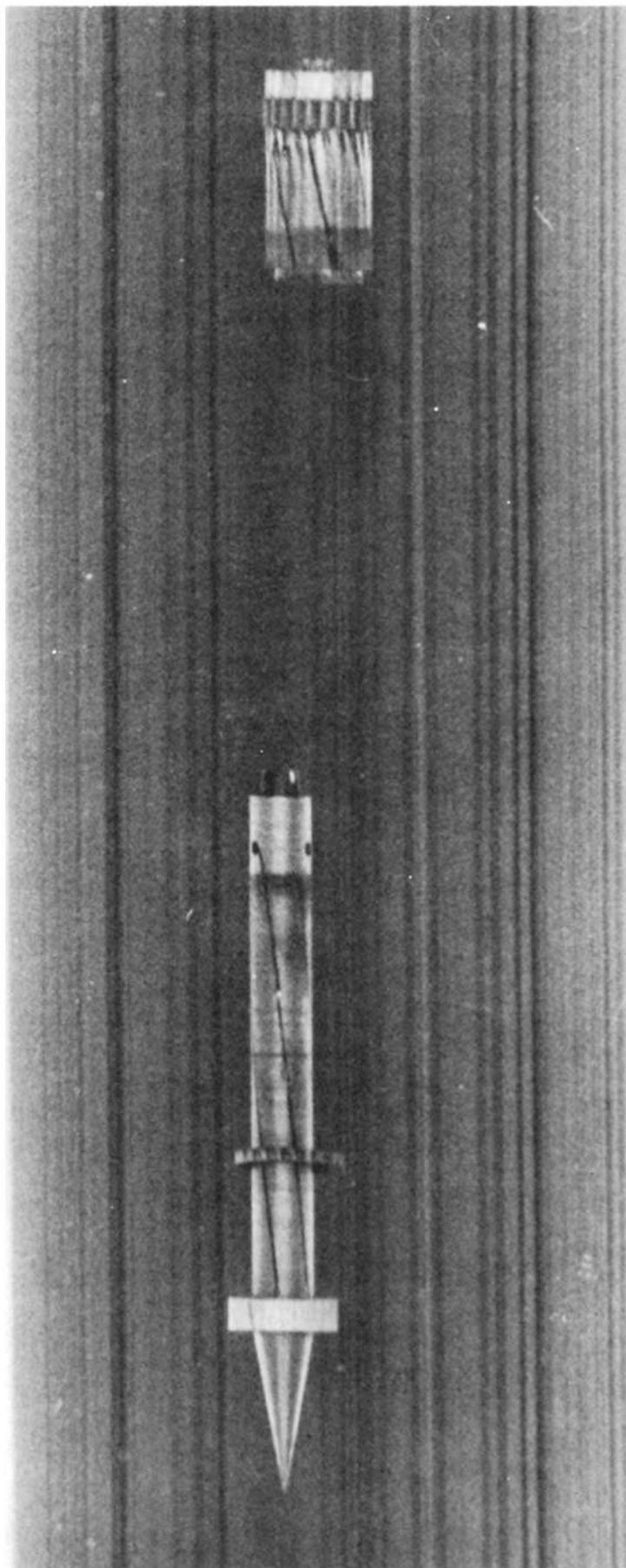


FIG. 5. SYNCHRO-BALLISTIC PICTURE OF MODEL AND SUBCALIBER SABOT

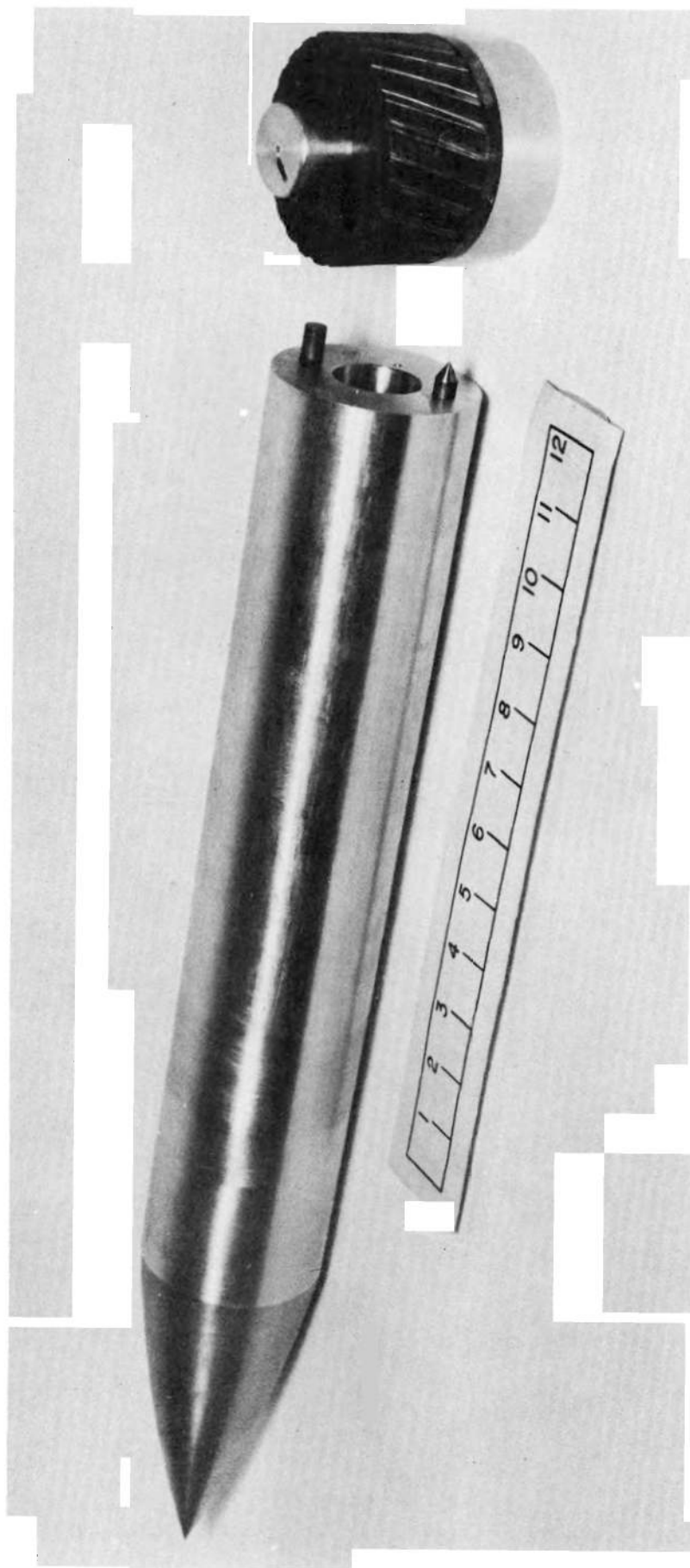


FIG. 6. PISTON SABOT FOR SPINNERS

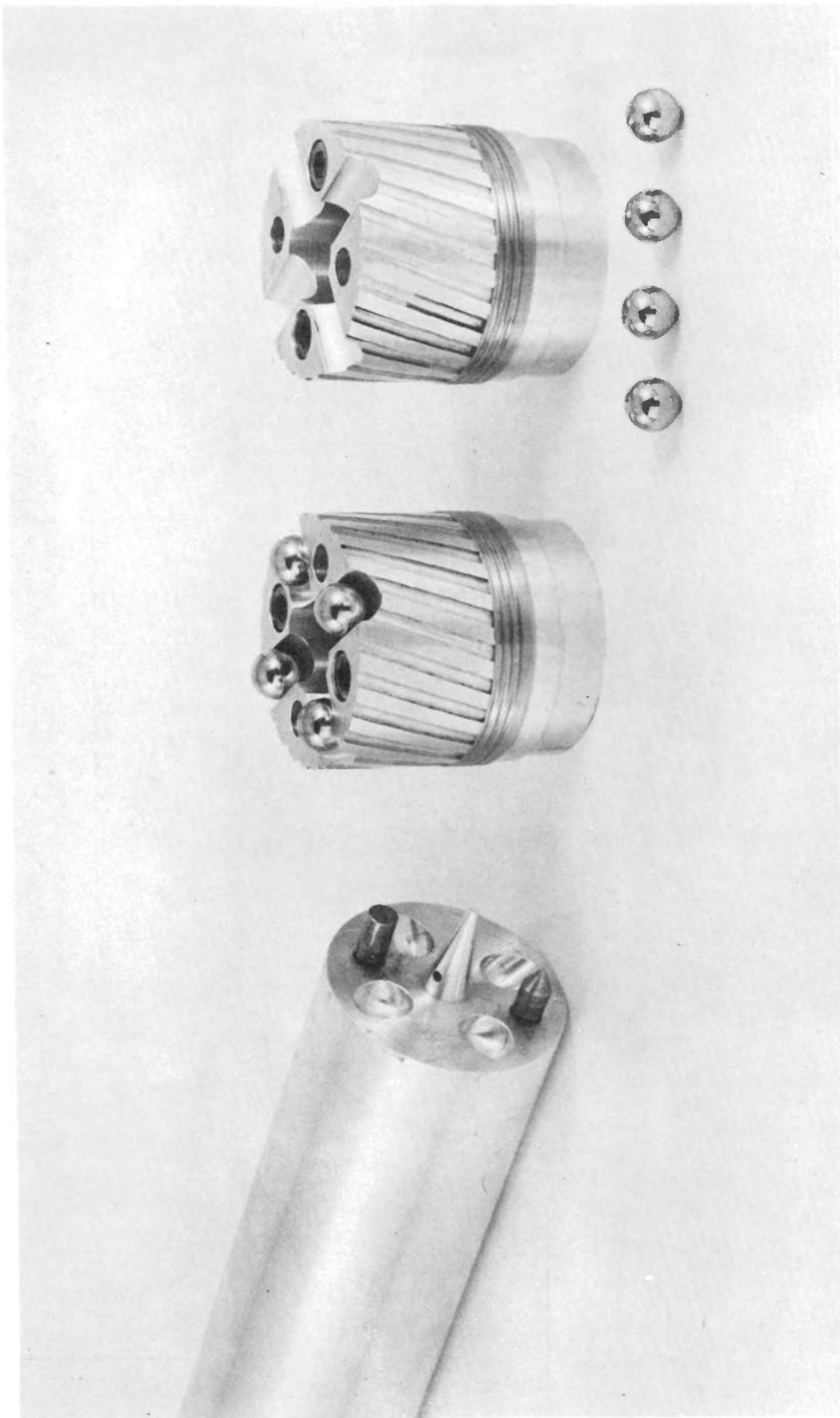


FIG. 7. BALL SABOT FOR SPINNERS

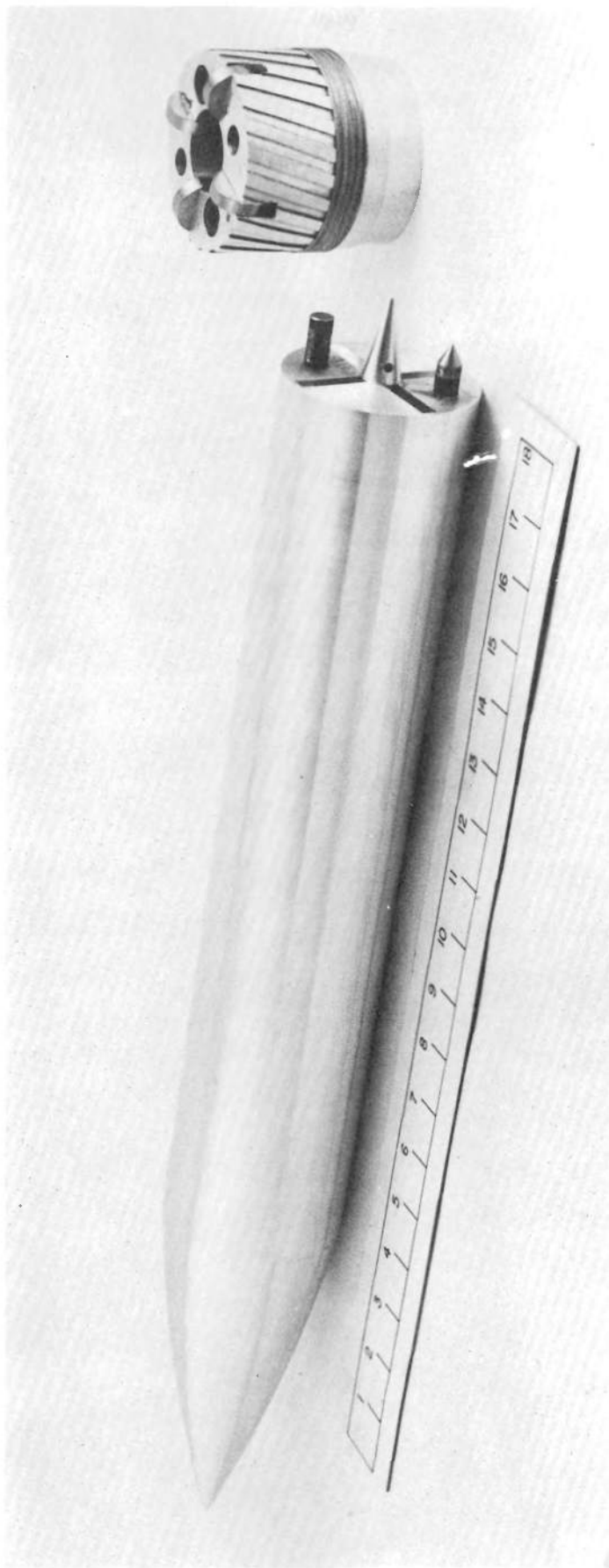


FIG. 8. DISC SABOT FOR SPINNERS

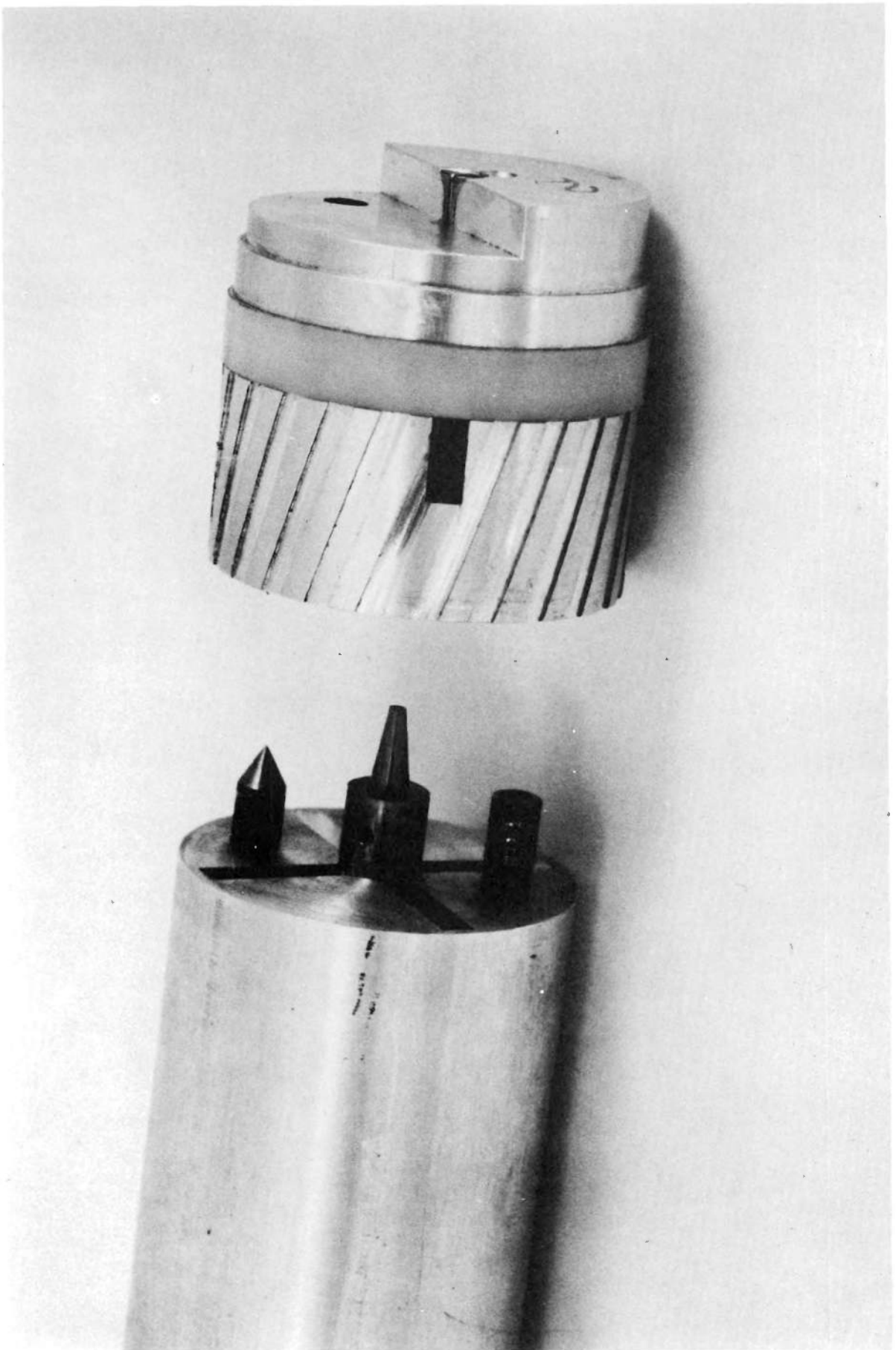


FIG. 9. YAW-INDUCING SABOT FOR SPINNERS

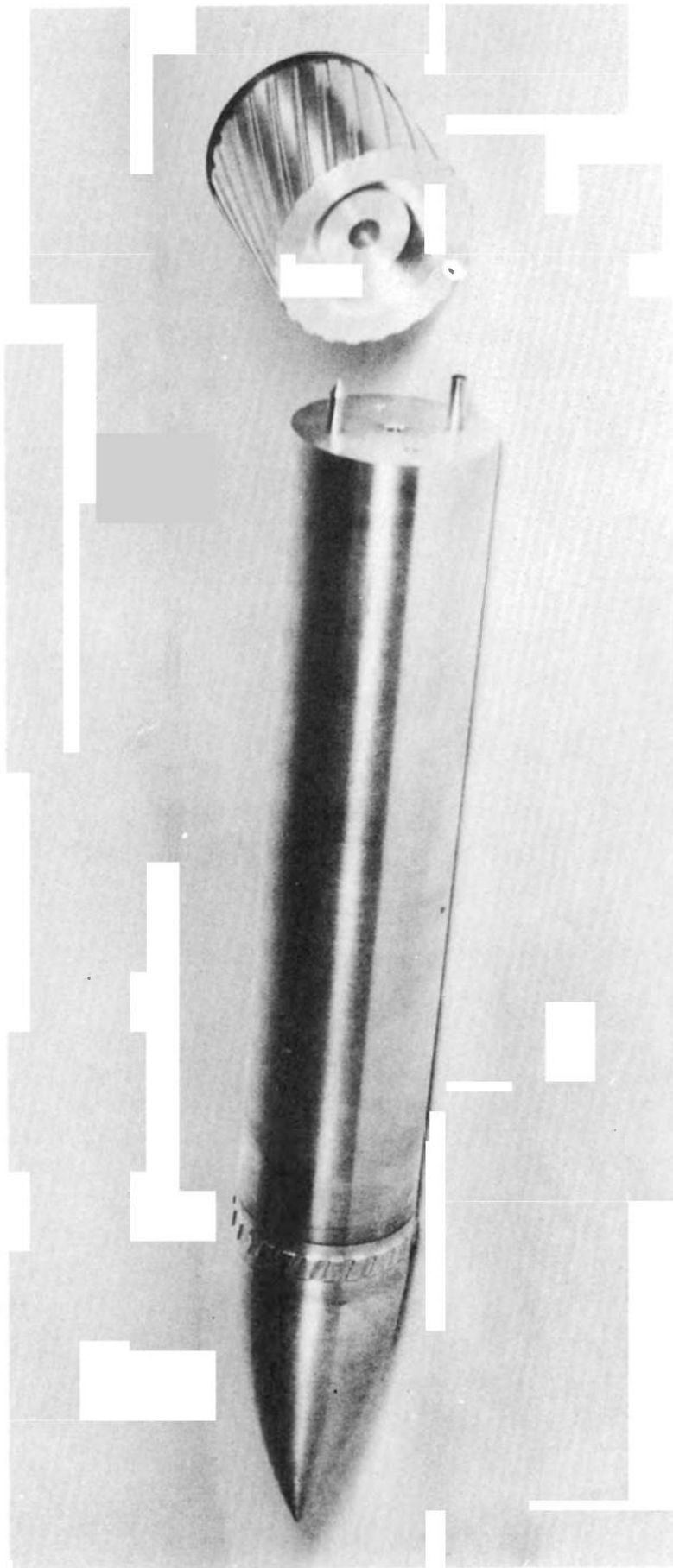


FIG. 10. FRICTION-DRIVE SABOT FOR SPINNERS

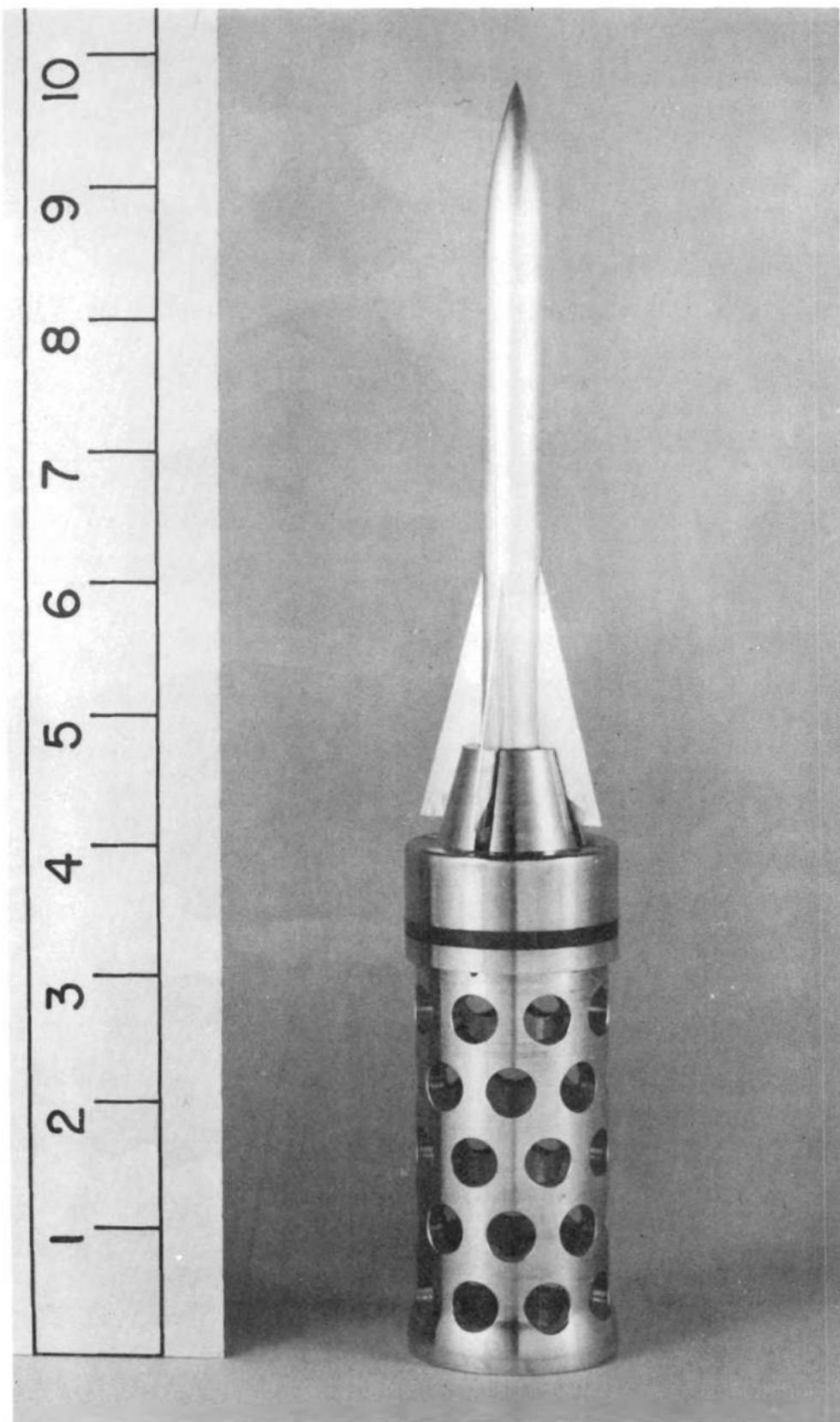


FIG. 11. FOLLOW-THRU SABOT FOR FINNERS

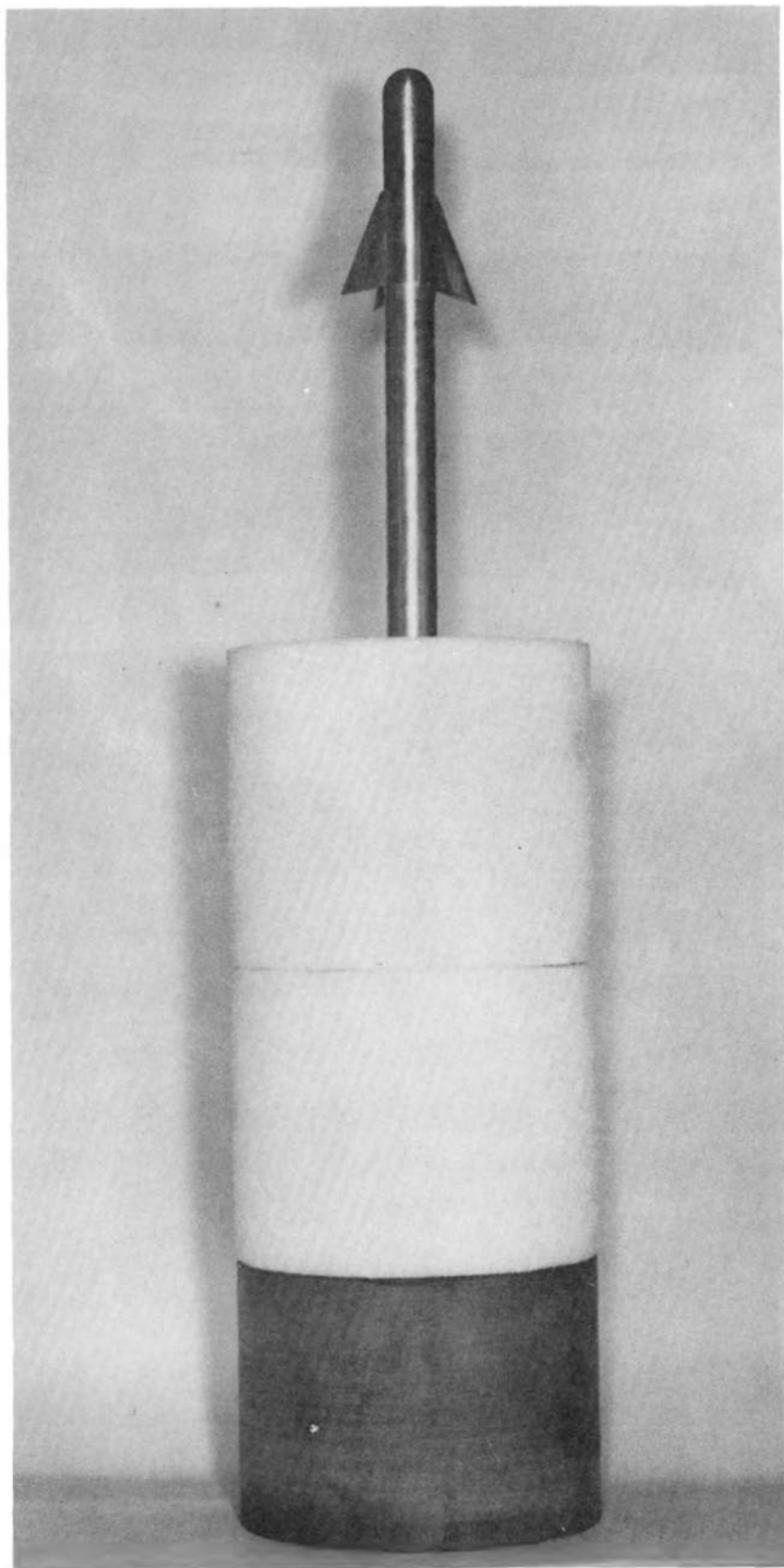


FIG. 12. SLUG-STYROFOAM SABOT FOR FINNERS

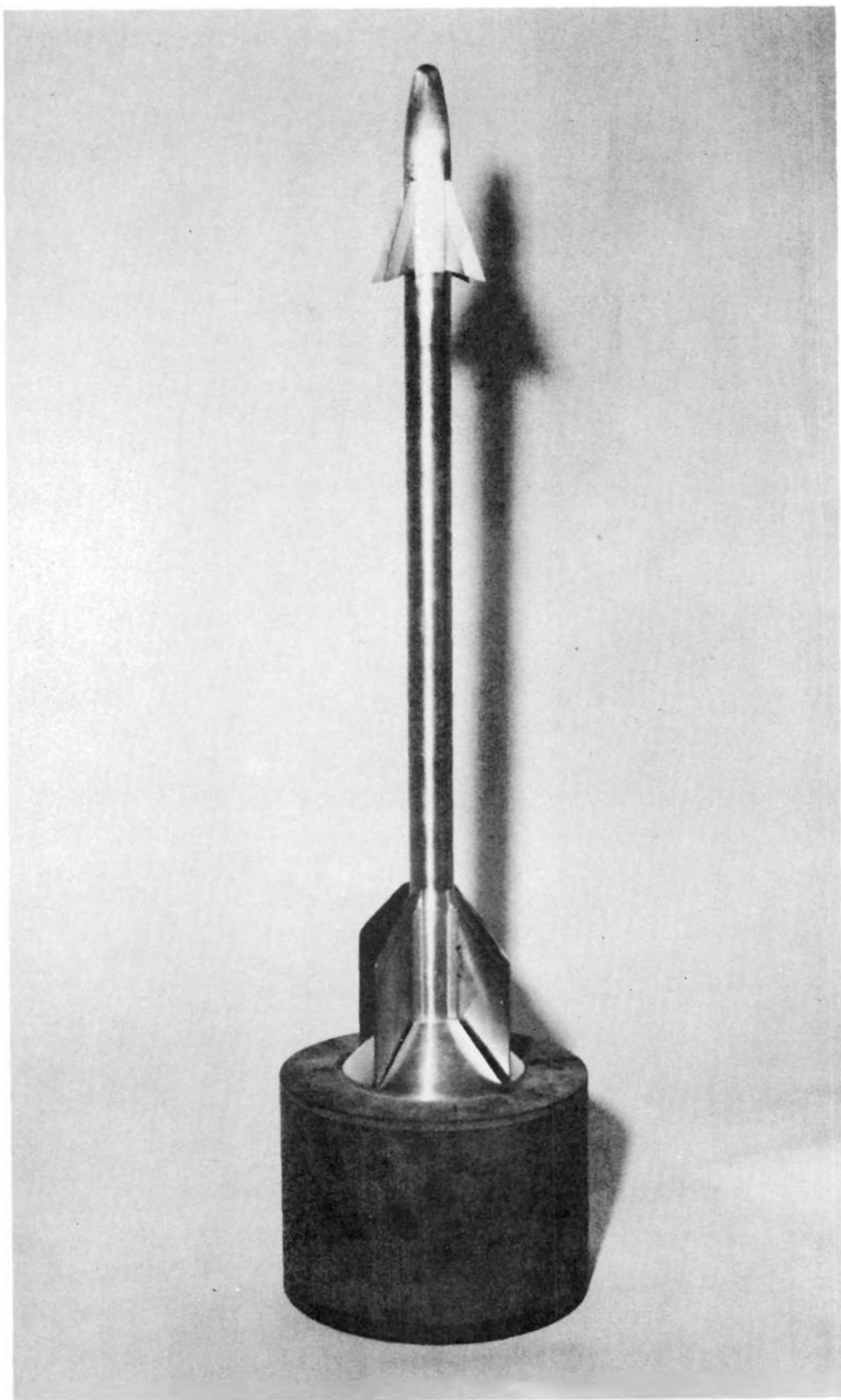


FIG. 13. SLUG-FOLLOW-THRU SABOT FOR FINNERS

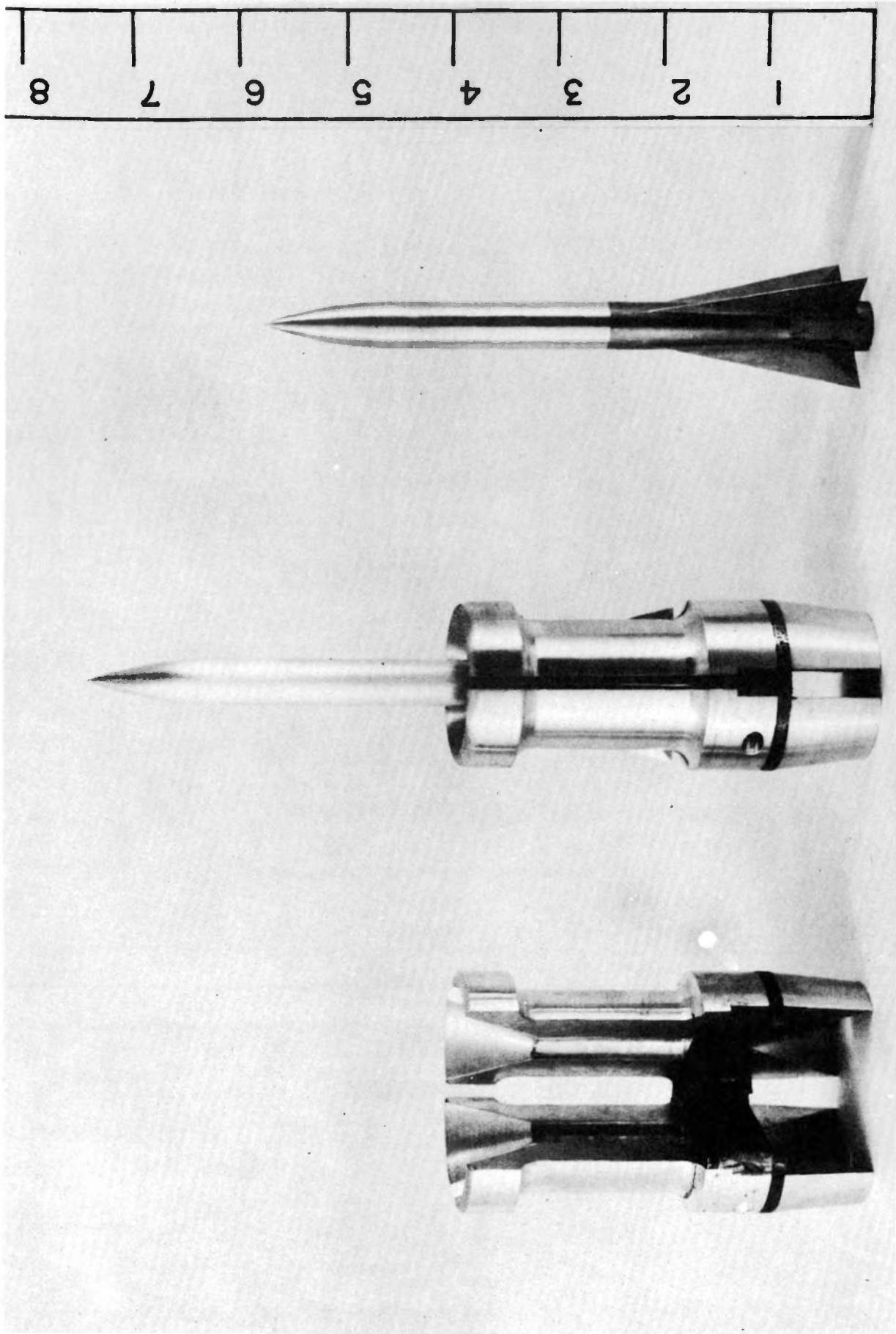


FIG. 14. BREAK-APART SABOT FOR FINNERS

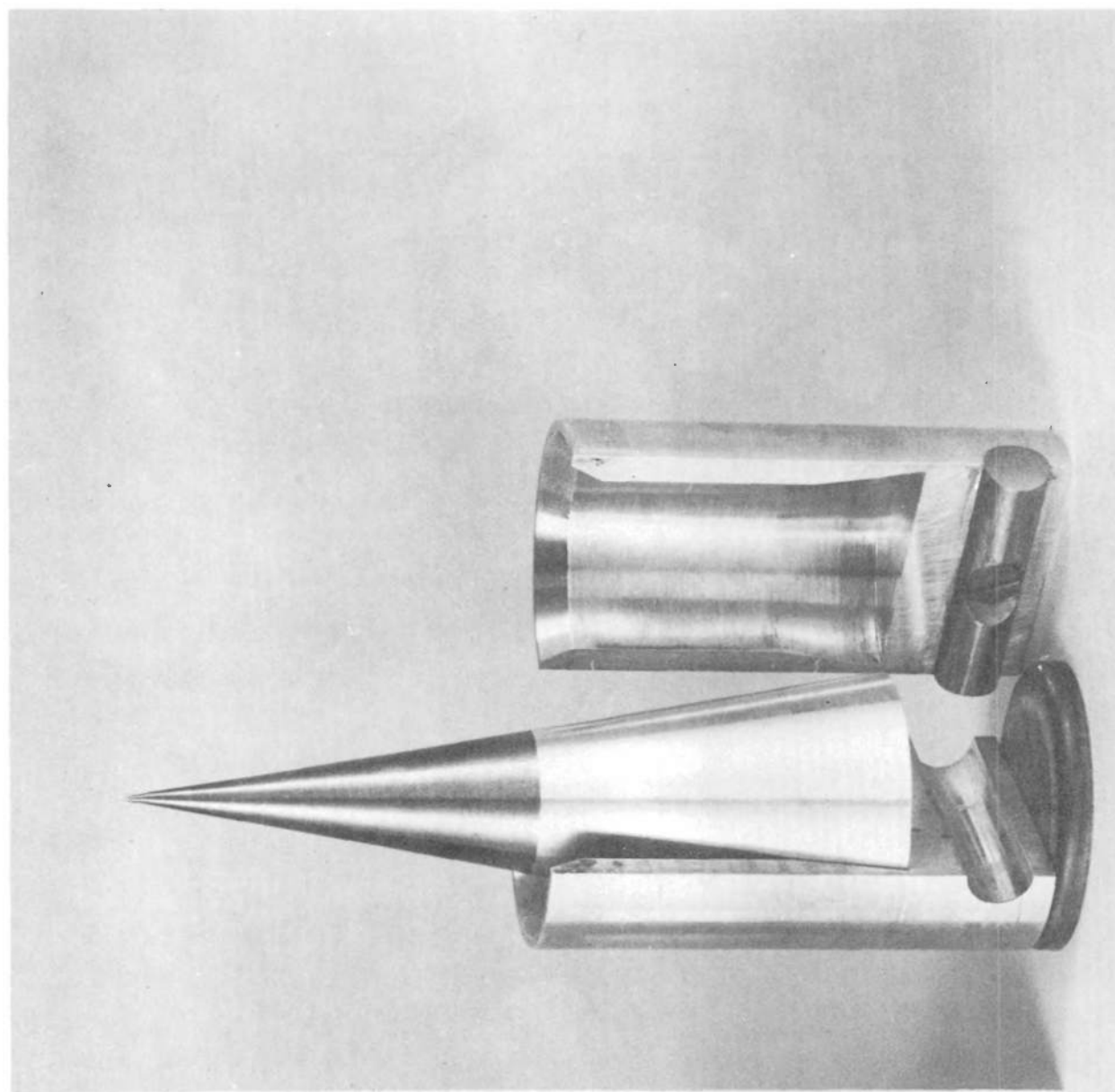
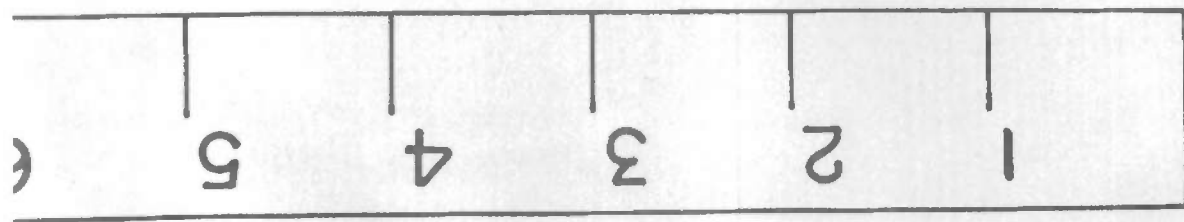


FIG. 15. BREAK-APART SABOT FOR CONES

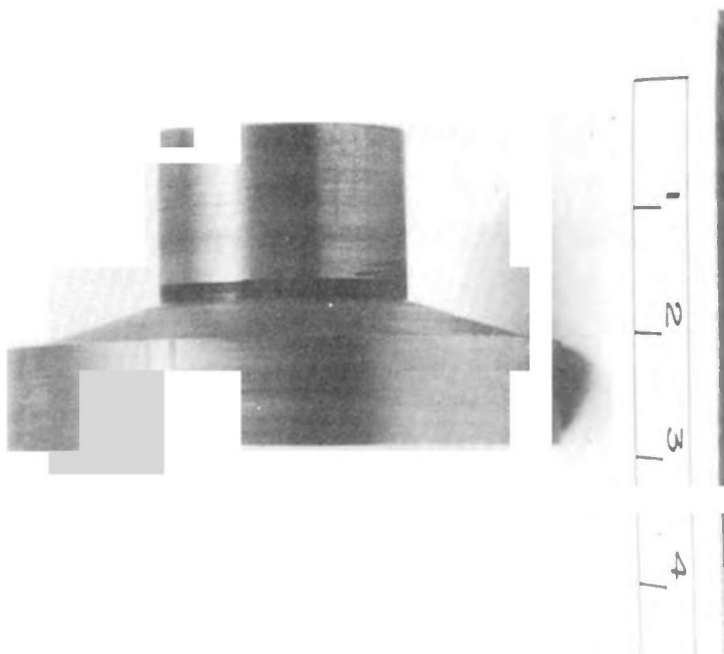
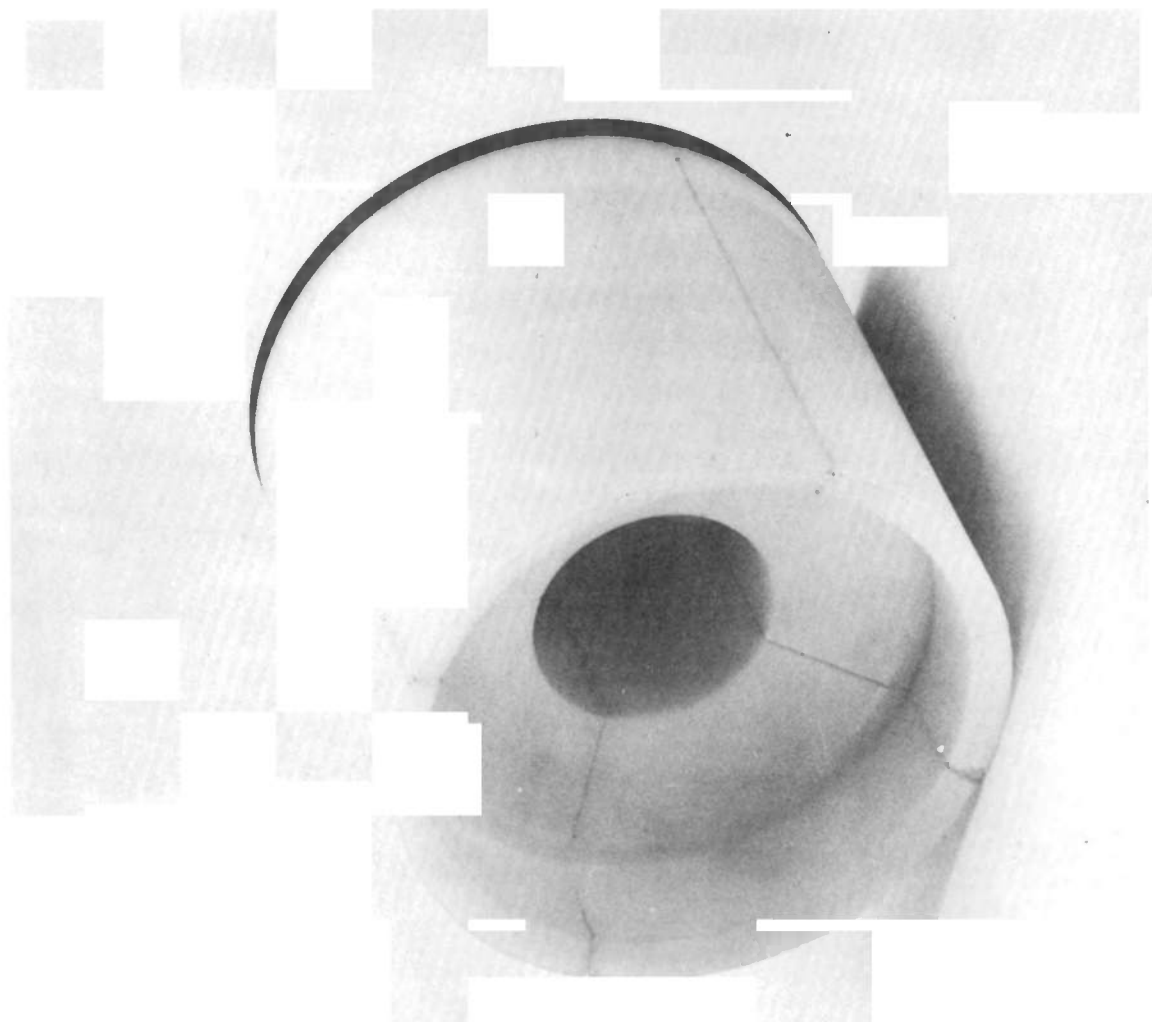


FIG. 16. BREAK-APART SABOT FOR FLINER HEADS

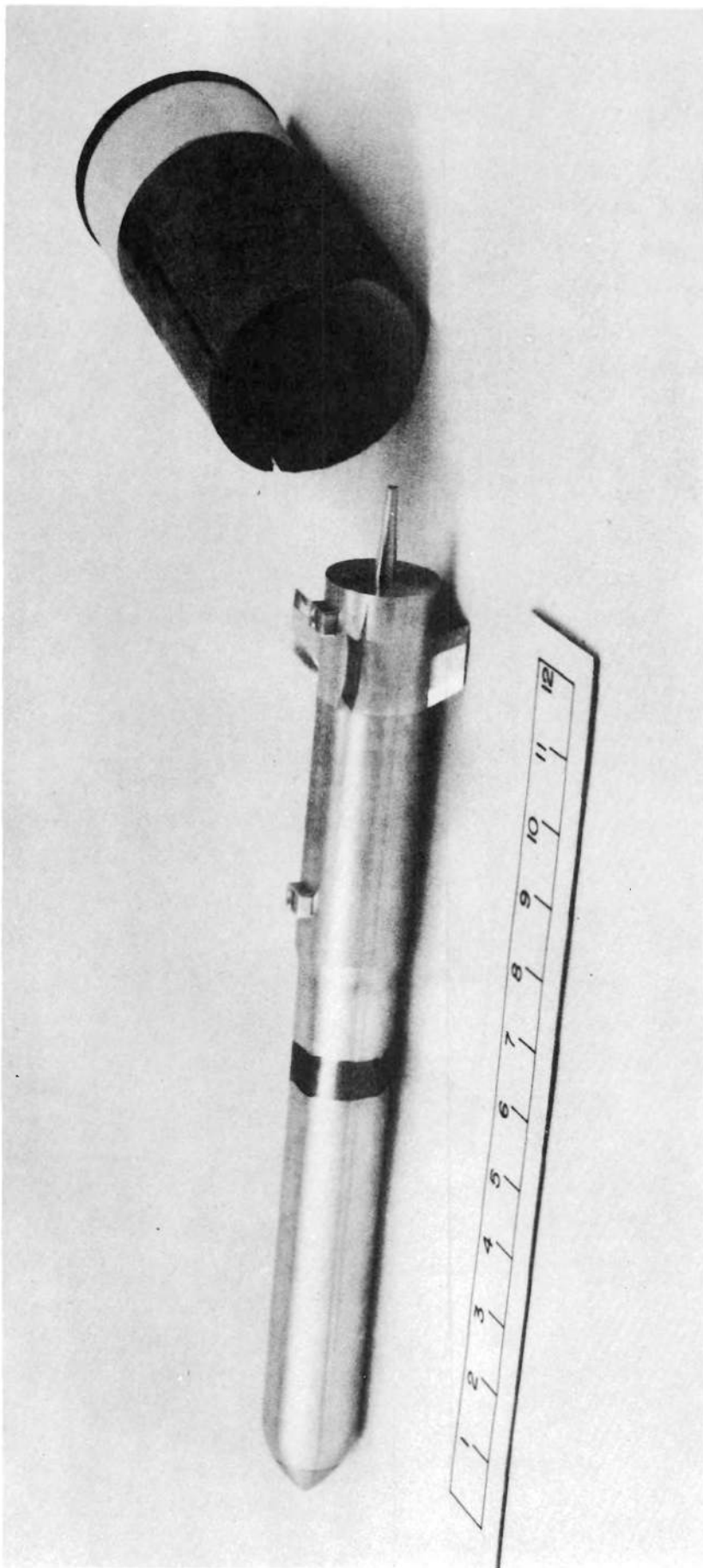


FIG. 17. BREAK-APART SABOT FOR FINNERS

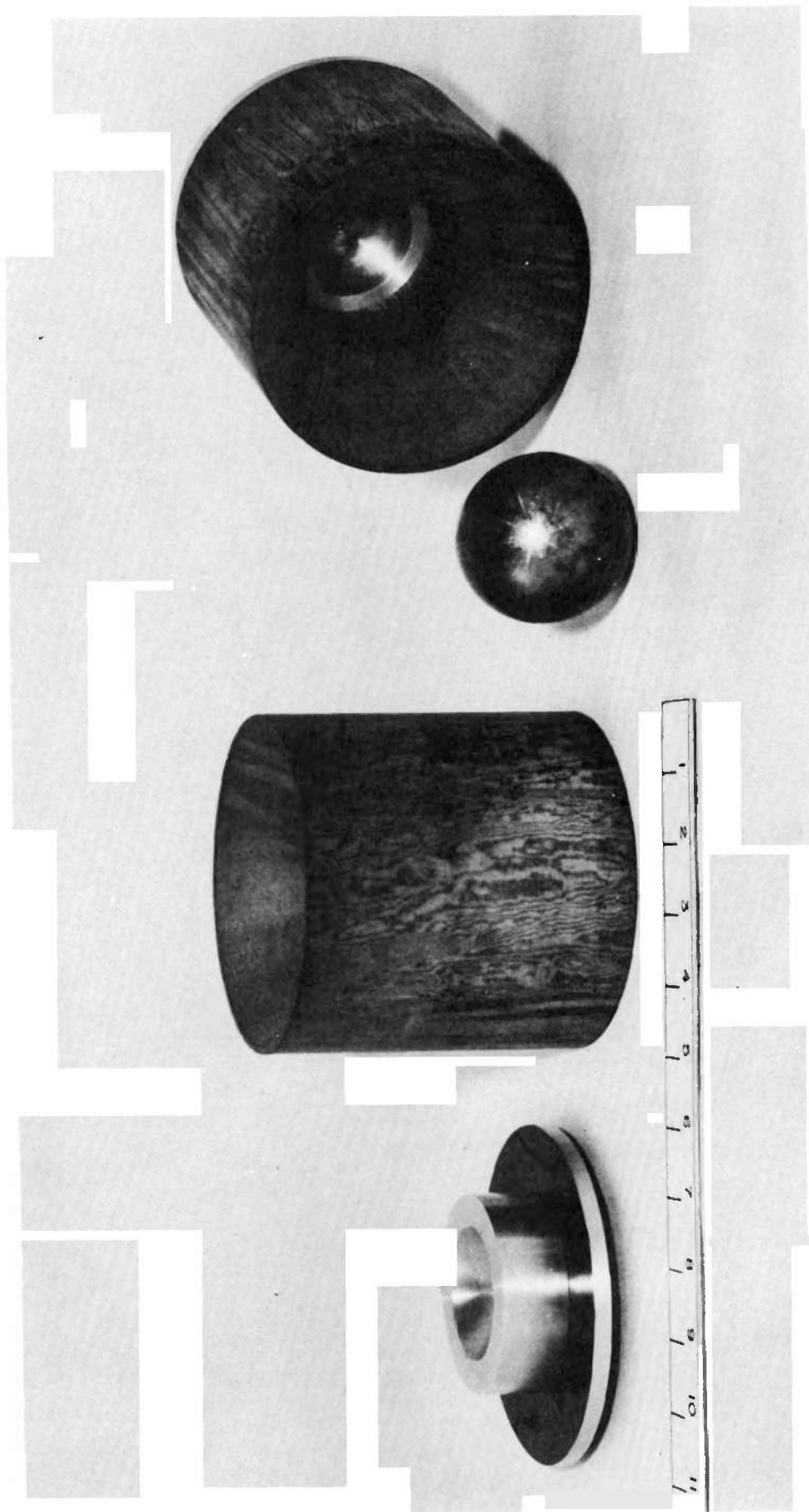


FIG. 13. BREAK-APART SABOT FOR BALLS

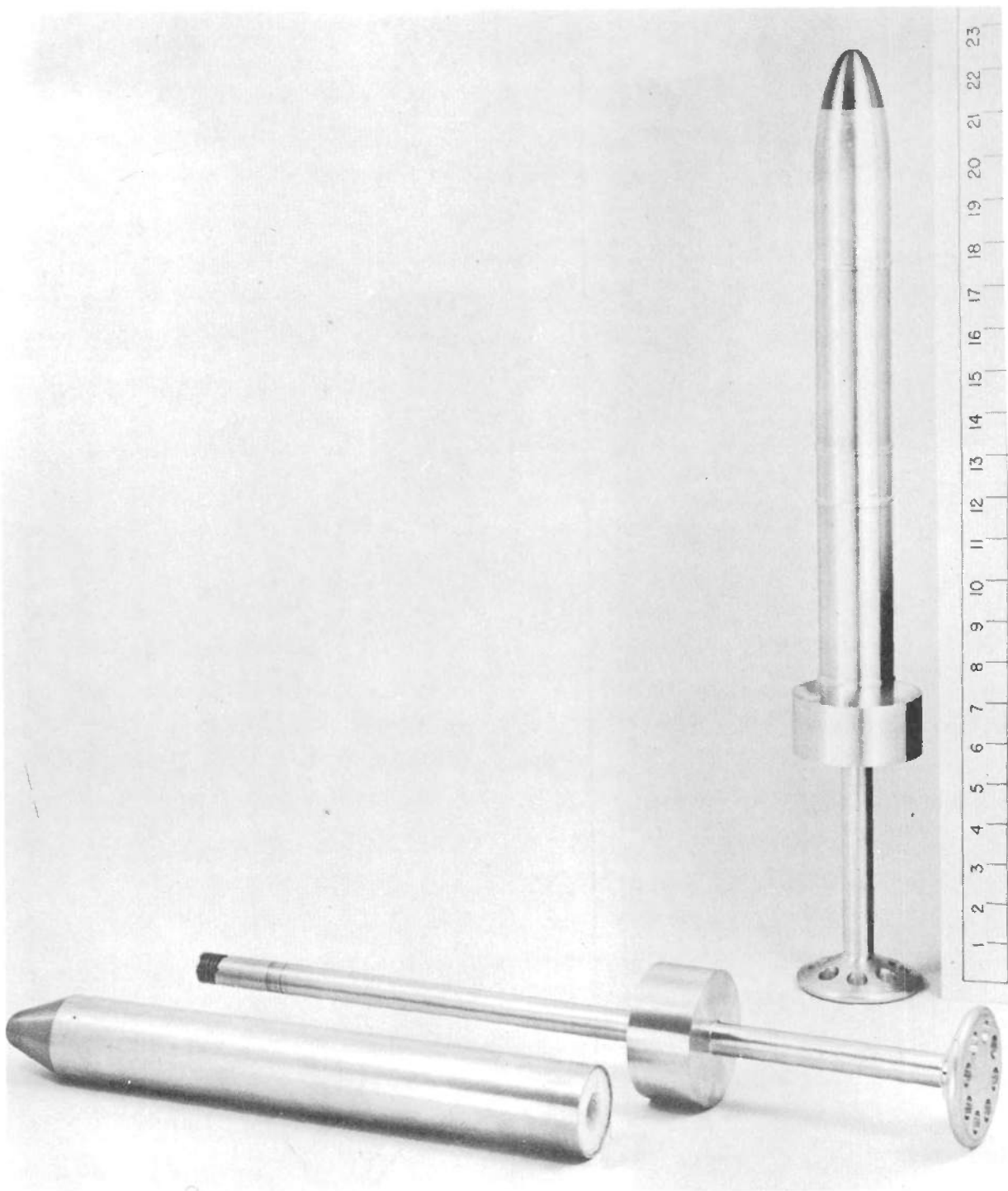


FIG. 19. FOLLOW-THRU SABOT FOR RODS

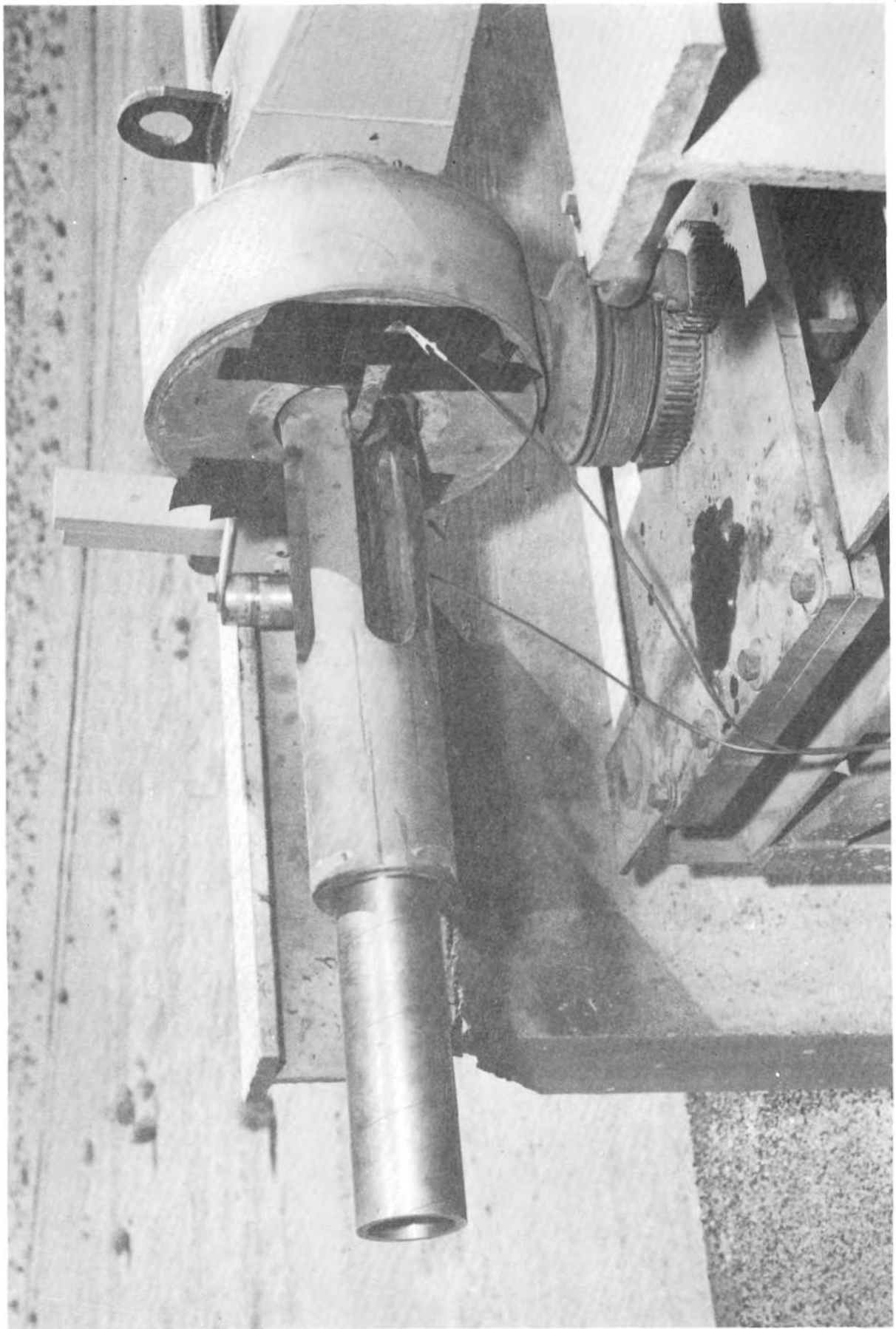


FIG. 20. SABOT STOPPER ATTACHMENT AND TUBE

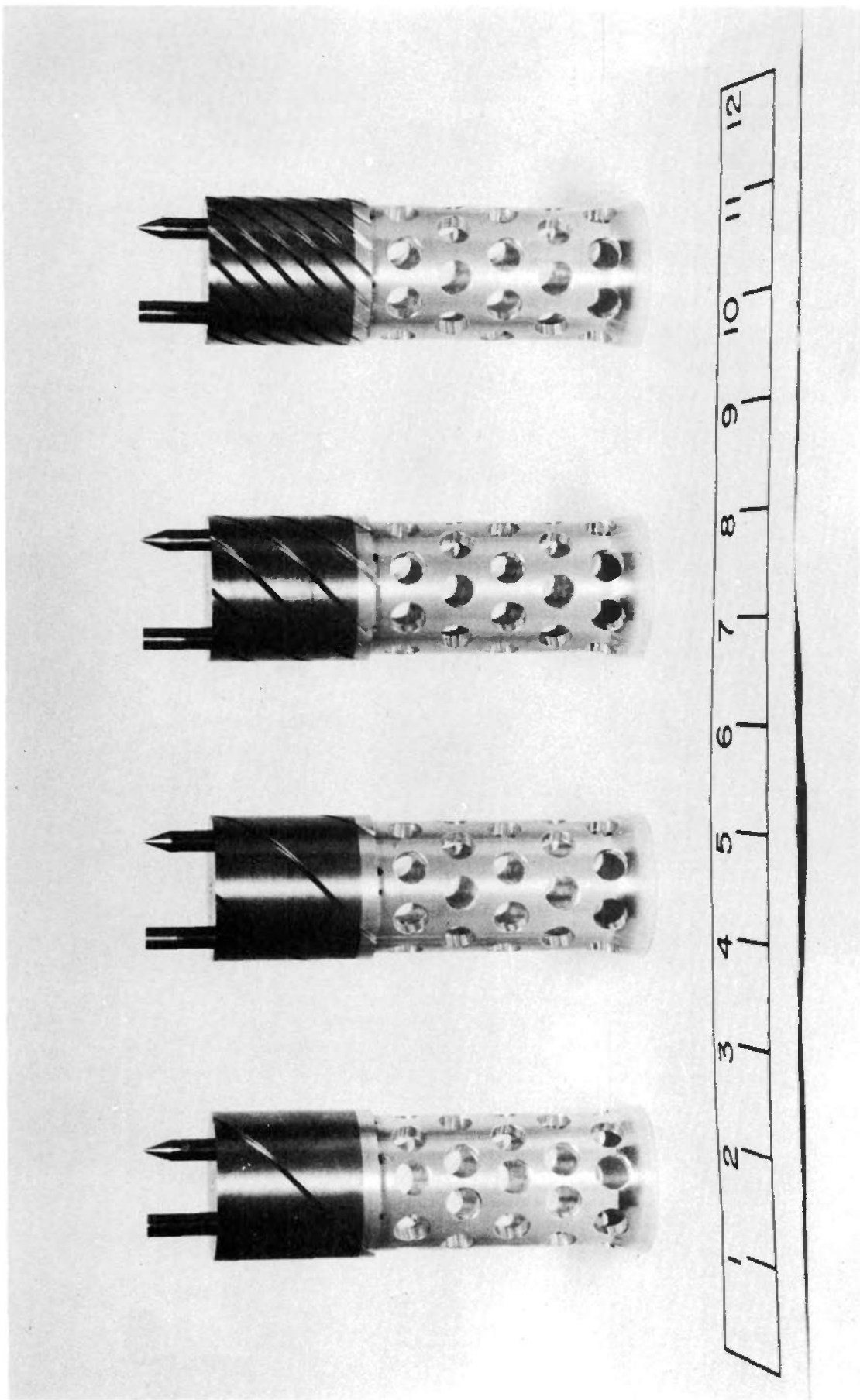


FIG. 21. FOLLOW-THRU SABOT FOR TURBINE DRIVES

MODEL LAUNCHING TECHNIQUES AND OTHER
ITEMS RELATED TO RANGE FIRINGS

Joseph E. Long
U. S. Naval Ordnance Laboratory
White Oak, Silver Spring, Maryland

INTENTIONALLY LEFT BLANK.

MODEL LAUNCHING TECHNIQUES AND OTHER ITEMS RELATED TO RANGE FIRINGS

In the early days of the NOL ranges the techniques used in launching models were quite simple. Finned missiles were fired from smoothbore guns using simply-constructed sabots. Spinning missiles were equipped with more or less conventional rotating bands and were fired from rifled guns. Many range techniques have recently been developed to aid in the solution of aeroballistic problems. Some of these developments will be described in this paper.

CONSTANT SPIN OF A FINNED MISSILE

When finned missiles are fired from smoothbore guns with little or no roll it is usual to determine the drag, restoring moment, normal force, and damping moment coefficients. An accidental cant given to the fins of a missile during manufacture may cause a model to roll at a sufficient rate to produce lunar motion. To avoid this resonant condition, the fins may be made with a larger cant. This increases the spin and makes it imperative that the Magnus moment coefficient be measured. To obtain this coefficient a finned model is made to travel down range with constant spin after it is fired from a rifled gun. The fins of the model are canted to maintain the same spin produced by the rifling of the gun. A four-finger peel-away sabot is used to launch the model as shown in Figure 1. The inside of the sabot is contoured so that the model will fit and bear along each finger. The outside of the sabot is pre-engraved along the entire length of the fingers and the sabot base, the engraving matching the rifling of the gun. The model and sabot must fit in the gun precisely. Otherwise the tail section of the model would unwind or the fins would bend. Figure 2 shows two recovered rounds. It can be seen that there was no fin damage. This same technique has been applied in guns up to three inches in diameter.

LAUNCHING SUBCALIBER PROJECTILES

It has been customary to determine the drag coefficient by firing scaled models, but the scaling has not included the details of the rifling marks left on the rotating band of the full-scale projectile. Instead, the

models were manufactured with oversized rotating bands and fired from guns with a smaller number of rifling grooves. It was subsequently found that the drag coefficient differed by about three percent between models fired with an oversized rotating band and models fired with scaled grooving and rotating bands. Recently, all grooving and rotating band details have been copied from recovered full-scale rounds. These reproduced details on a sub-caliber model are preserved in a sabot as shown in Figure 3. There are two pins in the base of the sabot, which engage holes in the model. The outside of the sabot is made larger than the rifling of the gun. A section of the sabot just aft of the position of the model base is weakened by reducing the sabot diameter, the thickness of this section depending on the velocity to be attained. At firing it is believed that the part of the sabot in front of the weak section breaks up in the gun. As the sabot base and model leave the gun they begin to separate as shown in Figure 4, and the model is free to fly down the range. Through this technique a more realistic drag curve can be obtained.

LAUNCHING SPHERES

In a recent program very small spheres were fired for drag determination. It was realized that they were too small to actuate the sparks by photoelectric triggering. To overcome this deficiency it was decided to fire a larger, triggering sphere with the smaller one. Actually several sizes of spheres were fired together. Figure 5 shows $1/32$, $1/16$, $3/32$, and $1/8$ inch diameter spheres that are loaded into either a synthetic rubber cup for low velocity or a nylon cup for high velocity firings. These spheres are held in the cup by a piece of lens tissue. This assembly is loaded into a 30-caliber cartridge case and fired in the range. It was discovered later in the program that the large diameter spheres were not necessary as the cups containing the spheres would travel down the range and trigger the sparks. By varying the air pressure in the range and shooting at different velocities, drag coefficients can be obtained for a wide variety of Reynolds and Mach numbers.

LAUNCHING MODEL AIRCRAFT

A great deal of publicity has been given recently to the "sonic booms" produced by high-speed aircraft. Speculations have been made as to the number of booms that one might expect to hear. A simple experiment was prepared in the Aerodynamics Range to study this. A model airplane (obtained from a box of cereal) was put into a 40-mm sabot consisting of two spring steel fingers, styrofoam, and a cylindrical sabot base as shown in Figure 6. At launching the spring steel fingers would pull the styrofoam away from the model allowing the model to fly down range. The shadowgraph in Figure 7 shows the shock pattern obtained from this model. From this pattern it is interesting to conjecture as to the number of booms that might be heard under various conditions of observation.

JET MODEL

Not all problems in the ranges are launching problems. Other difficulties arise in trying to make a model or some of its components do a particular job. For example, a program has been instituted to investigate what effects a jet exhausting from the base of a missile can have on the aerodynamic coefficients. Some means had to be employed whereby the shadowgraphic plates would not be exposed to a flaming jet. For an initial study a "Sparklet" bulb containing liquid CO_2 at 835 psi gauge was placed in a cone cylinder model as shown in Figure 8. A thin steel plate, not shown, was put on the base of the model to prevent the cap from popping out due to setback forces and allowing the CO_2 to escape at the time of firing. A hole was drilled in the center of the plate. To puncture a hole in the cap of the bulb a pin was fastened to the center of a disk, and the disk was placed just behind the plate in the gun. At firing, the pin would puncture the bulb allowing the CO_2 to escape. A shadowgraph of a model with a jet of CO_2 is shown in Figure 9. These models were fired at a Mach number of 0.5. Preliminary results indicate a considerable change in the drag and overturning moment coefficients due to the cold jets. Encouraged by these results it is planned to design a finned model with a nozzle and compressed gas supply for launching in the firing ranges.

FUZE ARMING

The ranges can perform a variety of tasks not necessarily associated with obtaining aerodynamic coefficients for a specific model. A 30-mm model was fired at 2800 ft/sec in the Pressurized Yaw Card Range under a pressure simulating an altitude of 40,000 feet specifically to determine whether or not the fuze armed itself under actual flight conditions. It was caught in cotton waste to prevent its destruction. The arming device consisted of a ball with a cylindrical hole containing a powder train. In flight the ball tends to rotate about the axis for which the moment of inertia is a maximum. Upon contact with a foreign object, a firing pin strikes and causes the powder train to burn. The powder train at burning causes the powder in the projectile to explode. As can be seen in Figure 10, the X-rayed noses of the models prior to firing show the holes with the powder trains in the balls to be in various positions. After these inert models were fired, all of them were recovered from the cotton waste and X-rayed again. The models penetrated the cotton waste to a depth of twenty-five feet. After firing (Figure 11) the holes were lined up axially (except for one) which would allow the pin to arm the fuze.

PLASTICS ROTATING BANDS

The Plastics Branch of the Chemistry Division at NOL has been working on a plastics material to replace the metal rotating bands on projectiles. If plastics can be used, gun wear can be decreased and the life of a rapid-fire gun can be increased. Models with plastics rotating bands were fired from the Block Mount Range to see which plastics could serve satisfactorily as a rotating band. Upon selecting the most promising plastics, additional models were fired in the Aerodynamics Range to insure that the proper spin was being attained. Some models were heated to 160 degrees Fahrenheit while other models were cooled to -76 degrees Fahrenheit to see that they would perform satisfactorily at any temperature that might be encountered. A maximum of 49 seconds was used in taking any one projectile from the furnace or freezer, putting it in the gun and firing it. The Microflash photographs of Figure 12 show that both the plastics on these models held intact under the two extreme temperature conditions.

SPIN TELEMETERING

In order to determine the spin rate of a small projectile, a spin sonde was developed in the ranges at NOL. Larger sondes are well-known, but this one was made to fit into a 20-mm shell. The construction and use of this spin sonde are given in NavOrd Report 3726. The sonde, shown in Figure 13, contains a condenser, resistor, transistor, and coil placed in a plastic potting compound. A battery was used which will supply 1.35 volts and which will operate the oscillator for 200 hours. The oscillator coil serves as a loop-type transmitting antenna with the longitudinal axis of the projectile lying in the plane of the loop or oscillator coil. The frequency of oscillation lies within the range from 455 to 465 kilocycles. A receiving antenna consists of an open wire transmission line running parallel to the projectile trajectory with the projectile trajectory midway between the wires. As the projectile rotates about its axis, the transmitting antenna emits a signal. At the receiver this signal will vary in intensity from zero to some maximum value and back to zero. For each revolution of the projectile there are two positions of maximum signal and two positions of zero signal. The transmitted signal is picked up by the receiving antenna and is displayed on a cathode-ray oscilloscope. The oscilloscope is photographed with a high-speed camera. Several models of the type shown in Figure 14 were fired in the Aerodynamics Range at a maximum velocity of 1200 ft/sec. These models were accelerated at about 30,000 g's. A sample measurement of the film strip indicated that over seven spin cycles it was possible to determine the spin rate of 1152 RPS with a standard deviation of 5.7 RPS. Another sonde under development at NOL is the base pressure sonde. A few shots have been made. Although these shots are not conclusive, the results are encouraging. Ground work is also being made toward the development of a temperature telemetering device.

HIGH-VELOCITY POWDER GUN FIRINGS

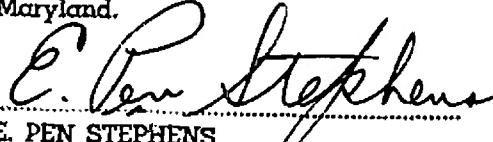
Improvements and modifications are constantly being made to the ranges and their instrumentation. Cylinders and spheres were recently fired in the Aerodynamics and Pressurized Ballistics Ranges in an attempt to determine the highest velocities at which the existing circuitry of the ranges would perform satisfactorily. Normal large chamber, smoothbore powder guns, 20, 30, and 40-mm

in diameter, were used. The models were made of nylon and weighed from about 20 grams to 50 grams. The maximum velocity obtained at the muzzle in the Aerodynamics Range at atmospheric pressure for a 40-mm model was about 7000 ft/sec. This range operated satisfactorily after slight changes were made in the circuits so that the models would trigger the sparks at each station. The maximum velocity obtained on a 30-mm model (Figure 15) in the Pressurized Ballistics Range at 0.07 atmosphere was about 9800 ft/sec at the muzzle. No changes were needed in the circuits of this range. Major effort is now being devoted to the development of models which will permit launching at such velocities and to the development of a shorter duration spark.

18 FEB 1957

(Date)

Released by the Commander, U. S. Naval
Ordnance Laboratory, White Oak, Silver
Spring, Maryland.


E. PEN STEPHENS
Technical Information Officer, Acting

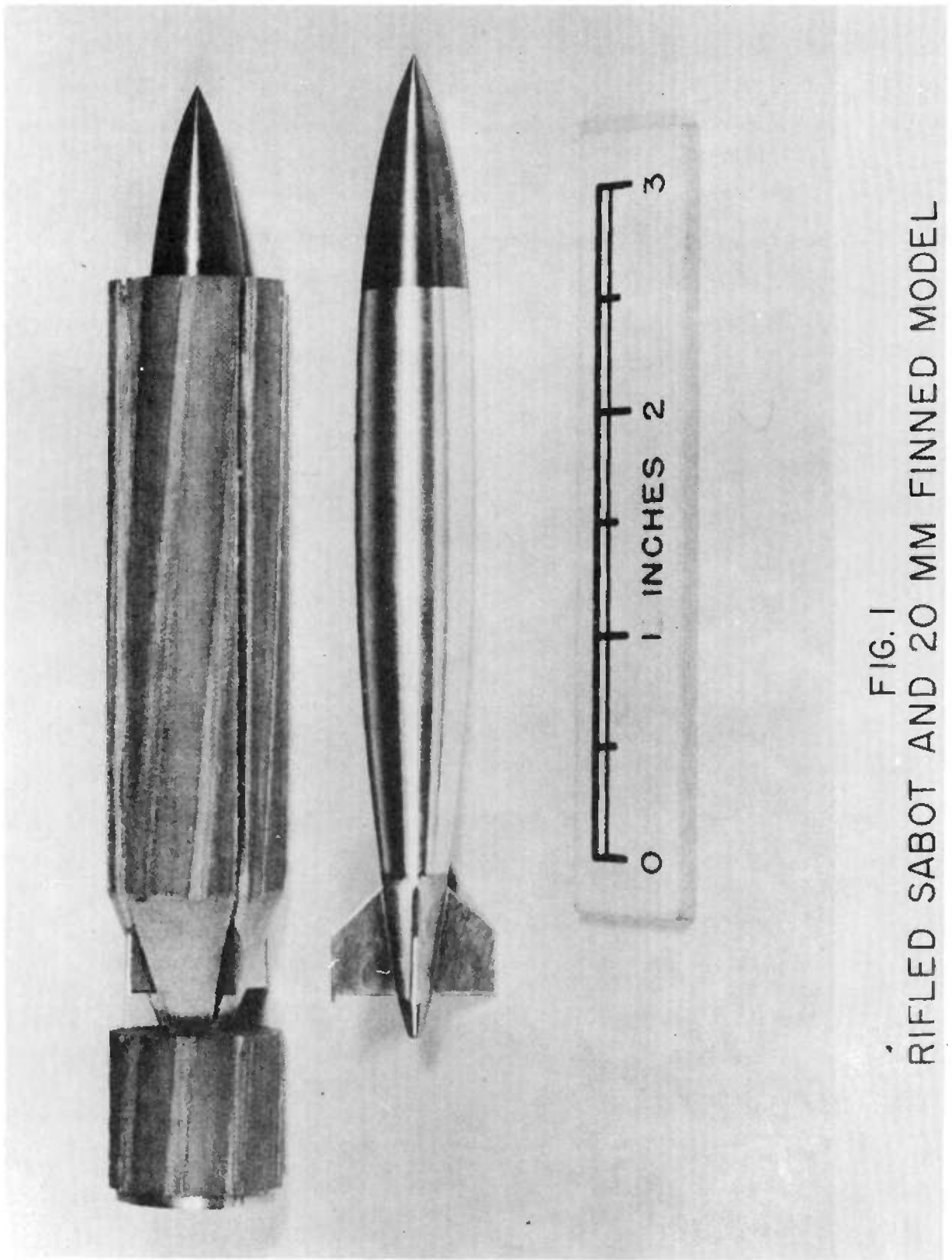


FIG. 1
RIFLED SABOT AND 20 MM FINNED MODEL

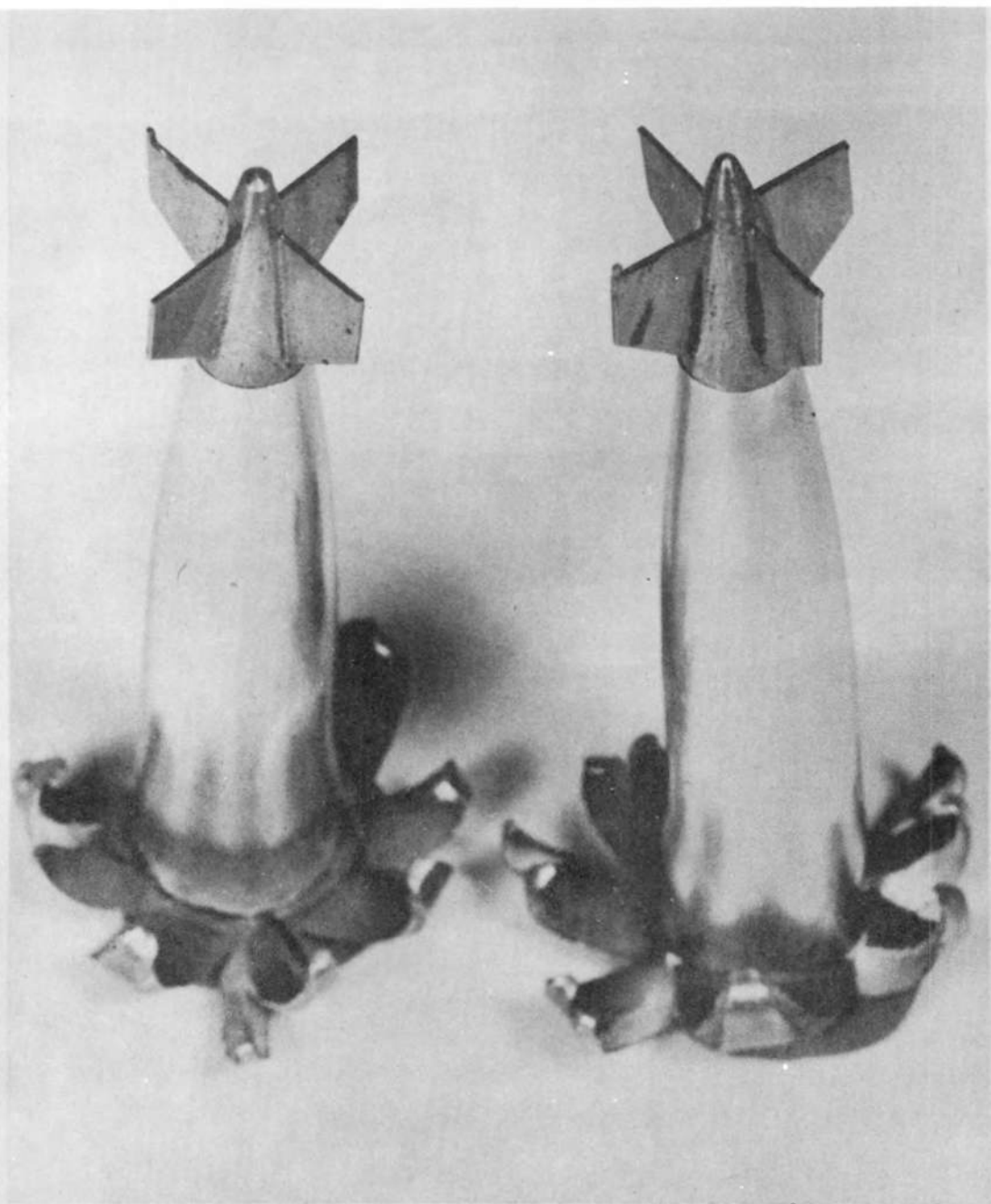


FIG. 2
RECOVERED 20 MM MODELS FIRED FROM A RIFLED GUN

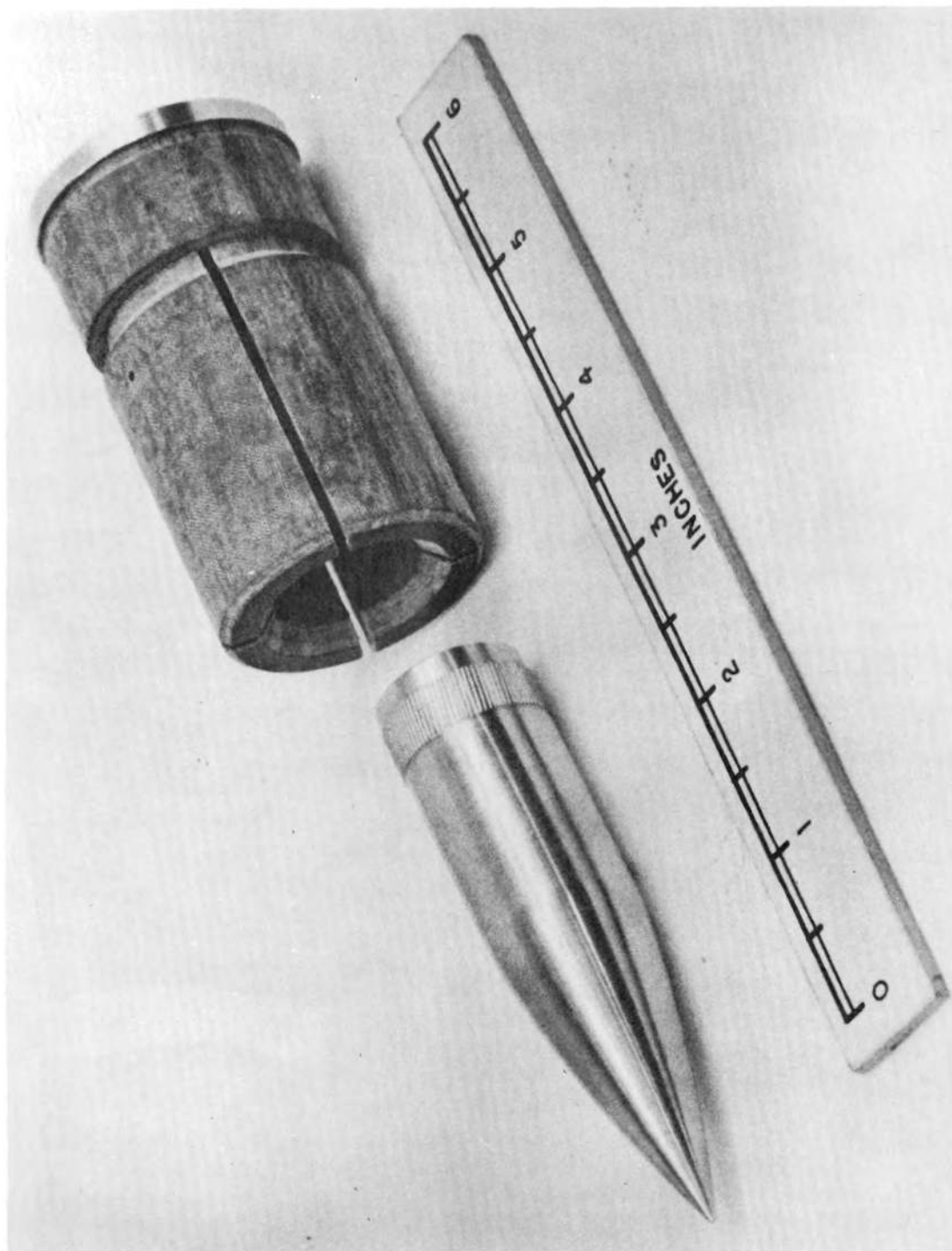
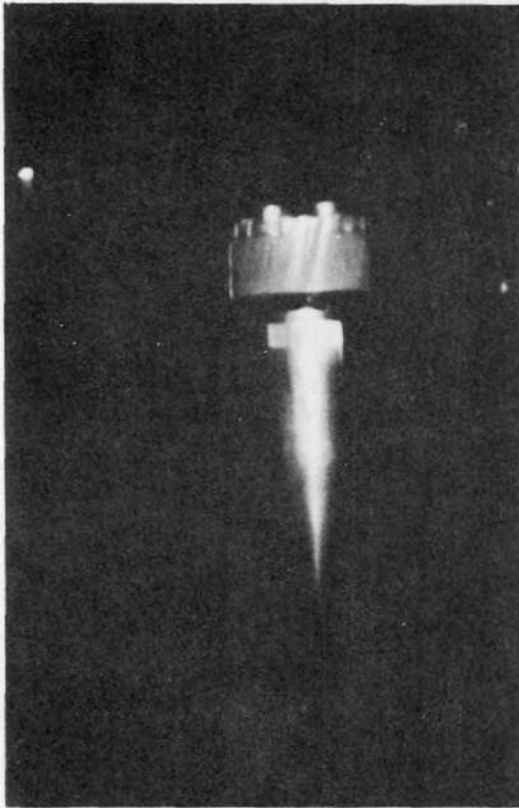


FIG. 3
22.4 MM MODEL (SUB CALIBER) AND 40 MM SABOT

10 FEET FROM MUZZLE



20 FEET FROM MUZZLE

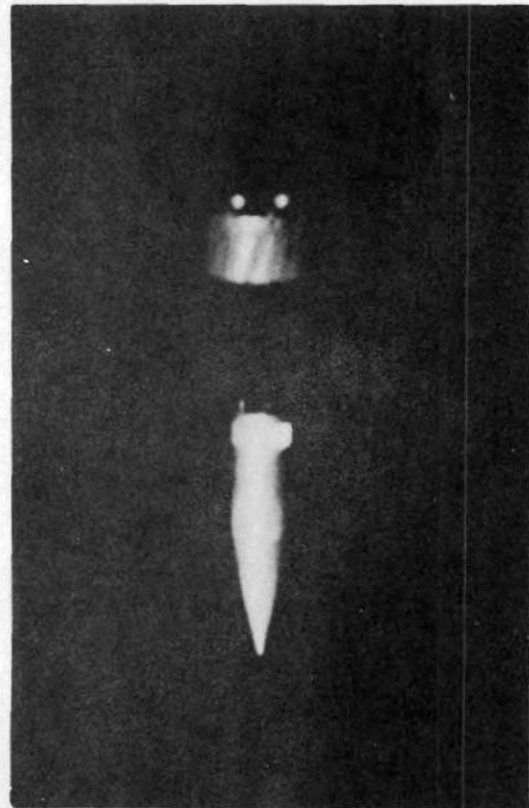


FIG. 4
SUB CALIBER MODEL FIRED FROM 40 MM SABOT

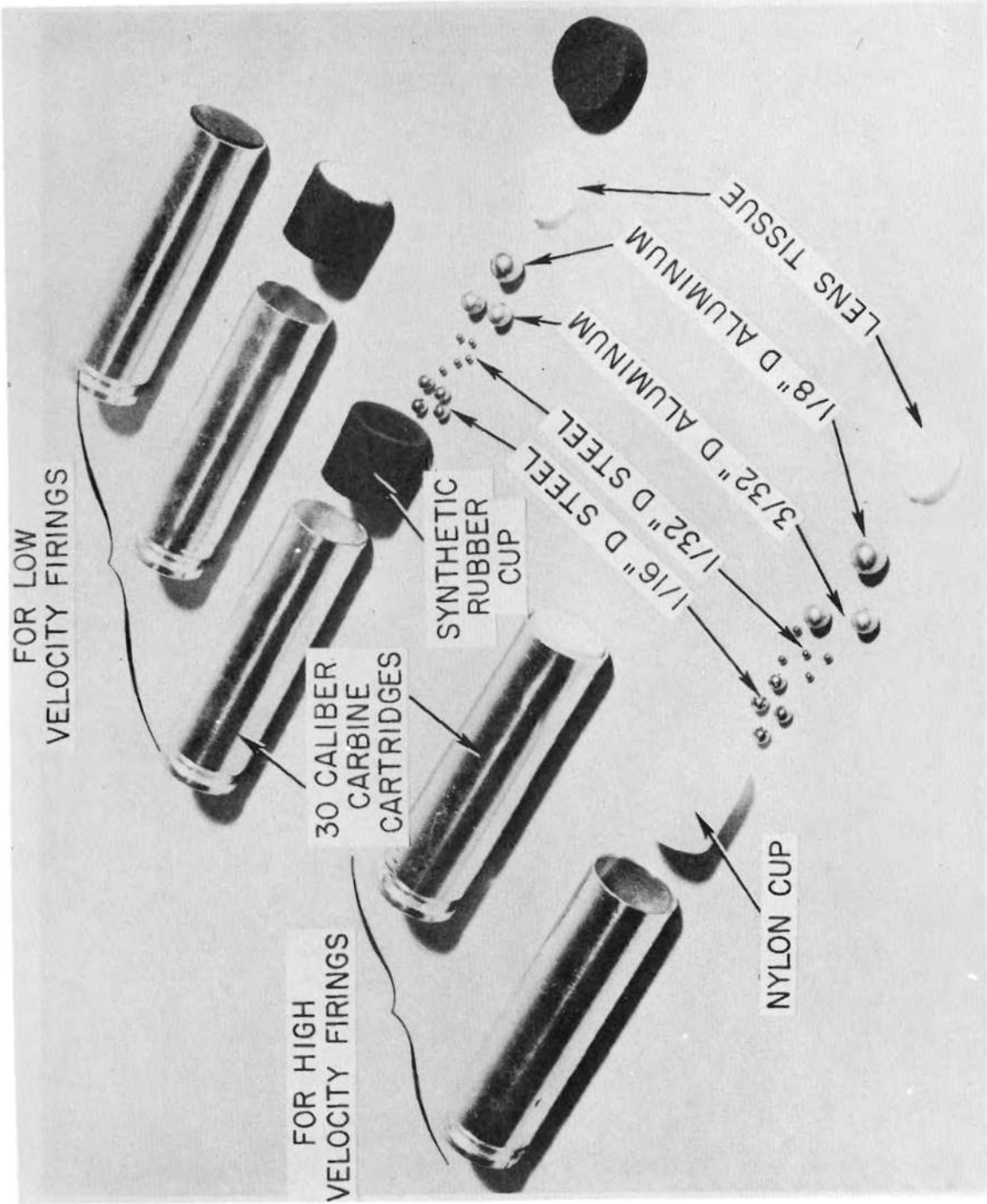


FIG. 5
SABOT FOR MULTIPLE LAUNCHING OF SPHERES

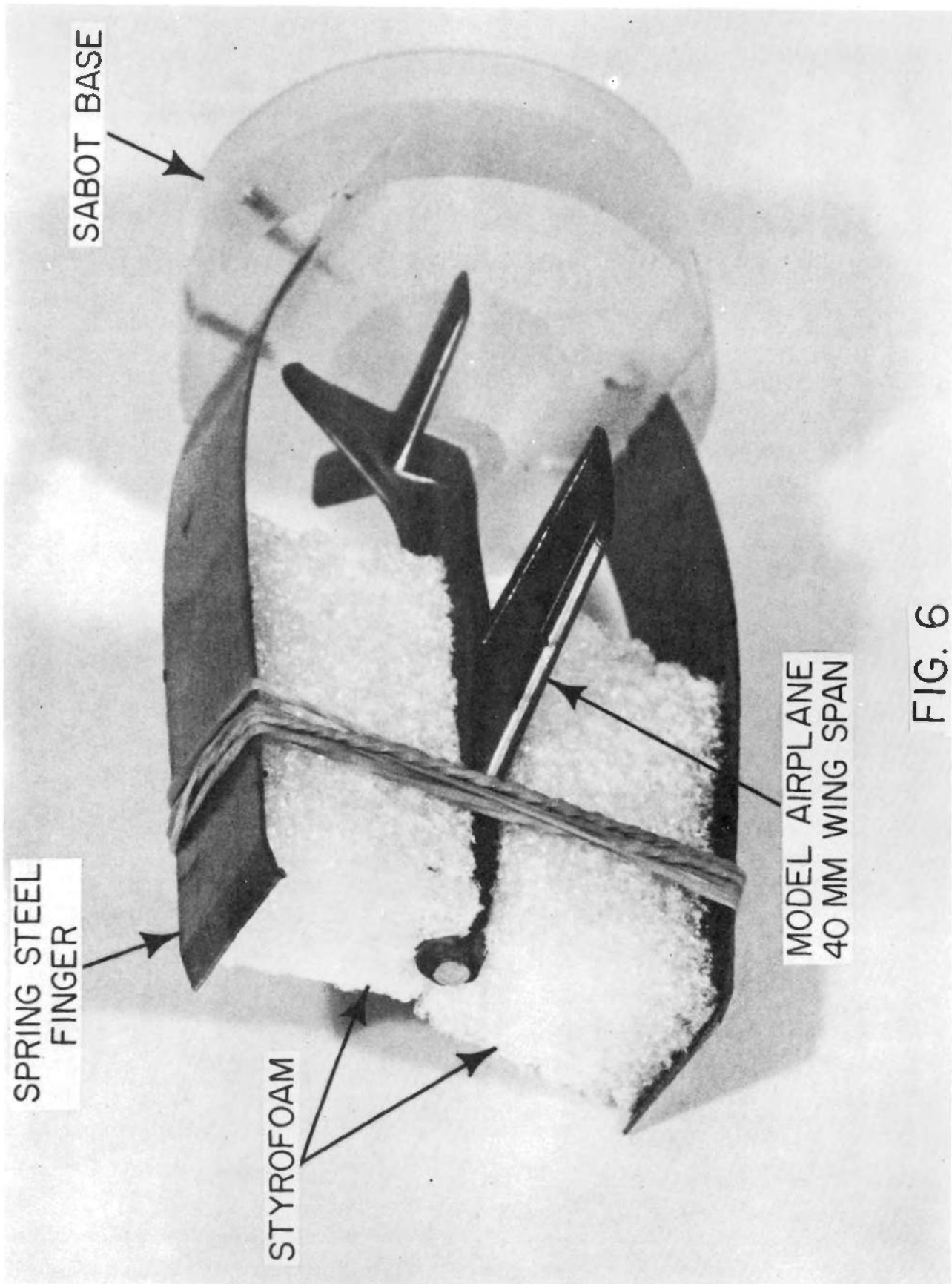


FIG. 6

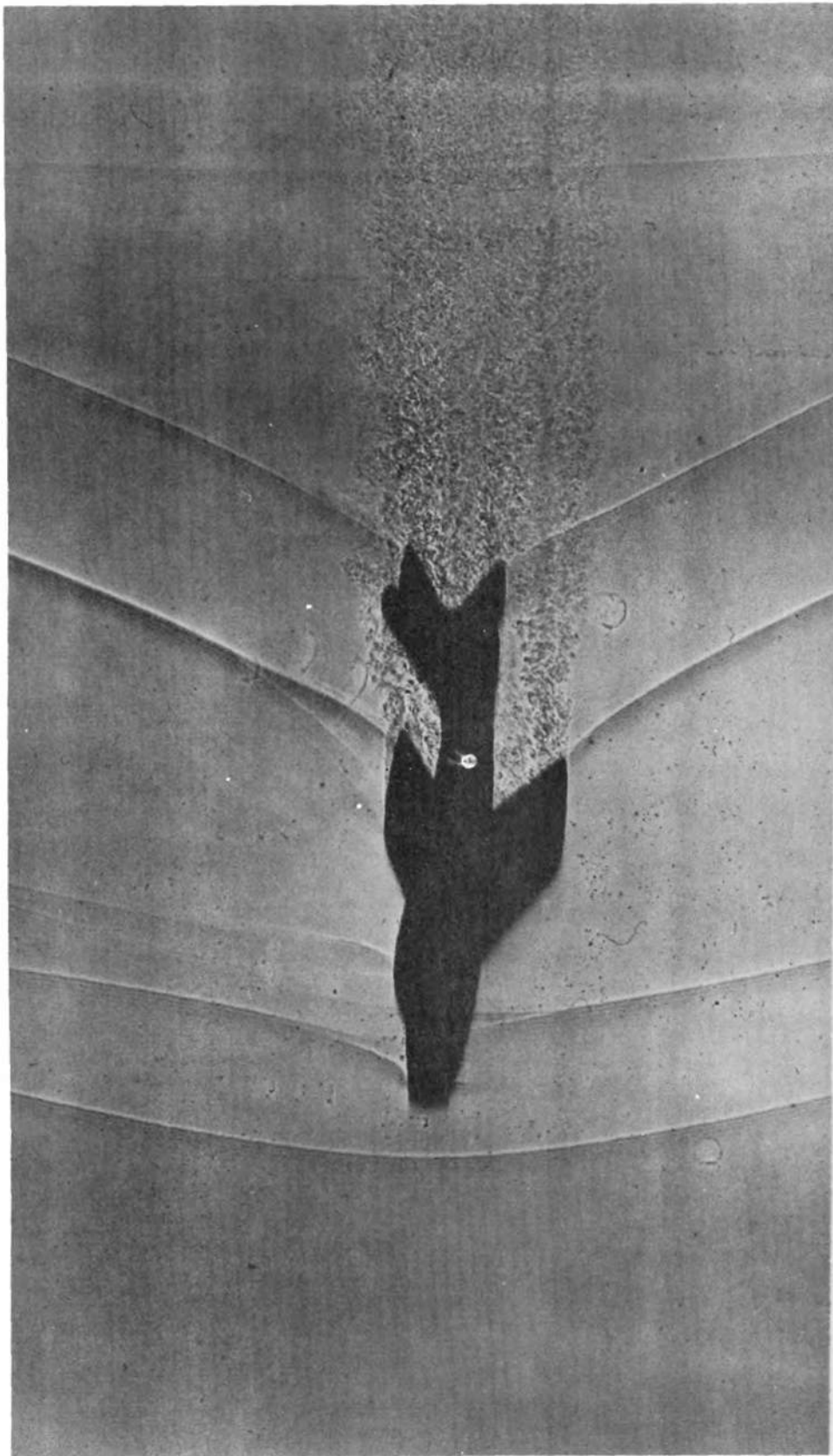


FIG. 7
MODEL AIRPLANE LAUNCHED IN THE
AERODYNAMIC RANGE

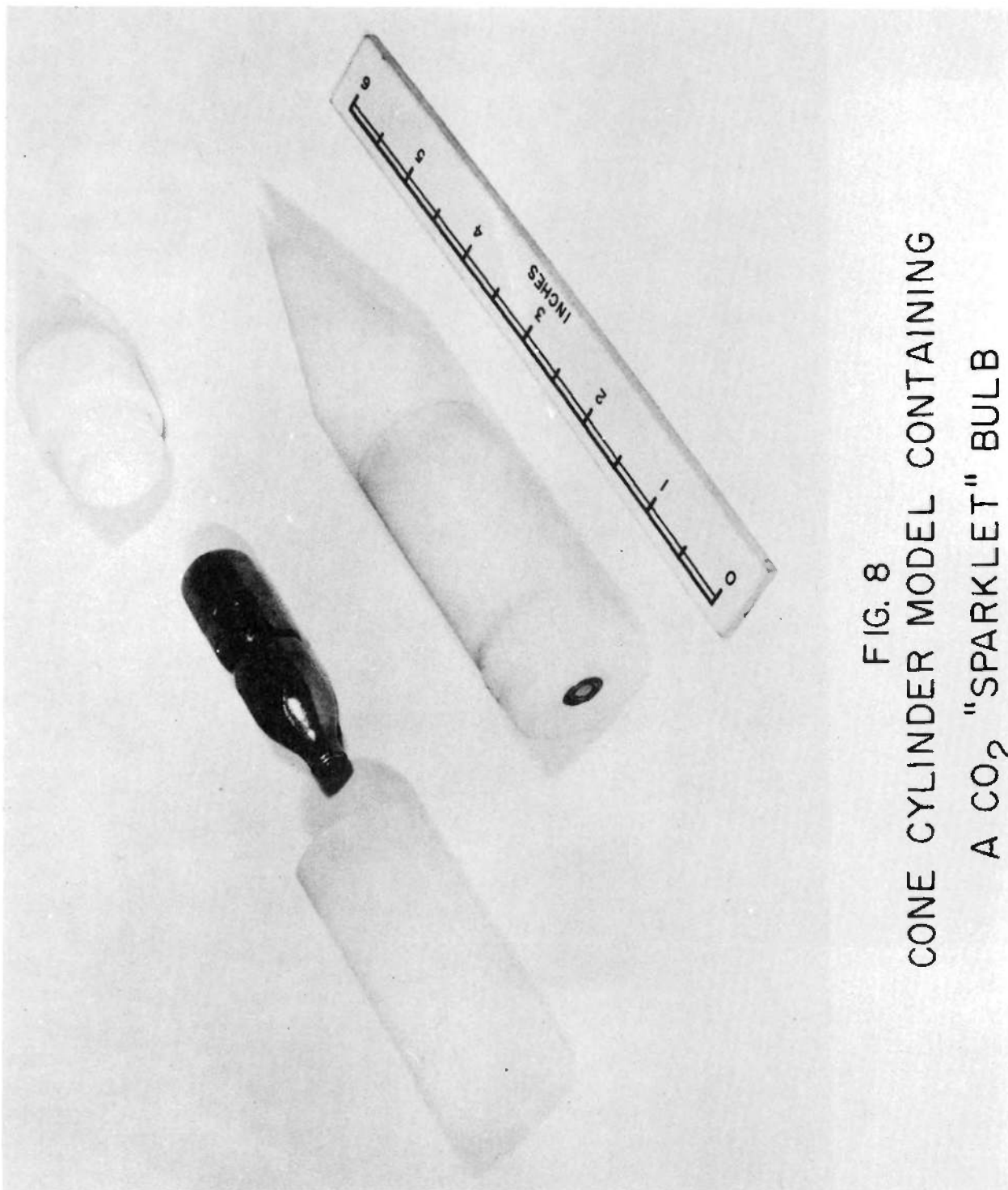


FIG. 8
CONE CYLINDER MODEL CONTAINING
A CO₂ "SPARKLET" BULB

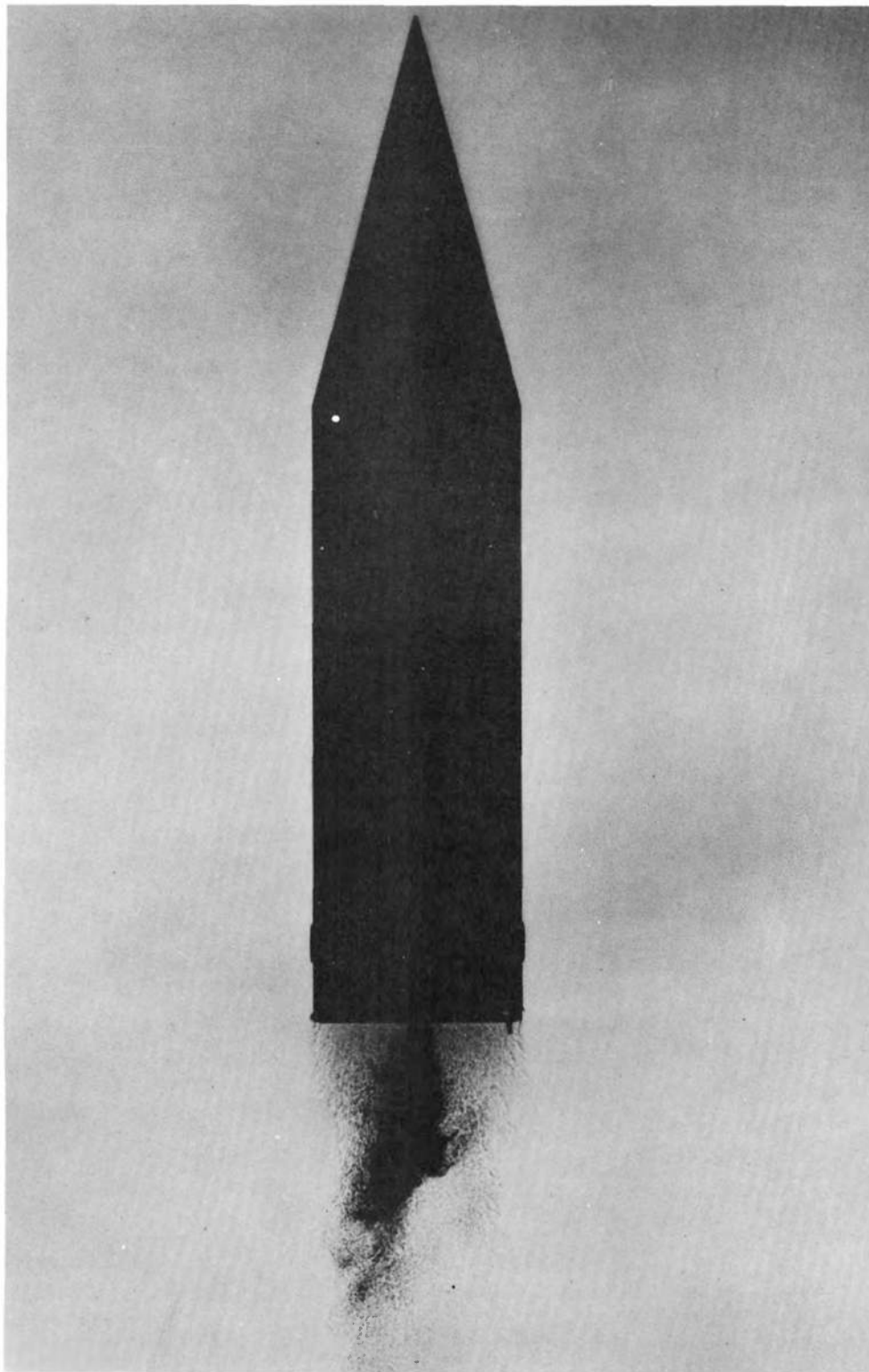


FIG. 9
CONE CYLINDER MODEL IN FREE-FLIGHT WITH A
COLD JET OF CO_2 EXHAUSTING FROM THE
MODEL BASE



1

4575

12

FIG. 10

X-RAY SAMPLE OF 30 MM FUZES BEFORE FIRING

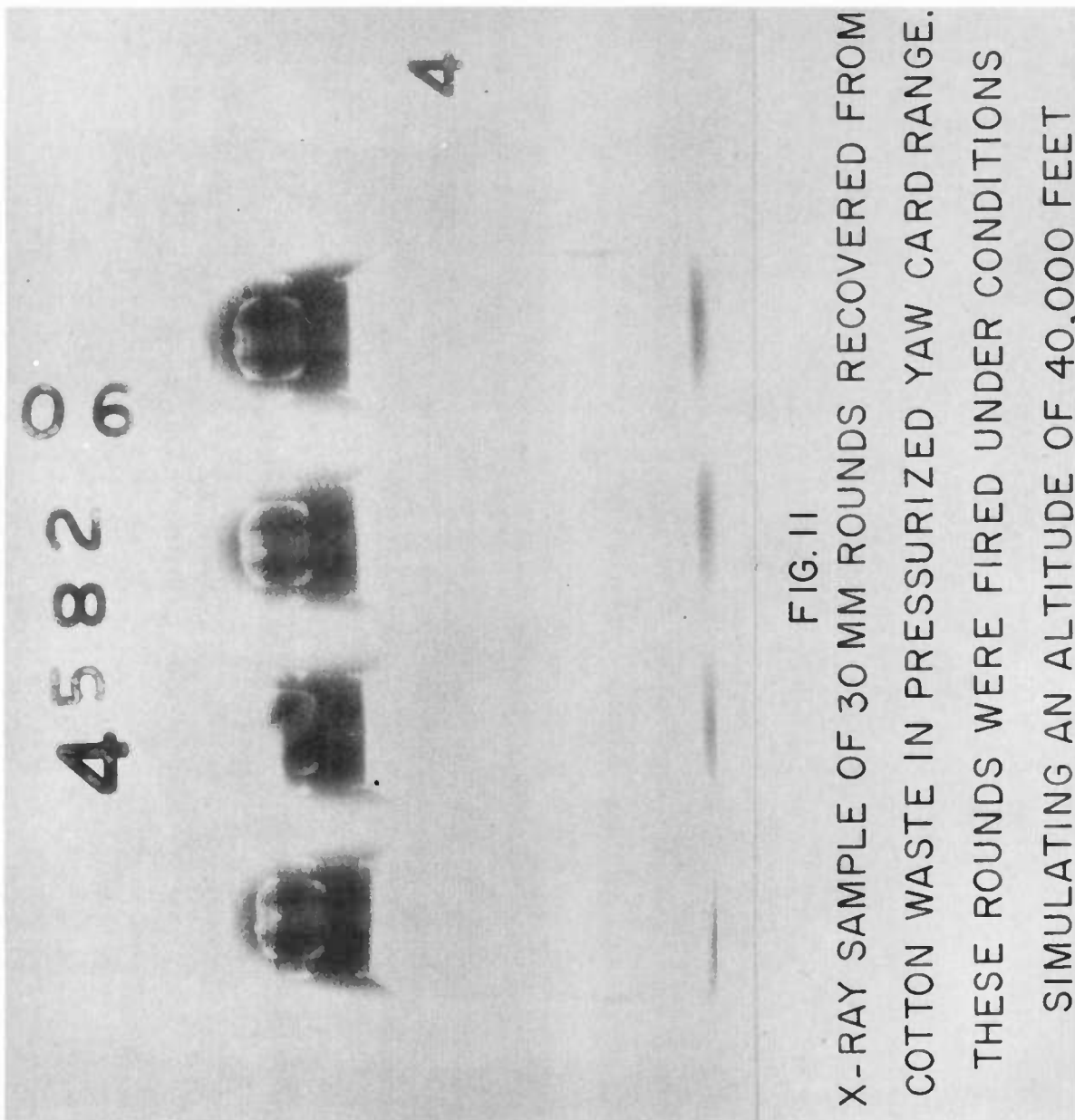


FIG. 11

X-RAY SAMPLE OF 30 MM ROUNDS RECOVERED FROM
COTTON WASTE IN PRESSURIZED YAW CARD RANGE.

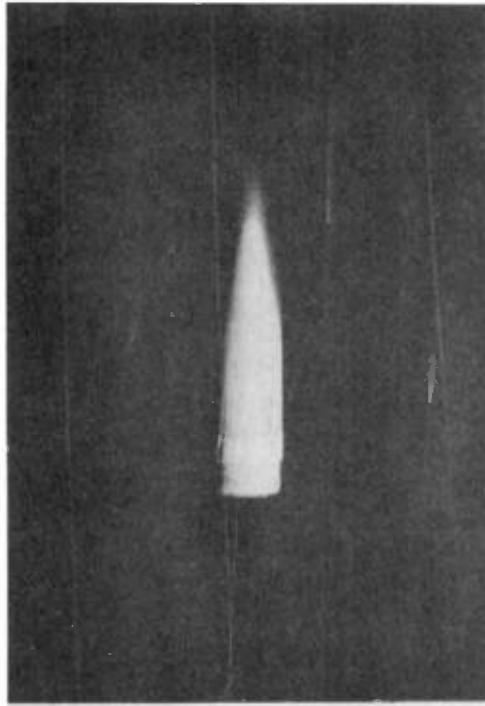
THESE ROUNDS WERE FIRED UNDER CONDITIONS

SIMULATING AN ALTITUDE OF 40,000 FEET

FREEZER TEMPERATURE = - 76° F

TIME FROM FREEZER
TO FIRING = 32 SECONDS

MUZZLE VELOCITY = 3800 FPS



FURNACE TEMPERATURE = 163° F

TIME FROM FURNACE
TO FIRING = 45 SECONDS

MUZZLE VELOCITY = 3300 FPS



FIG.12

MODELS WITH PLASTIC ROTATING BANDS

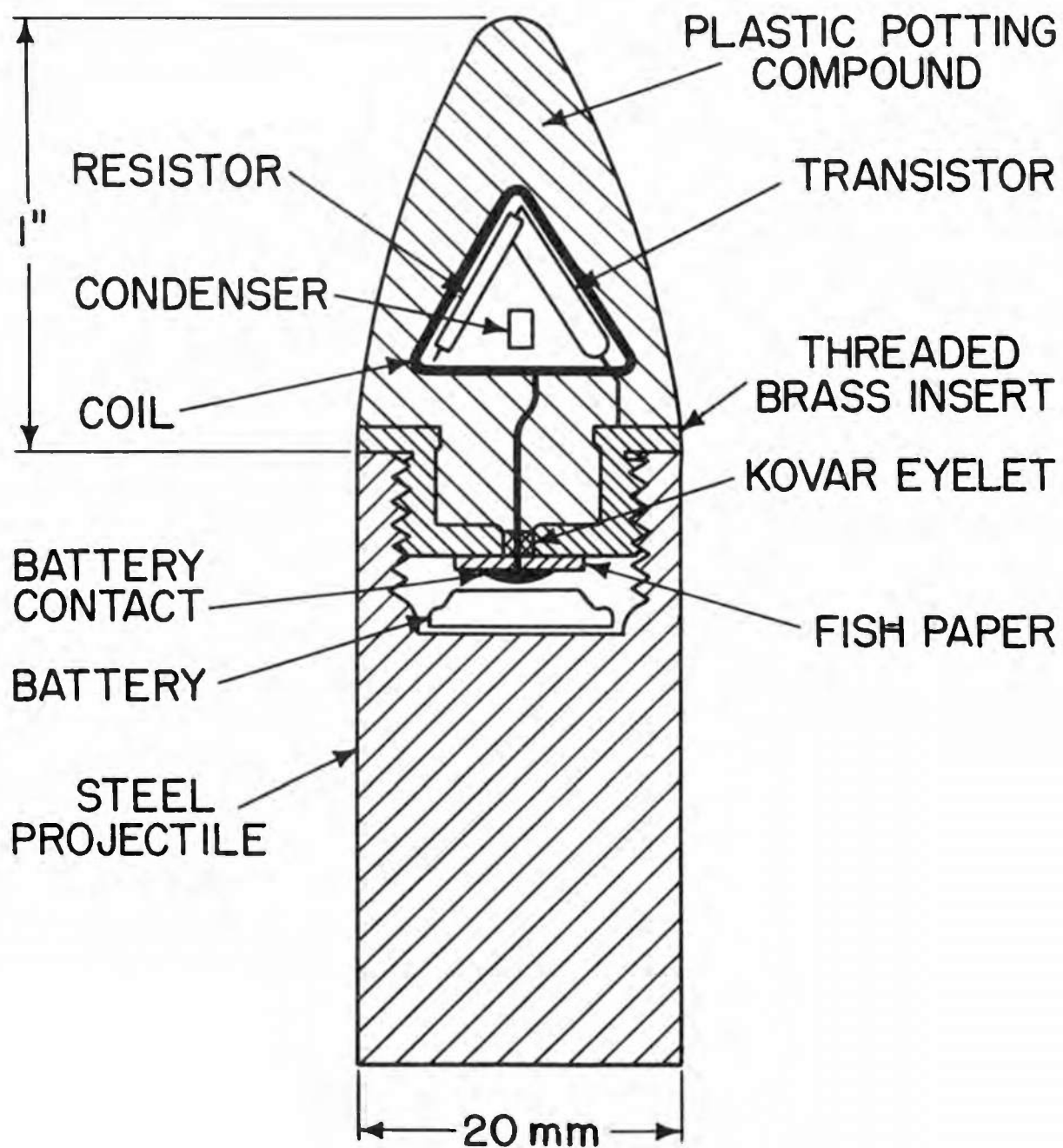
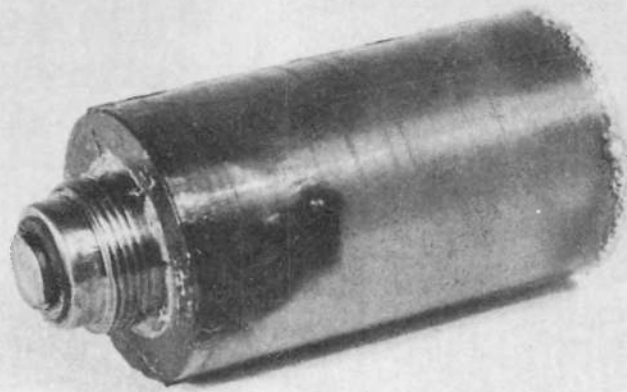
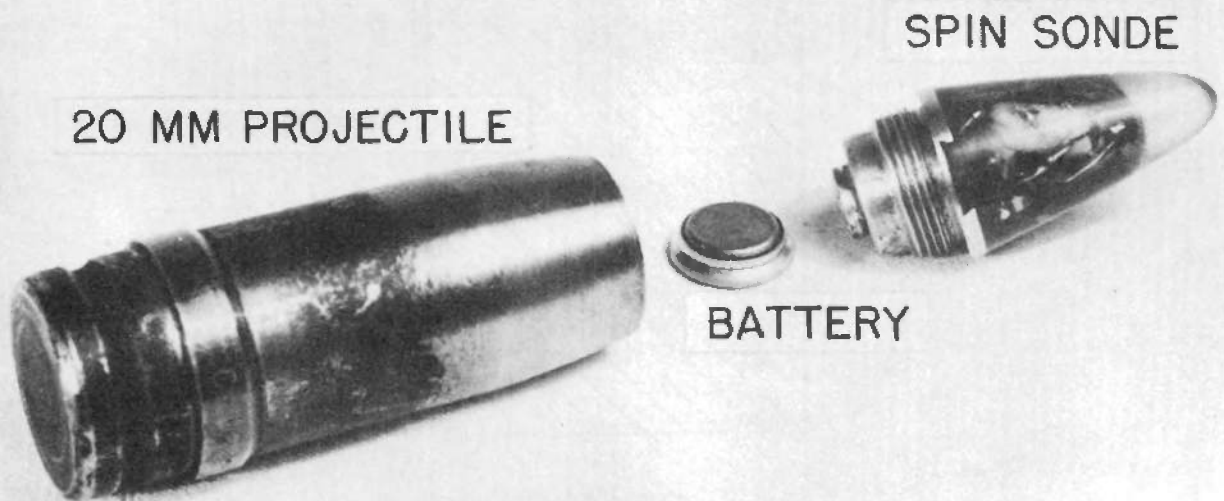


FIG. 13



SPIN SONDE AFTER POTTING



20 MM PROJECTILE

SPIN SONDE

BATTERY

FIG. 14

$$C_{D0} = 1.586$$

$$M = 7.99 \text{ AT STATION 12}$$

$$R_E = 0.304 \times 10^6$$

$$P_O = 50.9 \text{ MM HG}$$

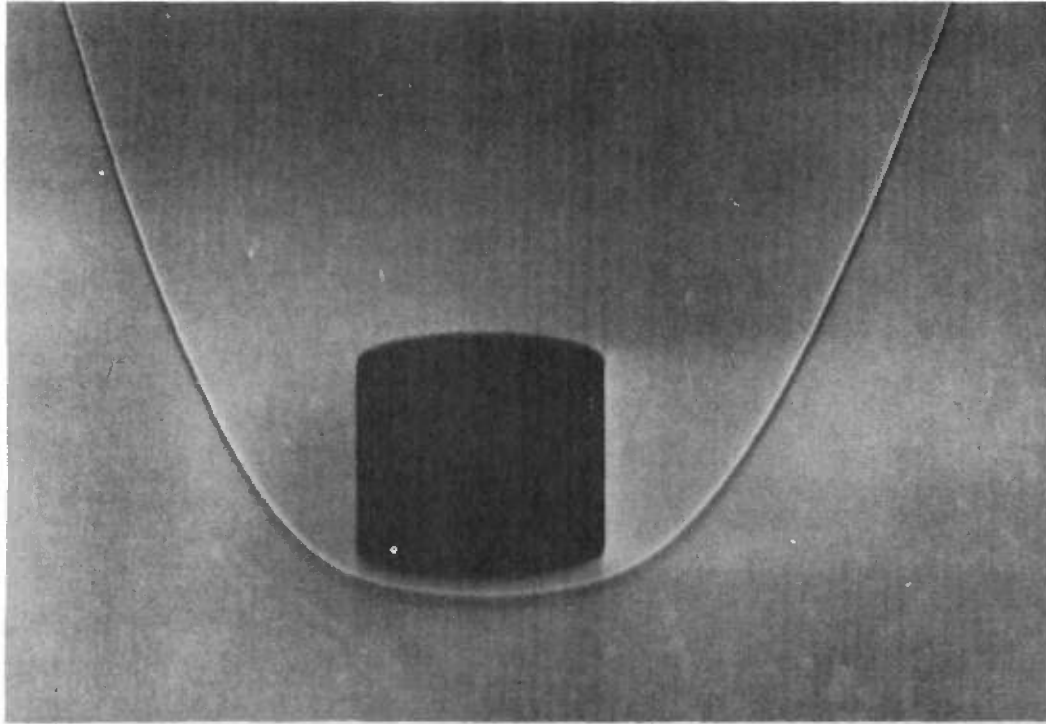


FIG. 15

A NYLON CYLINDER FIRED FROM A POWDER GUN
AT 9400 FPS

INTENTIONALLY LEFT BLANK.

APPENDIX

Part I

The following publications describe ranges presently in operation in North America.

1. Bull, G. V., "Some Aerodynamic Studies in the C.A.R.D.E. Aeroballistics Range", Canadian Aeronautical Journal, Vol. 2, No. 5, pp. 154-163, May 1956.
2. May, Albert and Williams, T. J., Free-Flight Ranges at the Naval Ordnance Laboratory, NAVORD Report 4063, July 1955.
3. Rogers, Walter K., Jr., The Transonic Free-Flight Range, BRL Report No. 849, Feb. 1953.
4. Seiff, Alvin, A Free-Flight Wind Tunnel for Aerodynamic Testing at Hypersonic Speeds, NACA Report 1222, May 1955.
5. Staff, Aeroballistics Laboratory, Dynamic Aeroballistic Evaluation, NOTS 1152, July 1955.

Part II

Additional information on North American range facilities can be obtained by writing to the following.

National Advisory Committee for Aeronautics
Ames Aeronautical Laboratory
Moffett Field, California
Attn: Mr. H. Julian Allen

Chief Superintendent
Canadian Armament Research and Development Establishment
P. O. Box 1427, Quebec, Province of Quebec, Canada
Attn: Dr. Gerald V. Bull

Commander
U. S. Naval Ordnance Test Station
China Lake, California
Attn: Dr. William Haseltine, Code 503

Commanding General
Aberdeen Proving Ground, Maryland
Attn: Dr. Boris G. Karpov, Ballistic Research Laboratories

Commander
U. S. Naval Ordnance Laboratory
White Oak, Silver Spring, Maryland
Attn: Dr. Albert May

DISTRIBUTION LIST

<u>No. of Copies</u>	<u>Organization</u>	<u>No. of Copies</u>	<u>Organization</u>
4	Chief of Ordnance Department of the Army Washington 25, D. C. Attn: ORDTB - Bal Sec ORDFU ORDFA ORDTX-AR	1	Commander Naval Air Development Ctr. Johnsville, Pennsylvania
		7	Commander Naval Ordnance Test Station China Lake, California Attn: Tech. Library W. R. Haseltine (Code 503) H. L. Newkirk (Code 503) E. B. Mayfield (Code 5015) W. H. Allan E. L. Dunn I. Highburg
10	British Joint Services Mission 1800 K Street, N. W. Washington 6, D. C. Attn: Mr. John Izzard, Reports Officer A. E. Clarke N. K. Walker		
10	Canadian Army Staff 2450 Massachusetts Ave. Washington 8, D. C. Of Interest to CARDE: G. V. Bull E. W. Greenwood G. H. Tidy D. A. G. Waldock D. W. Pounder H. R. Warren	2	Commander Naval Proving Ground Dahlgren, Virginia
		2	Commander Naval Research Laboratory Washington 25, D. C. Attn: W. W. Atkins R. H. Fuller
3	Chief, Bureau of Ordnance Department of the Navy Washington 25, D. C. Attn: ReO	13	Commander Naval Ordnance Laboratory White Oak Silver Spring, Maryland Attn: J. J. Brady V. C. Dawson J. N. Fedenia A. Greenwald R. K. Lobb H. H. Kurzweg J. E. Long A. May Z. I. Slawsky P. A. Thurston E. Winkler W. R. Witt F. De Merritt
2	Superintendent Naval Postgraduate School Monterey, California Attn: Dr. Head		
2	Commander Naval Air Missile Test Ctr. Point Mugu, California Attn: CT - 31 M. Fitzgerald		
1	Commanding Officer Naval Air Rocket Test Stn. Dover, New Jersey		

DISTRIBUTION LIST

<u>No. of Copies</u>	<u>Organization</u>	<u>No. of Copies</u>	<u>Organization</u>
1	Chief of Naval Research Code 438 Washington 25, D. C. Attn: F. S. Sherman	2	National Advisory Committee for Aeronautics 1512 H Street, N. W. Washington 25, D. C. Attn: I. H. Abbott R. E. May
5	Commander Wright Air Development Ctr. Wright-Patterson Air Force Base Ohio Attn: WCLSW - F. J. Huber WCLCO - M. Shorr WCLSS - Tung-Sheng Liu WCRR WCLSW-5	2	National Advisory Committee for Aeronautics Lewis Flight Propulsion Lab. 21000 Brookpark Road Cleveland 11, Ohio Attn: E. Reshotko F. K. Moore
1	Commander USAF Fighter Weapons School Nellis Air Force Base, Nevada	4	National Advisory Committee for Aeronautics Ames Aeronautical Lab. Moffett Field, California Attn: H. J. Allen T. Gearing L. Neice A. C. Charters
5	Commander Air Force Armament Center Eglin Air Force Base, Florida Attn: ACOTT ACB - C. M. Halton ACB - R. Jacobs ACB - J. E. Stevens ACB - A. S. Galbraith	6	National Advisory Committee for Aeronautics Langley Aeronautical Lab. Langley Field, Virginia Attn: J. D. Bird R. Hopko P. Huber A. Sabol C. E. Brown A. Busemann
4	Commander Air Research & Development Command P. O. Box 1395 Baltimore 3, Maryland Attn: Deputy for Development		
2	Commander Air Force Missile Test Center (MTE) Patrick Air Force Base, Florida	10	Director Armed Services Technical Information Agency Documents Service Center Knott Building Dayton 2, Ohio Attn: DSC-SD
2	U. S. Atomic Energy Commission Sandia Corporation P. O. Box 5400 Albuquerque, New Mexico Attn: H. R. Vaughn, Div. 5141 W. K. Cox	1	Assistant Secretary of Defense (R&D) The Pentagon, Room 3E116 Washington 25, D. C. Attn: I. Nestigen

DISTRIBUTION LIST

<u>No. of Copies</u>	<u>Organization</u>	<u>No. of Copies</u>	<u>Organization</u>
4	Director, JPL Ord Corps Installation Department of the Army 4800 Oak Grove Drive Pasadena 3, California Attn: M. Elmer H. R. Schurmier P. P. Wegener I. E. Newlan, Reports Group	1	Commanding Officer Chemical Corps Chemical and Radiological Labs. Army Chemical Center, Maryland
3	Assistant Secretary of Defense (R&D) Washington 25, D. C. Attn: Committee on Guided Missiles Committee on Ord. Committee on Aeronautics	3	Commanding Officer Picatinny Arsenal Dover, New Jersey Attn: Samuel Feltman Ammunition Labs.
2	Commanding General Frankford Arsenal Bridge and Tacony Streets Philadelphia 37, Pennsylvania	5	Commanding General Redstone Arsenal Huntsville, Alabama Attn: Technical Library W. D. Murphree D. H. Newby C. L. Northrop N. M. Shapiro
1	Commanding General Army Ballistic Missile Agency Huntsville, Alabama Attn: T. G. Reed	1	Johns Hopkins University Operations Research Office Department of the Army 7100 Connecticut Avenue Chevy Chase, Maryland Washington 15, D. C.
2	Commanding Officer Diamond Ordnance Fuze Labs. Building 92 Washington 25, D. C.	2	AVCO Manufacturing Company Advanced Development Corp. 20 South Union Street Lawrence, Massachusetts Attn: T. R. Munson W. B. Stephenson
1	Commanding Officer Watertown Arsenal Watertown 72, Massachusetts Attn: R. Muldoon	1	Commanding General Arnold Engineering Development Center Tullahoma, Tennessee Attn: Deputy Chief of Staff, R&D
1	Commanding Officer and Director David W. Taylor Model Basin Washington 7, D. C. Attn: Aerodynamics Lab.	1	THRU: District Chief Boston Ordnance Dist. Boston Army Base Boston 10, Mass.

DISTRIBUTION LIST

<u>No. of Copies</u>	<u>Organization</u>	<u>No. of Copies</u>	<u>Organization</u>
1	Armour Research Foundation of the Illinois Institute of Tech. Technology Center Chicago 16, Illinois Attn: Mr. W. Casier	1	Aircraft Armaments, Inc. Cockeysville, Maryland Attn: N. J. La Costa
	THRU: District Chief Chicago Ordnance Dist. 209 W. Jackson Blvd. Chicago, Illinois		THRU: Deputy Dist. Chief Baltimore Regional Office Philadelphia Ord. Dist. Main Post Office Baltimore 1, Maryland
4	Applied Physics Laboratory Johns Hopkins University 8621 Georgia Avenue Silver Spring, Maryland Attn: Mr. G. L. Seielstad R. H. Cramer L. L. Cronvich H. A. Wallskog	2	ARO, Inc. Gas Dynamic Facility Tullahoma, Tennessee Attn: M. K. Kingery A. J. Zazzi
	THRU: Naval Inspector of Ord. Applied Physics Lab. Johns Hopkins University 8621 Georgia Avenue Silver Spring, Maryland		THRU: District Chief Cincinnati Ord. Dist. Swift Bldg. 230 E. 9th Street Cincinnati 2, Ohio
2	Aerophysics Development Corp. P. O. Box 657 Pacific Palisades, Calif. Attn: Dr. W. Bollay D. Bitonda	3	Bell Aircraft Corporation P. O. Box 1 Buffalo 5, New York Attn: K. Pearce N. F. Meullen R. J. Whalen
	THRU: District Chief Los Angeles Ordnance Dist. 1 55 South Grand Avenue Pasadena, California		THRU: Air Force Plant Rep. Bell Aircraft Corp. Niagara Falls, New York
1	Adalia Limited 1410 Stanley Street Montreal 2, P. Q., Canada Attn: J. B. Reid		Boeing Airplane Company Bomber Weapons Unit (Mail Stop 18-54) Physical Research Staff Box 3707 Seattle 24, Washington Attn: D. Martin
	THRU: Canadian Army Staff 2450 Mass. Ave., N. W. Washington 8, D. C.		THRU: Air Force Plant Rep. Boeing Airplane Company Seattle, Washington

DISTRIBUTION LIST

<u>No. of Copies</u>	<u>Organization</u>	<u>No. of Copies</u>	<u>Organization</u>
1	Boeing Airplane Company Wichita, Kansas Attn: R. E. Wallace THRU: Air Force Plant Rep. Boeing Airplane Co. Wichita, Kansas	1	Chicago Midway Laboratories 6220 S. Drexel Avenue Chicago 37, Illinois Attn: M. F. Malis THRU: District Chief Chicago Ord. Dist. 209 W. Jackson Blvd. Chicago 6, Illinois
1	Boeing Airplane Company Plant 2 Seattle 14, Washington Attn: R. E. Bateman THRU: Air Force Plant Rep. Boeing Airplane Co. Seattle, Washington	3	Computing Devices of Canada, Ltd. P. O. Box 508 Ottawa, Ontario, Canada Attn: J. L. Howland C. B. Jeffery J. E. Smith THRU: Canadian Army Staff 2450 Mass. Avenue Washington 8, D. C.
1	Budd Company Red Lion Plant Philadelphia 15, Pennsylvania THRU: Deputy Dist. Chief Philadelphia Ord. Dist. 128 N. Broad Street Philadelphia 2, Pa.	1	Chance-Vought Aircraft, Inc. P. O. Box 5907 Dallas, Texas THRU: Bureau of Aero. Rep. Naval Industrial Reserve Plant Aeronautical P. O. Box 5907 Dallas, Texas
4	CONVAIR Div. of General Dynamics Corp. San Diego, California Attn: C. W. Frick E. Katz M. F. Romig S. V. Starr THRU: Bureau of Aero. Rep. CONVAIR San Diego, California	1	CONVAIR Division of General Dynamics Corp. Pomona Division P. O. Box 1011 Pomona, California THRU: Naval Inspector of Ord. 1675 West 5th Street Pomona, California Cornell University Graduate School of Aero. Engrg. Ithaca, New York Attn: Dr. W. R. Sears THRU: Bureau of Aero. Rep. P. O. Box 235 Buffalo 21, New York
1	Cornell Aero. Laboratory, Inc. 4455 Genesee Street Buffalo 21, New York Attn: Miss E. T. Evans, Library 1 THRU: Bureau of Aero. Rep. Cornell Aero. Lab., Inc. P. O. Box 235 Buffalo 21, New York		

DISTRIBUTION LIST

<u>No. of Copies</u>	<u>Organization</u>	<u>No. of Copies</u>	<u>Organization</u>
1	CONVAIR Div. of General Dynamics Corp. Fort Worth 1, Texas Attn: Mr. L. W. Bonnell THRU: Air Force Plant Rep. CONVAIR Fort Worth 1, Texas	1	Defense Research Board Room 4735 "A" Building Ottawa, Ontario, Canada Attn: J. L. Oatway THRU: Canadian Army Staff 2450 Mass. Ave., N. W. Washington 8, D. C.
3	CONVAIR Div. of General Dynamics Corp. Ord. Aerophysics Laboratory Daingerfield, Texas Attn: J. E. Arnold R. J. Volluz K. L. Goin THRU: Assistant Inspector of Naval Material Ord. Aerophysics Lab. Daingerfield, Texas	1	Directorate of Armament Dev. Army Headquarters Ottawa, Ontario, Canada Attn: W. B. Snarr THRU: Canadian Army Staff 2450 Mass. Avenue, N. W. Washington 8, D. C.
2	Canadair, Pl. Y P. O. Box 6087 Montreal, P. Q., Canada Attn: D. A. Jackman H. J. Luckert THRU: Canadian Army Staff 2450 Mass. Avenue, N. W. Washington 8, D. C.	1	Douglas Aircraft Co., Inc. El Segundo Division 827 Lapham Street El Segundo, California Attn: F. C. Newton THRU: Air Force Plant Rep. Douglas Aircraft Corp. 3855 Lakewood Blvd. P. O. Box 200 Long Beach 1, Calif.
1	Canadian Westinghouse Co. Electronic Division Longwood Road Hamilton, Ontario, Canada Attn: J. N. Leavitt THRU: Canadian Army Staff 2450 Mass. Ave., N. W. Washington 8, D. C.	3	Douglas Aircraft Co., Inc. Engineering Department 3000 Ocean Park Blvd. Santa Monica, California Attn: R. M. Wood, Library W. S. Cohen H. Klein THRU: District Chief Los Angeles Ord. Dist. 55 South Grand Ave. Pasadena 2, Calif.
1	Chamberlain Corp. Waterloo, Iowa Attn: E. R. Caponi THRU: Dist. Chief Chicago Ord. Dist. 209 W. Jackson Blvd. Chicago 6, Illinois		

DISTRIBUTION LIST

<u>No. of Copies</u>	<u>Organization</u>	<u>No. of Copies</u>	<u>Organization</u>
1	Emerson Electric Manufacturing Company 8100 W. Florissant Avenue St. Louis 21, Missouri Attn: Mr. G. Hauser THRU: St. Louis Air Procurement District Oklahoma City Air Materiel Area 1114 Market Street St. Louis, Missouri	1	General Electric Company Schenectady, New York Attn: Mr. F. V. Johnson, A&OE THRU: Rochester Ord. Dist. Branch Office General Electric Co. Bldg. 23, Room 232 Schenectady, New York Attn: Lt. Col. Davies
1	Firestone Tire and Rubber Co. Defense Research Division 1200 Firestone Parkway Akron 17, Ohio Attn: V. E. Lucas THRU: District Chief Cleveland Ord. Dist. Lincoln Bldg. 1367 E. 6th St. Cleveland 14, Ohio	2	General Mills, Inc. Engineering Research and Dev. 2003 E. Hennepin Avenue Minneapolis 13, Minnesota Attn: R. I. Hakomaki R. C. Huntington, Mech. Div. THRU: Milwaukee Air Procurement District 770 N. Plankinton Ave. Milwaukee, Wisconsin
6	General Electric Company 3198 Chestnut Street Philadelphia 4, Pennsylvania Attn: V. Kebely R. F. Peck J. Powers A. M. Smith W. R. Warren Y. A. Yoler THRU: Philadelphia Air Procurement Dist. 1411 Walnut Street Philadelphia 2, Penna.	3	Grumman Aircraft Engrg. Corp. Engineering Plant No. 5 Bethpage, New York Attn: R. L. Gustafson A. E. Munier R. A. Scheuing THRU: Bureau of Aero. Rep. Grumman Aircraft Engrg. Corp. Bethpage, L.I., New York
		2	Hughes Aircraft Company Aerodynamics Department Florence Avenue at Teal St. Culver City, California Attn: I. Naiman W. L. Phillips THRU: Air Force Plant Rep., WEAPD Hughes Aircraft Co. Florence Ave. at Teal St. Culver City, California

DISTRIBUTION LIST

<u>No. of Copies</u>	<u>Organization</u>	<u>No. of Copies</u>	<u>Organization</u>
1	M. W. Kellogg Company Foot of Danforth Avenue Jersey City 3, New Jersey Attn: Miss E. M. Hedley	1	Mass. Institute of Tech. Naval Supersonic Lab. 80-208 560 Memorial Drive Cambridge, Massachusetts Attn: F. H. Durgin
	THRU: Inspector of Naval Material Naval Industrial Reserve Shipyard Bldg. 13, Port Newark Newark 5, New Jersey		THRU: Inspector of Naval Material Dev. Contract Dept. Mass. Inst. of Tech. Cambridge 39, Mass.
3	Lockheed Aircraft Corp. Missile Systems Division Van Nuys, California Attn: E. Bershaded E. T. Cannon R. S. Swanson	1	Massachusetts Institute of Tech. Instrumentation Laboratory Cambridge 39, Massachusetts Attn: L.E. Wilkie (41-203
	THRU: Air Force Plant Rep., WEAD Lockheed Aircraft Corp. Factory "A", P.O. Box 551 Burbank, California		THRU: Inspector of Naval Material Dev. Contract Dept. Mass. Inst. of Tech. Cambridge 39, Mass.
1	Lockheed Aircraft Corp. Factory "A" P. O. Box 551 Burbank, Calif. Attn: Mr. Ed Baldwin	2	McDonnell Aircraft Corporation P. O. Box 516 St. Louis 3, Missouri Attn: R. M. Flesh R. E. Rohtert
	THRU: Air Force Plant Rep., WEAPD Lockheed Aircraft Corp. Factory "A", P.O. Box 551 Burbank, California		THRU: Bureau of Aero. Rep. McDonnell Aircraft Corp. P. O. Box 516 St. Louis 3, Missouri
4	Glenn L. Martin Company Baltimore, Maryland Attn: J. M. Bidwell M. L. Coon L. L. Jackson T. Reisert	1	National Research Council of Canada Defense Research Board Ottawa, Ontario, Canada
	THRU: Bureau of Aero. Rep. Glenn L. Martin Co. Baltimore 3, Maryland		THRU: Canadian Army Staff 2450 Mass. Avenue Washington 8, D. C.
		1	North American Aviation, Inc. Columbus, Ohio Attn: W. Simon
			THRU: Air Force Plant Rep. North American Aviation, Inc. Columbus Plant Columbus, Ohio

DISTRIBUTION LIST

<u>No. of Copies</u>	<u>Organization</u>	<u>No. of Copies</u>	<u>Organization</u>
4	North American Aviation, Inc. Missile Development Division 12214 Lakewood Blvd. Downey, California Attn: E. Briggs J. K. Dew R. B. Oliver J. Elms	1	Princeton University Head, Gas Dynamics Laboratory James Forrestal Research Center Princeton, New Jersey Attn: Prof. S. M. Bogdonoff
	THRU: Air Force Plant Rep. North American Aviation, Inc. Los Angeles International Airport Los Angeles 45, Calif.	2	THRU: Office of Naval Research 246 Broadway New York 13, New York
			The Ramo-Woolridge Corporation 5730 Arbor Vitae Street Los Angeles 45, California Attn: A. Ambrosio W. D. Hayes
1	North American Aviation, Inc. Los Angeles International Airport Los Angeles, California Attn: J. Covert G. Bussiere	3	THRU: District Chief Los Angeles Ord. Dist. 55 S. Grand Avenue Pasadena, California
	THRU: Air Force Plant Rep., WEAPD North American Aviation, Inc. Los Angeles International Airport Los Angeles, California		Republic Aviation Corporation Scientific Staff Farmingdale, New York Attn: W. McIlroy C. Rennemann R. Sanator
1	North Carolina State College Raleigh, North Carolina Attn: Prof. J. W. Cell	1	THRU: Air Force Officer-In-Charge Republic Aviation Corp. Farmingdale, L.I., New York
	THRU: District Chief Philadelphia Ord. Dist. 128 North Broad St. Philadelphia 2, Pa.		Republic Aviation Corporation Guided Missiles Division 233 Jericho Turnpike Mineola, New York Attn: R. M. Kennedy
1	Northrop Aircraft, Inc. Dept. 3483 Ogden Air Material Area Hawthorne, California Attn: D. C. Olmore	2	THRU: Air Force Officer-In-Charge Republic Aviation Corp. Farmingdale, L.I., New York
	THRU: Air Force Plant Rep., WEAPD Northrop Aircraft, Inc. Hawthorne, California		A. V. Roe Canada, Ltd. Aircraft Division Malton, Ontario, Canada Attn: J. A. Chamberlin W. Taylor
			THRU: Canadian Army Staff 2450 Mass. Ave., N. W. Washington 8, D. C.

DISTRIBUTION LIST

<u>No. of Copies</u>	<u>Organization</u>	<u>No. of Copies</u>	<u>Organization</u>
1	Sperry Gyroscope Company Div. of The Sperry Corp. Great Neck, L.I., New York Attn: J. J. Gallagher, Federal Dept.	1	University of Texas Military Physics Research Lab. 500 East 24th Street Austin, Texas THRU: Office of Naval Research Box 7786, University Stn. Austin 12, Texas
	THRU: Assistant Inspector of Naval Material c/o Sperry Gyroscope Co. Div. of Sperry Corp. Great Neck, L.I., N. Y.	1	United Aircraft Corporation Research Department East Hartford 8, Connecticut
1	University of Michigan Aero. Research Center Willow Run Airport Ypsilanti, Michigan Attn: J. E. Corey THRU: Commander Central Air Proc. Dist. W. Warren & Lonyo Aves. Detroit 32, Michigan		THRU: Bureau of Aero. Rep. Pratt and Whitney Aircraft Division United Aircraft Corp. East Hartford 8, Conn.
		1	Wright Aeronautical Division Curtiss-Wright Corporation Wood-Ridge, New Jersey Attn: Sales Dept. (Gov't)
3	University of Minnesota Rosemount Aero. Laboratories Rosemount, Minnesota Attn: R. V. Deleo R. Herman F. A. Moynihan		THRU: Air Force Plant Rep. Wright Aero. Division Curtiss-Wright Corp. Wood-Ridge, N. J.
		1	Westinghouse Electric Corporation Air Arm Division Friendship International Airport Baltimore, Maryland
1	University of Southern Calif. Engineering Center 3518 University Avenue Los Angeles 7, California Attn: H. R. Saffell, Director	1	THRU: Bureau of Aero. Rep. Glenn L. Martin Co. Baltimore 3, Maryland Professor George Carrier Division of Applied Science Harvard University Cambridge 38, Massachusetts
	THRU: Office of Naval Research Branch Office 1030 E. Green Street Pasadena, California		

DISTRIBUTION LIST

<u>No. of Copies</u>	<u>Organization</u>
1	Captain W. S. Diehl, USN, Ret. 4501 Lowell Street, N. W. Washington 16, D. C. THRU: National Advisory Committee for Aeronautics Subcommittee on Stability and Control 1512 H Street, N. W. Washington 25, D. C.
1	Professor C. B. Millikan Guggenheim Aeronautical Laboratory California Institute of Technology Pasadena 4, California
1	Dr. A. E. Puckett Hughes Aircraft Company Culver City, California
1	Dr. L. H. Thomas Watson Scientific Computing Laboratory 612 West 116th Street New York 27, New York

DISTRIBUTION LIST

To Receive UNCLASSIFIED Part Only

<u>No. of Copies</u>	<u>Organization</u>
1	California Institute of Technology Pasadena, California Attn: Library
1	Guggenheim Aeronautical Laboratory California Institute of Technology Pasadena, California Attn: Prof. H. W. Liepman
1	Professor Francis H. Clauser, Jr. Department of Aeronautics Johns Hopkins University Baltimore 18, Maryland
1	Institute of the Aeronautical Sciences, Inc. 2 E. 64th Street New York 21, New York Attn: John J. Glennon, Librarian
1	Professor J. B. Eades Engineering Department Virginia Polytechnic Institute Blacksburg, Virginia
1	Professor R. Truitt Engineering Department Virginia Polytechnic Institute Blacksburg, Virginia